




Universitat Autònoma de Barcelona

ADVERTIMENT. L'accés als continguts d'aquesta tesi queda condicionat a l'acceptació de les condicions d'ús establertes per la següent llicència Creative Commons:  http://cat.creativecommons.org/?page_id=184

ADVERTENCIA. El acceso a los contenidos de esta tesis queda condicionado a la aceptación de las condiciones de uso establecidas por la siguiente licencia Creative Commons:  <http://es.creativecommons.org/blog/licencias/>

WARNING. The access to the contents of this doctoral thesis it is limited to the acceptance of the use conditions set by the following Creative Commons license:  <https://creativecommons.org/licenses/?lang=en>

Influence of Organic Semiconductors Morphology, Structure and Processability on Organic Field-Effect Transistors Performance

Antonio Campos García

Under the supervision of Dr. Marta Mas Torrent

And tutored by Prof. Roser Pleixats Rovira

September 2018

Institut de Ciència de Materials de Barcelona

PhD Programme in Material Science

Universitat Autònoma de Barcelona

MARTA MAS TORRENT, Investigadora Científica del Consejo Superior de Investigaciones Científicas (CSIC) a l'Institut de Ciència de Materials de Barcelona (ICMAB) i **ROSER PLEIXATS ROVIRA**, Catedràtica de la Universitat Autònoma de Barcelona (UAB)

CERTIFIQUEN

Que en Antonio Campos García ha realitzat sota la seva direcció el treball que porta per títol “Influence of Organic Semiconductors Morphology, Structure and Processability on Organic Field-Effect Transistors Performance”, i que queda recollit en aquesta memoria per optar al grau de Doctor en Ciència de Materials.

I perquè així consti, signen el present certificat.

Dra. Marta Mas Torrent

Prof. Roser Pleixats Rovira

Bellaterra, 10 de setembre de 2018

ACKNOWLEDGEMENTS

Primero de todo me gustaría agradecer a la Dra. Marta Mas, a la Prof. Concepció Rovira y al Prof. Jaume Veciana por darme la oportunidad de realizar la tesis doctoral en su grupo y así haber podido entrar en el mundo de la investigación. Me gustaría agradecer especialmente a la Dra. Marta Mas por la dirección de la tesis. Su trabajo e implicación han sido fundamentales para la realización de este trabajo. También me gustaría agradecerle su paciencia y sus consejos que tanto me han ayudado a crecer personalmente.

Del mismo modo me gustaría agradecer al Dr. Raphael Pfattner su ayuda, enseñanzas e ideas que me ayudaron mucho al principio de la tesis.

The work carried out in this thesis would not have been possible without collaborations. Because of that, I would like to thank all the collaborators which have contributed to the research done in this thesis.

First I would like to thank Dr. Shi-Xia Liu, Dr. Yang Geng and all the other collaborators from the University of Bern for carrying out the synthesis of some TTF derivatives that made possible part of this thesis. I would also like to thank Dr. Stefan T. Bromley from the University of Barcelona for his theoretical calculations that added value and confirmed the hypothesis we extracted during our experimental work.

Especialment m'agradaria donar les gràcies al Prof. Joaquim Puigdollers per permetre'm utilitzar el seu laboratori, pels seus consells i per la seva ajuda amb les parts més físiques de la tesi.

También me gustaría agradecer a Ana Pérez, Esther Barrena y Carmen Ocal su estudio de AFM de los films de TTF-TCNQ.

I thank Dr. Maxim Shkunov of the Advanced Technology Institute (ATI) of the University of Surrey for hosting me during the three months of my stay there and for his help and his ideas. Thanks to Ruth and Kaspar for all the moments we shared and because you helped me to feel more like home.

Finally I would like to thank the people of the OFET team for the shared moments in the lab. Thanks to Dr. Francesca Leonardi and Qiaoming Zhang for their help regarding EGOFETs and, especially, to Qiaoming for helping me with some experiments while I was doing my stay in the University of Surrey. Thanks to Dr. Ajayakumar Murugan Rathamony for his help with the synthetic part. Thanks to Dr. Stamatios Georgakopoulos and Dr. Sergi Galindo for their help with the equipment and for the fruitful discussions, and to Dr. Tommaso Salzillo for his help regarding the polymorphism and the Raman and IR spectroscopy. Also thanks to Inés, Adrián and Simona and all the rest of the people that were always ready to give me a hand when I needed it.

ACKNOWLEDGEMENTS

Dejando de lado la parte científica, durante este tiempo en el ICMA B he tenido la suerte de trabajar en un ambiente muy agradable donde me he sentido parte del grupo desde el primer día y donde he estado rodeado de gente amable siempre dispuesta a ayudar. Por eso, por hacer mi día a día mucho más ameno y por otras muchas cosas, gracias a todos los miembros del grupo Nanomol. ¡Sois geniales! Me gustaría mencionar especialmente a aquellos que han estado durante toda la tesis o la mayor parte de ella, como son Francesc, Kike, Antonio y Amable.

Por último, me gustaría agradecerle a Inés todo el apoyo, sobre todo el personal pero también el científico, que me ha dado durante la tesis y por los ánimos en los momentos bajos. Sin ella esta tesis no hubiera sido posible. Muchas gracias por todo.

CONTENTS

Chapter 1: Introduction and Objectives

1.1. Organic Electronics	1
1.2. Organic Semiconductors	3
1.3. Charge Transport in Organic Semiconductors	9
1.4. Structure-Performance Relationship in Organic Semiconductors	13
1.5. Polymorphism	16
1.6. Charge Transport in Single-Crystals vs. Thin-Films	19
1.7. Organic Semiconductor Deposition Techniques	20
1.8. Organic Field-Effect Transistors	30
1.9. Objectives	42
1.10. References	43

Chapter 2: Correlation of Crystal Structure and Device Performance in OFETs based on Tetrathiafulvalene Derivatives

2.1. Introduction and Objectives	51
2.2. HOMO Stabilisation of π -Extended TTF Derivatives	54
2.3. Study of the π -Extension Impact on the Structure and Electronic Properties of TTF Derivatives	66
2.4. Summary	75
2.5. References	77

Chapter 3: A Sulfur-Bridged Annulene Derivative as Active Material for High Performance OFETs

3.1. Introduction and Objectives	81
3.2. Synthesis of DPTTA	83

3.3. Thin-Film Preparation and Characterisation	84
3.4. OFET Electrical Characterisation	90
3.5. EGOFET Electrical Characterisation	94
3.6. Summary	98
3.7. References	99

Chapter 4: Impact of Polymorphism and Morphology in a Thin-Film of a Benzothieno Benzothiophene Derivative on the OFET Performance

4.1. Introduction and Objectives	103
4.2. Effect of the Polymer Molecular Weight	108
4.3. Effect of the Deposition Speed and Temperature	114
4.4. Polymorph Stability	125
4.5. Device Architecture	128
4.6. Summary	135
4.7. References	136

Chapter 5: Solution-Processed OFETs based on Blended *n*-Type Semiconductors: the Role of the Polymer Binder

5.1. Introduction and Objectives	139
5.2. OFETs Prepared by BAMS Employing Blends of TCNQ:PS	141
5.3. OFETs Prepared by BAMS Employing Blends of PDI8CN2:PS	149
5.4. Summary	164
5.5. References	165

Chapter 6: Spray Printing of Organic Contacts and Organic Semiconductors

6.1. Introduction and Objectives	169
6.2. Spray Printing of TTF-TCNQ Electrodes for OFETs	172

6.3. Spray Printing on Antisolvent for the Formation of Organic Semiconductor Single-Crystals	182
6.4. Summary	188
6.5. References	189

Chapter 7: Experimental Methods

7.1. Materials	193
7.2. Organic Semiconductor Synthesis	197
7.3. OFET Fabrication	200
7.4. Organic Semiconductor Characterisation	206
7.5. Thin-Film and Single-Crystal Characterisation	207
7.6. Electrical Characterisation	209
7.7. References	211

Conclusions	213
--------------------	------------

CHAPTER 1 INTRODUCTION AND OBJECTIVES

1.1. ORGANIC ELECTRONICS

Silicon-based technology and devices have dominated the electronic panorama since it was born with the fabrication of the first operative field-effect transistor back in 1954 in Bell laboratories by Morris Tannenbaum. Since then, electronics have been progressively appearing in almost every aspect of our lives helping us to carry out things that were unthinkable half a century ago. In 1956 Gordon Moore, co-founder of Intel, described which is known today as Moore's law. That law was the observation that every 18-24 months the number of transistors in an integrated circuit doubles its number. Nowadays, we are able to have $2 \cdot 10^{10}$ transistors per microprocessor (e.g. the microprocessor Epyc 7601 – AMD) encouraging concepts like *Big Data* or *Internet of Things (IoT)* that require quick data processing. However, not all future applications require high-performance microprocessors, and for some applications other properties like low production cost, low power consumption, light-weight or flexibility are more desired. For those applications, the use of organic compounds and polymers as materials for electronics is becoming more and more important.

Talking of organic materials is talking about all the carbon-based molecules and polymers. These compounds display a range of properties such as light-weight,^[1] flexibility,^[2–5] tunability,^[6–8] and compatibility with printing processes.^[9–11] In particular, organic electronics is the subfield inside electronics that focus on the use of these materials for the fabrication of classic and innovative electronic devices. The term organic electronics was born together with the discovery of the first organic metal tetrathiafulvalene-tetracyanoquinodimethane (TTF-TCNQ) back in 1973 by Saitoh *et al.*^[12] The field of organic electronics includes all the devices where the active part is fabricated with organic materials. The most studied organic based devices are organic light-emitting diodes or OLEDs, organic solar cells or OPVs and organic field-effect transistors or OFETs.

OLEDs are, generally speaking, devices made of thin-film layers of organic materials sandwiched between two electrodes that emit light when stimulated by an electric current. The operation principle behind OLEDs is the emission of light caused by the recombination of holes and electrons. The first functional OLED was fabricated in 1987 by Tang *et al.*^[13] and nowadays they are arising great perspectives due to the emission of 'white light'.

The second type is the organic solar cell. These are devices made of organic materials that absorb light from the sun and turn it into electrical power. The physics behind the operation of

OPVs is the excitation of electrons in the electron-donor/electron-acceptor material interface forming an exciton (a quasiparticle formed by an electron and a hole) which is broken into a free electron and a free hole that diffuse to the electrodes generating electric current.

The third possible application of organic electronics is the OFET. In these devices, the current between two electrodes flows through an organic semiconductor (OSC). The resistance of this organic semiconductor is modulated by the strong electric field created by a third electrode. The first OFET ever fabricated was reported in 1987 by Koezuka *et al.*^[14] In that example the inorganic semiconductor of the traditional transistor was replaced by the organic oligomer polythiophene.

Since the moment organic electronics was born three decades ago, there has been an intensive community effort to develop this new concept. This effort has been focused on different approaches but pursuing the same goal: to develop this new field and to make it possible to produce real devices using this technology. Among the most relevant strategies we can find the following: i) design and synthesis of new organic semiconductors with improved electrical properties and solubility, ii) development of new methodologies to process organic semiconductors and also the other necessary parts of the devices and make those techniques compatible with roll-to-roll (R2R) processes to bring them closer to the large scale manufacturing, and iii) investigation of new geometries and structures to take advantage of the properties of these materials and overcome their drawbacks. Altogether has resulted in a remarkable improvement of the properties of the devices. As a matter of fact, nowadays, OFETs performance overcome the results obtained for amorphous silicon,^[15–18] organic solar cells have increased their efficiency reaching values of 13%^[19,20] and OLEDs are now being strongly used in commercial displays due to their high brightness.^[21]



Figure 1.1. 10.7" display produced by Plastic Logic GmbH made of organic devices.^[22]

1.2. ORGANIC SEMICONDUCTORS

ORGANIC SEMICONDUCTORS vs. INORGANIC SEMICONDUCTORS

Inorganic materials can be classified regarding their electrical resistivity (ρ), which is the fundamental property that quantifies how strongly a given material opposes to the flow of electric current. In this classification one can differentiate between metals, insulators and semiconductors. Metals exhibit low ρ values, typically below $10^{-6} \Omega\cdot\text{m}$, indicating their low resistance to the flow of electric current. On the other hand, insulators oppose strongly to the flow of electrons ($\rho > 10^{10} \Omega\cdot\text{m}$). These are the two extreme cases but in the middle we can find semiconductors, that typically exhibit values between $10^{10} \Omega\cdot\text{m}$ and $10^{-6} \Omega\cdot\text{m}$. Furthermore, these materials can be classified by what it is known as band gap, which is the energy necessary to promote an electron from the valence band to the conduction band of the inorganic semiconductor. In metals there is not a band gap because the valence and the conduction bands are not separated. However, in semiconductors the band gap is usually small enough to be overcome with thermal energy, in contrast to insulators, where the conduction band is not accessible from the valence band due to the large energy necessary to overpass the gap.^[23]

Inorganic semiconductors can be turned into more efficient semiconductors (extrinsic semiconductors) or even into conductors by introducing dopant atoms into their structure. Also, the unique property that makes semiconductors so especial is that their conductivity can be turned upon the influence of an electric field.

In addition, these three classes of materials also have different dependence of the ρ with the temperature. Metals increase their resistivity when the temperature is increased because the vibration of the crystal structure increases with the temperature. These vibrations or phonons scatter the flow of electrons, and hence reduce their speed making the material more resistive to the flow of current. On the other hand, semiconductors exhibit the opposite behaviour; an exponential decrease of the electrical resistivity is observed as the temperature rises and it is caused by the increase of free charges.

Alternatively, organic conductors are based on molecules or polymers formed mainly by C and H atoms in combination with other elements such as S, P, Se, etc. We can also classify these materials as metals, semiconductors or insulators, however, due to their intrinsic properties the conductivity values that they exhibit and the transport mechanisms differ strongly from inorganic materials.

Microscopically, inorganic semiconductors consist in atoms such as Si or Ge covalently bounded forming a giant net of atoms as depicted in **Figure 1.2a**. Thanks to the covalent bounds, the atoms inside this net are very close and their individual atomic orbitals fuse with the surrounding atoms forming bands of electronic orbitals that extend along the whole material. The energy of these covalent bounds that form inorganic semiconductors is

estimated to be in the range of 150 -1100 KJ/mol. On the other hand, organic semiconductors (OSCs) are formed by discrete small molecules or polymers that interact with each other through weak van de Waals forces (0.05 – 40 kJ/mol).^[24] An example of the supramolecular structure of an organic semiconductor (*i.e.* pentacene) is shown in **Figure 1.2b**. Hence, while the charge transport in inorganic semiconductors takes place *via* delocalised states following a band transport, the conductivity in organic materials is determined by the relative position of the π - π orbitals and the overlap between the molecular orbitals.

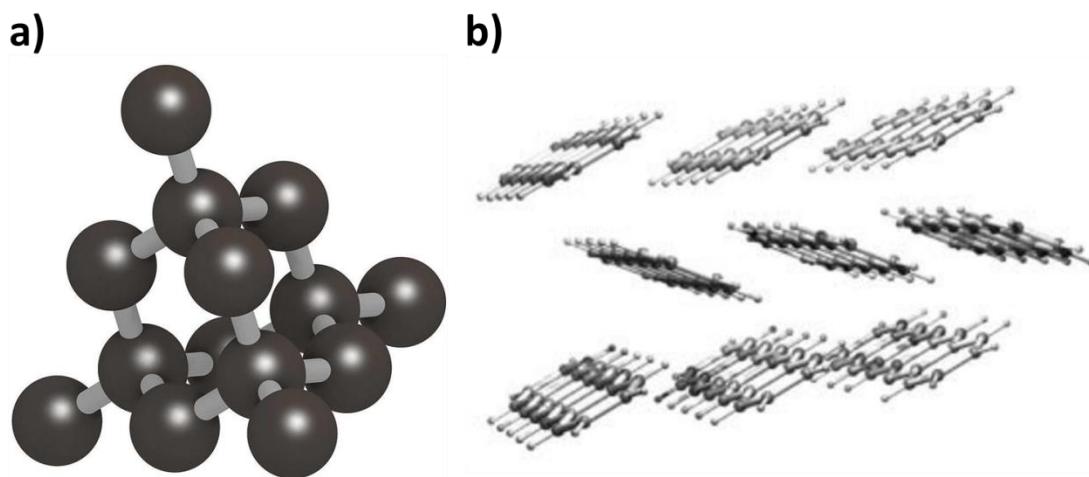


Figure 1.2. Crystal structures of **(a)** silicon and **(b)** the organic semiconductor pentacene.

The weaker interconnection between molecules, compared to the covalent bounds in inorganic semiconductors, in organic semiconductors result in lower speeds of electronic transport (*i.e.* mobility). For example, while high quality polycrystalline silicon displays an electron mobility of 1400 cm²/V·s and a hole mobility of 450 cm²/V·s,^[23] the best mobility values obtained for benchmark organic semiconductors are in the order of 10 cm²/V·s.^[15,16,25]

One of the main motivations in the development of organic electronics is the potential to process them at low cost and at lower temperatures compared to Si-based technology. Silicon for example, needs to be purified by costly procedures in highly controlled inert atmosphere for obtaining the slices of the giant silicon virtually defect-free single crystal that are known as wafers. Then, ions need to be implanted in order to, after the thermal treatments at high temperature, convert the non-doped silicon (*i.e.* intrinsic silicon) into the well-known high performance *p*-type or *n*-type semiconductor. These procedures produce a high-quality material that is the best material for high performance electronics. On the other hand, OSCs can be thermally evaporated in vacuum or processed using solution-based methodologies. In addition, due to the fact that these processes do not require high temperatures, organic semiconductors can be processed on plastic substrates, opening the door to the so-called flexible electronics.

It is also important to take into account that the goal of organic electronics is not to substitute inorganic electronics, which will be still the most important materials regarding high performance devices like for example processors or high efficiency solar cells, but to open a path to new technologies that involve the use of plastics and take advantage of properties such as flexibility, low-cost and light-weight.

ORGANIC SEMICONDUCTORS

Chemically speaking, OSCs are electroactive small conjugated molecules or polymers with a strongly π -conjugated system.^[18,26] In these conjugated systems there is a delocalisation of the π -electrons around the molecule that reduces the stress on the molecule of carrying a positive or a negative charge. Therefore, OSCs can be reduced or oxidised within an accessible potential. One can differentiate between three classes of OSCs by their polarity: *p*-type, *n*-type and ambipolar OSCs.

Firstly, *p*-type OSCs usually are electron donor molecules that can be easily oxidised and consequently their highest occupied molecular orbital (HOMO) energy is high (most *p*-type OSCs display an HOMO energy around -5.0 eV). In *p*-type OSCs, the majority of charge carriers are holes. On the other hand, *n*-type OSCs are electron acceptor molecules that can be easily reduced and display a low energy lowest unoccupied molecular orbital (LUMO) usually around -4.0 eV. In *n*-type OSCs the vast majority of charge carriers are electrons. Finally, ambipolar OSCs are a combination of *p*-type and *n*-type and can transport both holes and electrons depending on the electric field applied.

However, it has been demonstrated that OSCs are inherently ambipolar as they can transport holes or electrons depending on the work function of the metal employed to inject charges.^[27,28] However, the HOMO/LUMO energy also determines the stability of the semiconductor in ambient conditions, *i.e.* the resistance to water, oxygen and other adventitious agents. It was studied for arylene diimide-based *n*-type semiconductors that a LUMO energy lower than -4.0 eV was required to have a transistor able to work in air.^[6,29] In the case of *p*-type OSCs, HOMO energies lower than -5.0 eV are desired for improving the stability of OSCs, otherwise the semiconductor can be doped by the oxygen.^[30]

The lower intrinsic stability of *n*-type OSCs and the difficulty of synthesising molecules with such a low LUMO energy are the main reasons why, so far, *p*-type OSCs have been more studied and have displayed the best performances.^[15,17,31,32] However, even if for the majority of applications that involve the use of OSCs only one polarity is needed (*i.e.* display controllers, sensors, etc.), for making use of the so-called complementary metal-oxide semiconductor (CMOS) technology the use of *p*- and *n*-type semiconductors exhibiting similar performances is required. This technology is appealing for the development of devices with a reduced power consumption and an enhanced signal to noise ratio.

As previously mentioned, there are two types of OSCs: conjugated polymers and conjugated small molecules.

Polymer OSCs can be defined as long chains of interconnected electroactive and aromatic groups. These materials cannot be evaporated due to their high molecular weight and therefore, they can only be processed from solution. In solid state, the best performing films based on polymer OSCs are organised in microcrystalline structures that are embedded in an amorphous polymer matrix. In order to improve the order in solid state, polymers based on electron acceptor units combined with electron donor units (*i.e.* donor-acceptor copolymers) have been synthesised resulting in a significant increase of the performance. Although it is difficult to characterise the supramolecular structure of a polymer, it has been demonstrated by 2D-NMR that in these systems the attractive forces between electron-deficient and electron-rich groups has been the key factor to this improvement of the charge transport.^[33] The use of donor moieties like dithiopheneindeno[1,2-b]fluorene (TIF) or cyclopentadithiophene (CDT) together with acceptor unities like benzothiadiazole (BTZ) has resulted in donor-acceptor copolymers with remarkable hole mobilities of 3 and 10 cm²/V·s, respectively.^[34,35] Another example is the copolymer of naphthalenediimide (NDI) and bithiophene (2T) that has displayed *n*-type behaviour displaying mobility values in the same order that the mentioned *p*-type OSCs.^[52,53,54] The chemical structures of the mentioned polymers differentiating the donor and acceptor units are depicted in **Figure 1.3**.

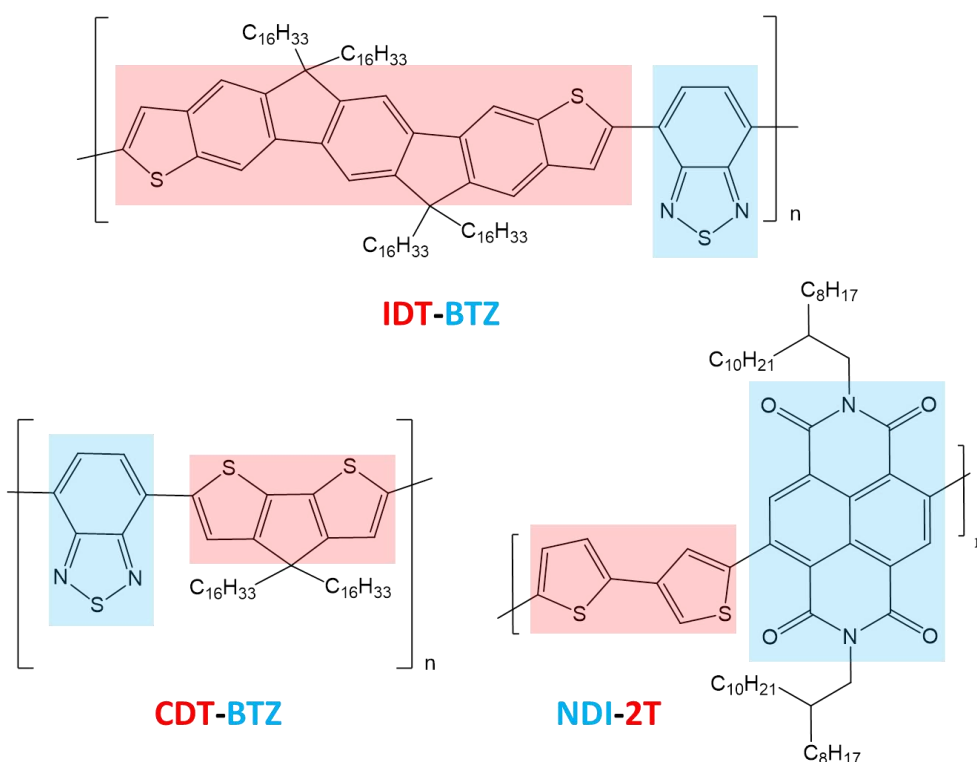


Figure 1.3. Benchmark donor-acceptor copolymers organic semiconductors. The red and blue parts indicate the electron donor and acceptor moieties, respectively.

On the other hand, conjugated small-molecule OSCs can be either thermally evaporated or deposited using solution-based techniques to obtain polycrystalline thin-films or single-crystals. Although single-crystals are not suitable for the mass-production of devices, they can reveal insight into the dominant charge transport mechanisms or unveil its structure-properties relationship. This information can help to improve the performance of a family of OSCs and also extract valuable knowledge for designing other semiconductors. Furthermore, small-molecule OSCs have displayed higher performances than polymer-based OSCs due to its higher structural order. Examples of benchmark small molecules are the *p*-type OSCs 6,13-bis(triisopropylsilylethynyl) pentacene (TIPS-pentacene), rubrene, 2,8-difluoro-5,11-bis(triethylsilylethynyl)anthradithiophene (diF-TESADT), dinaphtho[2,3-*b*:2',3'-*f*]thieno[3,2-*b*]thiophene (DNNT), dithiophenetetrathiafulvalene (DT-TTF), 2,7-dioctyl[1]benzothieno[3,2-*b*][1]benzothiophene (C8BTBT) and the *n*-type OSCs 6,13-bis((triisopropylsilyl)ethynyl)-5,7,12,14-tetraazapentacene (TIPS-TAP), N,N'-bis(n-octyl)-dicyanoperylene-3,4:9,10-bis(dicarboximide) (PDI8CN2) and the family of chlorinated naphthalenediimide with perfluoroalkyl chains as for example NDIF5Cl2.^[17,25,39] All of the mentioned small-molecule OSCs (**Figure 1.4**) have been reported to display state-of-the-art performances, some of them with mobility values around 10 cm²/V·s.

In this thesis we have focused our work on the study of small-molecule OSCs and from now on we will centre our attention on this class of materials.

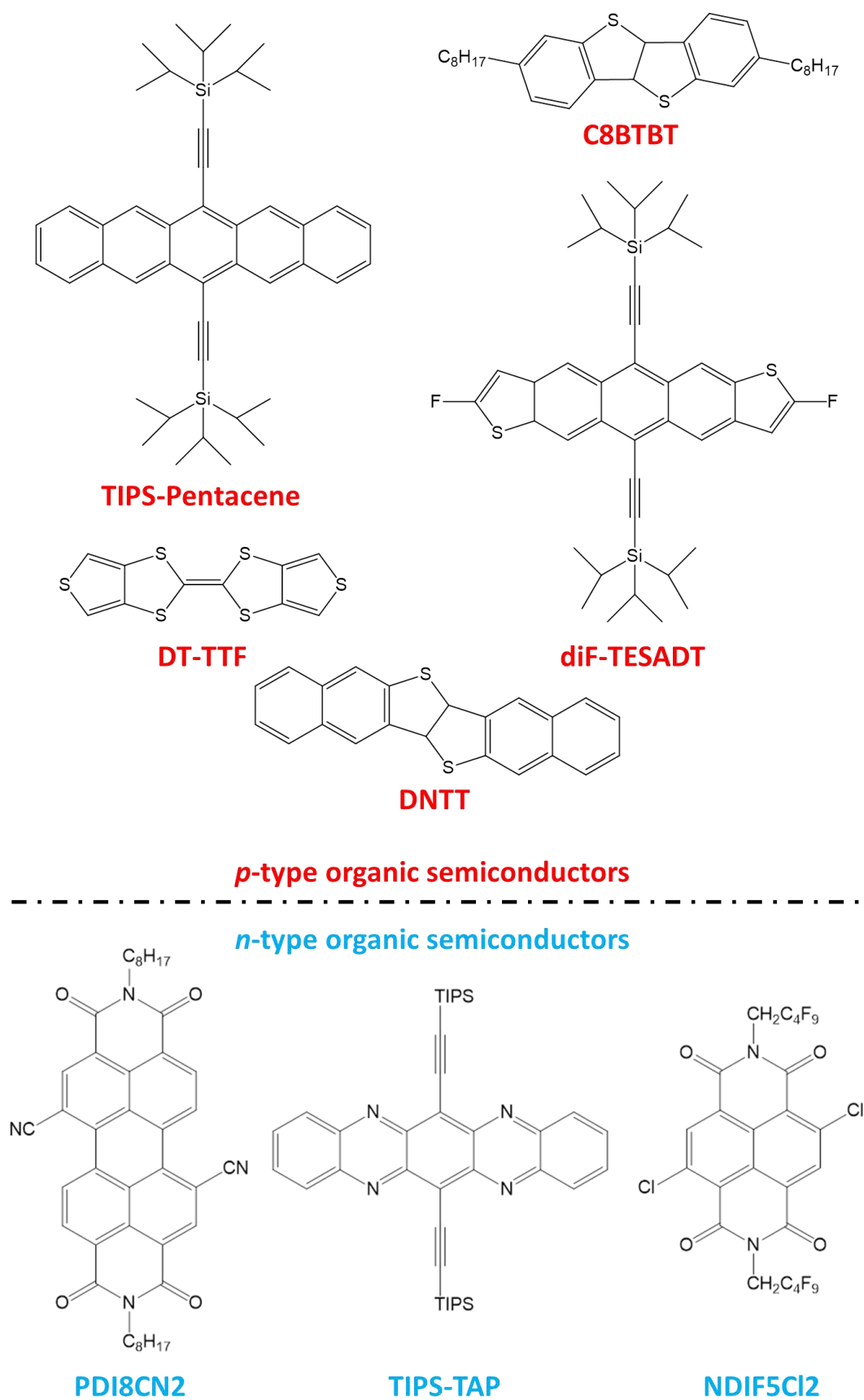


Figure 1.4. Molecular structures of benchmark small-molecule *p*- and *n*-type OSCs.

1.3. CHARGE TRANSPORT IN ORGANIC SEMICONDUCTORS

Although in OSCs it is difficult to associate a charge transport mechanism to a system, two extreme different transport regimes can be differentiated depending on if the charge-carriers are localised, *i.e.* hopping transport, or if they are not, *i.e.* band transport. Hopping transport is the most common charge transport regime associated to organic semiconductors, especially to those OSCs displaying low mobility values. It is defined like the regime in which the charge-carriers are localised and their movement is limited by the formation of polarons, which are quasiparticles composed by the charge-carrier and the changes produced in the crystalline structure caused by that charge. In other words, the presence of the charge produces a change in the carrying molecule, modifying its conformation in the space, also affecting the neighbour molecules.

According to the Marcus theory,^[40] which is the model used to explain the hopping transport, the process of charge transport can be described as the redox reaction between a charged and a neutral molecule. According to this theory, the electronic transport is controlled by two parameters: i) the transfer integral (t), which indicates the interaction between the HOMOs or LUMOs of two adjacent molecules and ii) the reorganisation energy (λ) that is the energy that takes into account the conformational changes that the molecules suffer due to the acceptance or release of a charge. The mobility of charge-carriers in an OSC is proportional to the transfer integral and inversely proportional to the reorganisation energy.

The transfer integral energy is calculated as the half splitting of the HOMOs of two adjacent molecules. In fact, the higher this energy is, the more delocalised the polaron is over the crystal structure of the material. The transfer integral is highly dependent on the distance and orientation between the molecules.^[41,42] Consequently, this parameter relies on the crystal structure and it cannot be easily controlled; however, the extension of the π -conjugation^[43] and the use of moieties that interact strongly are two of the used strategies to improve this parameter.^[44–47] **Figure 1.5** shows how the distance and the relative position of two neighbour tetracene molecules affect the hole and electron transfer integrals.^[24]

On the other hand, the reorganisation energy depends strongly on the molecular structure of the OSC. A potential energy diagram of the charge-carrier transfer is shown in **Figure 1.6**. In this figure it is shown the oxidation of the donor (D) and the reduction of the acceptor molecule that takes place in a charge transfer process. Upon oxidation, the donor changes its conformation (Q_D) to reduce its energy (λ_D). The other graph illustrates how the acceptor receives the charge and then changes its conformation (Q_A) to reach its equilibrium state, which also involves a loss of energy (λ_A). The total reorganisation energy of this process is the sum of λ_D and λ_A . In order to minimise this energy, the semiconductor design has been focused on rigid molecules that do not dramatically change their conformation while they hold a charge-carrier.^[48]

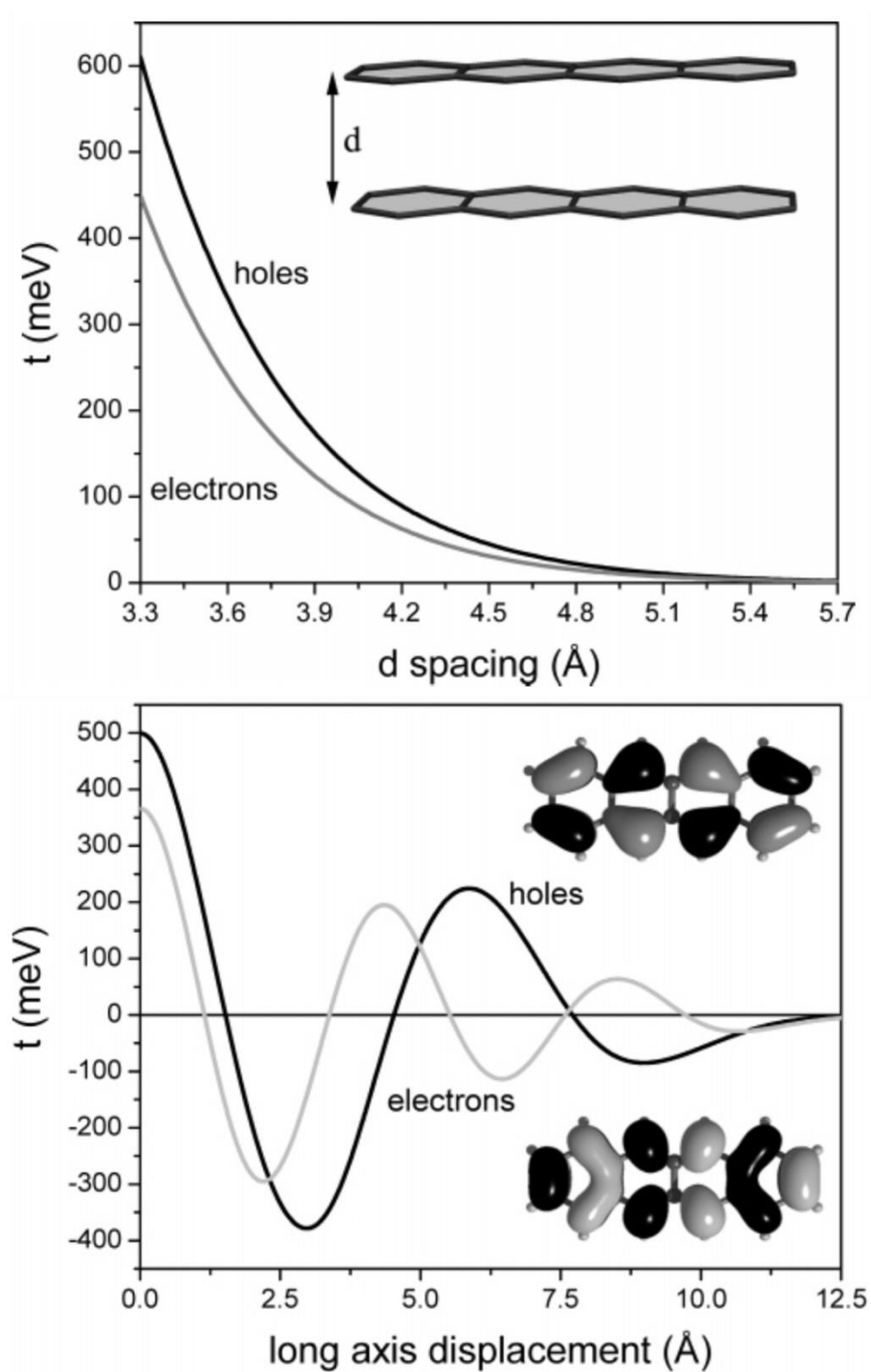


Figure 1.5. Evolution of calculated electron and hole transfer integrals for two cofacial tetracene molecules as a function of the intermolecular distance and of their relative positions. Figure extracted from reference [24].

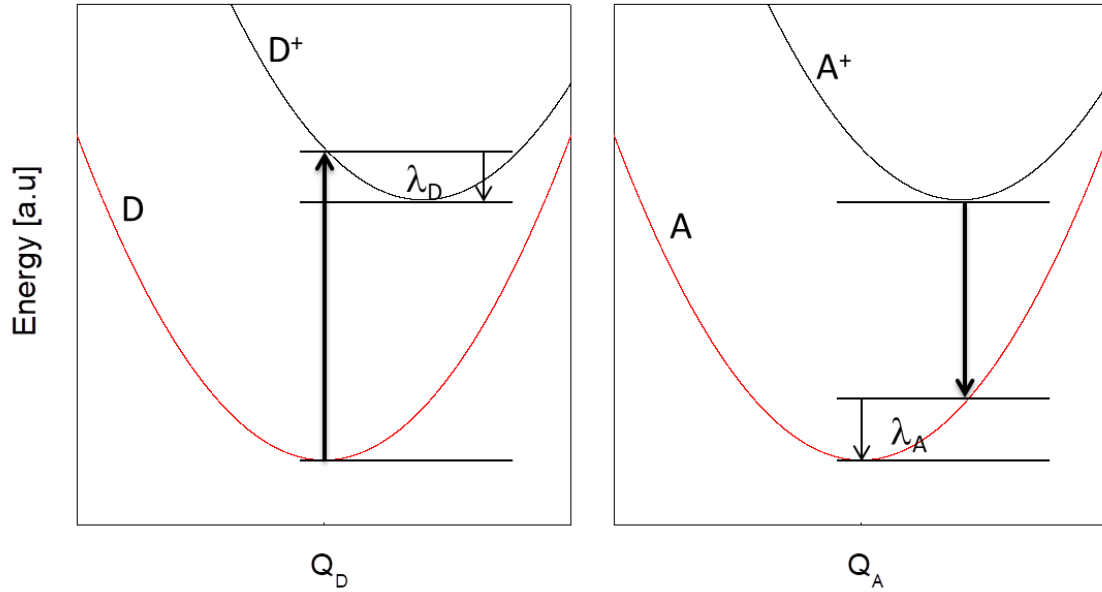


Figure 1.6. Scheme of the electron transfer reaction between a donor (D) and acceptor (A) molecule. λ corresponds to their respective reorganisation energies after the electron transfer.

One way to distinguish between hopping and band transport is the dependence of the charge mobility vs. the temperature. It was found that in highly ordered single crystals the mobility of charges decrease if the temperature is increased. As in the case of metals, this response to the temperature is typical of the band transport and is due to the scattering process by lattice phonons. An interesting example of this kind of behaviour in OSCs was reported by Mori *et al.* for the OSC C8BTBT.^[49] In this example, single-crystals of C8BTBT showed a mobility of 16 cm²/V·s at 300K that increased to 52 cm²/V·s upon cooling down to 80 K. On the other hand, more disordered systems follow a hopping transport regime, and in that case the lattice vibrations enhance the movement of the charge-carrier by providing the energy necessary to overcome the energetic barrier. The expression that describes the evolution of the mobility with the temperature can be generally described by the Arrhenius expression:^[24]

$$\mu_0(T) = \mu_\infty \cdot \exp\left(-\frac{E_A}{k_B T}\right) \quad (1.1)$$

Where μ_0 is the mobility at a certain temperature (T) and E_A is the activation energy of the system that can be correlated with the disorder of the system.

However, another possible microscopic interpretation of the transport inside an OSC is that charge-carriers travel in narrow delocalised bands and their motion is disturbed by the high concentration of traps present in the material.^[50–52] These traps may come from chemical impurities, defects of the crystal structure, grain boundaries, etc. In other words, the materials have an intrinsic mobility (μ_i) that is hindered by the presence of traps that dominate the

charge transport. This mechanism is called multiple trap and release. The charge-carriers can be released from the traps thermally if the energy difference between the trap and the Fermi level is less than $k_B \cdot T$, where k_B is the Boltzmann's constant. This thermal release of the charge-carrier would support the thermal activated behaviour of the electronic mobility observed in most OSCs. At this point we can differentiate between band states, where the electronic transport occurs, and trap states, whose presence hamper the electronic transport. The density of states (DoS) shape of an OSC could be described with two regions: a region with a high density of electronic states plus a region with a band-tail distribution of states extending within the band gap of the semiconductor (**Figure 1.6**).^[53–57] The density of trap states indicates the quality of a semiconducting system and is lower for pure single-crystals and higher for polycrystalline thin-films.

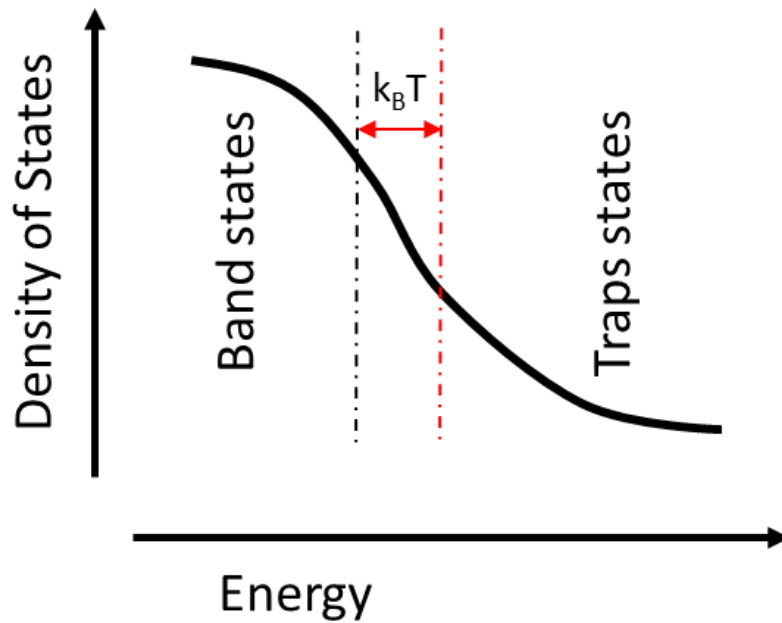


Figure 1.7. Schematic representation of the band tail differentiating the band and trap states. The thermal activation of shallow energy traps states is also represented with dashed lines.

1.4. STRUCTURE-PERFORMANCE RELATIONSHIP IN ORGANIC SEMICONDUCTORS

As aforementioned, the supramolecular organisation of the small-molecule OSCs (*i.e.* crystal structure) is one of the most important factors that determine the ability of these OSCs to transport charges. Among the most efficient crystal structures in OSCs regarding the charge transport we can find the displaced cofacial packing, the herringbone packing and the brickwork packing, all of them depicted in **Figure 1.8**. Even though one would expect that cofacial packing could be the most favourable situation for the overlap of the orbitals, it has been demonstrated that, in general, slightly displaced cofacial packing and herringbone-like motives lead to higher transfer integrals.^[24,58] Also relevant is the dimensionality in these structures, *i.e.* the directions charges can flow in a crystal structure. In some crystal structures, like displaced cofacial, there is usually only one relevant value of transfer integral; consequently, the charge can only travel along one direction (1D). On the other hand, crystal structures like herringbone or brickwork are inherently 2D. The dimensionality inside a material is an important matter because while a 2D OSC can avoid localised traps, like defects of the crystal structure, with alternative paths, a 1D-material cannot. This reduction of transport paths results in a decrease of the effective charge transport.

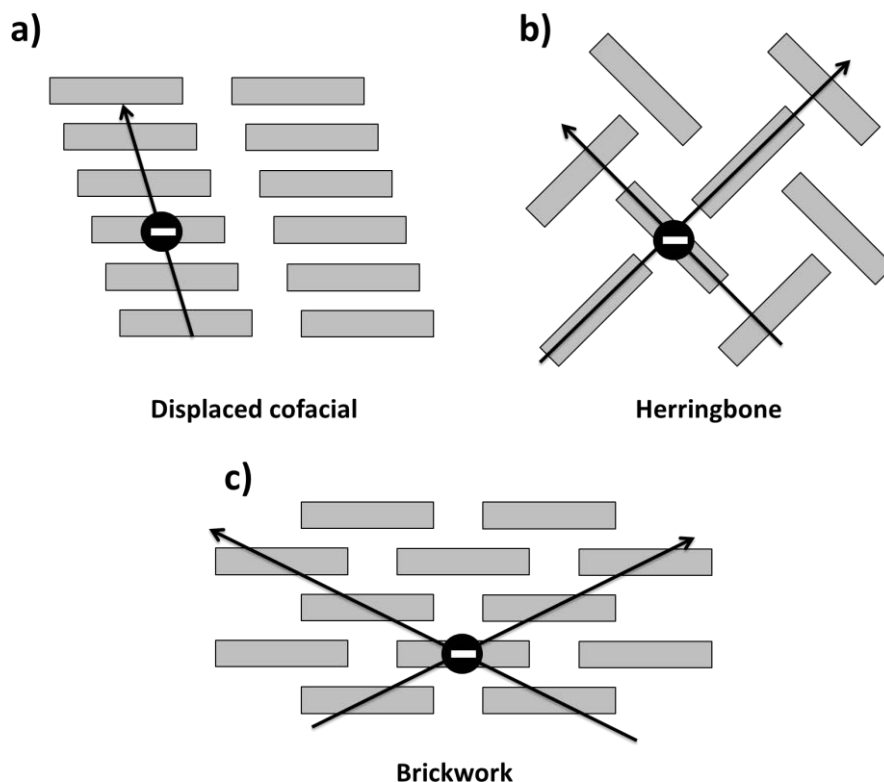


Figure 1.8. Typical crystal packings found in OSCs: **(a)** displaced cofacial, **(b)** herringbone-like and **(c)** brickwork-like crystal structures. The black arrows indicate the most likely charge transport directions.

Furthermore, it has been also observed that depending on the dimensionality of the crystal packing the charge transport can be anisotropic in the different directions of the crystal.^[59–61] This anisotropy can lead to differences of 2 or 3 orders of magnitude in the charge mobility and therefore, is a factor that should be taken into account when using OSCs as active layers in organic devices.

It has been demonstrated that small changes in the molecular structure can affect the crystal packing, strongly modifying the electrical properties of the material. For example, Mori *et al.* performed modifications on the molecular structure of TTF by adding phenyl rings and found that those variations affected the herringbone structure. In this case, the TTF with phenyl rings packed in a herringbone structure but with some of the molecules shifted in the long axis of the molecules. This positional shift affected the overlapping of the HOMOs of the TTF core and, consequently, caused a reduction of the hole mobility.^[62] Interestingly, in one of the cases it affected only the transport in the *b* axis and not in the *a* axis permitting the comparison between 1D and 2D transport. The mobility found for TTFs 1D was around two orders of magnitude lower than in the case of 2D, highlighting the importance of the dimensionality in the charge transport.

However, the correlation between the molecular structure and the crystal packing is still hard to predict by theoretical studies. Even though, the crystal structure cannot be fully ascertained from the molecular structure of the semiconductor, there are some lessons we have learnt from the high number of organic semiconductors that have been synthesised and characterised over the years. Especially, from those works in which the molecular structure of organic semiconductors were systematically modified and studied.^[63]

Among those lessons we can find that large π -systems like acenes,^[48,64–66] thiophenes^[47,67,68] or tetrathiafulvalenes^[44,69,70] are suitable for *p*-type OSCs and arylene diimides^[71–73] or azaacenes^[74] that contain fluorine atoms are perfect candidates for *n*-type OSCs. These moieties display suitable HOMO/LUMO energy values for stable electronic transport under air and as they tend to pack closely, high transfer integrals. In addition, they are also very rigid systems, *i.e.* low reorganisation energy.

One strategy used to enhance the interaction between cores has been the extension of the conjugation by adding more benzene rings or by fusing the OSC core with heterocycles. For example, the addition of a thiophene to the TTF structure, led to the OSC DT-TTF which displayed a better packing for electronic transport and consequently, gave rise to an increase in the mobility going from 1.5 to 6.2 cm²/V·s.^[75,76] Interestingly, in the case of DT-TTF, the change of position of the sulphur atom of the thiophene ring from the β position to the α position (*i.e.* α -DT-TTF) resulted in a crystal structure where TTF moieties form trimers and thus, due to the low extension of the HOMO overlap between these trimers, a dramatic reduction of the performance was observed (**Figure 1.9**).^[77] This latter case is a perfect example of how a small change in the molecular structure causes a dramatic change of the charge transport.

Furthermore, the addition of alkyl side chains has been demonstrated to be an optimal way for improving the intermolecular distance between OSC cores and also for enhancing the solubility of the material, which is clue for the solution processing of the material. For example, a set of

bis-(N-alkylpyrrolo[3,4-d]tetrathiafulvalene (PyTTF) derivatives with long alkyl chains were investigated as semiconductors when spin-coated on OFET structures.^[78] In that case, longer chains led to a stronger hydrophobic interaction between the alkyl chains, which reduced the intermolecular distance and enhanced the electronic overlap between their cores as checked by X-ray powder diffraction. This alkyl side chain effect was also investigated in benzothienothiophene derivatives with bulky isopropyl and *tert*-butyl groups. Interestingly, from the crystal structures and performance, it was observed that the molecule with the most bulky groups pack the closest leading to a higher performance.^[79]

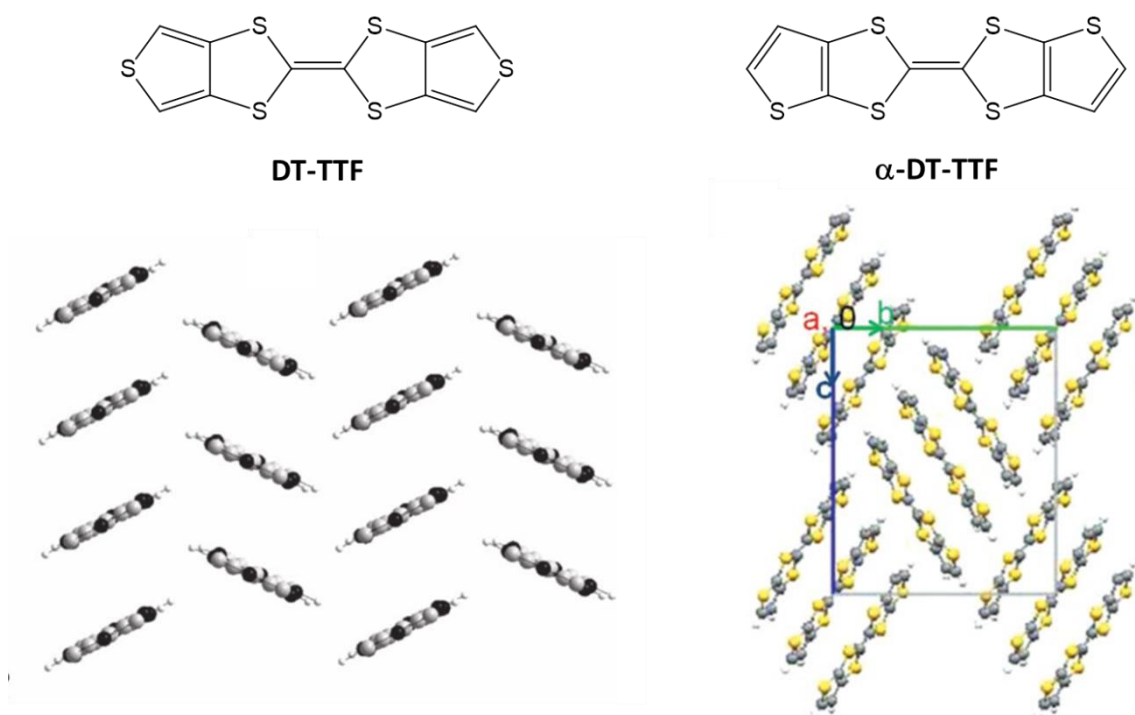


Figure 1.9. Molecular and crystal structures of DT-TTF (left) and α -DT-TTF (right).^[76,77]

1.5. POLYMORPHISM

Polymorphism is the ability of a molecule of packing in different crystal structures. As aforementioned, organic semiconductors are bonded by weak van der Waals forces and are expected to display different molecular arrangements with similar energy. In fact, it was estimated that approximately 30 % of organic molecules would present polymorphism at ambient pressure.^[80,81] These differences in the crystal structure of organic semiconductors can be critical for the charge transport and because of that, polymorphism must be controlled. Different polymorphs can be obtained as a result of forming the crystal at different temperatures, with different solvents or on different substrates.^[70,82] Also, depending on the speed of the crystallisation process, the molecule could crystallise in a metastable phase K that could lead to a more stable phase T with time.^[15]

The polymorphism of an organic semiconductor can be seen as the opportunity of improving the performance of a material, not by the laborious modification of its backbone, but by controlling the final crystal structure through the crystallisation process. To do so, understanding this crystallisation process and its thermodynamics and kinetics is crucial so as to be able to control the outcome and in order to be able to design new strategies to access to the desired structures.

A simple way of evaluating the crystallisation and understanding which is the most favourable polymorphic phase can be realised by plotting the free energy (G) vs. the transition coordinate (**Figure 1.10**). In this representation, the most important parameters are the activation energy (E_A) and the free energy difference of the phases (ΔG). Regarding these parameters it must be taken into account that: i) the crystallisation speed depends exponentially on the activation energy and ii) if equilibrium is available kinetically, the ratio between molecules in two different phases depends exponentially on the difference of free energy, being the most favoured phase the one that is thermodynamically more stable.

In **Figure 1.10a** there is a schematic representation of an undetermined OSC that can crystallise into two different polymorphs from solution. Upon the drying of the solvent and the subsequent raise of the free energy, this OSC can evolve into either a kinetic phase (K) or into a thermodynamic phase (T). The difference is that the E_A to crystallise into the kinetic phase is smaller, *i.e.* quicker crystallisation. Consequently, the most possible outcome is that the OSC crystallises first in the kinetic phase as shown in **Figure 1.10b**. Then, if the activation energy between the kinetic and the thermodynamic phase (*i.e.* E_A (K \rightarrow T)) is high, the system will remain in the kinetic phase. If, on the other hand, this E_A is low enough, the system will evolve spontaneously to the thermodynamic phase. This unstable kinetic phase will be named after metastable phase so as to be differentiated from the stable kinetic phase. Of course, if energy is provided to the system (temperature, light, etc.) or new reaction pathways are open (for instance, exposing the kinetic phase to a solvent vapour annealing) the kinetically stable phase can be induced to evolve to the thermodynamic phase.

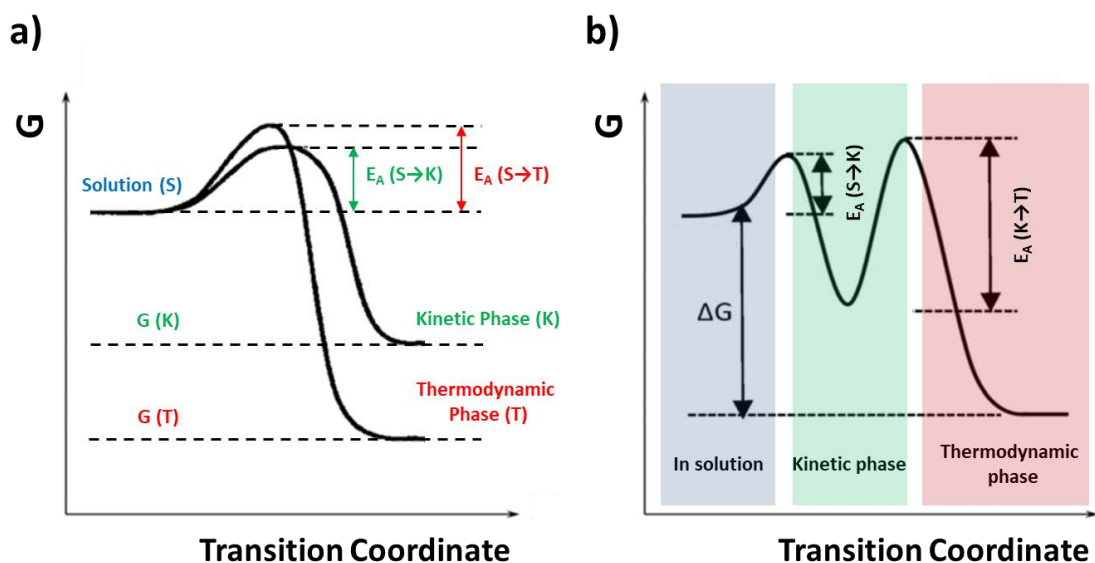


Figure 1.10. Free energy vs. transition coordinate indicating the activation energies of the transitions of (a) a system that can crystallise from solution to either a kinetic or a thermodynamic phase and (b) a system that crystallises first to a kinetic phase and then moves forward to a more stable thermodynamic phase. Adapted from Ref. ^[81].

It is also important to note that these diagrams can change depending on the solvent used, the temperature of the crystallisation or the presence of a heterogeneous agent that opens a new path to a new phase. When the heterogeneous agent is a surface, the crystal structures are known as surface-induced phases (SIP) and a good number of organic semiconductors display this type of phases.^[83] Therefore, even though some common points can be extracted as general for organic semiconductors, each system must be studied individually.

A particularly interesting molecule regarding its polymorphism and the way of accessing to the different phases is the case of the OSC dibenzotetrathiafulvalene (DB-TTF). This organic semiconductor displayed a fair mobility in the range of 0.1-1 cm²/V·s as single-crystal of the α phase. However, this material crystallises in four different crystalline structures (α , β , γ , δ) depending on the deposition conditions.^[70] It has been studied that in this system, the α phase is the most stable thermodynamically and can be grown from drop casting of a solution of DB-TTF in chlorobenzene, process that usually needs around one day to be completely finished at room temperature. β phase single crystals were grown by saturating a DB-TTF solution in hot toluene and cooling it down slowly afterwards; however, following that methodology, a mixture of α and β phase single crystals were obtained. On the other hand, the γ phase is the most favourable kinetically and was obtained by rapid deposition of DB-TTF together with polystyrene (PS) on Si/SiO₂ substrates. Even in thin-film, the γ phase displayed a good mobility of around 0.2-0.3 cm²/V·s with textbook like characteristics.^[84] It has been also demonstrated that if the deposition was not quick enough or if the film thickness grew beyond a certain value, the γ phase started to coexist with the more stable α phase, in which case lower mobility values were obtained.^[42] Lastly, the δ phase was grown by the drop casting of DB-TTF solution in isopropanol:nitromethane 1:1 as well as by vapour deposition under vacuum.

Another interesting case has been reported with the OSC 6,13-Bis(triisopropylsilyl)ethynyl)pentacene (TIPS-pentacene). The addition of the bulky tri(isopropyl)silyl ethynyl group modified the herringbone structure of pentacene and turned it into a brick-wall packing. For TIPS-pentacene, three different polymorphs were found and all of them packed in a brick-wall crystal structure. However, for these three polymorphs, the relative position of the molecules was slightly different, *i.e.* different intermolecular distance and shifted molecular overlapping, causing a huge impact on the electronic properties (**Figure 1.11**). Surprisingly, the polymorph (phase **Figure 1.11c**) that displayed the smallest intermolecular distance also displayed the slowest charge transport. This result was supported by the calculated transfer integral values which concluded that even if the intermolecular distance was smaller (2.82 Å), the molecular overlapping was less efficient than in the other phases.^[85]

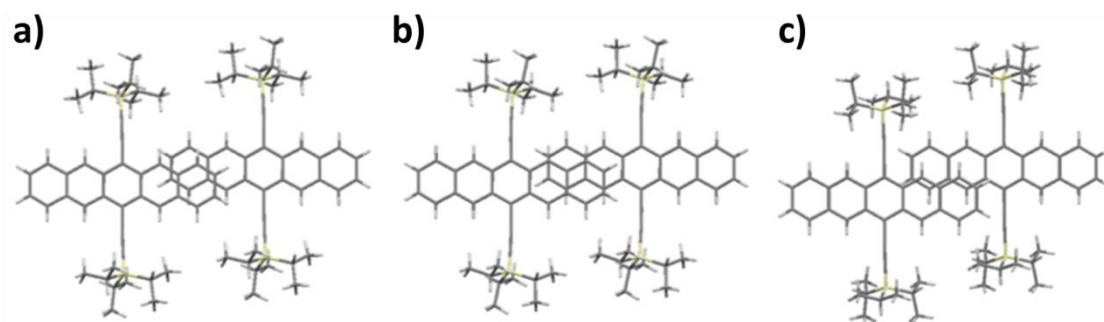


Figure 1.11. Images of the *ab* plane of the three polymorphs of TIPS-pentacene. The highest transfer integral was found for the structure (b), then (a) and (c).^[85]

1.6. CHARGE TRANSPORT IN SINGLE CRYSTALS vs. THIN FILMS

The study of the charge transport using single crystals is the best way to study the intrinsic properties of an organic semiconductor. However, the manipulation of single crystals is too complicated to implement them in real devices. The alternative to single-crystals is the use of polycrystalline thin-films. One of the main differences between these two systems is the presence of grain boundaries (GBs) in thin-films. GBs are the limits of each crystalline domain and, usually in optimised films, are limited by the presence of another grain. It has been demonstrated that the presence of GBs can be directly related to the amount of traps in thin-films.^[86] Therefore, the existence of GBs is detrimental for the charge transport and thus, the formation of big crystalline domains is pursued when optimising the deposition conditions of an OSC in order to minimise this effect.

In addition to the grain size, the effect of the different orientation of neighbour domains can be critical for the charge transport. This relative orientation may cause a small effect (slight misalignment) or an important detrimental effect (strong misalignment) on the mobility (**Figure 1.12**).^[87] In fact, the alignment of the domains upon the deposition of the semiconductor can reduce the hindering effect of the GBs. This domain alignment has been studied as a way of improving the charge mobility to up one order of magnitude with respect to a film with randomly oriented domains.^[88–90] However, this alignment is only an important factor if the presence of GBs is high, which is not a desired situation for an optimised thin-film. Furthermore, the alignment of the domains also resulted in an increased anisotropy of the electronic transport, being improved in the direction parallel to the coating and hampered in the perpendicular direction. In some cases, the anisotropy in mobility reached values beyond 20, highlighting the power of this strategy.^[91]

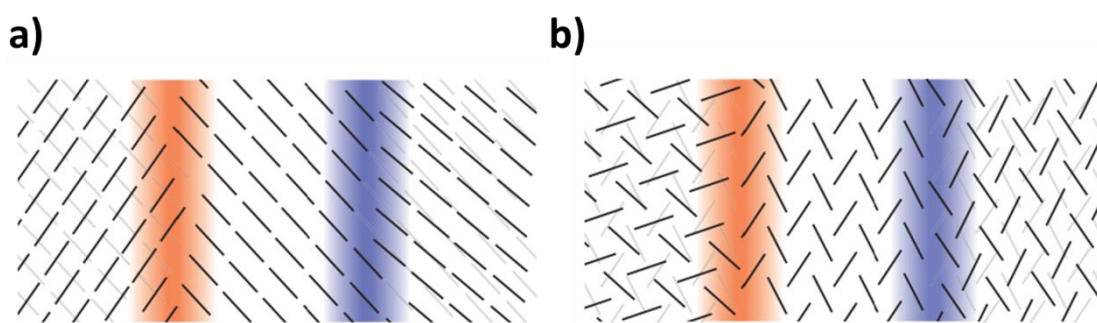


Figure 1.12. Grain boundaries in a **(a)** displaced cofacial and **(b)** herringbone packing. Blue line indicates a slightly misaligned grain boundary and the red line corresponds to a strongly misaligned one. Figure extracted from reference [87].

1.7. ORGANIC SEMICONDUCTOR DEPOSITION TECHNIQUES

The techniques for depositing organic semiconductors can be subdivided into two main categories: i) vapour-phase depositions techniques and ii) solution-based deposition techniques, such as drop casting, spin coating, dip coating, spray coating, blade coating, zone casting and bar-assisted meniscus shearing.

PHYSICAL VAPOUR DEPOSITION

The physical vapour deposition or PVD consists in the thermal evaporation of the organic semiconductor in vacuum. The process is performed inside a vacuum chamber with usually a pressure in the range from 10^{-6} to 10^{-8} mbar in order to reduce the sublimation point of the material below the point where the material starts to degrade. In this kind of deposition the material is typically placed on an alumina boat (highly resistant to the temperature). The opening of the boat is directed to the target where the organic semiconductor is going to be deposited when the vapour pressure of the semiconductor, which increases with the temperature, reaches the pressure of the chamber.

This technique not only deposits the organic semiconductor but also works as a purification step. This purification process works like sublimation where one can get rid of the lower boiling point impurities (they will be evaporated before the organic semiconductor) and the higher sublimation point impurities will remain in the boat where the material is placed. To avoid the contamination of the substrate where we want to deposit our semiconductor, the target is protected with a shutter that can be opened when the real deposition starts. In this system, to control the amount of material that is deposited and to know the rate of deposition a quartz microbalance is used. The physics behind it is that the quartz microbalance will change its resonance when a mass is attached to it, so with a previous calibration, the amount of material deposited can be measured. A schematic representation of an evaporation chamber is depicted in **Figure 1.13**.

In addition, it has been reported that increasing the substrate temperature is usually beneficial for achieving higher crystallinity as the molecules on the substrate have enough energy to move and rearrange in larger crystallites. This effect was also observed for very low rate depositions (around 0.1 \AA/s) and it has been concluded that is due to the smaller kinetic energy of the evaporated molecules.^[55,92]

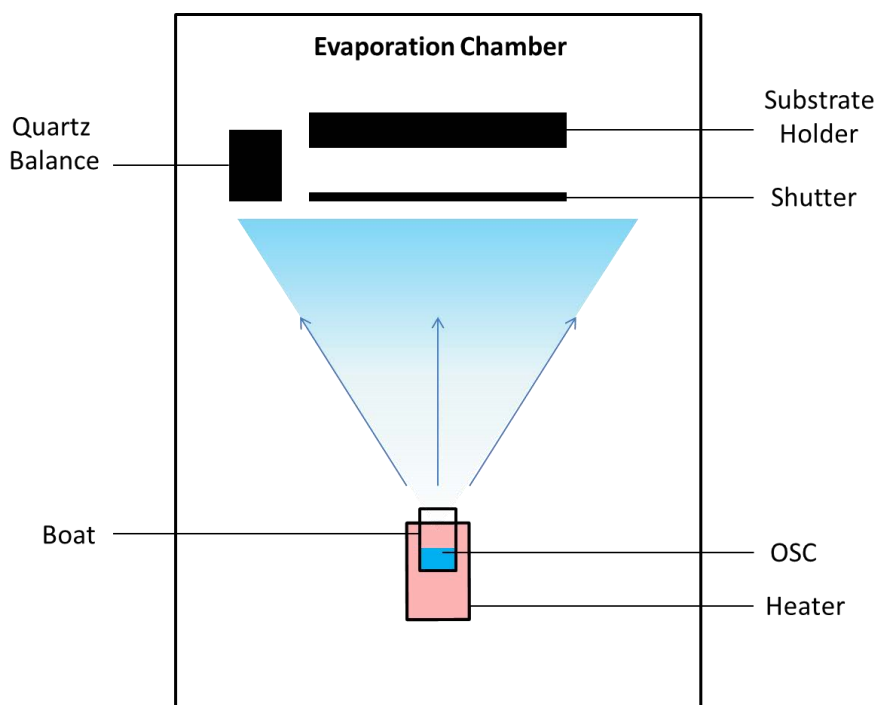


Figure 1.13. Schematic representation of a thermal evaporation system.

DROP CASTING

Drop casting is probably the simplest technique for the deposition of organic semiconductors. It consists in the deposition of a drop of the OSC solution on the target substrate and then in waiting for the solvent to dry. A schematic representation of drop casting is shown in **Figure 1.14**. This method is traditionally used to obtain single-crystals of the organic semiconductors but is not suitable for obtaining reproducible depositions or to be applied in large scale.

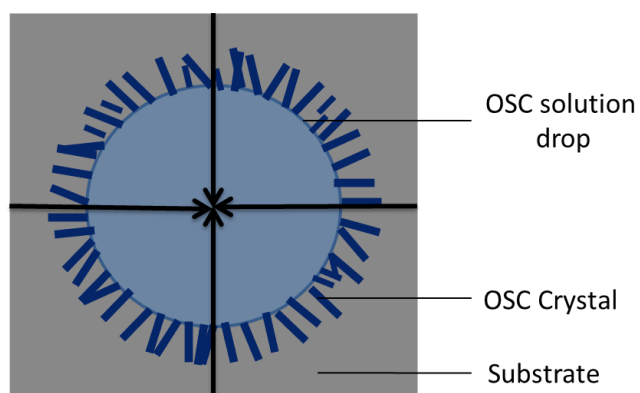


Figure 1.14. Schematic representation of the crystal formation in a drop casting experiment. The black arrows indicate the evaporation direction of the solvent.

There are some factors that must be taken into account for a successful drop casting:

- i) The edge of the drop should not touch the edge of the substrate so as to avoid the nucleation in that region.
- ii) The rate of evaporation depends on the boiling point (*b.p.*) and on the vapour pressure of the solvent used. For high *b.p.* the increase of the substrate temperature can be considered to reduce the time of evaporation.
- iii) If an organic semiconductor is particularly hard to crystallise or we want a larger crystal, the evaporation rate of the solvent can be reduced by covering the substrate with a Petri dish.
- iv) Usually, the crystal growth in a drop casting experiment is aligned to the solvent evaporation direction, from the edge to the centre of the drop.^[93,94]
- v) The density of single crystals is proportional to the solution concentration.

SPIN COATING

Spin coating is one of the most used techniques for the deposition of OSC thin-films with uniform thickness. The procedure consists in depositing some drops of the solution of the OSC on the substrate and the subsequently spinning at high speed of the sample (**Figure 1.15**). The rotation spreads the solution all over the substrate ejecting the surplus and also drying the thin-film. The thickness of the resulting film is known to be dependent on the solution concentration and viscosity and also inversely proportional to the angular speed of the coating. This technique is simple and quick but it cannot be upscaled and therefore cannot be applied for large area applications.

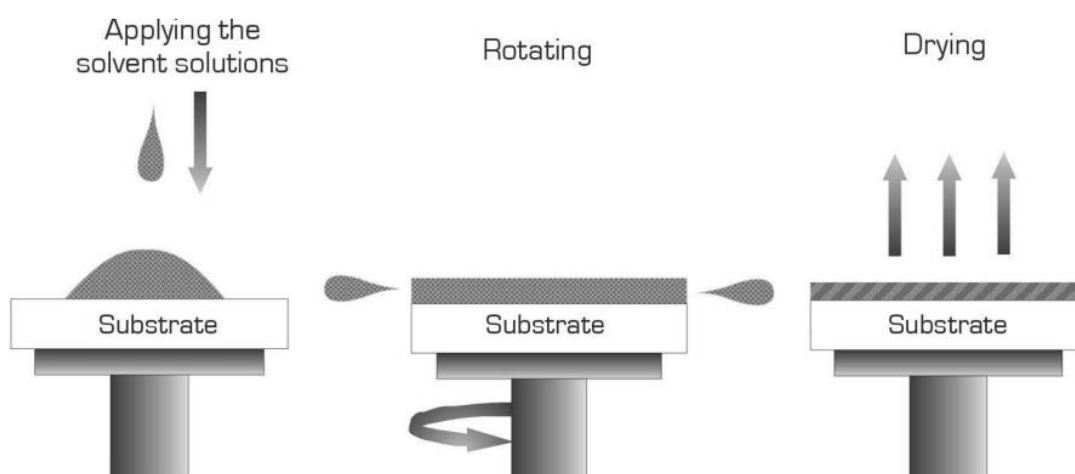


Figure 1.15. Spin coating process. Image extracted from reference [95].

DIP COATING

Dip coating consists in the vertical withdrawal of a substrate immersed in an OSC solution (**Figure 1.16**). The thickness of the film is determined by the speed at which the substrate is removed from the OSC solution and the properties of the solution, like its *b.p.* and the OSC concentration. This technique can be easily upscaled; however, one of its drawbacks is that it requires large volumes of solution to be performed, consequently, increasing the cost of production.

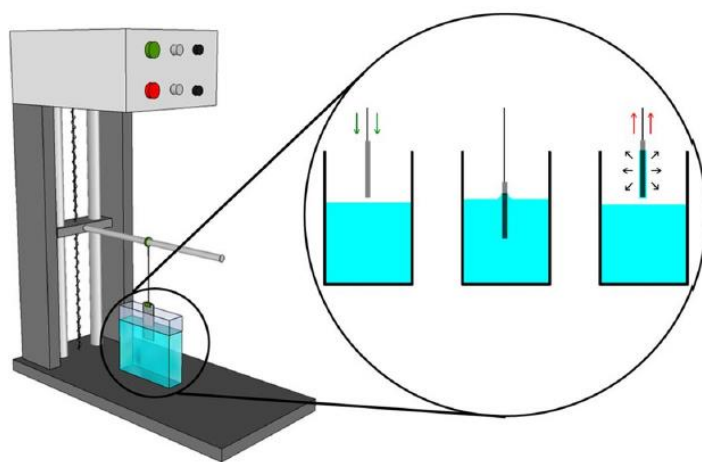


Figure 1.16. Schematic representation of a dip coating deposition. Image extracted from reference [96].

SPRAY COATING

Spray coating is based on the atomisation of an OSC solution due to the high pressure of a gas carrier, usually N_2 , and the deposition of these small droplets on a target substrate (**Figure 1.17**). These droplets are ejected from a nozzle and its shape and size as well as the gas carrier pressure are key parameters that determine the morphology of the thin-film. Furthermore, in this technique it is important that the droplets evaporate shortly after reaching the substrate so as to avoid the accumulation and the inevitably formation of a wet film. To do so, the choice of solvent, gas carrier pressure, distance nozzle-substrate and the temperature of the substrate must be taken into account.^[97–99] This technique is discussed more in detail in Chapter 6 where it was applied for the deposition of an organic metal and also for the deposition of OSCs.

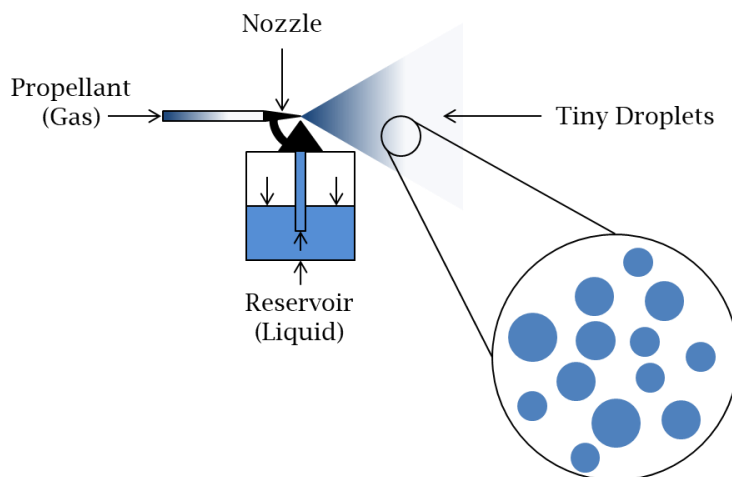


Figure 1.17. Schematic representation of spray coating.

BLADE COATING

In this technique, first, the solution of the OSC is dropped onto the substrate and then either the blade is passed over the substrate or the substrate is moved. The blade leaves behind it a uniform wet film that after solvent evaporation a uniform thin-film is formed (**Figure 1.18**). If required the substrate can be heated in order to help the evaporation process, especially, for the higher boiling point solvents. The distance between the substrate and the blade fixes the amount of solution that remains on the film and therefore, together with the solution concentration, controls the film thickness. This technique can be used in a similar manner if the blade is changed for a wired bar (wire coating). Also, an important advantage of this technique is that the coating speed can be potentially very high reaching values of tens of cm/s.^[100] Consequently, it can be adapted to roll-to-roll deposition processes for large scale production.

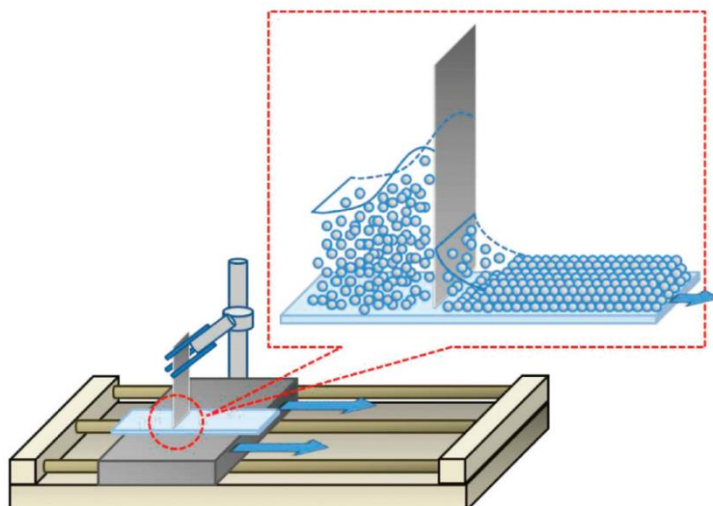


Figure 1.18. Schematic representation of a blade coating. Image reproduced from reference [101].

ZONE CASTING

Zone casting consists in the continuous deposition of an OSC solution by a flat nozzle on a moving substrate as shown in **Figure 1.19**. This substrate is kept at a certain temperature in order to control the solvent evaporation. Usually the movement on the substrate in this technique is very slow (speed < 1 mm/s) and leads to highly anisotropic polycrystalline films.

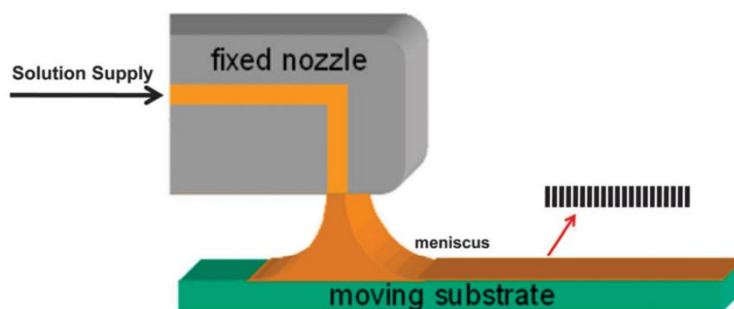


Figure 1.19. Schematic representation of zone casting.^[102]

BAR-ASSISTED MENISCUS SHEARING

Bar-assisted meniscus shearing (BAMS) is a variant of the traditional blade coating that has been used and developed in our group and will be extensively used in this thesis. This deposition technique consists in pouring an OSC solution in between a substrate placed on a hot plate and a bar separated $\sim 500\ \mu\text{m}$ apart forming a confined meniscus.^[84] Subsequently, the substrate is displaced in parallel to the bar at a constant speed (**Figure 1.20**). BAMS can be classified among the meniscus-guided techniques. These techniques have demonstrated to be able to form high crystallinity thin-films at speed compatible with roll-to-roll processes. Furthermore, unlike spin coating where approximately 90 % of the solution is ejected, in meniscus-guided techniques the material use can be up to 99 % in processes involving large areas.^[103]

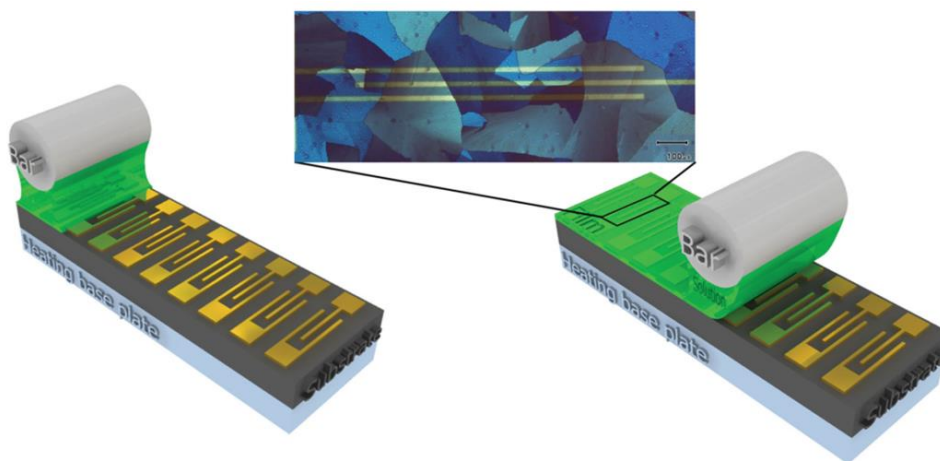


Figure 1.20. Schematic illustration of the BAMS coating technique.^[84]

In this technique, there is a meniscus formed by an OSC solution that when moves over a substrate leaves behind part of the solution. The thickness of the wet film that is left behind depends on the viscosity of the solution, the surface tension of the solution, the speed of the bar/substrate movement, the surface energy of the substrate and the interaction between the bar and the solution, among others. Furthermore, the solvent evaporation rate that depends on the solvent used and the substrate temperature also play a role on the physics of the film formation. The crystallisation of the organic semiconductor is thus controlled by the concentration of the OSC, the solvent evaporation rate and the surface underneath that can act as a nucleation agent.^[65] Considering all this complexity, the final film morphology cannot be easily predicted.

However, even if the final outcome is impossible to predict, there is some theory that we can apply to these systems. For example, in this technique, similarly to the dip coating, three deposition regimes can be differentiated:

- i) The evaporative regime, which is the regime where the speed of the bar/substrate is the lowest and the drying process of the wet film is affected by the presence of the meniscus. In the evaporative regime the thickness of the film is inversely proportional to the speed of the coating. This effect is caused by the same deposition time per shorter unit length which permits the deposition of more material in the same place.
- ii) The Landau-Levich regime. At high coating speeds the viscosity of the solution dominates over the solvent evaporation and a wet film is left behind and only dries when the meniscus is far away. Inversely to what happens in the evaporative regime, in this regime the thickness of the film is proportional to the speed of the bar.
- iii) The last regime is in fact not a real regime itself but the intersection of the evaporative and the Landau-Levich regimes.^[104] In this regime, we find the minimum of the film thickness, which is interesting especially for surface-induced polymorphs, and is where for some OSCs the larger crystalline domains were found.^[105] In **Figure 1.21a** there is a representation of the film thickness vs. the coating speed also indicating

approximately the deposition regimes of thin-films fabricated by dip coating. Further, the values of domain size and film thickness and roughness as a function of the coating speed for a blend of DB-TTF and polystyrene deposited by BAMS are shown in Figure 1.21b.^[42] Interestingly, the best performing devices were the ones prepared with the intermediate regime.

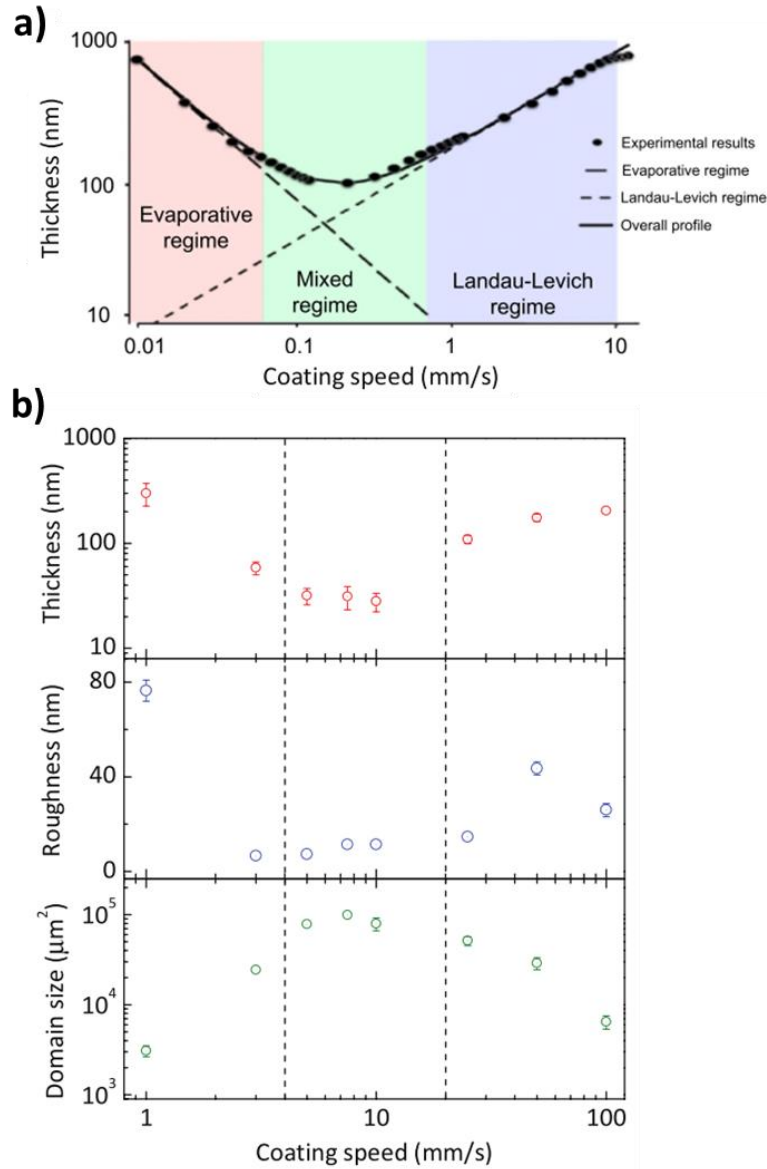


Figure 1.21. a) Graph indicating the different evaporation regimes evaluating the thickness of the thin-film vs. the coating speed extracted from reference [103]. **(b)** Thickness, roughness and domain size vs. the coating speed for films of DB-TTF with polystyrene where the three regimes and their effect on the morphology can be observed. The graph is reproduced from reference [42].

The strategy of blending organic semiconductors with polymers either insulating or semiconducting for tuning the solution processability and thin-film properties, is now commonly employed in organic electronics and thin-film transistors. When a thin-film is composed of two or more materials, it is likely to result in different microstructural variations and phase separation. Therefore, in OSC:polymer binder composites, there can be several factors that finally determine the overall phase behaviour, like for instance the kinetics of evaporation of the solvent. Also, the thermodynamics of the mixing between components and the different contributions of the entropy and the enthalpy to the free energy variation of the mixing (ΔG_M) is important. For example, in polymer A/polymer B systems, the entropy change on mixing is negligible. So, phase separation is common, since mixing is only favourable when a strong enthalpic interaction between components is present.

Blending OSCs with binding polymers is a common strategy used to enhance the processability of the OSCs that tend to suffer from dewetting problems when deposited as thin-films. Upon the addition of polymer, the solution viscosity raises resulting in thin-films displaying more homogeneous morphologies. Furthermore, it has been demonstrated that in this kind of thin-films processed by spin-coating, BAMS and other solution shearing techniques, a vertical phase separation takes place. Typically, during the solvent evaporation the OSC crystallises on top of the binding polymer (**Figure 1.22a**). Such bottom polymer layer confers stability to the OSC by reducing the contact between the OSC and the polar dielectric, usually SiO_2 . The direct contact of the OSC since avoids the direct contact of the OSC with the polar dielectric, usually SiO_2 . In polar dielectrics water dipoles are present, which act as charge carrier traps reducing the performance of the OSC.^[106,107]

Additionally, it has been reported that during the deposition of thin-films of C8BTBT and PS by BAMS, in addition to the typical vertical phase separation where the OSC crystallised on top of PS, the presence of a very thin layer of polymer on top of the OSC layer was also observed (**Figure 1.22b-e**).^[108–110] This very thin skin layer (*i.e.* only a few nanometres) covered the OSC reducing the direct contact of the OSC and the environment. This reduction of the OSC/air interface inhibited the accumulation of dipoles and the oxidation of the OSC enhancing the device stability.

Furthermore, the processing of OSCs together with binding polymers also results in a better organisation of the OSC that crystallises in larger domains, thus, reducing the density of grain boundaries. As aforementioned, the lower density of grain boundaries leads to a lower density of traps, which has a positive impact on the electronic transport. However, there are several parameters that have a strong impact on the crystallisation of the OSC when it is deposited blended with a polymer such as the solvent choice, the OSC:polymer weight ratio, the molecular weight and nature of the polymer, and the deposition technique and parameters, among others. Several examples based on thin-films of benchmark OSCs such as TIPS-pentacene and C8BTBT blended with PS have been reported displaying state-of-the-art performances with mobilities of the order of $10 \text{ cm}^2/\text{V}\cdot\text{s}$.^[17,32]

In addition to blend systems of OSC:insulating polymer, thin-films based on mixtures where the insulating polymer was changed for a semiconducting polymer have also been reported with remarkable results. For example, Anthopoulos et al. have reported thin-films based on 2,8-difluoro-5,11-bis(triethylsilylethynyl)anthradithiophene (diF-TESADT) and the conjugated polymer poly(fluorene-co-triarylamine) (PF-TAA) with a hole mobility up to $5 \text{ cm}^2/\text{V s}$.^[111] They attributed the improved electronic transport found in these films when compared to the thin-films based on small molecule OSC and insulating polymer to the more conductive grain boundaries as they confirmed by conductive atomic force microscopy measurements.^[112]

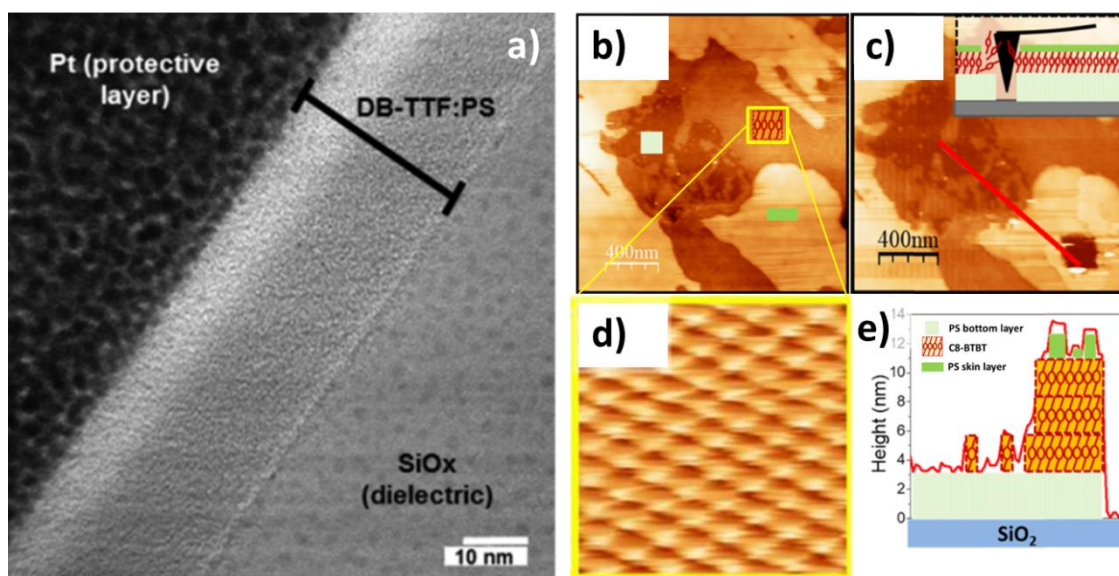


Figure 1.22. **(a)** Energy-filtered transmission electron microscopy image of a DB-TTF:polystyrene (PS) thin-film cross section where the vertical phase separation and the bottom layer of PS can be observed. Image extracted from reference [108]. **(b)** AFM image of a thin-film of C8BTBT:PS where three different regions were identified. **(c)** Same AFM image now indicating the profile path depicted in **(e)** where the different composition along the profile is shown. **(d)** Molecular resolution image of C8BTBT obtained by lateral force AFM obtained in the region highlighted in **(b)**. Images extracted from reference [110].

Another strategy to improve the performance of thin-films based on blends of small molecule OSCs and polymers is the addition of dopants. The controlled addition of dopants results in an enhancement of the electronic transport within the film. This improvement has been attributed to the filling of traps by the dopant that results in a more ideal performance. A representative example reported by Panidi *et al.* of this effect is the addition of $\text{B}(\text{C}_6\text{H}_5)_3$ to diF-TESADT: poly(triarylamine) (PTAA) thin-films resulting in mobility values up to $8 \text{ cm}^2/\text{V s}$.^[16] It is also important to take into account that a dopant addition exceeding the optimum amount can lead to high conductivities in off state, which is not desired in OFET devices.

1.8. ORGANIC FIELD-EFFECT TRANSISTORS

An organic field-effect transistor (OFET) is a three terminal device where the current flowing along an organic semiconductor contacted with the source and drain electrodes can be tuned by the application of a voltage in the gate electrode. The gate electrode is isolated from the other electrodes by a dielectric. It is important to note that in these devices only the first few monolayers of organic semiconductor, it has been estimated from 5 to 10 nm,^[24] are turned conductive by the presence of the electric field.

TRANSISTOR GEOMETRIES

There are four main architectures that have been used in OFETs:

- i) The bottom-gate bottom-contact (BGBC) architecture where the gate electrode is below the dielectric layer and on top of it there are the source and drain electrodes. In this configuration the OSC is deposited on top of the aforementioned structure.
- ii) The top-contact bottom-gate (TCBG) configuration consists in the same gate electrode and dielectric but prior to the source and drain fabrication, the organic semiconductor is deposited. In this architecture, usually, the source and drain electrodes are deposited through a shadow mask on the OSC.
- iii) The third architecture is the bottom-contact top-gate (BCTG) configuration. Here, the semiconductor is deposited on top of a substrate with pre-patterned source and drain electrodes, and afterwards the dielectric is deposited either from evaporation or solution. Finally, the gate electrode is evaporated on top of the dielectric.
- iv) The last architecture is the top-contact top-gate (TCTG), in this configuration the OSC is deposited first onto a substrate that will not take part in the operation process of the transistor, and then on top of the semiconductor the source and drain electrodes are deposited, after that the dielectric layer and on top of it, and finally, the gate electrodes. Among all these architectures the most used in this thesis have been the BCBG and TGBC architectures.

Schemes of all the mentioned configurations are depicted in **Figure 1.23**.

There are some differences between the architectures regarding the device performance. In principle it is expected that TCBG and BCTG display lower contact resistance between the organic semiconductor and the source electrode than BCBG and TCTG. This effect is caused by the limited area of contact between the channel of the semiconductor and the source electrode in BCBG and TCTG. Another factor that must be taken into account is that, practically, in TC configurations, the penetration of Au atoms into the OSC during the

evaporation of the electrodes usually reduces the contact resistance making the TCBG architecture the one that commonly displays the best charge injection. Furthermore, top gate configurations encapsulate the organic semiconductor improving its stability towards harmful agents present in air. This methodology has been commonly used for preparing OFETs of unstable OSCs inside a glovebox to enhance its stability when exposed to ambient conditions.^[113,114]

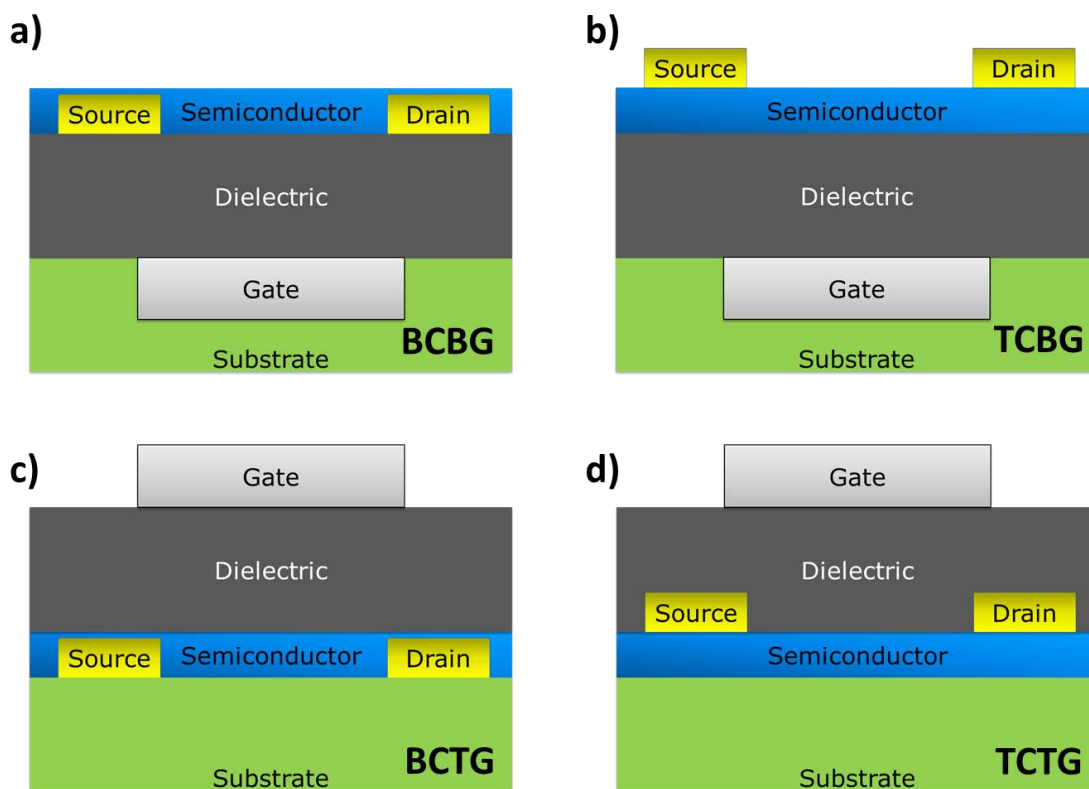


Figure 1.23. (a) Bottom-Contact Bottom-Gate (BCBG), (b) Top-Contact Bottom-Gate (TCBG), (c) Bottom-Contact Top-Gate (BCTG) and (d) Top-Contact Top-Gate (TCTG) OFET geometries.

ELECTROLYTE-GATED ORGANIC FIELD-EFFECT TRANSISTORS

One of the main future applications of OFETs is to be used as platforms for sensing due to their inherent sensitivity to changes in the dielectric interface with the OSC and with the gate electrode and also because of their potential as transducers. In 2010 Horowitz *et al.* published a new transistor geometry (depicted in **Figure 1.24**) where an electrolyte (distilled water in that specific case) in direct contact with the OSC acted as dielectric. Since these devices operate in an aqueous environment, new paths towards sensing were opened using the two above-mentioned transistors interfaces.^[115]

In these devices, upon the application of a voltage in the gate electrode, the ions in the electrolyte (for instance H^+ and OH^- in pure water) form a dense Debye-Helmholtz layer in the

gate electrode/electrolyte interface and in the electrolyte/OSC interface (shown in the zoom in **Figure 1.24**). Consequently, a large capacitance in the $\mu\text{F}/\text{cm}^2$ range is created. This huge capacitance compared to the usual capacitance found in solid dielectrics, in the order of nF/cm^2 range, assures the low voltage operation of the device.^[116]

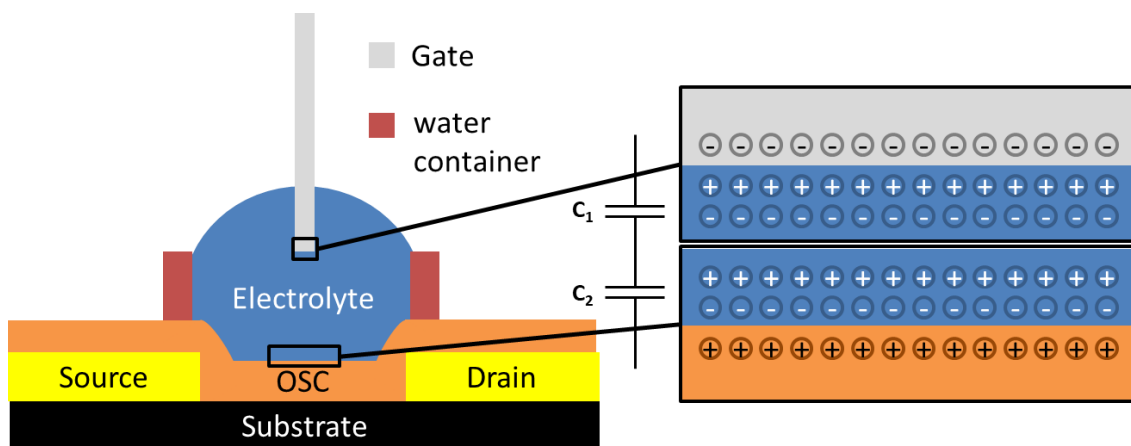


Figure 1.24. Schematic representation of an EGOFET with a zoom in the OSC/electrolyte and electrolyte/gate electrode interfaces depicting the electrochemical double layers formed upon the application of a voltage to the gate electrode.

However, prior to their use as sensing platforms the robustness and reliability of the transistor must be tested. This matter has been the key issue that has been holding back the development of EGOFETs as sensors until recently. The stability problem comes from the fact that organic semiconductors are delicate molecules sensitive to moisture and oxygen and a candidate to be used as OSC layer for EGOFETs must resist water and other possibly aggressive agents. Furthermore, it is important to remember that since the dielectric is water, the charge accumulates only within the first 5-10 nm of the OSC in contact with the liquid dielectric. Therefore, finding new stable OSC films in the media of use is crucial for the progress of EGOFETs and, undoubtedly, the choice of the OSC and its processing is of critical importance. For instance, a high degree of crystallinity has demonstrated to provide an enhanced blocking against ion diffusion.^[117]

Importantly, the addition of binding polymers has been demonstrated to be an efficient strategy to improve the stability of EGOFETs against water or strong aqueous ionic solutions.^[84,108,118] This approach has improved the transistor stability towards water because of the presence of a very thin skin layer of the insulating polymer that avoids the direct contact water/OSC and hence protecting the semiconductor.^[110] It is important to notice that this skin layer is only a few nanometers thick and it cannot prevent completely the diffusion of water or oxygen through it but its presence has demonstrated to lead to an increase of the device stability. For instance, in a previous work of the group, DB-TTF, which is a molecule very sensitive to moisture, has displayed excellent performance when used in EGOFET configuration yet only when deposited together with polystyrene (PS).^[84,108]

OPERATION PRINCIPLE AND MAIN DEVICE CHARACTERISTICS

The operation principle of an organic field-effect transistor is based on the ability to modulate the conductivity of the organic semiconductor by the application of a gate voltage (V_{GS}). To explain this effect we will focus this discussion on the operation of an *n*-type OFET, however for *p*-type OFETs the principle is the same but with the opposite voltage values, the conduction in the semiconductor is through the HOMO instead of the LUMO and the charge-carriers are holes instead of electrons. In these devices, we need to take into account the Fermi energy of the electrodes which is determined by the work function of the metal and the HOMO and LUMO bands of the organic semiconductor (**Figure 1.25a**). The high electric field created by the gate electrode ($V_{GS} > 0$) shifts the HOMO and LUMO energies of the OSC downwards (**Figure 1.25b**). Then, the states of the LUMO band of the semiconductor become accessible and the electrons start to accumulate in it. In other words, the LUMO band is filled partially with electrons from the electrodes and, consequently, the OSC becomes a conductor. Finally, under the application of a potential difference between the source and drain electrodes (V_{DS}), the electrons start to flow (**Figure 1.25c**).

It can be easily observed that the alignment of the Fermi energy of the metal and the HOMO/LUMO energy of the *p*-type/*n*-type OSC, respectively, is a key factor that determine the efficient charge injection in the material. In addition, it can be also observed that OSCs could potentially be considered ambipolar if the work function of the electrodes is properly aligned with the HOMO so holes can be transported, and with the LUMO so electrons can flow.^[27,28] However, most OSCs are considered *p*- or *n*-type and only have either the HOMO or the LUMO within an accessible voltage from the electrodes.

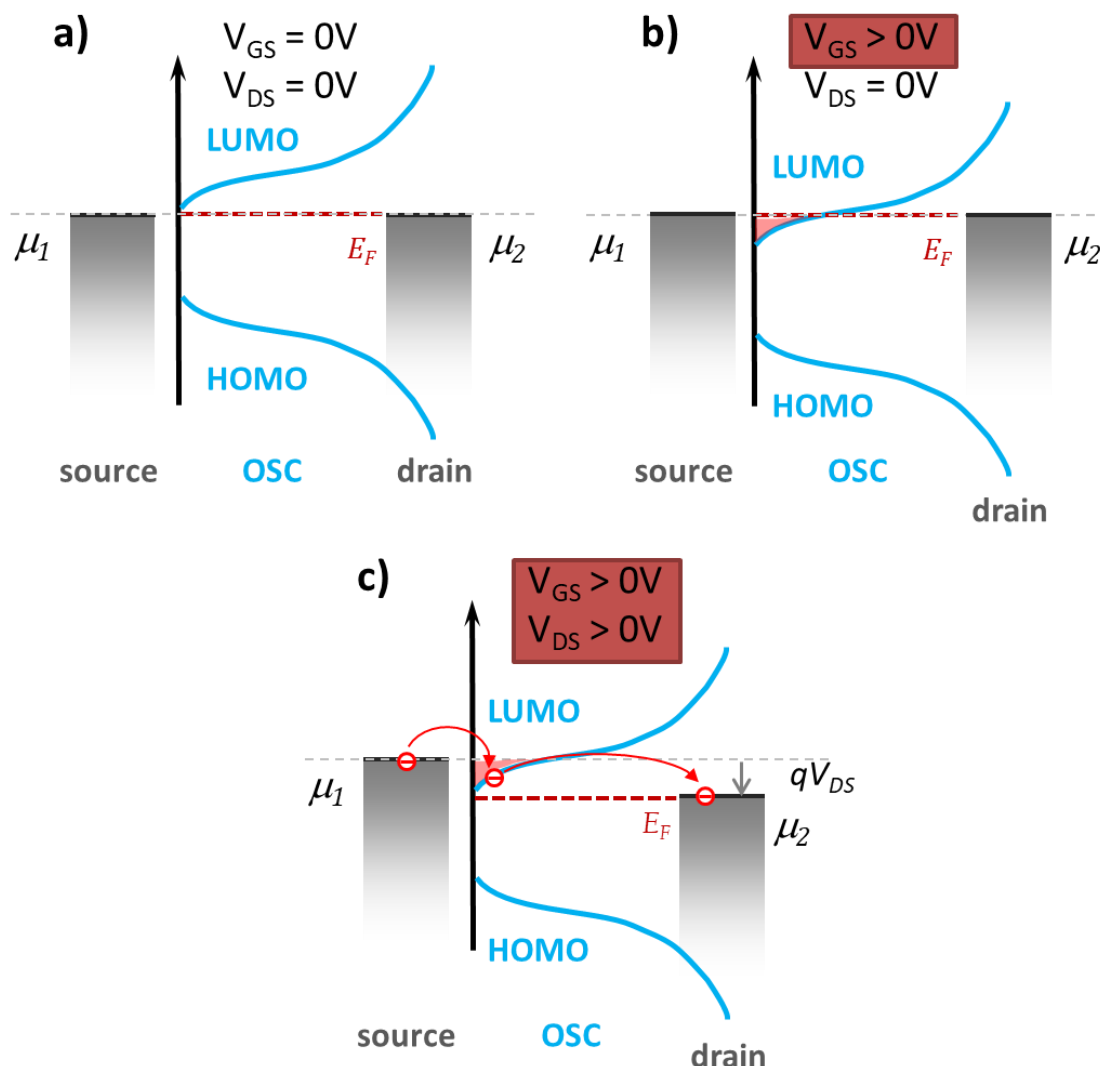


Figure 1.25. Schematic illustration of the operation of an n-type organic field-effect transistor depicting the work function of the metal electrodes and the HOMO/LUMO of the organic semiconductor. **(a)** No gate voltage (V_{GS}) or drain voltage (V_{DS}) is applied and therefore, no charges are accumulated in the OSC. **(b)** Under the application of a V_{GS} , the energy of the HOMO and LUMO bands are shifted downwards, thus, filling the OSC with electrons and consequently, increasing its electrical conductivity. **(c)** Upon the application of a V_{DS} the electrons start to flow.

To describe the current voltage characteristics of an OFET mathematically, Horowitz *et al.* developed a simple comprehensive model based on the model for metal-oxide-semiconductor field-effect transistors (MOSFETs) of traditional inorganic electronics.^[119] However, the model is based on three assumptions that are not strictly correct for most OFETs. i) The charge carrier mobility (μ) is assumed to be constant within the range of operation. ii) There is no parasitic contact resistance between the electrodes and the organic semiconductor. iii) The electric field perpendicular to the channel created by the gate electrode is significantly stronger than the one created by the source and drain electrodes.

In this model the OFET operates in two distinct regimes. The so-called linear regime can be defined as the regime where $|V_{DS}| \ll |V_{GS} - V_{TH}|$. In this regime the source-drain current (I_{DS}) increases linearly with the V_{DS} and the following equation can be obtained:

$$I_{DS,lin} = \frac{W \cdot \mu_{FE,lin} \cdot C_i}{L} \cdot \left[(V_{GS} - V_{TH}) \cdot V_{DS} - \frac{V_{DS}^2}{2} \right] \quad (1.2)$$

Where $I_{DS,lin}$ is the source drain current in linear regime, W and L the channel width and length, respectively, $\mu_{FE,lin}$ is the field-effect mobility in linear regime, C_i is the dielectric capacitance per area in F/cm^2 , and V_{TH} is the threshold voltage.

The other regime is called saturation regime and can be defined as the regime where $|V_{DS}| \gg |V_{GS} - V_{TH}|$. It is named saturation regime because at this point I_{DS} does not depend anymore on the V_{DS} and it can be described by the following equation:

$$I_{DS,sat} = \frac{W \cdot \mu_{FE,sat} \cdot C_i}{2 \cdot L} \cdot (V_{GS} - V_{TH})^2 \quad (1.3)$$

Where $I_{DS,sat}$ is the source drain current in the saturation regime and $\mu_{FE,sat}$ is the field-effect mobility in the saturation regime.

In an OFET basically two different device characteristics are measured. First, the output characteristics are obtained when the I_{DS} is measured sweeping the source-drain voltage at a constant gate voltage. The other characteristic is the transfer characteristic. To measure this characteristic, the I_{DS} is evaluated as a function of the V_{GS} at a constant V_{DS} . An example of the output and transfer characteristics of a p -type OFET with almost ideal characteristics is shown in **Figure 1.26**.

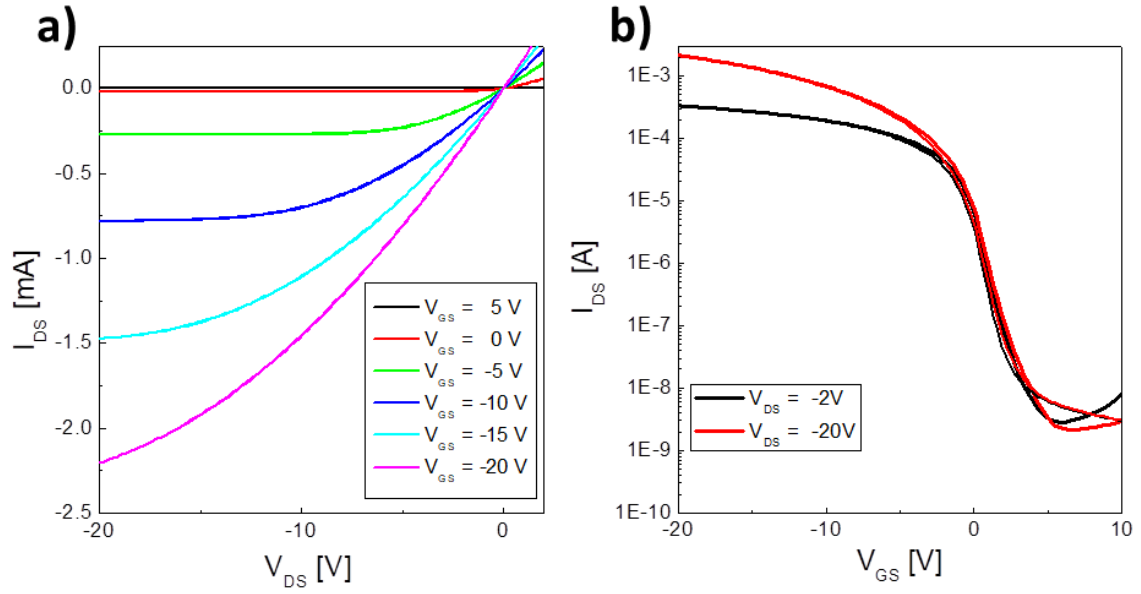


Figure 1.26. a) Output and (b) transfer characteristics of a *p*-type organic field-effect transistor.

FIELD-EFFECT MOBILITY

The mobility of a material (μ) can be described as the speed of charge-carriers inside a material when an electric field is applied. However, the parameter that can be extracted from the OFET characteristics is the field-effect mobility (μ_{FE}). In an ideal case, the field-effect mobility and the intrinsic material mobility will be the same, however, in real devices the presence of the contact resistance and traps is always present reducing the μ_{FE} value. In fact, the μ_{FE} can be different for devices that use the same OSC depending on how the semiconductor has been processed, the electrodes employed, the dielectric chosen, etc. The field-effect mobility is the most important figure of merit in order to compare the performance of OFETs. It can be calculated in the linear regime and in the saturation regime from the transfer characteristics.

For extracting the μ_{FE} in the linear regime we can use the following equation:

$$\mu_{FE,lin} = \frac{L}{W \cdot C_i \cdot |V_{DS}|} \cdot \left(\frac{\partial I_{DS,lin}}{\partial V_{GS}} \right)_{V_{DS}=constant} \quad (1.4)$$

From this equation $\mu_{FE,lin}$ can be extracted by plotting the $I_{DS,lin}$ vs. V_{GS} and calculating the slope of the curve. Then, this slope can be introduced in the equation 1.4 for obtaining $\mu_{FE,lin}$. One can also plot the $\mu_{FE,lin}$ vs. V_{GS} to obtain some additional information of the gate voltage dependence of the mobility. In the most ideal case, the mobility should be independent of the gate voltage.

For the saturation regime, one can use the following equation derived from equation 1.3:

$$\mu_{FE,sat} = \frac{2 \cdot L}{W \cdot C_i} \cdot \left(\frac{\partial \sqrt{|I_{DS,sat}|}}{\partial V_{GS}} \right)_{V_{DS}=constant} \quad (1.5)$$

One can extract the mobility from the transfer characteristics in saturation regime by plotting the square root of the absolute value of I_{DS} vs. V_{GS} and extracting the value of the slope through a linear fit, and then introducing this value into equation 1.5. As well as for the $\mu_{FE,lin}$ the dependence of the $\mu_{FE,sat}$ with respect to the gate voltage can be evaluated.

THRESHOLD VOLTAGE AND SWITCH ON VOLTAGE

In conventional MOSFETs the threshold voltage (V_{TH}) is an important parameter which is needed for circuit design. The classical V_{TH} used in MOSFET theory is defined as the onset of the strong inversion. However, most of the OFETs operate in the accumulation regime and no source-drain current is observed in the inversion regime. A widely used method to extract the V_{TH} consists in plotting the square root of the absolute value of the saturation current as a function of the gate voltage. The resulting straight line for an ideal device can be used to detect the intercept point with the V_{GS} axis, which would be the threshold voltage. Mostly due to the gate voltage dependence of the mobility, in real devices, the square root of the absolute value of the source-drain current does not always give a straight line. This method depends strongly on the range used to perform the fit and is purely empirical.

The switch on voltage (V_{SO}) is another parameter that can be used to determine when a transistor is turned on. In other words, this parameter defines when the channel starts to form, which can be clearly seen when the absolute value of the source-drain current is plotted against the V_{GS} in semilogarithmic scale. In that plot, the switch on voltage can be seen as the voltage at which the current starts to depend on the gate voltage. In an ideal semiconductor no difference should be observed between the threshold voltage and the switch on voltage and they both should be zero.

ON/OFF CURRENT RATIO

The on current (I_{ON}) in highly performing devices has to be as high as possible. This parameter depends strongly on the device geometry, and by increasing the channel width it can be significantly higher. The off current (I_{OFF}) should be as low as possible since it reflects the quality and the purity of the material. The device should really switch off when the right

voltage is applied. This leads us to another important device parameter, which is the on/off ratio ($I_{ON/OFF}$). Strictly speaking, only on/off ratio in the same transfer characteristics can be compared. This parameter gives information about the switching efficiency of the OFET.

The extraction of the on/off current ratio together with all the aforementioned OFET parameters is shown in **Figure 1.27**.

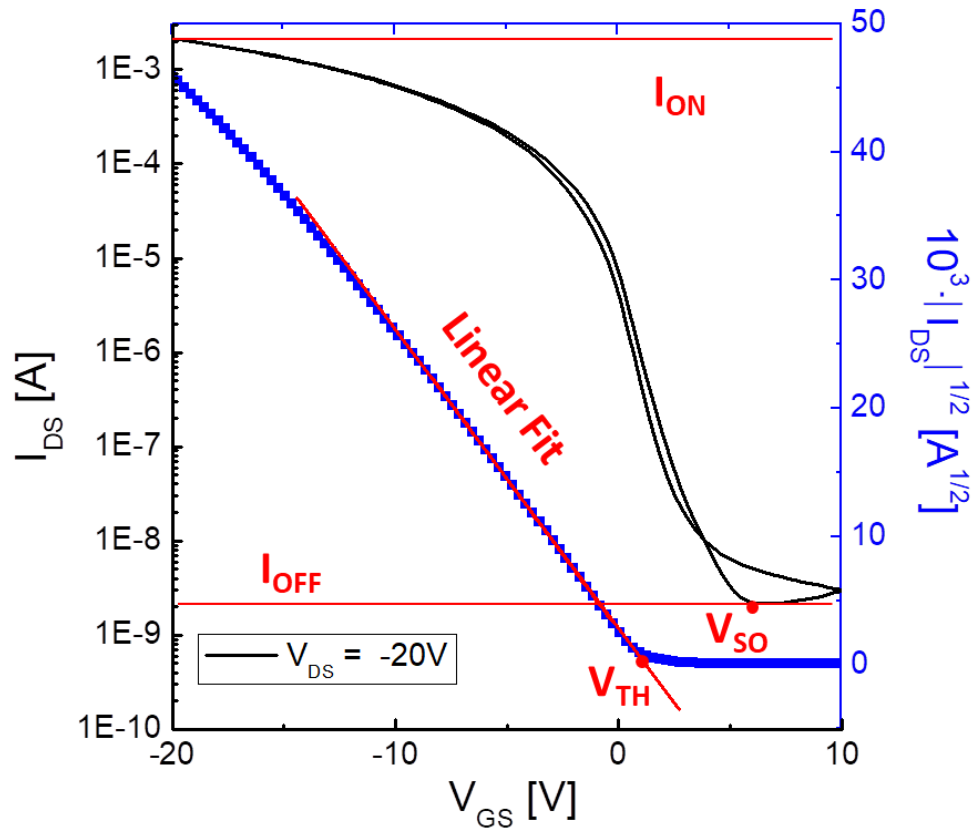


Figure 1.27. OFET parameters extraction shown in a typical transfer curve measured in the saturation regime.

SUBTHRESHOLD SWING

The subthreshold region is the region where the gate voltage is below the threshold voltage. This region is important because it gives information of how effective is the accumulation of charges upon the application of a gate voltage. The subthreshold swing (SS) is the parameter that quantifies how sharply is turned on by the gate voltage. The subthreshold swing is defined as the voltage necessary to increase the source-drain current one order of magnitude. It is important to keep in mind that a small value of SS would permit the switch on of the device within a small voltage and hence reducing the power consumption of the final device.

Furthermore a small subthreshold swing indicates a low density of traps; thus, SS can be an indicator of the OSC/dielectric interface quality.^[120,121]

$$SS = \frac{\partial V_{GS}}{\partial (\log I_{DS})} \quad (1.6)$$

In fact, the following equation correlates the SS with the trap density (N_T):^[32,122]

$$N_T \approx \left[\frac{q SS \log(e)}{k_B T} - 1 \right] \frac{C_i}{q^2} \quad (1.7)$$

Where q is the charge of an electron, k_B is the Boltzmann's constant and T is the temperature.

TRAPPING OF CHARGE CARRIERS AND HYSTERESIS EFFECTS

It has been mentioned before that even the purest single crystals have a certain number of structural defects and chemical impurities. To obtain high performance devices it is important to have well formed OSC/dielectric and OSC/electrode interfaces to avoid hysteresis effects in the source-drain current between forward and backwards sweeps.^[123] Defects found in those interfaces can lead to the formation of traps, reducing the overall performance of the transistor.

CONTACT RESISTANCE

The contact resistance is the electrical resistance given by the electrode/OSC interface. We have already mentioned that to have an effective injection, also known as ohmic contacts, the HOMO/LUMO energies of the semiconductor must be aligned with the work function of the metal. When in a transistor we refer that there is an ohmic contact, it means that the contact resistance is negligible compared with the channel resistance. On the other hand, when the levels are not aligned, an energy barrier will be formed that will prevent the correct injection of charges into the channel. However, the value of the contact resistance alone is not enough to determine how it will affect to the device performance.

We can describe the resistance of a transistor as the contact resistance of the source and the OSC (R_{SO}), plus the resistance of the channel (R_{CH}) and the resistance of the contact OSC/drain (R_{OD}):

$$R = R_{SO} + R_{CH} + R_{OD} = R_C + R_{CH} \quad (1.8)$$

To have an ideal performance it is important that the contact resistances, usually unified in the parameter contact resistance (R_C), are not significant compared with the channel resistance. However, the improvement of the OSC properties has opened the discussion about the high importance of the channel resistance in OFETs. In fact, it has been discussed that the presence of contact resistance in high performance OFETs is leading to the report of overestimated values of the field-effect mobility.^[39,124,125]

To extract the contact resistance the most common methodologies are the Y-function method, the transmission line method (TLM), and the four-point probe method. First, in the Y-function method the R_C is extracted from the transfer characteristics of a single device. This useful method, however, cannot ascertain the dependence of the contact resistance with the V_{GS} .

Secondly, the TLM method consists in the fabrication of homogeneous devices with different channel lengths. It is assumed that when increasing the channel length the only parameter that changes in equation 1.8 is the resistance of the channel. Therefore, by plotting the resistance of the devices at a certain V_{GS} vs. their channel length, the contact resistance can be extracted from the y-intercept of the linear fit of these points.^[126,127] The device resistance can be extracted from the linear fit of the I_{DS} in the linear regime of the output characteristics. Furthermore, with this method the dependence of the contact resistance with the gate voltage can be ascertained.

Thirdly, the four-point probe method requires the use of a pattern with two outer electrodes and other two inner electrodes, which will be used to measure the potential inside the channel. In this method a constant decay of the potential over the channel is assumed to calculate the contact resistance. The advantage over the other methods is that the resistance of the source and the drain electrode can be measured separately.

All the equations for the three methods and their advantages and drawbacks are depicted in **Figure 1.28**.

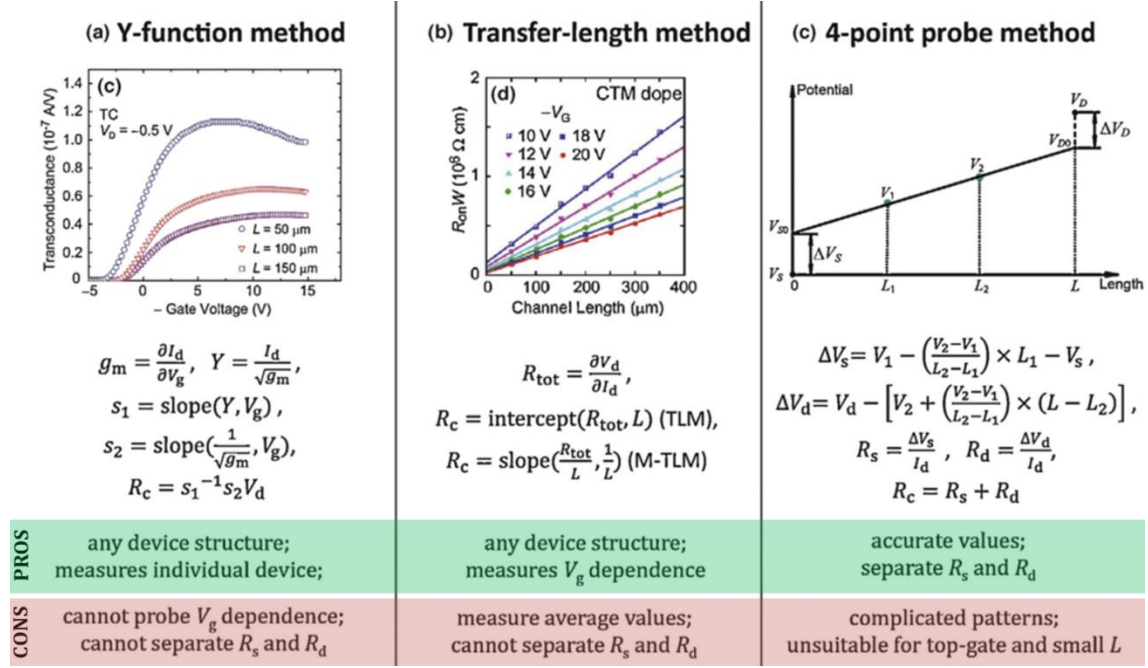


Figure 1.28. Description of the three most common methods to extract the contact resistance in OFETs also showing their different equations. Figure extracted from reference [128].

1.9. OBJECTIVES

The main objectives of this thesis are centred on the study of organic semiconductors and their behaviour as active layer in organic field-effect transistors (OFETs). The purpose of this work is to understand how all the different parameters involving the organic semiconductor and its deposition affect the performance of the final device and also to find strategies to enhance its performance and stability. Hence, the general objectives of this thesis are the following:

- Study of a family of organic semiconductors based on the electroactive moieties tetrathiafulvalene and benzothiadiazole as active layers in evaporated thin-film and single-crystal OFETs. Correlation of their molecular and crystal structure with their performance and stability.
- Synthesis of the new π -extended tetrathiafulvalene derivative, bis(naphto[1,2-*d*])tetrathiafulvalene, and its implementation in thin-film OFETs. Investigation of the influence of the aromatisation of the molecule on the device performance.
- Fabrication of solution-processed thin-film OFETs of a quite unexplored OSC semiconductor based on a sulphur-bridged annulene macrocycle (*i.e.* meso-diphenyl tetrathia[22]annulene[2,1,2,1]) using the technique bar-assisted meniscus shearing (BAMS) and investigation of its potential as active layer in water-gated organic field-effect transistors.
- Fabrication of solution-processed OFETs based on a high performance benzothienobenzothiophene derivative that presents polymorphism and study of how the deposition parameters and the use of a polymer binder affect the final thin-film structure and device performance.
- Preparation and optimisation of *n*-type OFETs based on tetracyanoquinodimethane and N,N'-bis(*n*-octyl)-dicyanoperylene-3,4:9,10-bis(dicarboximide) by BAMS. Study of the role of the polymer binder on the device stability and reliability.
- Exploration of the spray printing technique to deposit organic electrodes based on the organic metal tetrathiafulvalene-tetracyanoquinodimethane and to prepare large single crystals based on benchmark OSCs.

1.10. REFERENCES

- [1] M. C. Choi, Y. Kim, C. S. Ha, *Prog. Polym. Sci.* **2008**, *33*, 581.
- [2] S. Georgakopoulos, F. G. del Pozo, M. Mas-Torrent, *J. Mater. Chem. C* **2015**, *3*, 12199.
- [3] Y. Khan, A. E. Ostfeld, C. M. Lochner, A. Pierre, A. C. Arias, *Adv. Mater.* **2016**, *28*, 4373.
- [4] E. Laukhina, R. Pfattner, L. R. Ferreras, S. Galli, M. Mas-Torrent, N. Masciocchi, V. Laukhin, C. Rovira, J. Veciana, *Adv. Mater.* **2010**, *22*, 977.
- [5] A. T. Zocco, H. You, J. a Hagen, A. J. Steckl, *Nanotechnology* **2014**, *25*, 094005.
- [6] B. A. Jones, A. Facchetti, M. R. Wasielewski, T. J. Marks, *J. Am. Chem. Soc.* **2007**, *129*, 15259.
- [7] J. H. Dou, Y. Q. Zheng, Z. F. Yao, Z. A. Yu, T. Lei, X. Shen, X. Y. Luo, J. Sun, S. D. Zhang, Y. F. Ding, G. Han, Y. Yi, J. Y. Wang, J. Pei, *J. Am. Chem. Soc.* **2015**, *137*, 15947.
- [8] O. Fenwick, C. Van Dyck, K. Murugavel, D. Cornil, F. Reinders, S. Haar, M. Mayor, J. Cornil, P. Samorì, *J. Mater. Chem. C* **2015**, *3*, 3007.
- [9] Y.-Y. Noh, Y. Xu, M. Caironi, T. D. Anthopoulos, *Semicond. Sci. Technol.* **2015**, *30*, 100301.
- [10] K. Manoli, M. Magliulo, M. Y. Mulla, M. Singh, L. Sabbatini, G. Palazzo, L. Torsi, *Angew. Chemie - Int. Ed.* **2015**, *54*, 12562.
- [11] G. Grau, J. Cen, H. Kang, R. Kitsomboonloha, W. J. Scheideler, V. Subramanian, *Flex. Print. Electron.* **2016**, *1*, 023002.
- [12] P. W. Anderson, P. A. Lee, M. Saitoh, *Solid State Commun.* **1973**, *13*, 595.
- [13] C. W. Tang, S. A. Vanslyke, *Appl. Phys. Lett.* **1987**, *51*, 913.
- [14] H. Koezuka, A. Tsumura, T. Ando, *Synth. Met.* **1987**, *18*, 699.
- [15] Y. Yuan, G. Giri, A. L. Ayzner, A. P. Zoombelt, S. C. B. Mannsfeld, J. Chen, D. Nordlund, M. F. Toney, J. Huang, Z. Bao, *Nat. Commun.* **2014**, *5*, 3005.
- [16] J. Panidi, A. F. Paterson, D. Khim, Z. Fei, Y. Han, L. Tsetseris, G. Vourlias, P. A. Patsalas, M. Heeney, T. D. Anthopoulos, *Adv. Sci.* **2017**, *5*, 1700290.
- [17] I. Temiño, F. G. Del Pozo, M. R. Ajayakumar, S. Galindo, J. Puigdollers, M. Mas-Torrent, *Adv. Mater. Technol.* **2016**, *1*, 1600090.
- [18] H. Sirringhaus, *Adv. Mater.* **2014**, *26*, 1319.
- [19] J. Hou, O. Inganäs, R. H. Friend, F. Gao, *Nat. Mater.* **2018**, *17*, 119.

- [20] W. Zhao, S. Li, H. Yao, S. Zhang, Y. Zhang, B. Yang, J. Hou, *J. Am. Chem. Soc.* **2017**, *139*, 7148.
- [21] T. Fleetham, G. Li, J. Li, *Adv. Mater.* **2017**, *29*, 1601861.
- [22] "Plastic logic 10.7" display," can be found under <https://www.plasticlogic.com/product/10-7-display-2/>, **2018**.
- [23] S. M. Sze, K. K. Ng, *Physics of Semiconductor Devices*, John Wiley & Sons, Inc., **2006**.
- [24] V. Coropceanu, J. Cornil, D. A. da Silva Filho, Y. Olivier, R. Silbey, J. L. Brédas, *Chem. Rev.* **2007**, *107*, 926.
- [25] X. Xu, Y. Yao, B. Shan, X. Gu, D. Liu, J. Liu, J. Xu, N. Zhao, W. Hu, Q. Miao, *Adv. Mater.* **2016**, *28*, 5276.
- [26] M. Mas-Torrent, C. Rovira, *Chem. Soc. Rev.* **2008**, *37*, 827.
- [27] B. D. Naab, S. Himmelberger, Y. Diao, K. Vandewal, P. Wei, B. Lussem, A. Salleo, Z. Bao, *Adv. Mater.* **2013**, *25*, 4663.
- [28] C. Moreno, R. Pfattner, M. Mas-Torrent, J. Puigdollers, S. T. Bromley, C. Rovira, J. Veciana, R. Alcubilla, *J. Mater. Chem.* **2012**, *22*, 345.
- [29] J. Dhar, U. Salzner, S. Patil, *J. Mater. Chem. C* **2017**, *5*, 7404.
- [30] H. Sirringhaus, *Adv. Mater.* **2009**, *21*, 3859.
- [31] A. F. Paterson, N. D. Treat, W. Zhang, Z. Fei, G. Wyatt-Moon, H. Faber, G. Vourlias, P. A. Patsalas, O. Solomeshch, N. Tessler, M. Heeney, T. D. Anthopoulos, *Adv. Mater.* **2016**, *28*, 7791.
- [32] M. R. Niazi, R. Li, E. Qiang Li, A. R. Kirmani, M. Abdelsamie, Q. Wang, W. Pan, M. M. Payne, J. E. Anthony, D. M. Smilgies, S. T. Thoroddsen, E. P. Giannelis, A. Amassian, *Nat. Commun.* **2015**, *6*, 8598.
- [33] H. N. Tsao, D. M. Cho, I. Park, M. R. Hansen, A. Mavrinskiy, D. Y. Yoon, R. Graf, W. Pisula, H. W. Spiess, K. Müllen, *J. Am. Chem. Soc.* **2011**, *133*, 2605.
- [34] H. Chen, M. Hurhangee, M. Nikolka, W. Zhang, M. Kirkus, M. Neophytou, S. J. Cryer, D. Harkin, P. Hayoz, M. Abdi-Jalebi, C. R. McNeill, H. Sirringhaus, I. McCulloch, *Adv. Mater.* **2017**, *29*, 1702523.
- [35] M. Li, C. An, W. Pisula, K. Müllen, *Acc. Chem. Res.* **2018**, *51*, 1196.
- [36] M. Caironi, M. Bird, D. Fazzi, Z. Chen, R. Di Pietro, C. Newman, A. Facchetti, H. Sirringhaus, *Adv. Funct. Mater.* **2011**, *21*, 3371.
- [37] K. J. Baeg, M. Caironi, Y. Y. Noh, *Adv. Mater.* **2013**, *25*, 4210.
- [38] R. Matsidik, A. Luzio, S. Hameury, H. Komber, C. R. McNeill, M. Caironi, M. Sommer, *J.*

- Mater. Chem. C* **2016**, *4*, 10371.
- [39] A. F. Paterson, S. Singh, K. J. Fallon, T. Hodsden, Y. Han, B. C. Schroeder, H. Bronstein, M. Heeney, I. McCulloch, T. D. Anthopoulos, *Adv. Mater.* **2018**, 1801079.
 - [40] R. A. Marcus, *Angew. Chem. Int. Ed.* **1993**, *32*, 1111.
 - [41] J. Chen, M. Shao, K. Xiao, A. J. Rondinone, Y. L. Loo, P. R. C. Kent, B. G. Sumpter, D. Li, J. K. Keum, P. J. Diemer, J. E. Anthony, O. D. Jurchescu, J. Huang, *Nanoscale* **2014**, *6*, 449.
 - [42] S. Galindo, A. Tamayo, F. Leonardi, M. Mas-Torrent, *Adv. Funct. Mater.* **2017**, *27*, 1700526.
 - [43] J. L. Brédas, D. Beljonne, V. Coropceanu, J. Cornil, *Chem. Rev.* **2004**, *104*, 4971.
 - [44] H. Jiang, X. Yang, Z. Cui, Y. Liu, H. Li, W. Hu, C. Kloc, *CrystEngComm* **2014**, *16*, 5968.
 - [45] R. Pfattner, S. T. Bromley, C. Rovira, M. Mas-Torrent, *Adv. Funct. Mater.* **2016**, *26*, 2256.
 - [46] Y. Geng, R. Pfattner, A. Campos, J. Hauser, V. Laukhin, J. Puigdollers, J. Veciana, M. Mas-Torrent, C. Rovira, S. Decurtins, S. X. Liu, *Chem. - A Eur. J.* **2014**, *20*, 7136.
 - [47] S. Haas, Y. Takahashi, K. Takimiya, T. Hasegawa, *Appl. Phys. Lett.* **2009**, *95*, 2007.
 - [48] S. T. Bromley, M. Mas-Torrent, P. Hadley, C. Rovira, *J. Am. Chem. Soc.* **2004**, *126*, 6544.
 - [49] J. Cho, T. Higashino, T. Mori, *Appl. Phys. Lett.* **2015**, *106*, 193303.
 - [50] W. L. Kalb, B. Batlogg, *Phys. Rev. B* **2010**, *81*, 035327.
 - [51] J. Puigdollers, a. Marsal, S. Cheylan, C. Voz, R. Alcubilla, *Org. Electron. physics, Mater. Appl.* **2010**, *11*, 1333.
 - [52] J. Noolandi, *Phys. Rev.* **1977**, *16*, 4466.
 - [53] I. I. Fishchuk, A. Kadashchuk, S. T. Hoffmann, S. Athanasopoulos, J. Genoe, H. Bässler, A. Köhler, *Phys. Rev. B* **2013**, *88*, 125202.
 - [54] M. R. Shijeesh, L. S. Vikas, M. K. Jayaraj, J. Puigdollers, *J. Appl. Phys.* **2014**, *116*, 024507.
 - [55] J. Puigdollers, M. Della Pirriera, A. Marsal, A. Orpella, S. Cheylan, C. Voz, R. Alcubilla, *Thin Solid Films* **2009**, *517*, 6271.
 - [56] A. Campos, S. Riera-Galindo, J. Puigdollers, M. Mas-Torrent, *ACS Appl. Mater. Interfaces* **2018**, *10*, 15952.
 - [57] W. L. Kalb, S. Haas, C. Krellner, T. Mathis, B. Batlogg, *Phys. Rev. B* **2010**, *81*, 155315.
 - [58] M. Mas-Torrent, C. Rovira, *Chem. Rev.* **2011**, *111*, 4833.
 - [59] C. Reese, Z. Bao, *Adv. Mater.* **2007**, *19*, 4535.
 - [60] T. J. Pundsack, N. O. Haugen, L. R. Johnstone, C. Daniel Frisbie, R. L. Lidberg, *Appl. Phys.*

- Lett.* **2015**, *106*, 113301.
- [61] J. Y. Lee, S. Roth, Y. W. Park, *Appl. Phys. Lett.* **2006**, *88*, 252106.
- [62] B. Noda, H. Wada, K. Shibata, T. Yoshino, M. Katsuhara, I. Aoyagi, T. Mori, T. Taguchi, T. Kambayashi, K. Ishikawa, H. Takezoe, *Nanotechnology* **2007**, *18*, 424009.
- [63] C. Wang, H. Dong, L. Jiang, W. Hu, *Chem. Soc. Rev.* **2018**, *47*, 422.
- [64] G. Giri, R. Li, D.-M. Smilgies, E. Q. Li, Y. Diao, K. M. Lenn, M. Chiu, D. W. Lin, R. Allen, J. Reinspach, S. C. B. Mannsfeld, S. T. Thoroddsen, P. Clancy, Z. Bao, A. Amassian, *Nat. Commun.* **2014**, *5*, 3573.
- [65] M. R. Niazi, R. Li, M. Abdelsamie, K. Zhao, D. H. Anjum, M. M. Payne, J. Anthony, D. M. Smilgies, A. Amassian, *Adv. Funct. Mater.* **2016**, *26*, 2371.
- [66] G. Giri, E. Verploegen, S. C. B. Mannsfeld, S. Atahan-Evrenk, D. H. Kim, S. Y. Lee, H. A. Becerril, A. Aspuru-Guzik, M. F. Toney, Z. Bao, *Nature* **2011**, *480*, 504.
- [67] Y. Li, S. P. Singh, P. Sonar, *Adv. Mater.* **2010**, *22*, 4862.
- [68] K. Takimiya, S. Shinamura, I. Osaka, E. Miyazaki, *Adv. Mater.* **2011**, *23*, 4347.
- [69] M. Mas-Torrent, P. Hadley, N. Crivillers, J. Veciana, C. Rovira, *ChemPhysChem* **2006**, *7*, 86.
- [70] A. Brillante, I. Bilotti, R. G. Della Valle, E. Venuti, S. Milita, C. Dionigi, F. Borgatti, A. N. Lazar, F. Biscarini, M. Mas-Torrent, N. S. Oxtoby, N. Crivillers, J. Veciana, C. Rovira, M. Leufgen, G. Schmidt, L. W. Molenkamp, *CrystEngComm* **2008**, *10*, 1899.
- [71] R. Ponce Ortiz, H. Herrera, R. Blanco, H. Huang, A. Facchetti, T. J. Marks, Y. Zheng, J. L. Segura, *J. Am. Chem. Soc.* **2010**, *132*, 8440.
- [72] B. A. Jones, A. Facchetti, T. J. Marks, M. R. Wasielewski, *Chem. Mater.* **2007**, *19*, 2703.
- [73] R. C. Savage, E. Orgiu, J. M. Mativetsky, W. Pisula, T. Schnitzler, C. L. Eversloh, C. Li, K. Müllen, P. Samorì, *Nanoscale* **2012**, *4*, 2387.
- [74] F. Paulus, J. U. Engelhart, P. E. Hopkinson, C. Schimpf, A. Leineweber, H. Sirringhaus, Y. Vaynzof, U. H. F. Bunz, *J. Mater. Chem. C* **2016**, *4*, 1194.
- [75] H. Jiang, X. Yang, Z. Cui, Y. Liu, H. Li, W. Hu, Y. Liu, D. Zhu, *Appl. Phys. Lett.* **2007**, *91*, 2005.
- [76] R. Pfattner, M. Mas-Torrent, I. Bilotti, A. Brillante, S. Milita, F. Liscio, F. Biscarini, T. Marszalek, J. Ulanski, A. Nosal, M. Gazicki-Lipman, M. Leufgen, G. Schmidt, W. M. Laurens, V. Laukhin, J. Veciana, C. Rovira, L. W. Molenkamp, V. Laukhin, J. Veciana, C. Rovira, *Adv. Mater.* **2010**, *22*, 4198.
- [77] R. a L. Silva, A. I. Neves, M. L. Afonso, I. C. Santos, E. B. Lopes, F. Del Pozo, R. Pfattner, M. Mas-Torrent, C. Rovira, M. Almeida, D. Belo, *Eur. J. Inorg. Chem.* **2013**, 2440.

- [78] I. Doi, E. Miyazaki, K. Takimiya, Y. Kunugi, *Chem. Mater.* **2007**, *19*, 5230.
- [79] G. Schweicher, V. Lemaure, C. Niebel, C. Ruzié, Y. Diao, O. Goto, W. Y. Lee, Y. Kim, J. B. Arlin, J. Karpinska, A. R. Kennedy, S. R. Parkin, Y. Olivier, S. C. B. Mannsfeld, J. Cornil, Y. H. Geerts, Z. Bao, *Adv. Mater.* **2015**, *27*, 3066.
- [80] T. L. Threlfall, *Analyst* **1995**, *120*, 2435.
- [81] H. Chung, Y. Diao, *J. Mater. Chem. C* **2016**, *4*, 3915.
- [82] K. P. Goetz, J. Tsutsumi, S. Pookpanratana, J. Chen, N. S. Corbin, R. K. Behera, V. Coropceanu, C. A. Richter, C. A. Hacker, T. Hasegawa, O. D. Jurchescu, *Adv. Electron. Mater.* **2016**, *2*, 1600203.
- [83] A. O. F. F. Jones, B. Chattopadhyay, Y. H. Geerts, R. Resel, *Adv. Funct. Mater.* **2016**, *26*, 2233.
- [84] F. G. Del Pozo, S. Fabiano, R. Pfattner, S. Georgakopoulos, S. Galindo, X. Liu, S. Braun, M. Fahlman, J. Veciana, C. Rovira, X. Crispin, M. Berggren, M. Mas-Torrent, *Adv. Funct. Mater.* **2016**, *26*, 2379.
- [85] Y. Diao, K. M. Lenn, W. Y. Lee, M. A. Blood-Forsythe, J. Xu, Y. Mao, Y. Kim, J. A. Reinspach, S. Park, A. Aspuru-Guzik, G. Xue, P. Clancy, Z. Bao, S. C. B. Mannsfeld, *J. Am. Chem. Soc.* **2014**, *136*, 17046.
- [86] G. Horowitz, M. E. Hajlaoui, *Synth. Met.* **2001**, *122*, 185.
- [87] J. Rivnay, L. H. Jimison, J. E. Northrup, M. F. Toney, R. Noriega, S. Lu, T. J. Marks, A. Facchetti, A. Salleo, *Nat. Mater.* **2009**, *8*, 952.
- [88] G. Giri, S. Park, M. Vosgueritchian, M. M. Shulaker, Z. Bao, *Adv. Mater.* **2014**, *26*, 487.
- [89] H. R. Tseng, H. Phan, C. Luo, M. Wang, L. A. Perez, S. N. Patel, L. Ying, E. J. Kramer, T. Q. Nguyen, G. C. Bazan, A. J. Heeger, *Adv. Mater.* **2014**, *26*, 2993.
- [90] S. G. Bucella, A. Luzio, E. Gann, L. Thomsen, C. R. McNeill, G. Pace, A. Perinot, Z. Chen, A. Facchetti, M. Caironi, *Nat. Commun.* **2015**, *6*, 8394.
- [91] T. Mori, T. Oyama, H. Komiyama, T. Yasuda, *J. Mater. Chem. C* **2017**, *5*, 5872.
- [92] F. Liscio, S. Milita, C. Albonetti, P. D'Angelo, A. Guagliardi, N. Masciocchi, R. G. Della Valle, E. Venuti, A. Brillante, F. Biscarini, *Adv. Funct. Mater.* **2012**, *22*, 943.
- [93] H. Li, B. C.-K. Tee, G. Giri, J. W. Chung, S. Y. Lee, Z. Bao, *Adv. Mater.* **2012**, *24*, 2588.
- [94] H. Li, B. C. K. Tee, J. J. Cha, Y. Cui, J. W. Chung, S. Y. Lee, Z. Bao, *J. Am. Chem. Soc.* **2012**, *134*, 2760.
- [95] L. A. Dobrzanski, S. M., *J. Achiev. Mater. Manuf. Eng.* **2012**, *52*, 7.
- [96] T. Coan, G. S. Barroso, G. Motz, A. Bolzán, R. A. F. Machado, *Mater. Res.* **2013**, *16*, 1366.

- [97] A. H. Lefebvre, V. G. McDonell, *Atomization and Sprays*, CRC Press, Boca Raton, Florida, **1990**.
- [98] W. Shi, S. Han, W. Huang, J. Yu, *Appl. Phys. Lett.* **2015**, *106*, 043303.
- [99] B. S. Hunter, J. W. Ward, M. M. Payne, J. E. Anthony, O. D. Jurchescu, T. D. Anthopoulos, *Appl. Phys. Lett.* **2015**, *106*, 223304.
- [100] Y. H. Chang, S. R. Tseng, C. Y. Chen, H. F. Meng, E. C. Chen, S. F. Horng, C. S. Hsu, *Org. Electron. physics, Mater. Appl.* **2009**, *10*, 741.
- [101] H. Yang, P. Jiang, *Langmuir* **2010**, *26*, 13173.
- [102] Y. Su, M. Ouyang, P. Liu, Z. Luo, W. Xie, J. Xu, *ACS Appl. Mater. Interfaces* **2013**, *5*, 4960.
- [103] X. Gu, L. Shaw, K. Gu, M. F. Toney, Z. Bao, *Nat. Commun.* **2018**, *9*, 534.
- [104] M. Faustini, B. Louis, P. A. Albouy, M. Kuemmel, D. Grosso, *J. Phys. Chem. C* **2010**, *114*, 7637.
- [105] S. Riera-Galindo, A. Tamayo, M. Mas-Torrent, *ACS Omega* **2018**, *3*, 2329.
- [106] P. A. Bobbert, A. Sharma, S. G. J. Mathijssen, M. Kemerink, D. M. De Leeuw, *Adv. Mater.* **2012**, *24*, 1146.
- [107] S. G. J. Mathijssen, M. Kemerink, A. Sharma, M. Cölle, P. A. Bobbert, R. A. J. Janssen, D. M. De Leeuw, *Adv. Mater.* **2008**, *20*, 975.
- [108] F. Leonardi, S. Casalini, Q. Zhang, S. Galindo, D. Gutiérrez, M. Mas-Torrent, *Adv. Mater.* **2016**, *28*, 10311.
- [109] K. Zhao, O. Wodo, D. Ren, H. U. Khan, M. R. Niazi, H. Hu, M. Abdelsamie, R. Li, E. Q. Li, L. Yu, B. Yan, M. M. Payne, J. Smith, J. E. Anthony, T. D. Anthopoulos, S. T. Thoroddsen, B. Ganapathysubramanian, A. Amassian, *Adv. Funct. Mater.* **2016**, *26*, 1737.
- [110] A. Pérez-Rodríguez, I. Temiño, C. Ocal, M. Mas-Torrent, E. Barrena, *ACS Appl. Mater. Interfaces* **2018**, *10*, 7296.
- [111] J. Smith, W. Zhang, R. Sougrat, K. Zhao, R. Li, D. Cha, A. Amassian, M. Heeney, I. McCulloch, T. D. Anthopoulos, *Adv. Mater.* **2012**, *24*, 2441.
- [112] S. Hunter, T. D. Anthopoulos, *Adv. Mater.* **2013**, *25*, 4320.
- [113] D. K. Hwang, C. Fuentes-Hernandez, J. Kim, W. J. Potscavage, S. J. Kim, B. Kippelen, *Adv. Mater.* **2011**, *23*, 1293.
- [114] R. Ahmed, A. Kadashchuk, C. Simbrunner, G. Schwabegger, M. A. Baig, H. Sitter, *ACS Appl. Mater. Interfaces* **2014**, *6*, 15148.
- [115] L. Torsi, M. Magliulo, K. Manoli, G. Palazzo, *Chem. Soc. Rev.* **2013**, *42*, 8612.
- [116] L. Kergoat, L. Herlogsson, D. Braga, B. Piro, M.-C. Pham, X. Crispin, M. Berggren, G.

- Horowitz, *Adv. Mater.* **2010**, *22*, 2565.
- [117] Q. Zhang, F. Leonardi, S. Casalini, M. Mas-Torrent, *Adv. Funct. Mater.* **2017**, *27*, 1703899.
- [118] Q. Zhang, F. Leonardi, S. Casalini, I. Temiño, M. Mas-Torrent, *Sci. Rep.* **2016**, *6*, 39623.
- [119] G. Horowitz, B. G. Horowitz, *Adv. Mater.* **1998**, *5*, 365.
- [120] S. Scheinert, G. Paasch, M. Schrödner, H. K. Roth, S. Sensfuß, T. Doll, *J. Appl. Phys.* **2002**, *92*, 330.
- [121] A. Wang, I. Kymissis, V. Bulović, A. I. Akinwande, *IEEE Trans. Electron Devices* **2006**, *53*, 9.
- [122] M. H. Yoon, C. Kim, A. Facchetti, T. J. Marks, *J. Am. Chem. Soc.* **2006**, *128*, 12851.
- [123] N. I. Craciun, Y. Zhang, A. Palmaerts, H. T. Nicolai, M. Kuik, R. J. P. Kist, G. A. H. Wetzelaer, J. Wildeman, J. Vandenbergh, L. Lutsen, D. Vanderzande, P. W. M. Blom, *J. Appl. Phys.* **2010**, *107*, 124504.
- [124] E. G. Bittle, J. I. Basham, T. N. Jackson, O. D. Jurchescu, D. J. Gundlach, *Nat. Commun.* **2016**, *7*, 10908.
- [125] H. H. Choi, K. Cho, C. D. Frisbie, H. Sirringhaus, V. Podzorov, *Nat. Mater.* **2017**, *17*, 2.
- [126] P. V Necliudov, M. S. Shur, D. J. Gundlach, T. N. Jackson, *Solid. State. Electron.* **2003**, *47*, 259.
- [127] D. Kumaki, T. Umeda, S. Tokito, *Appl. Phys. Lett.* **2008**, *92*, 2006.
- [128] C. Liu, Y. Xu, Y. Y. Noh, *Mater. Today* **2015**, *18*, 79.

CHAPTER 2 CORRELATION OF CRYSTAL STRUCTURE AND DEVICE PERFORMANCE IN OFETS BASED ON TETRATHIAFULVALENE DERIVATIVES

2.1. INTRODUCTION AND OBJECTIVES

The ability to tune the electronic and crystal structure of organic semiconductors (OSCs) and, hence, their properties is one of the main pillars of organic electronics. Although an actual molecular design is not possible yet due to the difficulty in predicting the crystal structure packing, many structure-properties relationships studies have been carried out and can be exploited towards the improvement of an OSC.^[1-3] Furthermore, the design of novel semiconductors and their study is a necessary step to gain further insights into the molecular properties required for achieving high device performance. The main molecular properties of an OSC that determine its performance as active material in OFETs are: the electronic characteristics, the structural ones and the side chains.

The *electronic properties* of an OSC comprise the energy orbitals of the molecule. Particularly interesting are the lowest unoccupied molecular orbital (LUMO) and the highest occupied molecular orbital (HOMO) energies. As commented in the introduction chapter, in *n*-type OSCs the transport of electrons takes place through the LUMO orbital and, therefore, its energy is desired to be as close as possible (in absolute value) to the metal work function to reduce the contact resistance. However, the alignment is not the only factor to take into account because the stability of the semiconductor is also controlled by the LUMO energy. For instance, a LUMO energy under approximately -4.0 eV is usually necessary to avoid the reduction/improve the stability of the semiconductor in ambient conditions.^[4-8]

On the other hand, the transport properties in *p*-type semiconductors, which transport holes, are governed by the HOMO shape and its energy. It has been studied that the HOMO energy of the semiconductors must be lower than -5.0 eV to be stable. However, taking into account that the work function of Au (*i.e.* the most used metal for organic electronics) is around 5.0-5.1 eV, there is a compromise between stability (the lower the better) and alignment in order to optimise the device performance.^[4,9]

The *structural properties* determine the intermolecular interactions that impact on the transport mechanism. It is generally agreed that the transport in OSCs is dominated by the hopping transport. According to Marcus theory,^[10] transport efficiency is evaluated by two parameters: the transfer integral (t) between the orbitals (HOMO or LUMO depending on the polarity) of two neighbour molecules and the reorganisation energy (λ), which is determined by the conformational changes that occur when the OSC accepts or donates an electron.

For achieving high mobility it is necessary to maximise the transfer integral and to minimise the reorganisation energy. Typically, more planar and rigid molecular systems will give rise to lower λ values since the molecular geometry of the charged and neutral molecule will be more similar.^[11,12] On the other hand, the transfer integral is a variable which generally depends on the relative positions and orientation of neighbouring molecules and the shapes of their frontier orbitals. It is expected that, for instance, the extension of the π -conjugation improves the intermolecular electronic interaction.^[13]

Last but not least, the *addition of side chains* like alkyl or perfluorinated chains to a semiconducting core can improve its solubility, packing or stability. Therefore, this kind of modification is crucial to develop high quality materials for solution deposition, which is key for the development of low-cost devices with potential for practical applications.^[14,15]

As said before, in order to realise a molecular structure-performance relationship, it is imperative to perform systematic studies carrying out controlled molecular modifications in the organic semiconductor backbone.^[16–18] For that, dibenzotetrathiafulvalene (DB-TTF) (**Figure 2.1**) has been chosen as the model material because OFETs based on it have shown excellent performance with a fairly high mobility of the order of 0.1-1 cm²/V·s in single crystals. However, DB-TTF thin films are easily oxidized in air, which hampers the applicability of this material.^[19–23] Therefore, since there is still possible room for improvement, modifications in the molecular structure could improve its stability in air and may also improve the charge-carrier mobility and, hence, turn it into a more suitable material for applications.

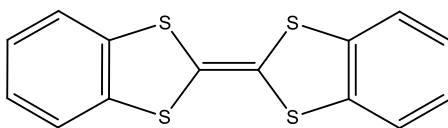


Figure 2.1. DB-TTF molecular structure.

The main objectives pursued in this chapter are: i) the modification of the DB-TTF electronic properties through the addition of different groups to modify the HOMO energy and the study of the final devices stability, and ii) the modification of the TTF structural properties by the expansion of the π -conjugation by adding an extra aromatic ring to potentially increase t and reduce λ . To fulfil these objectives, the small-molecule organic semiconductors presented in **Figure 2.2** have been synthesised and applied in organic field-effect transistors.

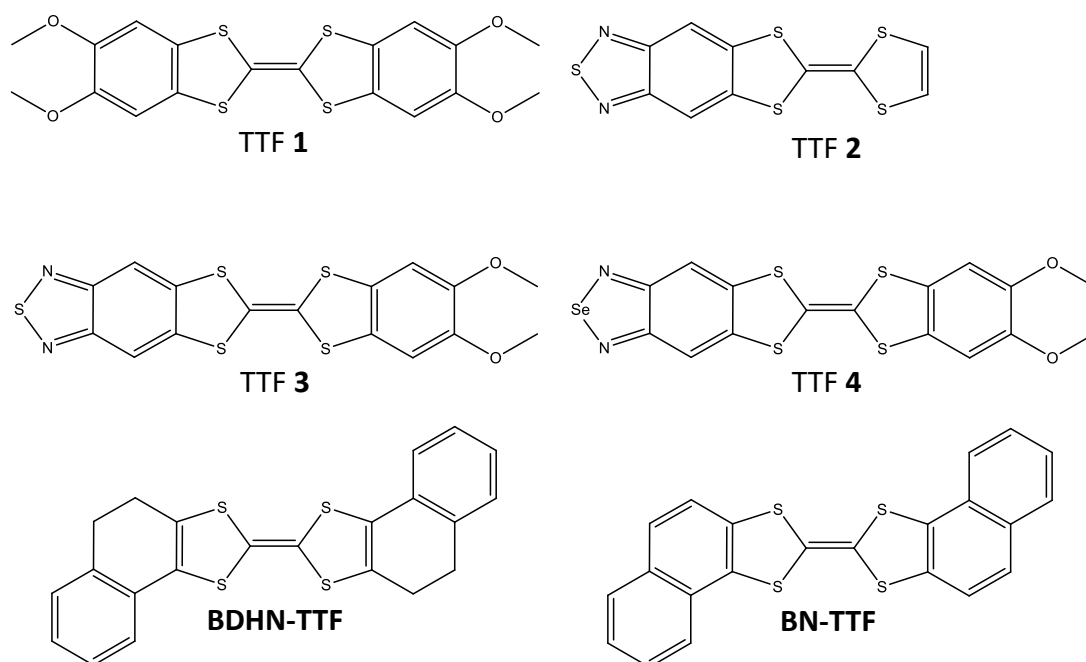


Figure 2.2. Molecular structures of the organic semiconductors used in this chapter.

2.2. HOMO STABILISATION OF π -EXTENDED TTF DERIVATIVES¹

Even though there is a wide range of chemical groups that can alter the molecular orbitals of the OSCs,^[16,24,25] we found particularly interesting the use of electron-deficient nitrogen heterocycles, which in the last years have become a key ingredient in the design of new organic semiconductors.^[26–28] These moieties are often embedded in simple conjugated structures or polymers, whereby their electron-deficient character serves to stabilise and spatially localize the LUMO and, therefore, function as E_{LUMO} lowering and π -extenders. However, they are also interesting for *p*-type semiconductors because of the increased air-stability that promote to the material due to the lowering of the HOMO energy. Moreover, because of their strong electron-withdrawing properties, a permanent dipole inside the molecules is formed. As a consequence, these rigid donor-acceptor (D-A) ensembles can impart a strong dipole-dipole interaction, leading to enhanced intermolecular π - π interactions and a larger *t* between molecules. Such factors are crucial for achieving high carrier mobility.^[29,30] Furthermore, the addition of electron-rich heteroatoms to the core of the OSC, such as O, S or halogens, can enhance this dipole effect due to the *push-pull* effect between them and the electron-withdrawing group.^[31,32]

Here we investigate the influence on the electronic and structural properties when an electron-deficient nitrogen heterocycle, benzothiadiazole (BTD),^[33–37] and an electron-rich group, methoxy, have been fused directly to the DB-TTF skeleton (**Figure 2.2**). The objective is to study the sole effect of the methoxy group (TTF-**1**), the effect of the BTD moiety (TTF-**2**) and the effect of both groups together (TTF-**3**) and to compare them with respect to DB-TTF. Furthermore, the sulphur of TTF-**3** was substituted for selenium (TTF-**4**) to shed light to how the introduction of a more polarisable heteroatom may affect the electronic properties.^[38,39] In addition, single-crystal and thin-film OFETs based on these materials were prepared and characterised.

DESIGN AND SYNTHESIS²

The synthetic pathway to prepare TTFs **1-4** is outlined in **Figure 2.3**. The target compound **1** was prepared by a phosphite-mediated homo-coupling reaction of the corresponding ketone precursor **7**, which is accomplished by a reaction of 4,5-bis-thiobutylveratrole with CS₂ followed by oxidation in the presence of Hg(OAc)₂.^[40–43] The formation of compound **6** involved

¹ This work has been published in Geng, Y. et al. Chem. - A Eur. J. **2014**, 20, 7136–7143 and Geng, Y. et al. Chem. - A Eur. J. **2014**, 20, 16672–16679. The part of the work related with OFET fabrication and characterisation was carried out in collaboration with Dr. Raphael Pfattner.

² All the synthetic work was carried out by Dr. Yan Geng in the group of Prof. Silvio Decurtins and Dr. Shi-Xia Liu (University of Bern).

the well-known cleavage of the C-S bond in liquid ammonia by alkali metals to afford an intermediate disodium salt of 1,2-dithio-4,5-dimethoxybenzene which can easily react with CS₂.^[44–46] Compound **2** was obtained by a phosphite-mediated cross-coupling reaction of the corresponding ketone precursor **9** with vinylene trithiocarbonate. The transformation of compound **8** to the precursor **9** was accomplished in good yield in the presence of Hg(OAc)₂. The target compounds **3** and **4** were obtained by a phosphite-mediated cross-coupling reaction of the corresponding thione precursor **8** and **11**.^[29,30] The conversion of **10** into **11** was readily achieved in the presence of SeO₂.^[47] All new compounds were purified by chromatographic separation and/or recrystallization. Their molecular structures were characterised by NMR, HRMS and elemental analysis.

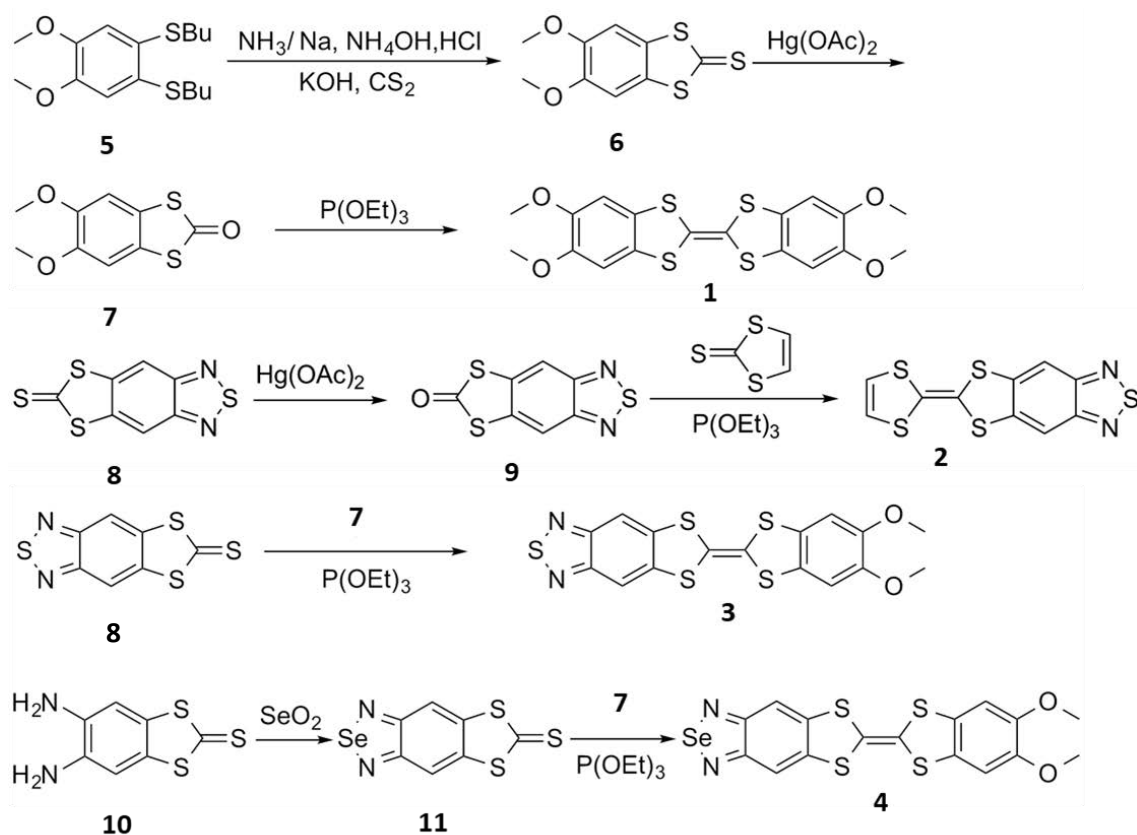


Figure 2.3. Synthetic routes to TTF 1-4.

ELECTRONIC PROPERTIES

The oxidation potentials of TTF-**1** to **4**, were measured by cyclic voltammetry using Pt wires as counter and working electrodes and a silver wire as pseudo-reference electrode (**Table 2.1** and **Figure 2.4**). Ferrocene/Ferrocenium (Fc/Fc⁺) was used as internal reference, showing an oxidation potential of 0.44 V vs. Ag(s) under the experimental conditions employed (see Chapter 7: Experimental methods). The four compounds showed two oxidation waves that are

attributed to the formation of the TTF radical cation and dication species. In addition, the fusion of the electron withdrawing BTd moiety to the TTF core leads to a positive shift of the oxidation potentials, thus increasing the stability to oxygen. Under the premise that the energy level of Fc/Fc^+ is 4.8 eV below the vacuum level,^[48] the HOMO energy level of **1-4** can be estimated according to: $E_{\text{HOMO}}^{\text{exp}} = -[E_{\text{onset}}^{\text{exp,ox1}} + 4.8]$ (eV), where $E_{\text{onset}}^{\text{ox1}}$ stands for the oxidation potential of the first redox wave versus Fc/Fc^+ .^[49] For the three molecules, the HOMO levels were found in the range from -4.5 to -4.9 eV. No reduction processes were observed under the used conditions for TTFs **1**, **3** and **4** down to -1.5 V vs. Ag(s). However, TTF **2** does exhibit a non-reversible reduction wave at -1.36 V corresponding to the reduction of the BTd moiety (LUMO localisation).

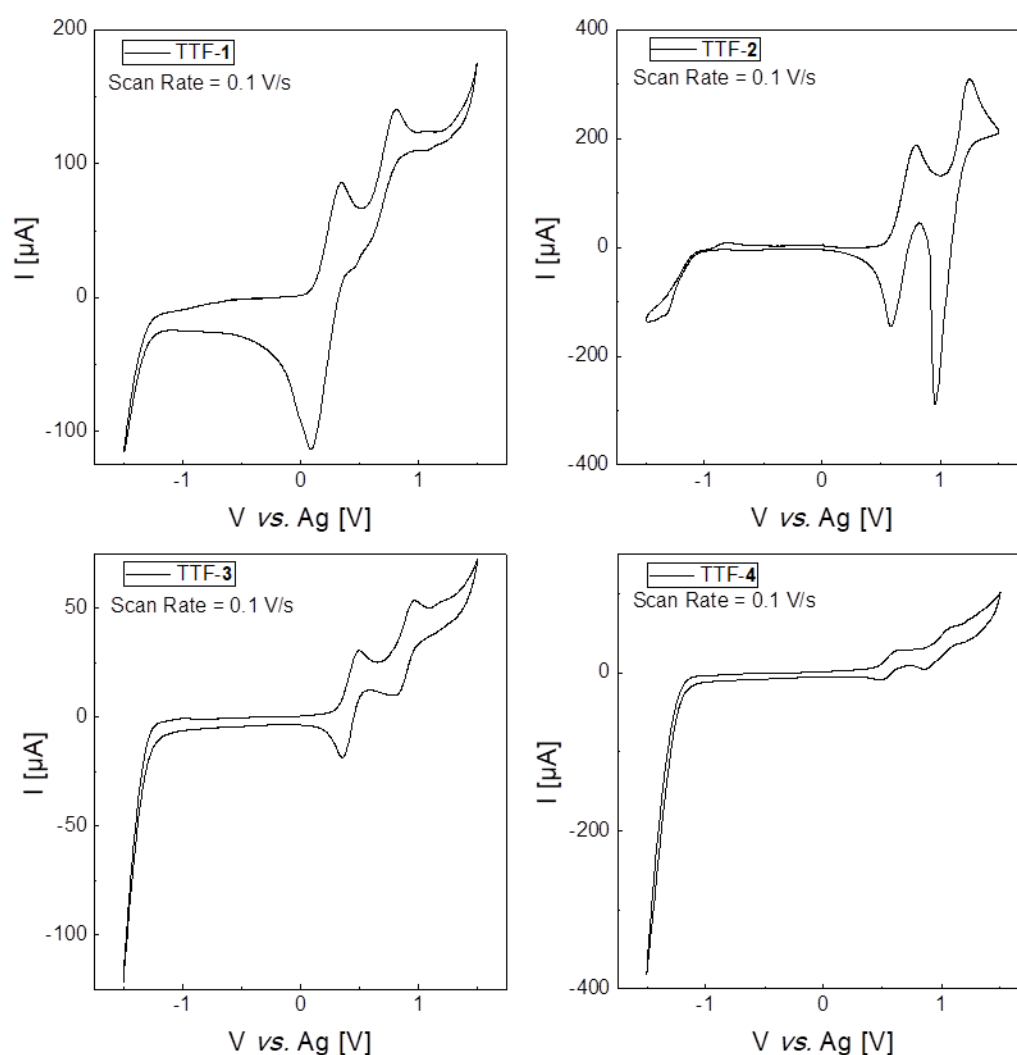


Figure 2.4. Cyclic voltammeteries of TTFs (**1-4**).

Table 2.1. Electrochemical data displayed are redox potentials vs. Fc/Fc^+ . The onset of the first oxidation peak ($E_{\text{onset}}^{\text{ox1}}$) is used to obtain the HOMO energy ($E_{\text{HOMO}}^{\text{exp}}$) through the formula previously mentioned in the text. UV-vis spectroscopy data in the table correspond to the lowest energy absorption (A_{max}) and its extinction coefficient (ϵ). The optical band gap (E_g^{opt}) was determined from the onset of the lowest energy electronic absorption. HOMO and LUMO calculated energies and the band gap ($E_{\text{HOMO}}^{\text{calc}}$, $E_{\text{LUMO}}^{\text{calc}}$, E_g^{calc}).

Compound		1	2	3	4
Electrochemical Data	$E_{1/2}^{\text{ox1}}$ [V]	-0.29	0.26	-0.01	0.11
	$E_{1/2}^{\text{ox2}}$ [V]	0.25	0.68	0.46	0.59
	$E_{\text{onset}}^{\text{ox1}}$ [V]	-0.34	0.10	-0.11	0.02
	$E_{\text{HOMO}}^{\text{exp}}$ [eV]	-4.5	-4.9	-4.7	-4.8
UV/vis data	A_{max} [cm^{-1}]	$3.31 \cdot 10^4$	$2.02 \cdot 10^4$	$2.07 \cdot 10^4$	$1.95 \cdot 10^4$
	ϵ [$\text{M}^{-1}\text{cm}^{-1}$]	$2.81 \cdot 10^4$	$1.04 \cdot 10^4$	$1.06 \cdot 10^4$	$1.16 \cdot 10^4$
	E_g^{opt} [eV]	3.35	2.11	2.13	2.03
DFT calculations data	$E_{\text{HOMO}}^{\text{calc}}$ [eV]	-4.46	-5.11	-5.08	-5.08
	$E_{\text{LUMO}}^{\text{calc}}$ [eV]	-1.14	-2.44	-2.70	-2.79
	E_g^{calc} [eV]	3.32	2.67	2.38	2.29

Optical absorption spectra were obtained in tetrahydrofuran (THF) solution and are shown in **Figure 2.5a**. All these compounds exhibit intense absorption bands at $\lambda < 400$ nm, with extinction coefficients (ϵ) of the order of $2 \cdot 10^4 \text{ M}^{-1}\text{cm}^{-1}$. Additionally, all compounds except **1** show an intense absorption band peak from 485 nm to 511 nm. According to previous works of Decurtins *et al.*,^[50–53] this lowest energy absorption band corresponds to an intramolecular charge-transfer transition from the HOMO localised on the TTF to the LUMO localised on the BTd moiety as depicted in **Figure 2.5b**.

Then, the optical HOMO-LUMO gap (E_g^{opt}) was calculated using the onset of the lowest energetic absorption peak for each compound. The obtained E_g^{opt} values are in fairly good agreement with the corresponding E_g^{calc} values depicted in **Table 2.1**. It is worthwhile noting that band gaps can be tuned by the incorporation of different substituents into the TTF structure as well as by a variation of the heteroatom in the BTd moiety.

Density functional theory (DFT) calculations³ were performed for TTFs **1–4** by using B3LYP functional^[54] and a 6-311G+ (d,p) basis set as implemented in the Gaussian09 code.^[55] All of the investigated molecules have a quite planar skeleton, which is beneficial for intermolecular interactions, and which favours charge-carrier mobility. Compared with **1**, it is clear that **2** and **3** possess a low-lying HOMO and LUMO levels upon replacing methoxy groups with the 2,1,3-chalcogendiazole ring. Furthermore, the ring with the two methoxy groups attached to the TTF causes a shift to positive values of both the HOMO and the LUMO as it can be observed when **2** is compared with **3**. Exchanging sulphur by selenium appears to lead a further slight decrease in the LUMO energy level. The match between the relative magnitudes and the absolute quantitative values of the calculated HOMO energy levels and HOMO-LUMO gaps and the

³ Theoretical calculations were carried out by Prof. Stefan T. Bromley (University of Barcelona).

corresponding experimental HOMO energy and energy gap values obtained from cyclic voltammetry and absorption spectra data, respectively, are in nearly all cases rather good. The small differences between experiment and theory (0.03-0.56 eV for E_g and 0.04-0.38 eV for E_{HOMO}) are quite acceptable, especially considering the approximations in the theoretical calculations (e.g., absence of explicit solvent effects and intermolecular interactions). As expected, in all cases, the HOMO is localised on the TTF core, whereas the LUMO is mainly located on the BTB unit in TTFs **2-4** and on the TTF core in TTF **1** (Figure 2.5b).

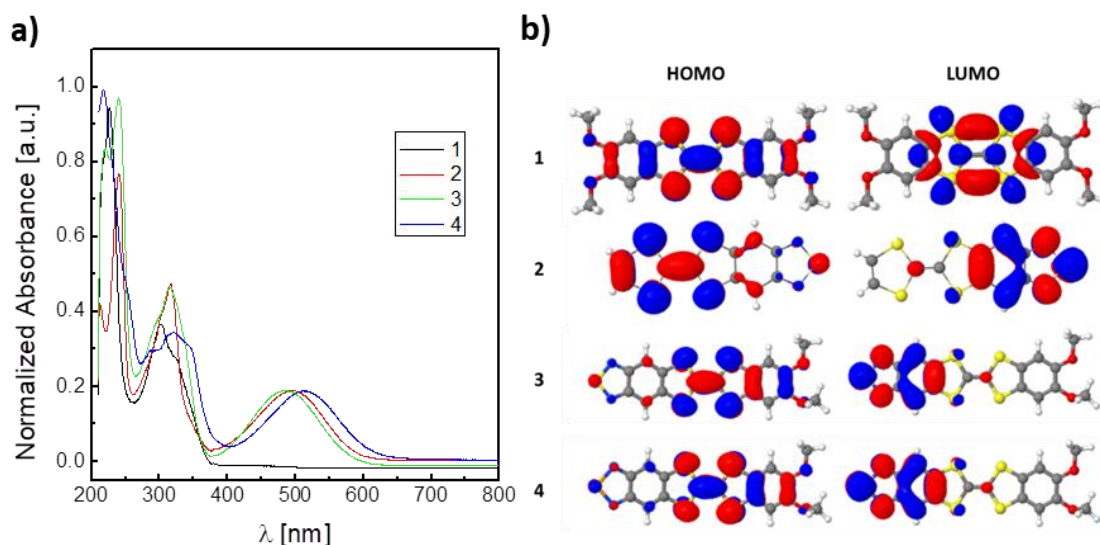


Figure 2.5. a) UV-vis spectra in THF of **1-4** and (b) HOMO and LUMO orbitals of TTFs **1-4**.

CRYSTAL STRUCTURE AND THIN-FILM CHARACTERISATION

Orange single crystals that were suitable for X-ray analysis, with a block-shaped morphology, were grown by slow evaporation of a CH_2Cl_2 /Hexane (1:1) solution of the molecule. The results showed that TTF **1** crystallises in a solvate-free form in the monoclinic space group $P2_1/c$. The molecule lies on an inversion centre; therefore, the asymmetric unit comprises half of the molecule. An ORTEP drawing of **1** is shown in Figure 2.6a. The molecule is distinctly planar; the rms deviation from a least-square plane through all the atoms (excluding the hydrogen atoms) is only 0.049 Å, and for the TTF core alone it is 0.017 Å. In the crystal structure, adjacent molecules are arranged in a nearly orthogonal manner, forming a herringbone packing as displayed in Figure 2.6b. Close S...S intermolecular contacts of 3.758 Å in the bc plane are found, together with some short C...S contacts of 3.375 and 3.468 Å and a weak O...H interaction with a distance of 2.510 Å.

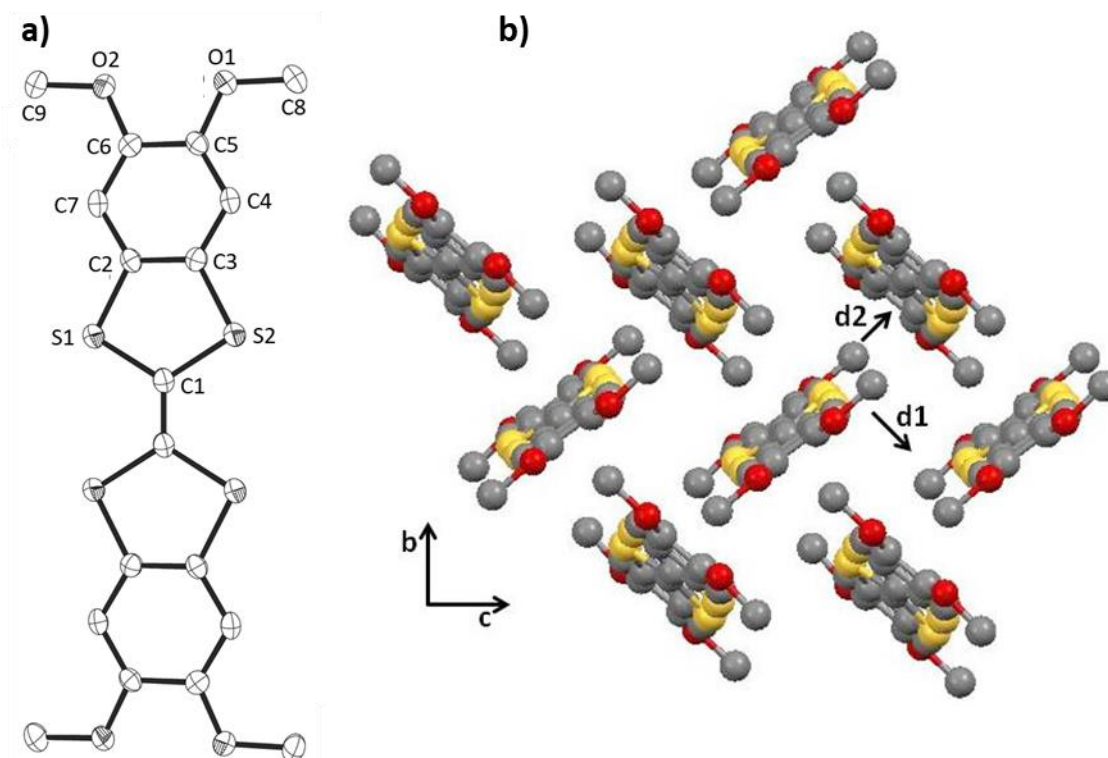


Figure 2.6. **(a)** ORTEP drawing and atomic numbering scheme of TTF **1**. Ellipsoids are set at 50 % probability, hydrogen atoms have been removed for clarity. **(b)** Crystal packing of TTF **1**.

Dimers of **1** taken from the experimental crystal structure were used to calculate the hole transfer integrals, t_h . Following Ref. ^[56], DFT calculations using the PW91 functional^[57] and a 6-31G (d,p) basis set were employed to calculate the HOMO energy splitting in the dimers (where t_h are taken to be the half of the HOMO splitting energies). Considering the crystal structure, three close pairs of neighbouring molecules were considered (two of them are indicated in **Figure 2.6b**). A large transfer integral of 224.0 meV was found in the d_1 direction and also a significant value of 56.2 meV along the edge-to-face d_2 direction. However, almost negligible electronic interactions of 0.1 meV can be found between neighbouring molecules along the a axis. Similar intermolecular interactions in TTFs have been shown to lead to high electronic intermolecular overlap and high charge carrier field-effect mobility.^[58]

In view of subsequent device fabrication, solution-grown single-crystals were fabricated with TTFs **1-4** by drop casting on Si/SiO₂ substrates a solution in 1,2-dichlorobenzene at a concentration of 0.5 mg/ml at 100°C for **1-3**, and at room temperature for **4**. In the case of **2**, the molecule crystallised forming rather big crystalline thin films. On the other hand, with TTFs **1, 3** and **4**, elongated plate-like crystals were obtained. In parallel, thermally evaporated thin-films of these materials on bare Si/SiO₂ and on Si/SiO₂ modified with the hydrophobic self-assembled monolayer (SAM) octadecyltrichlorosilane (OTS) were also fabricated.

Both drop-casted solution-grown single crystals and thermally evaporated thin-films of TTFs **1-4** were characterised by X-ray powder diffraction (XRPD). In the case of **1, 3** and **4**, the obtained XRPD patterns for both single-crystal and thin-films exhibited the same group of

reflections, which is a strong indication that they belong to the same crystalline phase (**Figure 2.7**). Furthermore, in the case of **1**, the XRPD reflections coincide with the aforementioned resolved single-crystal structure of this material (**Figure 2.6**). Considering that the observed reflections correspond to $[h\ 0\ 0]$, we can affirm that the bc plane is parallel to the substrate, which matches with the directions in which short S...S contacts are found and also larger transfer integrals were calculated.

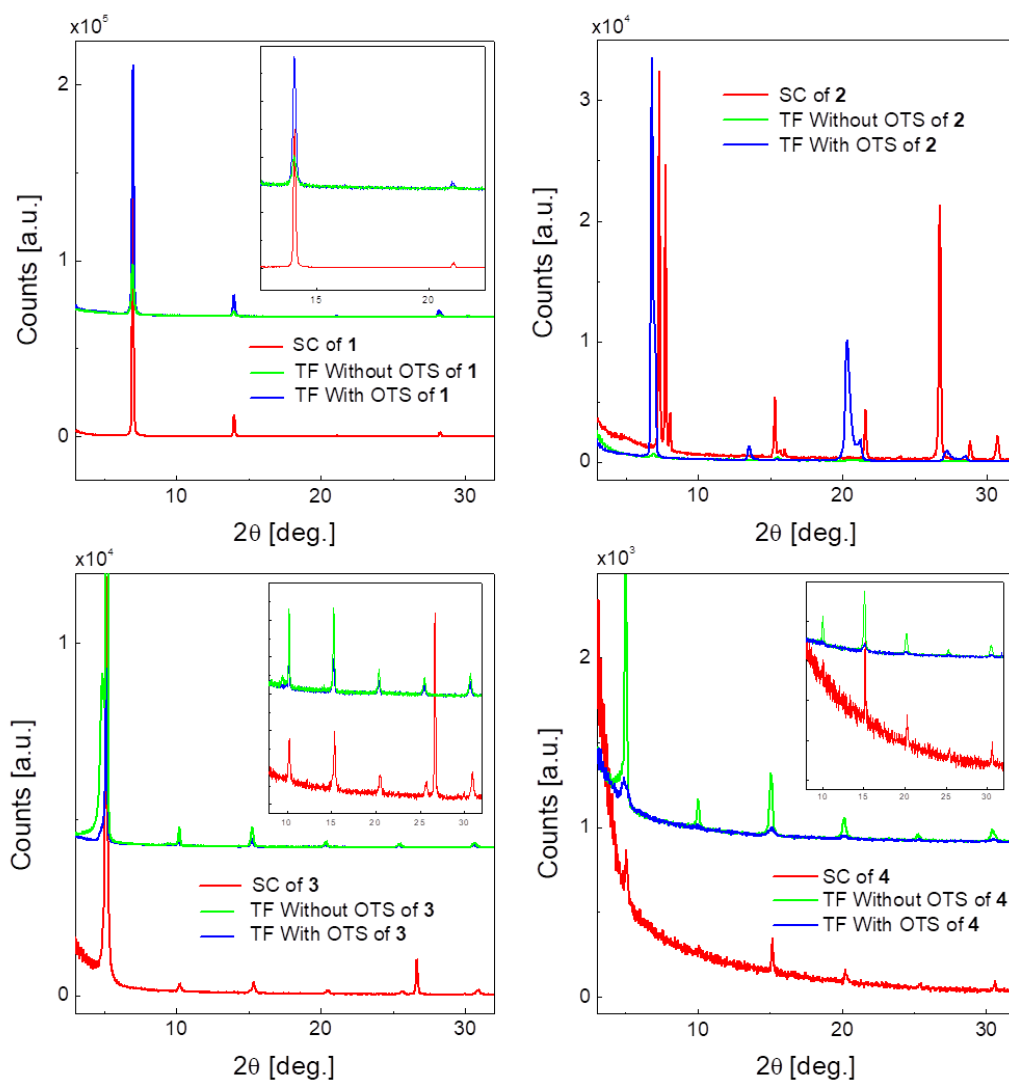


Figure 2.7. Single-crystal (SC) and thin-film (TF) X-ray powder diffraction of the TTFs **1-4**.

In the case of TTF **2**, both single-crystal and thin-film were characterised by XRPD as well but the reflections did not coincide with the already reported crystalline structure for this material. Moreover, the single-crystal reflections did not match with those found in the thin-film (**Figure 2.7**), indicating the formation of two new polymorphs when the material is crystallised on a surface, an effect commonly found in organic semiconductors, including TTFs.^[23,59]

Atomic force microscopy (AFM) analysis was carried out for the thermally evaporated thin-films. **Figure 2.8** shows typical AFM images of TTFs **1-4** that have been grown on top of a Si/SiO₂/OTS substrate; the images clearly show microcrystals in topography. The crystallites in the film of **1** have an average size of 0.25 μm^2 , but the films were very rough with a root mean square roughness (δ_{RMS}) of 172 nm. In contrast, the size of the crystallites in the thin-films of **3** and **4** were smaller (*ca.* 0.1 μm^2) and the δ_{RMS} values were 17.5 nm and 8.8 nm, respectively. Finally, the thin-film fabricated with TTF **2** had the biggest crystallites of 1.5 μm^2 and a relatively low δ_{RMS} value of 12.4 nm.

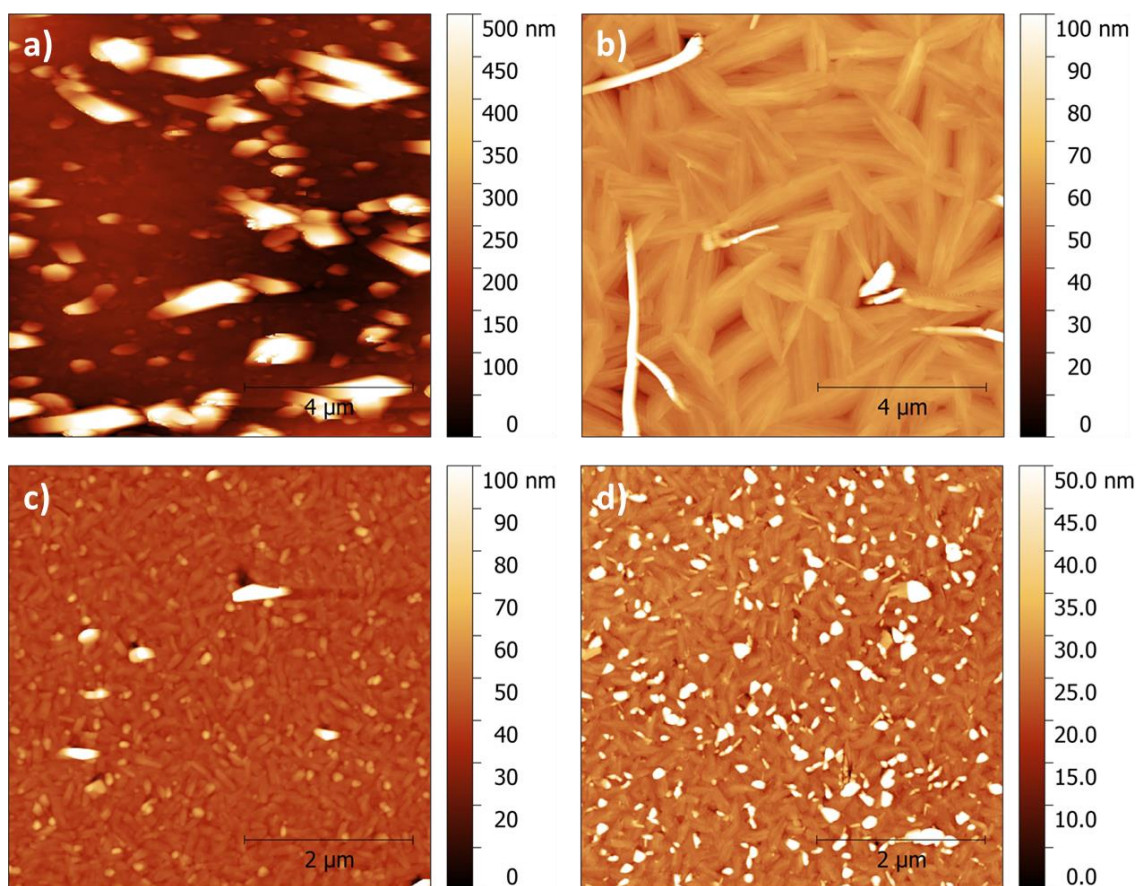


Figure 2.8. Atomic force microscopy images of evaporated thin-films made of TTFs (a) **1**, (b) **2**, (c) **3** and (d) **4**.

SINGLE-CRYSTAL ORGANIC FIELD-EFFECT TRANSISTORS

Source and drain contacts were fabricated on top of the crystals **1**, **2** and **3** prepared by drop casting using graphite paste. However, due to the small crystal size of **4**, prefabricated source and drain contacts made of Au/Cr were used. Optical microscope images of all single crystal OFETs are depicted in **Figure 2.9**.

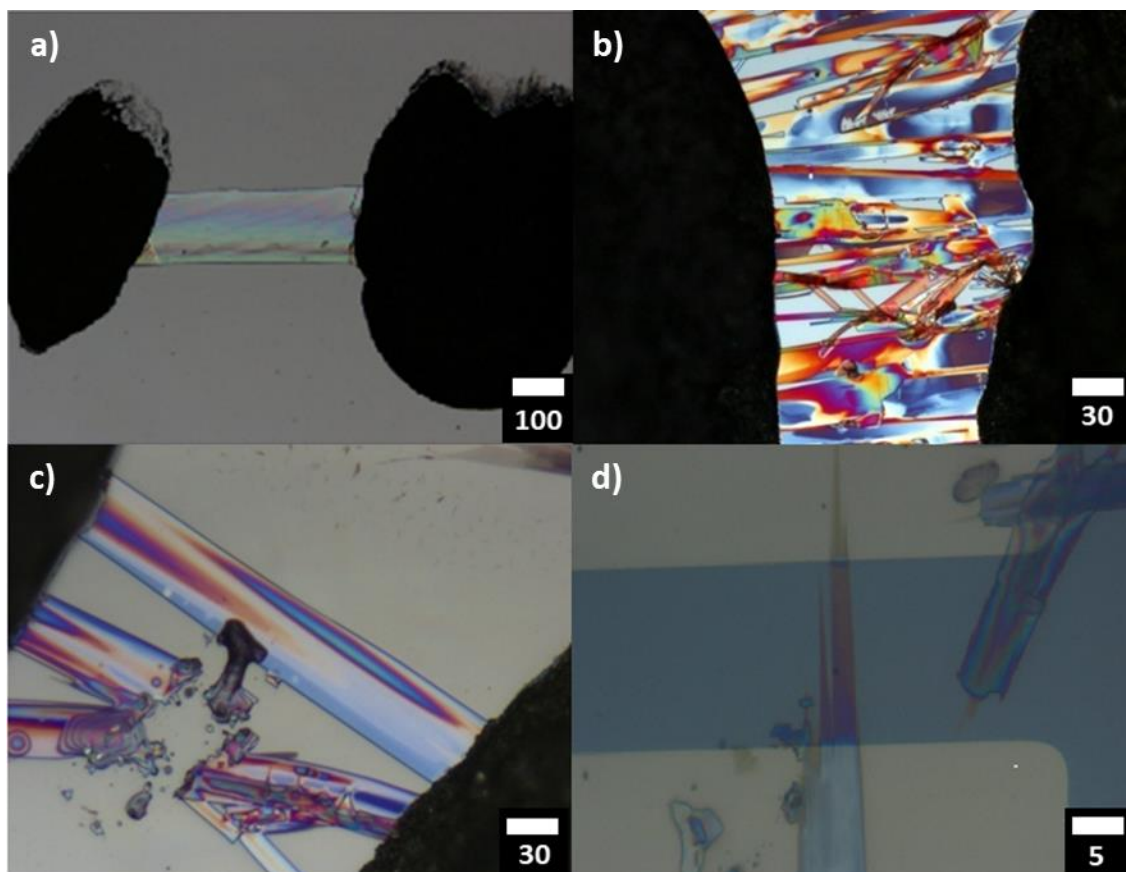


Figure 2.9. Optical microscope images of solution-grown single-crystal OFETs of TTFs (a) **1**, (b) **2**, (c) **3** and (d) **4**. Source and drain contacts of **1**, **2** and **3** were fabricated with graphite paste on top of the single crystal, whereas contacts of compound **4** were prefabricated Au/Cr electrodes (bottom contact). Scale bar corresponds to the number below in μm .

The OFET characteristics of a typical single crystal based on TTFs **1-4** measured under ambient conditions and in darkness are shown in **Figure 2.10**. These transistors show typical electrical *p*-channel characteristics. The channel dimensions were measured with an optical microscope and the measured width and length values are shown together with the extracted OFET parameters in **Table 2.2**. A negligible hysteresis was observed between forward and reverse V_{GS} sweeps. Furthermore, as displayed in **Table 2.2**, a low threshold voltage (V_{TH}) from -4 to -0.3 V was extracted in the saturation regime, indicating a low level of unintentional doping of the active material. The threshold values found for all the OSCs are considered quite low in OFETs and point towards a favourable organic/dielectric interface with a modest number of charge trapping. From the saturation regime, a field-effect mobility ($\mu_{FE,sat}$) from 0.040 to 0.001 $\text{cm}^2/\text{V}\cdot\text{s}$ was extracted. This mobility is of the same order as other solution-processed TTF OFETs.^[60,61] A set of four devices was measured for each compound exhibiting similar values in terms of device performance and OFET characteristics. Last but not least, it should be highlighted that all the devices turned out to be stable in air for over a week.

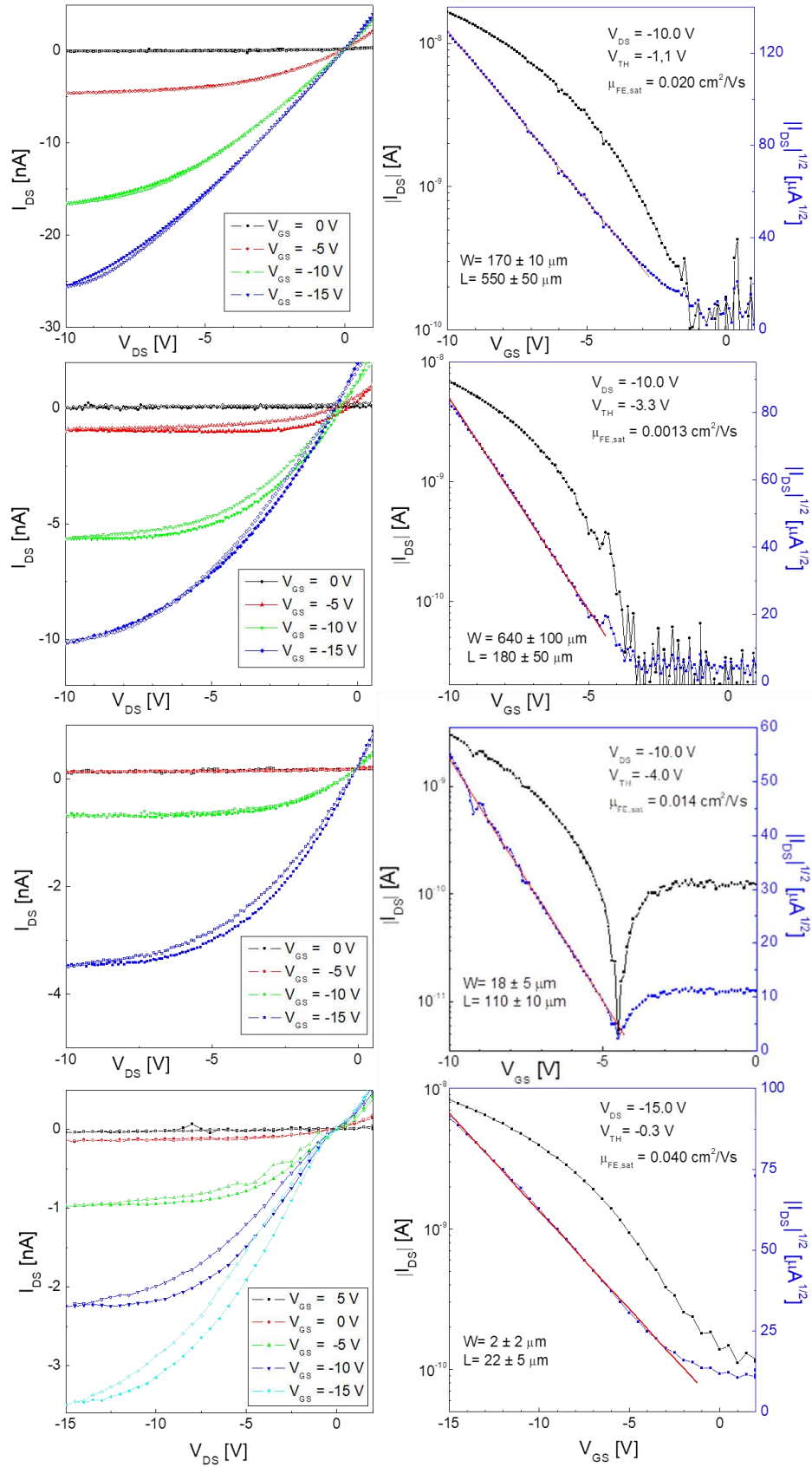


Figure 2.10. Output (left) and transfer (right) characteristics of single-crystal OFETs based on TTFs 1, 2, 3 and 4 displayed in order from top to bottom.

Table 2.2. Main parameters of single-crystal (SC) and thin film (TF) OFETs based on TTFs **1-4**. $\mu_{FE,sat}$ and V_{TH} were extracted from the saturation regime. Parameters shown for single crystals correspond to the best working transistors, even though for all the compounds, more OFETs with similar characteristics were also measured. TF values displayed are the average of 12 transistors.

	TTF-1		TTF-2		TTF-3		TTF-4	
	$10^3 \cdot \mu_{FE,sat}$ [cm ² /V·s]	V_{TH} [V]	$10^3 \cdot \mu_{FE,sat}$ [cm ² /V·s]	V_{TH} [V]	$10^3 \cdot \mu_{FE,sat}$ [cm ² /V·s]	V_{TH} [V]	$10^3 \cdot \mu_{FE,sat}$ [cm ² /V·s]	V_{TH} [V]
SC	20	-1.1	1.3	-3.3	14	-4.0	40	-0.3
TF in vacuum	4.2 ± 0.3	-11 ± 2	2.7 ± 0.4	-11 ± 2	0.8 ± 0.1	-34 ± 2	1.6 ± 0.2	-30 ± 8
TF in air	3.1 ± 0.6	5 ± 4	3.1 ± 0.6	-8 ± 3	0.4 ± 0.1	-28 ± 7	1.3 ± 0.1	-23 ± 8

THIN-FILM ORGANIC FIELD-EFFECT TRANSISTORS

Thin-film transistors were fabricated by thermal evaporation of the organic material in a bottom-contact bottom-gate configuration on Si/SiO₂/OTS substrates. Gold was used as source and drain electrodes. The first electrical characterisation carried out in darkness and mild vacuum ($P = 50$ mbar and *deposition rate* = 0.5 Å/s) was performed directly after transferring the devices from the evaporation chamber to a microscope probe station equipped with a vacuum chamber. The transfer and output characteristics of the freshly prepared transistors are shown in **Figure 2.11**. **Table 2.2** displays a summary of the average, extracted from 12 transistors, field-effect mobility and threshold voltage of the measured thin-film transistors fabricated with TTFs **1-4** and also the parameters of the same devices measured in air. We observe that the V_{TH} extracted for all four compounds gave negative values, which might be an indication of structural disorder at the very edge of the semiconductor/dielectric interface, especially in compounds **3** and **4**. Except in the case of **2**, the mobilities extracted in the saturation regime exhibited values around one order of magnitude lower than those of the single crystals, showing good performance and reproducibility for all the devices. Similar field-effect mobilities in the range of $0.8 \cdot 10^{-3}$ to $4.2 \cdot 10^{-3}$ cm²/V·s were obtained for TTFs **1-4**. Subsequently, the samples were measured in air and, in agreement with the calculated and experimentally found HOMO levels, compound **1** showed the lowest stability under ambient conditions. This was reflected in the fact that in the device measurements performed in air a large shift of the threshold voltage of around +14 V was found for devices based on **1**, whereas for the devices employing **2**, **3** and **4** as organic semiconductor, a smaller shift of +3, +6 and +7, respectively, was observed. Thus, we can affirm that the 2,1,3-chalcogendiazole moiety supports the stabilisation of the materials. It is also worth mentioning that these thin-films were also prepared on Si/SiO₂ without OTS. In all cases, slightly lower performances and less air-stable devices were obtained, probably due to a less favoured organic semiconductor/dielectric interface.

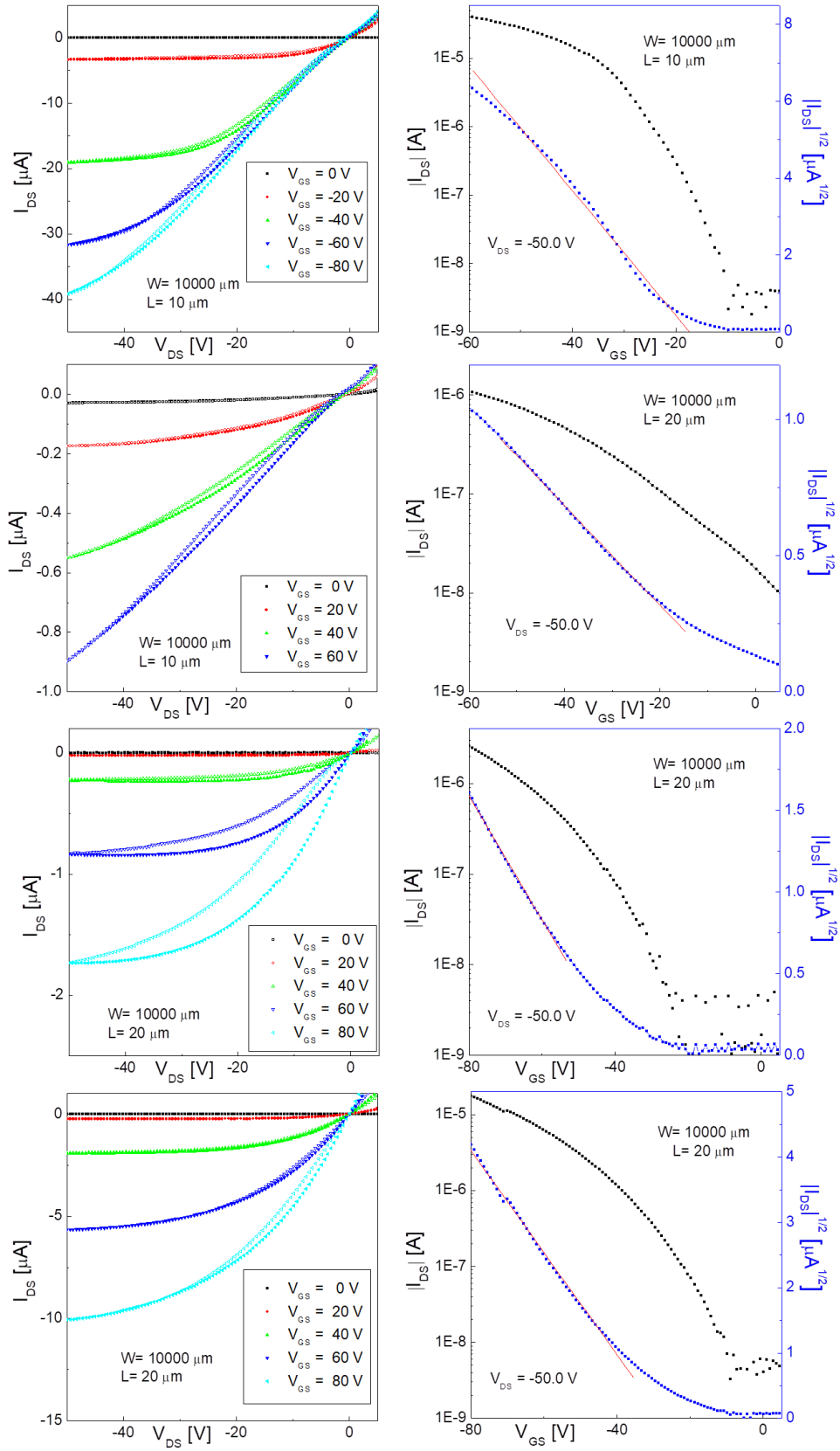


Figure 2.11. Output (left) and transfer (right) characteristics of thin-film OFET based on TTFs **1**, **2**, **3** and **4** displayed in order from top to bottom.

2.3. STUDY OF THE π -EXTENSION IMPACT ON THE STRUCTURE AND ELECTRONIC PROPERTIES OF TTF DERIVATIVES⁴

The structural properties of the molecules are very sensitive to the molecular structure and any modification in it can cause a huge change in the crystal packing, hence the overall electronic transport. Historically, several modifications to the OSC core have been performed to improve t and λ .^[1,62] Probably, among all the modifications, the extension of the π -conjugation is one of the oldest and more popular paths.^[63]

Usually, the extension of the conjugation leads to a broader delocalization of the charge and, due of that, the conformation of the molecule is less affected when a charge is accepted/donated. This more subtle conformation change between the charged and uncharged state is translated into a reduction of the λ .^[64] Furthermore, the extension of the delocalisation causes an extension of the HOMO/LUMO orbitals making more efficient the intermolecular interactions, which means that t is increased.

Here, we have extended the π -conjugation of DB-TTF by adding benzene rings. In particular, we studied: BDHN-TTF and BN-TTF (**Figure 2.2**). While BN-TTF is fully aromatic, BDHN-TTF is not fully conjugated and hence we expected to observe some differences in the transport properties due to the changes in their structural and electronic properties.^[65]

DESIGN AND SYNTHESIS

BDHN-TTF was purchased from Sigma-Aldrich and was used as reagent to obtain BN-TTF. To do so, BDHN-TTF was oxidised with 2,3-dichloro-5,6-dicyano-1,4-benzoquinone (DDQ) in dry toluene under inert conditions and the mixture was refluxed for 20 hours (**Figure 2.12**). To be used as organic semiconductor BN-TTF was purified by recrystallization in dry toluene obtaining it as a brownish powder with 61 % yield. BN-TTF was unambiguously identified by ¹H NMR, mass spectrometry (MALDI-TOF), infrared spectroscopy (ATR-IR) and differential calorimetry. Mass spectra and the data extracted from the differential calorimetry scans are shown in **Figure 2.13**.

⁴ This work has been published in Campos, A. et al. *CrystEngComm* **2016**, *18*, 6149–6152.

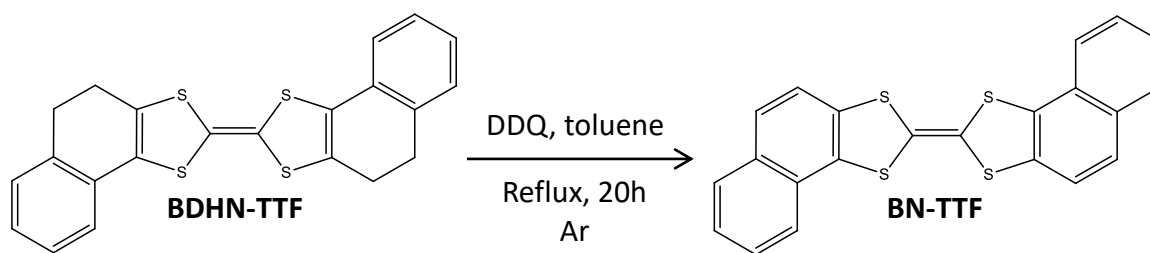


Figure 2.12. Reaction scheme for obtaining BN-TTF.

a)

Molecule	Temperature peak [°C]	Area [mJ]	ΔH [J/g]
BDHN-TTF	220.2	108.3	62.83
BN-TTF	284.7	115.9	76.05

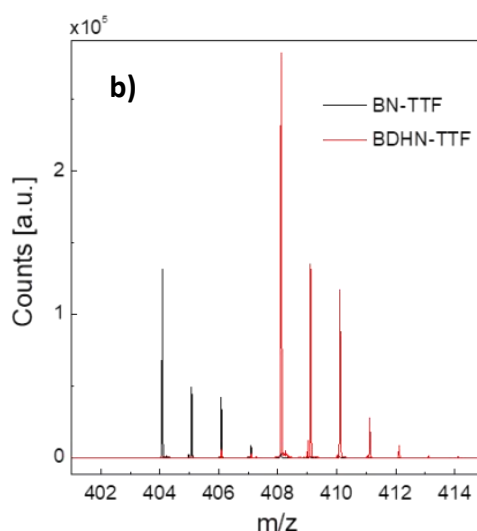


Figure 2.13. a) Table with the data extracted from the differential scanning calorimetry of BDHN-TTF and BN-TTF, respectively. **(b)** MALDI-TOF mass spectra of both molecules.

ELECTRONIC PROPERTIES

The electronic characteristics of the two TTF derivatives were investigated by cyclic voltammetry using Ag/AgCl as the reference electrode, platinum wires as working and counter electrode and a 0.1 M solution of tetrabutylammonium hexafluorophosphate in dichloromethane as the electrolyte. In both voltammograms two reversible oxidation peaks were observed, attributed to the sequential oxidation of the TTF to the radical cation and dication species (values displayed in **Table 2.3**). It is noticed that the oxidation of BN-TTF takes place at a higher voltage than that of BDHN-TTF, in agreement with a lower HOMO energy.

Under the premise that the energy level of Ag/AgCl is 4.7 eV below the vacuum level, the HOMO energy level of BN-TTF and BDHN-TTF can be estimated according to the following equation: $E_{\text{HOMO}}^{\text{exp}} = -[E_{\text{onset}}^{\text{ox1}} + 4.7]$ (eV).^[66,67] These data are included in **Table 2.3**. UV-vis spectra (**Figure 2.14**) were recorded for both materials in dichloromethane and the onset of the least energetic band was used to determine the energy gap between the HOMO and the LUMO (E_g^{opt}).

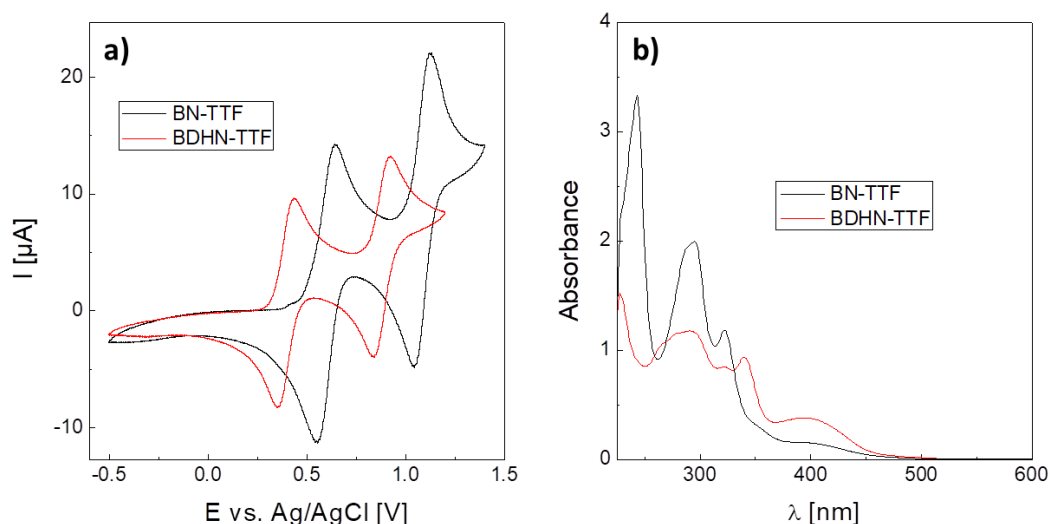


Figure 2.14. a) Cyclic voltammograms and b) UV-vis spectra of BN-TTF and BDHN-TTF in dichloromethane.

Table 2.3. Electrochemical data displayed include redox potentials vs. Ag/AgCl. The onset of the first oxidation peak ($E_{\text{onset}}^{\text{ox1}}$) is used to obtain the HOMO energy ($E_{\text{HOMO}}^{\text{exp}}$) through the formula previously mentioned in the text. UV-vis spectroscopy data in the table correspond to the lowest energy absorption (A_{max}) and its extinction coefficient (ϵ). The optical band gap was determined from the onset of the lowest energy electronic absorption. HOMO and LUMO and the band gap calculated energies ($E_{\text{HOMO}}^{\text{calc}}$, $E_{\text{LUMO}}^{\text{calc}}$, E_g^{calc}).

Compound		BDHN-TTF	BN-TTF	ΔE
Electrochemical Data	$E_{1/2}^{\text{ox1}}$ [V]	0.44	0.64	+0.20
	$E_{1/2}^{\text{ox2}}$ [V]	0.92	1.13	+0.21
	$E_{\text{onset}}^{\text{ox1}}$ [V]	0.33	0.51	+0.18
	$E_{\text{HOMO}}^{\text{exp}}$ [eV]	-5.03	-5.21	+0.18
UV/vis data	A_{max} [cm^{-1}]	$2.17 \cdot 10^4$	$2.14 \cdot 10^4$	-
	E_g^{opt} [eV]	2.70	2.65	-0.05
DFT calculations data	$E_{\text{HOMO}}^{\text{calc}}$ [eV]	-4.63	-4.86	+0.23
	$E_{\text{LUMO}}^{\text{calc}}$ [eV]	-1.37	-1.63	+0.26
	E_g^{calc} [eV]	3.26	3.23	-0.03

The electronic characteristics of BN-TTF and BDHN-TTF were also calculated by density functional theory (DFT) using the B3-LYP functional and a 6-311G+(d,p) basis set. All reported DFT calculations were carried out with the same Gaussian09 code.

As seen in **Table 2.3**, the experimentally obtained E_g^{opt} and E_{HOMO}^{exp} values by UV-vis and cyclic voltammetry, respectively, are in reasonable agreement with the calculated HOMO and gap energies. Although the calculated absolute values of the gap and HOMO energy is *ca.* 0.4-0.5 eV higher than experimental estimates, the corresponding differences in these energies between the two compounds match very well. Hence, clearly the aromatisation of BDHN-TTF leads to a lowering of the HOMO level.

CRYSTAL STRUCTURES AND THIN-FILM CHARACTERISATION

High quality orange block-shaped single crystals of BDHN-TTF were grown by slow evaporation of a solution of the molecule in *p*-xylene. BDHN-TTF crystallised in a solvate-free form in the monoclinic space group $P2_1/c$. The crystal structure contains half of a molecule in the asymmetric unit cell. Each TTF is clearly bended in a chair-like conformation (**Figure 2.15a**). The angle between the planes formed by the TTF core and the external benzene ring is 19.3° . BDHN-TTF crystallises forming layers of molecules in the *bc* plane following a herringbone fashion (*i.e.* edge-to-face orientation) as can be observed in **Figure 2.15b**. Within these sheets there are short edge-to-edge S \cdots S contacts (3.619 Å) along *c*.

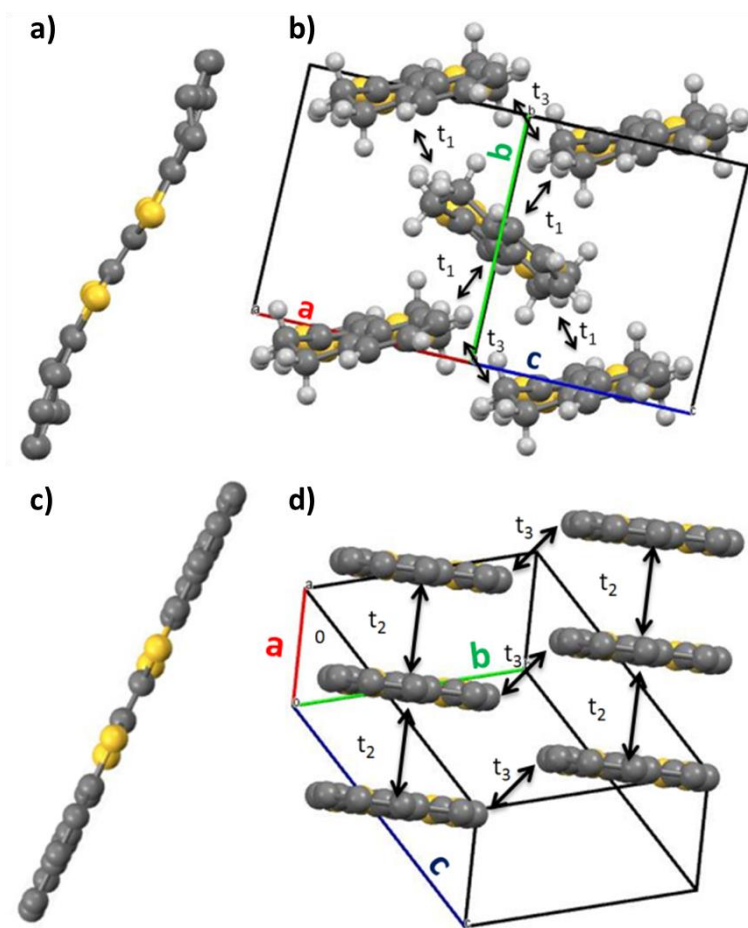


Figure 2.15. **(a)** and **(c)** Non-planar BDHN-TTF and planar BN-TTF molecules, respectively, found in their crystal structures. H atoms are omitted for clarity. **(b)** BDHN-TTF packing following a herringbone network. The t_1 and t_3 arrows indicate the directions where the integrals transfer have been calculated. **(d)** BN-TTF packing in a displaced cofacial structure showing the electronic couplings (t_2 and t_3). H atoms were also omitted here for clarity.

Yellow needle-shaped single crystals of BN-TTF were grown by diffusion of diethyl ether into a solution of the molecule in chlorobenzene. In this case, the molecule crystallised in the triclinic space group P-1 and the asymmetric unit cell also consists of half of a BN-TTF molecule, and hence each naphthalene unit is equivalent. In the case of BN-TTF molecule, the molecules are very flat, as expected due to the extended aromatic molecular structure (**Figure 2.15c**). The molecules stack in columns along the a axis slightly shifted along the molecular axis, with an interplanar spacing of 3.574 Å (**Figure 2.15d**). Short S...S contacts (3.927 Å) are also found within the stack and between stacks (3.642 Å).

Dimers of BDHN-TTF and BN-TTF taken from the resolved crystals structure were used to calculate their hole transfer integrals. As recommended in Ref. [55], DFT calculations⁵ using the PW91 functional were conducted to calculate the HOMO energy splitting of the dimers (t for hole conduction is defined as half of the HOMO energy splitting). The calculated values show

⁵ Theoretical calculations were performed by Prof. Stefan T. Bromley (University of Barcelona).

that a significant electronic interaction is found for the edge-to-face orientation for BDHN-TTF, with a minor edge-to-edge component. In BN-TTF, however, the preferential transport direction is face-to-face, suggesting a strong 1D favoured electronic path (**Table 2.4**). Furthermore, the calculated t values predict a slightly stronger intermolecular electronic coupling in BDHN-TTF crystals (109 meV) than in BN-TTF (97 meV).

Table 2.4. BDHN-TTF and BN-TTF reorganisation energies and most significant HOMO transfer integrals.

Compound	λ	Edge-to-face, t_1	Edge-to-face, t_2	Edge-to-edge, t_3
BDHN-TTF	235 meV	109 meV	-	29 meV
BN-TTF	219 meV	-	97 meV	2 meV

Furthermore, the reorganisation energy, λ , was calculated using a B3LYP/6-311+G(d,p) level of theory was used and it was found to be slightly lower in the BN-TTF case due to its more rigid and planar structure (**Table 2.4**), which is more favourable for charge transport.

Evaporated thin-films on Si/SiO₂/OTS were prepared and characterised by XRPD and AFM (**Figure 2.16**). The semiconductors were deposited by thermal evaporation ($P = 9 \cdot 10^{-7}$ mbar and *deposition rate* = 0.2-0.3 Å/s). The diffractogram of BDHN-TTF showed clear equidistant diffraction peaks indicative of the crystallinity of the film as well as the high orientation of the crystals. By comparison with the resolved crystal structure it is possible to conclude that both the thin-film and the single-crystal belong to the same phase. The peaks correspond to the ($h\ 0\ 0$) reflections and thus, the crystals are oriented with a bc plane parallel to the substrate, that is, the plane where significant electronic interactions exist (**Figure 2.16a**). Accordingly, the AFM images show that the BDHN-TTF films are formed by 2D plate-like structures (**Figure 2.16c**).

In contrast to the BDHN-TTF film, BN-TTF XRPD pattern shows only two peaks that seem to correspond to the ($0\ 0\ 1$) and ($0\ 1\ 0$) diffractions of the reported single-crystal phase (**Figure 2.16b**). The AFM images seem to confirm that BN-TTF prefers to form more 1D tape-like structures (**Figure 2.16d**). These results point out that the crystals grow with the a axis parallel to the surface (*i.e.* the longest crystal direction of the BN-TTF crystals), which corresponds to the stacking and the electronic transport direction.

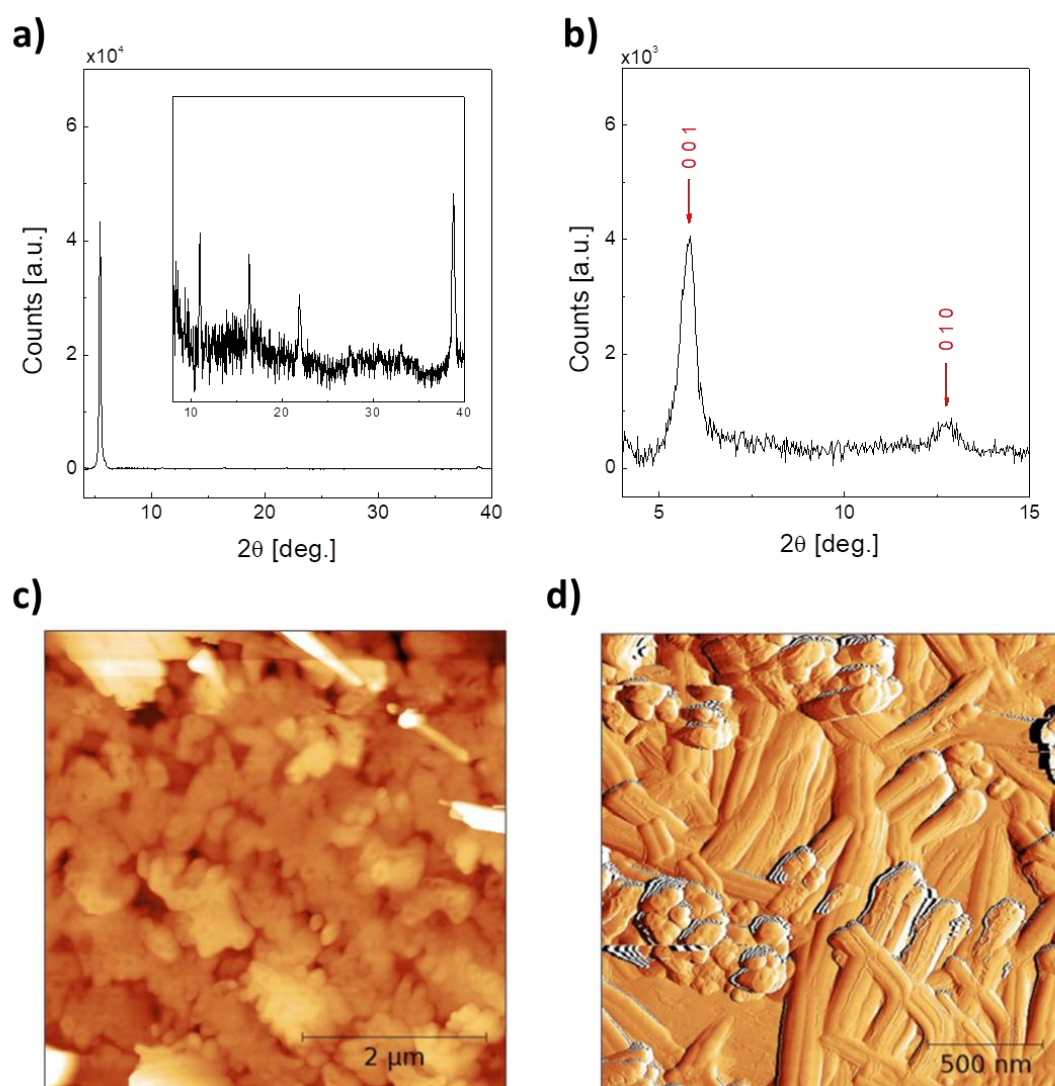


Figure 2.16. **a)** and **(b)** X-ray powder diffractograms of BDHN-TTF and BN-TTF thin films, respectively. **(c)** and **(d)** atomic force microscope images of BDHN-TTF and BN-TTF thin-films, respectively.

THIN-FILM ORGANIC FIELD-EFFECT TRANSISTORS

Thin-film OFETs were fabricated on a bottom-gate bottom-contact configuration using Si/SiO₂ substrates modified with a SAM of OTS with interdigitated Cr/Au source and drain contacts ($W = 25 \text{ mm}$ and $L = 25 \text{ }\mu\text{m}$). The TTFs were thermally evaporated on the top using the previously mentioned conditions.

Electrical measurements of the transistors were carried out inside a glovebox with levels of oxygen and water below 1 ppm to avoid the oxidation of the TTFs. Both materials behave as *p*-type organic semiconductors. BDHN-TTF OFETs display a mobility of $1 \cdot 10^{-3} \text{ cm}^2/\text{V}\cdot\text{s}$ with a threshold voltage of -11 V and low hysteresis (**Figure 2.17a-b**). However, some contact resistance can be found in these devices as observed with the S-shape of the output characteristics at low drain voltage. This is probably caused by the concentration of defects on the gold-semiconductor interface.^[7]

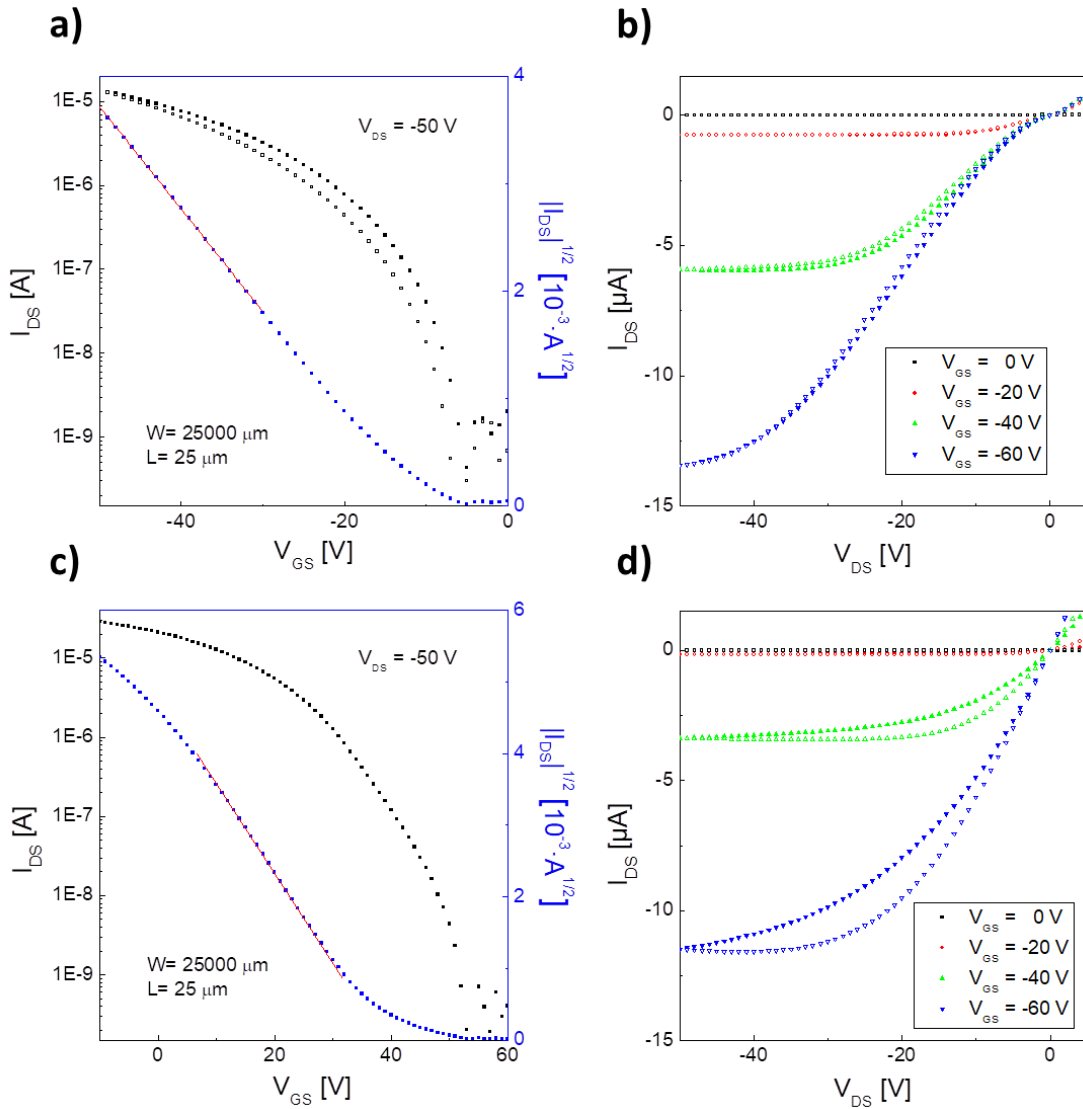


Figure 2.17. (a) and (b) transfer and output characteristics of BDHN-TTF, respectively. (c) and (d) transfer and output characteristics of BN-TTF, respectively.

On the other hand, BN-TTF transistors, after being thermal annealed for one hour at 100 °C, have a mobility value of $2 \cdot 10^{-3} \text{ cm}^2/\text{V}\cdot\text{s}$ with a large positive threshold voltage of +33 V (**Figure 2.17c-d**). Such a large positive threshold has also been typically found for the similar material DB-TTF.^[20,22,68] From the electrical characterisation, it can be concluded that both materials show similar mobility values. We believe that the different dimensionality of the two materials plays a crucial role. The two dimensional character of BDHN-TTF crystals leads to efficient edge-to-face electronic intermolecular interaction and field-effect mobilities comparable to those found in BN-TTF.

2.4. SUMMARY

To sum up, in the first part of the chapter, we have studied the influence of adding an electron deficient moiety and an electron rich one to the OSC dibenzotetrathiafulvalene on the resulting electronic and structural properties. Compared with the organic semiconductor **1**, the electron-withdrawing moiety BTd in **2**, **3** and **4** plays a crucial role in tuning the electronic properties. Based on the electrochemical data and DFT calculations, it can be concluded that the dominant electronic transitions of **2**, **3** and **4** in the visible region show significant intramolecular charge-transfer character. This result can be accounted for by the direct fusion of the BTd unit to the TTF core, forming a rigid and planar π -conjugated molecular system. Particularly, our investigation on the effect of the BTd moiety to the properties of these compounds reveals a lowering of both the LUMO and the HOMO energy levels, leading to an increase in the air stability of the OFETs fabricated with these materials but without affecting drastically the device mobility. It has been also demonstrated that single-crystal transistors based on **4** exhibit a remarkable hole mobility as well as good ambient stability.

Subsequently, comparing **1** and DB-TTF or **2** and **3** it can be noticed that the presence of the methoxy groups attached to the core has increased the HOMO and LUMO energy levels, which may be useful, for instance, to approach the HOMO energy of certain low-lying HOMO organic semiconductors to the gold work function for enhancing the charge injection and hence the OFET performance. Last but not least, the conclusion that can be extracted by comparing **3** and **4** is that by changing S for Se there is a subtle enhancement in the transistor parameters. However, the lack of a resolved structure makes impossible to completely assure that this effect is coming only from the atom substitution and not from a change in the crystal structure.

In essence, this part of the work provides insights into the HOMO stabilisation in π -extended TTF derivatives by virtue of the electron-withdrawing character of the unit BTd, thus leading to improvement of the OFET devices. Further work will be focused on finely-tuning TTF-BTd topologies through appropriate molecule functionalization to modulate the intermolecular interactions and thin-film morphologies for achieving high-performance OFETs.

Regarding the second part of the chapter, we have reported here the crystal structure of BDHN-TTF and BN-TTF as well as their electronic properties experimentally and theoretically. The reorganisation energy values estimated for BN-TTF are reduced with respect to BDHN-TTF revealing that the extension of the π -system should be beneficial for charge transport. However, it is observed that the molecular modifications also have a strong impact on the crystal structure. BDHN-TTF crystallises in a herringbone pattern exhibiting significant molecular interactions in the *bc* plane, whilst BN-TTF shows a 1D displaced cofacial packing.

Thin-film OFETs were fabricated with both materials exhibiting similar transistor performance which can be accounted for the balance between the calculated reorganisation energy values, transfer integrals and the electronic dimensionality. Thus, we demonstrate that molecular

CHAPTER 2

engineering is important in order to obtain high mobility materials; however, the crystal structure, which is harder to predict, and, specifically, the electronic dimensionality also play a crucial role.

2.5. REFERENCES

- [1] R. Pfattner, S. T. Bromley, C. Rovira, M. Mas-Torrent, *Adv. Funct. Mater.* **2016**, *26*, 2256.
- [2] C. Ruzie, J. Karpinska, A. Laurent, L. Sanguinet, S. Hunter, T. D. Anthopoulos, V. Lemaure, J. Cornil, A. R. Kennedy, O. Fenwick, P. Samori, G. Schweicher, B. Chattopadhyay, Y. H. Geerts, *J. Mater. Chem. C* **2016**, *4*, 4863.
- [3] X. Xu, Y. Yao, B. Shan, X. Gu, D. Liu, J. Liu, J. Xu, N. Zhao, W. Hu, Q. Miao, *Adv. Mater.* **2016**, *28*, 5276.
- [4] M. Mas-Torrent, C. Rovira, *Chem. Soc. Rev.* **2008**, *37*, 827.
- [5] M. Mas-Torrent, C. Rovira, *Chem. Rev.* **2011**, *111*, 4833.
- [6] B. A. Jones, A. Facchetti, M. R. Wasielewski, T. J. Marks, *J. Am. Chem. Soc.* **2007**, *129*, 15259.
- [7] C. Liu, Y. Xu, Y. Y. Noh, *Mater. Today* **2015**, *18*, 79.
- [8] H. Sirringhaus, *Adv. Mater.* **2009**, *21*, 3859.
- [9] K. Zhou, H. Dong, H.-L. Zhang, W. Hu, *Phys. Chem. Chem. Phys.* **2014**, *16*, 22448.
- [10] R. A. Marcus, *Angew. Chem. Int. Ed.* **1993**, *32*, 1111.
- [11] S. T. Bromley, M. Mas-Torrent, P. Hadley, C. Rovira, *J. Am. Chem. Soc.* **2004**, *126*, 6544.
- [12] V. Coropceanu, J. Cornil, D. A. da Silva Filho, Y. Olivier, R. Silbey, J. L. Brédas, *Chem. Rev.* **2007**, *107*, 926.
- [13] J. L. Brédas, D. Beljonne, V. Coropceanu, J. Cornil, *Chem. Rev.* **2004**, *104*, 4971.
- [14] J. E. Anthony, J. S. Brooks, D. L. Eaton, S. R. Parkin, *J. Am. Chem. Soc.* **2001**, *123*, 9482.
- [15] T. Izawa, E. Miyazaki, K. Takimiya, *Adv. Mater.* **2008**, *20*, 3388.
- [16] F. Otón, R. Pfattner, E. Pavlica, Y. Olivier, G. Bratina, J. Cornil, J. Puigdollers, R. Alcubilla, X. Fontrodona, M. Mas-Torrent, J. Veciana, C. Rovira, *CrystEngComm* **2011**, *13*, 6597.
- [17] J. Y. Back, H. Yu, I. Song, I. Kang, H. Ahn, T. J. Shin, S.-K. Kwon, J. H. Oh, Y.-H. Kim, *Chem. Mater.* **2015**, *27*, 1732.
- [18] B. A. Jones, A. Facchetti, M. R. Wasielewski, T. J. Marks, **2007**, *56*, 15259.
- [19] M. Mas-Torrent, P. Hadley, S. T. Bromley, N. Crivillers, J. Veciana, C. Rovira, *Appl. Phys. Lett.* **2005**, *86*, 012110.
- [20] Naraso, J. Nishida, S. Ando, J. Yamaguchi, K. Itaka, H. Koinuma, H. Tada, S. Tokito, Y. Yamashita, *J. Am. Chem. Soc.* **2005**, *127*, 10142.

- [21] K. Shibata, K. Ishikawa, H. Takezoe, H. Wada, T. Mori, K. Shibata, K. Ishikawa, H. Takezoe, *Appl. Phys. Lett.* **2008**, *92*, 023305.
- [22] T. Yamada, T. Hasegawa, M. Hiraoka, H. Matsui, Y. Tokura, G. Saito, *Appl. Phys. Lett.* **2008**, *92*, 233306.
- [23] A. Brillante, I. Bilotti, R. G. Della Valle, E. Venuti, S. Milita, C. Dionigi, F. Borgatti, A. N. Lazar, F. Biscarini, M. Mas-Torrent, N. S. Oxtoby, N. Crivillers, J. Veciana, C. Rovira, M. Leufgen, G. Schmidt, L. W. Molenkamp, *CrystEngComm* **2008**, *10*, 1899.
- [24] F. Otón, R. Pfattner, E. Pavlica, Y. Olivier, E. Moreno, J. Puigdollers, G. Bratina, J. Cornil, X. Fontrodona, M. Mas-Torrent, J. Veciana, C. Rovira, *Chem. Mater.* **2011**, *23*, 851.
- [25] F. Otón, R. Pfattner, N. S. Oxtoby, M. Mas-Torrent, K. Wurst, X. Fontrodona, Y. Olivier, J. Cornil, J. Veciana, C. Rovira, *J. Org. Chem.* **2011**, *76*, 154.
- [26] X. K. Gao, Y. Wang, X. D. Yang, Y. Q. Liu, W. F. Qiu, W. P. Wu, H. J. Zhang, T. Qi, Y. Liu, K. Lu, C. Y. Du, Z. G. Shuai, G. Yu, D. B. Zhu, *Adv. Mater.* **2007**, *19*, 3037.
- [27] L. Tan, Y. Guo, Y. Yang, G. Zhang, D. Zhang, G. Yu, W. Xu, Y. Liu, *Chem. Sci.* **2012**, *3*, 2530.
- [28] N. M. Tucker, A. L. Briseno, O. Acton, H. L. Yip, H. Ma, S. A. Jenekhe, Y. Xia, A. K. Y. Jen, *ACS Appl. Mater. Interfaces* **2013**, *5*, 2320.
- [29] Y. Li, S. P. Singh, P. Sonar, *Adv. Mater.* **2010**, *22*, 4862.
- [30] J. Fan, J. D. Yuen, M. Wang, J. Seifter, J. H. Seo, A. R. Mohebbi, D. Zakhidov, A. Heeger, F. Wudl, *Adv. Mater.* **2012**, *24*, 2186.
- [31] L. Yan, Y. Zhao, H. Yu, Z. Hu, Y. He, A. Li, O. Goto, C. Yan, T. Chen, R. Chen, Y.-L. Loo, D. F. Perepichka, H. Meng, W. Huang, *J. Mater. Chem. C* **2016**, *4*, 3517.
- [32] C. Yao, X. Chen, Y. He, Y. Guo, I. Murtaza, H. Meng, *RSC Adv.* **2017**, *7*, 5514.
- [33] Y. Wu, W. Zhu, *Chem. Soc. Rev.* **2013**, *42*, 2039.
- [34] C. R. Belton, A. L. Kanibolotsky, J. Kirkpatrick, C. Orofino, S. E. T. Elmasly, P. N. Stavrinou, P. J. Skabara, D. D. C. Bradley, *Adv. Funct. Mater.* **2013**, *23*, 2792.
- [35] L. V. Brownell, K. Jang, K. A. Robins, I. C. Tran, C. Heske, D.-C. Lee, *Phys. Chem. Chem. Phys.* **2013**, *15*, 5967.
- [36] M. Scarongella, A. Laktionov, U. Rothlisberger, N. Banerji, *J. Mater. Chem. C* **2013**, *1*, 2308.
- [37] G. Yang, C. Di, G. Zhang, J. Zhang, J. Xiang, D. Zhang, D. Zhu, *Adv. Funct. Mater.* **2013**, *23*, 1671.
- [38] Y. Geng, R. Pfattner, A. Campos, J. Hauser, V. Laukhin, J. Puigdollers, J. Veciana, M. Mas-Torrent, C. Rovira, S. Decurtins, S. X. Liu, *Chem. - A Eur. J.* **2014**, *20*, 7136.

- [39] Y. Geng, R. Pfattner, A. Campos, W. Wang, O. Jeannin, J. Hauser, J. Puigdollers, S. T. Bromley, S. Decurtins, J. Veciana, C. Rovira, M. Mas-Torrent, S. X. Liu, *Chem. - A Eur. J.* **2014**, *20*, 16672.
- [40] X. Guo, S. R. Puniredd, M. Baumgarten, W. Pisula, K. Müllen, *J. Am. Chem. Soc.* **2012**, *134*, 8404.
- [41] M. Zhang, H. N. Tsao, W. Pisula, C. Yang, A. K. Mishra, K. Müllen, *J. Am. Chem. Soc.* **2007**, *129*, 3472.
- [42] J. Hou, H.-Y. Chen, S. Zhang, G. Li, Y. Yang, *J. Am. Chem. Soc.* **2008**, *130*, 16144.
- [43] H. N. Tsao, D. M. Cho, I. Park, M. R. Hansen, A. Mavrinskiy, D. Y. Yoon, R. Graf, W. Pisula, H. W. Spiess, K. Müllen, *J. Am. Chem. Soc.* **2011**, *133*, 2605.
- [44] K. Takimiya, S. Shinamura, I. Osaka, E. Miyazaki, *Adv. Mater.* **2011**, *23*, 4347.
- [45] K. Xiao, Y. Liu, T. Qi, W. Zhang, F. Wang, J. Gao, W. Qiu, Y. Ma, G. Cui, S. Chen, X. Zhan, G. Yu, J. Qin, W. Hu, D. Zhu, *J. Am. Chem. Soc.* **2005**, *127*, 13281.
- [46] I. McCulloch, C. Bailey, M. Giles, M. Heeney, I. Love, M. Shkunov, D. Sparrowe, S. Tierney, *Chem. Mater.* **2005**, *17*, 1381.
- [47] D. Coucouvanis, A. R. Paital, Q. Zhang, N. Lehnert, R. Ahlrichs, K. Fink, D. Fenske, A. K. Powell, Y. Lan, *Inorg. Chem.* **2009**, *48*, 8830.
- [48] J. Pommerehne, H. Vestweber, W. Guss, R. F. Mahrt, H. Bässler, M. Porsch, J. Daub, *Adv. Mater.* **1995**, *7*, 551.
- [49] D. Mi, H. U. Kim, J. H. Kim, F. Xu, S. H. Jin, D. H. Hwang, *Synth. Met.* **2012**, *162*, 483.
- [50] W. Wang, N. Zhao, Y. Geng, S.-B. Cui, J. Hauser, S. Decurtins, S.-X. Liu, *RSC Adv.* **2014**, *4*, 32639.
- [51] H. P. Jia, J. Ding, Y. F. Ran, S. X. Liu, C. Blum, I. Petkova, A. Hauser, S. Decurtins, *Chem. - An Asian J.* **2011**, *6*, 3312.
- [52] F. Pop, A. Amacher, N. Avarvari, J. Ding, L. M. L. Daku, A. Hauser, M. Koch, J. Hauser, S. X. Liu, S. Decurtins, *Chem. - A Eur. J.* **2013**, *19*, 2504.
- [53] A. Amacher, H. Luo, Z. Liu, M. Bircher, M. Cascella, J. Hauser, S. Decurtins, D. Zhang, S.-X. Liu, *RSC Adv.* **2014**, *4*, 2873.
- [54] P. J. Stephens, F. J. Devlin, C. F. Chabalowski, M. J. Frisch, *J. Phys. Chem.* **1994**, *98*, 11623.
- [55] D. J. Frisch, M. J.; Trucks, G.W.; Schlegel, H. B.; Scuseria, G. E.; Robb, M. A.; Cheeseman, J. R.; Scalmani, G.; Barone, V.;Mennucci, B.; Petersson, G. A.; Nakatsuji, H.; Caricato, M.; Li, X.; Hratchian, H. P.; Izmaylov, A. F.; Bloino, J.; Zheng, G.; Sonnenber, *Gaussian, Inc. Wallingford CT* **2009**, *2*.

- [56] J. Huang, M. Kertesz, *J. Chem. Phys.* **2005**, 122, 234707.
- [57] J. Perdew, J. Chevary, S. Vosko, K. Jackson, M. Pederson, D. Singh, C. Fiolhais, *Phys. Rev. B* **1993**, 48, 4978.
- [58] C. Moreno, R. Pfattner, M. Mas-Torrent, J. Puigdollers, S. T. Bromley, C. Rovira, J. Veciana, R. Alcubilla, *J. Mater. Chem.* **2012**, 22, 345.
- [59] A. O. F. Jones, Y. H. Geerts, J. Karpinska, A. R. Kennedy, R. Resel, C. Röthel, C. Ruzié, O. Werzer, M. Sferrazza, *ACS Appl. Mater. Interfaces* **2015**, 7, 1868.
- [60] X. Gao, W. Wu, Y. Liu, W. Qiu, X. Sun, G. Yu, D. Zhu, *Chem. Commun.* **2006**, 2750.
- [61] I. Doi, E. Miyazaki, K. Takimiya, Y. Kunugi, *Chem. Mater.* **2007**, 19, 5230.
- [62] H. Jiang, X. Yang, Z. Cui, Y. Liu, H. Li, W. Hu, C. Kloc, *CrystEngComm* **2014**, 16, 5968.
- [63] J. Mei, Y. Diao, A. L. Appleton, L. Fang, Z. Bao, *J. Am. Chem. Soc.* **2013**, 135, 6724.
- [64] A. A. Bakulin, A. Rao, V. G. Pavelyev, P. H. M. van Loosdrecht, M. S. Pshenichnikow, D. Niedzialek, J. Cornil, D. Beljonne, R. H. Friend, *Science (80-.)*. **2012**, 335, 1340.
- [65] A. Campos, N. Oxtoby, S. Galindo, R. Pfattner, J. Veciana, S. T. Bromley, C. Rovira, M. Mas-Torrent, *CrystEngComm* **2016**, 18, 6149.
- [66] T. Lee, C. A. Landis, B. M. Dhar, B. J. Jung, J. Sun, A. Sarjeant, H. J. Lee, H. E. Katz, *J. Am. Chem. Soc.* **2009**, 131, 1692.
- [67] A. J. Bard, L. R. Faulkner, J. Leddy, C. Zoski, *Electrochemical Methods: Fundamentals and Applications*, **1980**.
- [68] J. Nagakubo, M. Ashizawa, T. Kawamoto, A. Tanioka, T. Mori, *Phys. Chem. Chem. Phys.* **2011**, 13, 14370.

CHAPTER 3 A SULFUR-BRIDGED ANNULENE DERIVATIVE AS ACTIVE MATERIAL FOR HIGH PERFORMANCE OFETS¹

3.1. INTRODUCTION AND OBJECTIVES

In 2011, Singh *et al.* synthesised a new family of organic semiconducting molecules based on the unit tetrathia[22]annulene[2,1,2,1].^[1] In that work, three different *meso*-substituted derivatives were synthesised and studied showing that the double phenyl-substituted compound or **DPTTA** (**Figure 3.1**) displayed fairly good organic semiconductor properties with a hole mobility of 0.25 cm²/V·s in evaporated thin-film OFETs and 0.7 cm²/V·s in single-crystal OFETs. Furthermore, DPTTA crystallised with all the sulphur atoms in the same plane in a displaced cofacial structure with an interplanar distance of 3.746 Å and also short C...C contacts between molecular stacks of 3.719 Å.

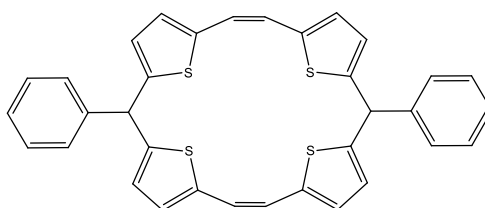


Figure 3.1. DPTTA molecular structure.

DPTTA was also exploited as p-type OSC cocrystallised with n-type OSCs, mainly tetracyanoquinodimethane (TCNQ) and derivatives, to form donor/acceptor cocrystals, some of which exhibited remarkable hole and electron mobilities.^[2–4] However, despite the high potential of this material as active component in devices, to the best of our knowledge, thin-films of this material had never been processed by any solution-based processing technique, which clearly hindered its applicability into real devices.

¹ This work has been published in Campos, A. et al. *Adv. Electron. Mater.* **2017**, 1700349.

Solution-based processing techniques have demonstrated to be the way towards low-cost processing due to the simplicity of the deposition and the lack of involved expensive processes. Yet, not all the solution-based processing techniques are suitable for all kind of applications or scales.^[5] For instance, spin coating is an interesting technique for achieving good crystallinity in thin-films but it is not compatible with high throughput processes. In contrast, techniques based on solution shearing have demonstrated that can be useful to be included in up scaled processes and can also lead to high quality crystalline thin-films necessary for organic electronics of small molecules.^[6–9] Among the solution-shearing techniques, our group has developed one in which the solution is sheared with a bar and so it is named Bar-Assisted Meniscus Shearing (BAMS).^[6,10] BAMS has demonstrated to be capable of forming very thin-films (20–40 nm) with high crystallinity of small molecule OSCs. This is typically realised at a linear output speed of 1 cm/s and the width of coating is only limited by the bar size. A more detailed description of BAMS technique can be found in Chapter 1. Importantly, BAMS has demonstrated its full potential when the OSC is mixed with a polymer binder.

As commented in the introduction, one promising approach for facilitating thin film processability of small molecule OSCs is based on employing solutions of the semiconductor with binding polymers.^[6,8,11] Thin-films prepared from such kind of blends have often displayed superior performance compared to the pristine OSC film once integrated in electronic devices due to an enhanced crystallinity and improved device stability towards adventitious agents.^[10]

Further, the addition of binding polymers combined with BAMS has demonstrated to be an efficient strategy to improve the stability of electrolyte-gated organic field-effect transistors (EGOFETs) against water or strong ionic aqueous solutions.^[10,12,13] Such an enhanced water stability comes from the high crystallinity of the films and their self-encapsulation by a thin binding polymer layer.^[13,14] For instance, in a previous work of the group, dibenzotetrathiafulvalene (DB-TTF), which is a molecule very sensitive to the moisture, has displayed excellent performance when used in EGOFET configuration and deposited together with polystyrene (PS).^[10,12]

The objective of this thesis chapter is to develop a route towards the solution-processing of DPTTA by BAMS to shed some light on the potential of this quite uncharted material. To do so, first DPTTA was synthesised. Then, we proceeded to optimise a suitable formulation mixing it with different molecular weight polystyrenes. The resulting films were fully characterised and subsequently applied as active materials in OFETs and EGOFETs.

3.2. SYNTHESIS OF DPTTA²

The synthesis of DPTTA was performed following the previously reported route.^[1] The synthetic pathway carried out is shown in **Figure 3.2**.

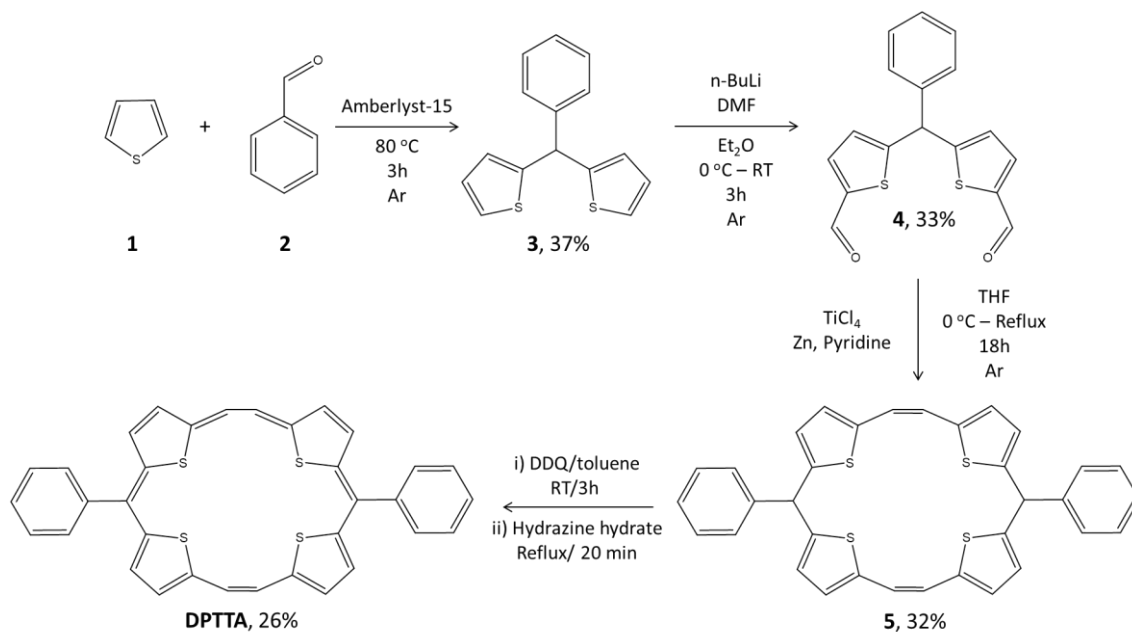


Figure 3.2. Synthetic route to DPTTA.

In the first step, target compound **3** was obtained with a 37% yield by an acid-catalysed aldehyde condensation with thiophene and benzaldehyde in the presence of a heterogeneous acid catalyst such as Amberlyst-15. Subsequently, a diformylation reaction on **3** with DMF as reagent and butyl lithium as base was accomplished to obtain **4** with a 33% yield. Afterwards, a McMurry coupling reaction was carried out with **4** reacting with Zn, pyridine and titanium chloride to finally obtaining **5** with 32% yield. Finally, DPTTA was obtained by oxidation of **5** with 2,3-dichloro-5,6-dicyano-1,4-benzoquinone (DDQ) and the subsequent treatment with hydrazine. More detailed information about this synthesis can be found in the experimental methods chapter. All compounds were purified by chromatographic separation and the identity of DPTTA was confirmed by ¹H-NMR.

² This work was carried out in collaboration with Dr. Ajayakumar M. R. (ICMAB-CSIC).

3.3. THIN-FILM PREPARATION AND CHARACTERISATION

Films processed by BAMS of pristine DPTTA were tested but, due to the low solubility of the material even when using hot solvents such as chlorobenzene or dichlorobenzene that usually work quite well with this kind of apolar and aromatic molecules, it was impossible to deposit a homogeneous and crystalline film. As commented before, not only the amount of solubilised molecule but also the viscosity of the solution determines the success of forming a homogeneous film. Hence, for the thin-film processing of DPTTA it was required to blend it with binding polymers. In particular, we chose polystyrene (PS) which has shown to give promising results with other OSCs.^[6,8]

DPTTA and PS blend solutions were deposited using different ratios of DPTTA:PS and PS of different molecular weights (3, 10 and 100 kg/mol, namely PS 3k, 10k and 100k, respectively) with a total concentration in the range 15-26 mg/mL and using anisole and chlorobenzene (CB) as solvents. The detailed information about the main screening tests performed with DPTTA is displayed in **Table 3.1**. In all the formulations the concentration of DPTTA could not exceed 7.5 mg/mL due to its aforementioned low solubility. The conventional BAMS setup requires the use of a metallic bar so that the solution can form a meniscus between the bar and the heated substrate. Subsequently, the bar is displaced at a specific velocity. However, our first attempts for preparing films of DPTTA blended with PS on Si/SiO₂ substrates failed. As depicted in **Figure 3.3**, the resulting films were not crystalline. Interestingly, when the material of the bar was changed from stainless steel to polytetrafluoroethylene (PTFE), a homogeneous polycrystalline film was obtained (**Figure 3.4**).

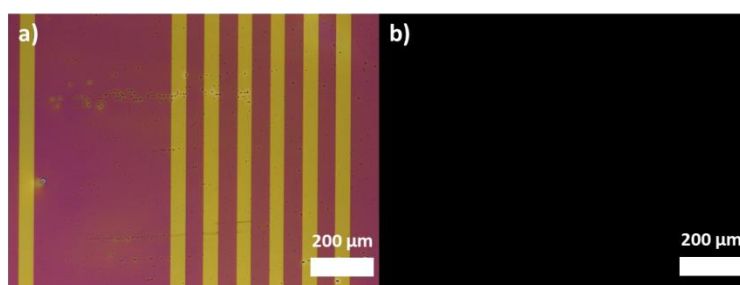


Figure 3.3. a) Optical and (b) polarized optical microscope images of a DPTTA:PS film deposited by BAMS with a metal bar.

It is worth mentioning that this is not the first time that changing the surface energy of the shearing component makes a difference in the resulting film. For instance, Giri *et al.* reported an increase in the OFET performance when the solution was sheared using a hydrophobic self-assembled monolayer (SAM) modified glass plate for depositing the organic semiconductor.^[9] In our case, we suggest that the different meniscus shape caused by the hydrophobicity of the bar is the most likely reason for the two different behaviors observed in the present case. The fine control of the above mentioned experimental conditions and the pre-heating of the blend

solution to avoid material precipitation were fundamental requirements for obtaining good coatings with high reproducibility and small device-to-device variation in terms of electrical performance and film morphology.

In addition, the use of self-assembled monolayers (SAMs) to modify the substrate (*i.e.* dielectric and electrodes) was investigated. Four different molecules were chosen: thiophenol (TP) and pentafluorothiophenol (PFBT) that have a thiol group that can react with the gold electrodes and, on the other side, trichloro(phenethyl)silane (PETS) and octadecyltrichlorosilane (OTS) that can be covalently bonded to the silicon oxide through the trichlorosilane group. The role of the SAMs on the electrodes is to modify the surface energy on the gold and to change the work function of the electrode with the objective to improve the contact resistance and hence the overall performance of the transistor.^[15] PFBT SAMs have also been reported to interact strongly with the OSCs and promote the OSC nucleation.^[16] SAMs on the silicon oxide are commonly used because of their ability to passivate the silanol groups that can act as traps for the charge carriers.^[17] It should be kept in mind that the modification of the substrate also alters the surface wettability and, hence, can have a strong impact on the resulting thin-films.

It is important to remark that in the common protocols of SAM formation in oxide substrates, there is a step of activation of the surfaces to create reactive OH groups. This is usually accomplished by an ozone treatment. Ozone treatment can also be carried out to simply enhance the solution wettability on the surface since it becomes more hydrophilic.

In our particular case, the use of SAMs on the silicon oxide was attempted but due to the hydrophobicity of the surface no film was formed. On the other hand, the functionalization of the electrodes with TP led to a quantitative improvement of the device performance (*e.g.* comparing experiments number 11 and number 16 from **Table 3.1**). The improvement was even superior when instead of TP, PFBT was used. However, we observed that the O₃ treatment shifted the threshold voltage to positive values and modified the film morphology. Because of that, we decided to avoid this treatment.

Table 3.1. Summary of the most relevant coating experiments carried out with DPTTA:PS.

#	Polymer	Ratio OS:PS	C [mg/mL]	Solvent	T [°C]	Bar Speed [mm/s]	Bar	O ₃	SAM	$\mu_{FE,sat}$ [cm ² /V·s]	V _{TH} [V]
1	PS3k	1:3	20.0	Anisole	105	10	Metal	No	No	-	-
2	PS3k	1:4	20.0	Anisole	105	10	Metal	No	No	-	-
3	PS3k	1:2	20.0	Anisole	105	10	Metal	No	No	-	-
4	PS3k	1:2	25.0	Anisole	105	10	Metal	No	No	-	-
5	PS3k	1:2	15.0	Anisole	105	10	Metal	No	No	-	-
6	PS3k	1:2	20.0	Anisole	105	1	Metal	No	No	-	-
7	PS3k	1:2	20.0	Anisole	105	10	Teflon	No	No	0.22	12
8	PS3k	1:2	25.0	Anisole	105	10	Teflon	No	No	0.24	6.6
9	PS3k	1:2	20.0	Anisole	105	10	Teflon	Yes	No	$1.4 \cdot 10^{-3}$	7.6
10	PS3k	2:5	23.0	Anisole	105	10	Teflon	Yes	No	$2.1 \cdot 10^{-3}$	6.3
11	PS3k	1:2	22.6	CB	105	10	Teflon	Yes	No	0.10	11
12	PS3k	2:5	23.0	CB	105	10	Teflon	Yes	No	0.35	16
13	PS3k	1:2	22.6	CB	105	10	Teflon	No	No	0.23	1.1
14	PS3k	2:5	23.0	CB	105	10	Teflon	No	No	0.34	2.1
15	PS3k	1:2	20.0	Anisole	105	10	Teflon	Yes	TP	0.20	27
16	PS3k	1:2	22.6	CB	105	10	Teflon	Yes	TP	0.53	13
17	PS3k	2:5	26.0	CB	105	10	Teflon	Yes	TP	0.55	4.1
18	PS3k	1:2	20.0	Anisole	105	10	Teflon	Yes	PFBT	0.22	17
19	PS3k	1:2	22.6	CB	105	10	Teflon	Yes	PFBT	0.55	31
20	PS3k	2:5	26.0	CB	105	10	Teflon	Yes	PFBT	0.66	15
21	PS3k	1:2	22.6	CB	105	10	Teflon	No	PFBT	0.71	0.30
22	PS3k	2:5	26.0	CB	105	10	Teflon	No	PFBT	0.14	1.3
23*	PS3k	1:3	26.0	CB	105	10	Teflon	No	PFBT	0.57	0.47
24*	PS10k	1:2	22.6	CB	105	10	Teflon	No	PFBT	1.03	0.0
25*	PS100k	1:2	22.6	CB	105	10	Teflon	No	PFBT	0.55	0.34
26*	PS10k	1:3	20.0	CB	105	10	Teflon	No	PFBT	0.67	0.86

*Selected Formulations

Regarding the ratio in mass, it was observed with PS3k that going from 1:2 to 1:3 (experiments 21 and 23) reduced slightly the mobility but since the formulation was richer in polymer it was also more viscous producing a more homogeneous and reproducible film. This was not necessary for PS10k and PS100k because the solution was viscous enough to form a proper polycrystalline film with the 1:2 ratio. In experiment 26, the main objective was to obtain a film with a larger amount of PS to be more stable in the EGO-FET configuration later. It has been observed while carrying out these tests that the main source of defects was the precipitation of DPTTA. For this reason, the concentration of DPTTA was reduced from 7.5 mg/mL in experiment 24 to 5.0 mg/mL in experiment 26 while keeping constant the amount of polymer to still have a viscous formulation. From all these results, we decided to perform a more in-depth study with the films prepared using the conditions of experiments 23, 24, 25 and 26. From now on, these formulations are named after formulation **1**, **2**, **3** and **4**, respectively.

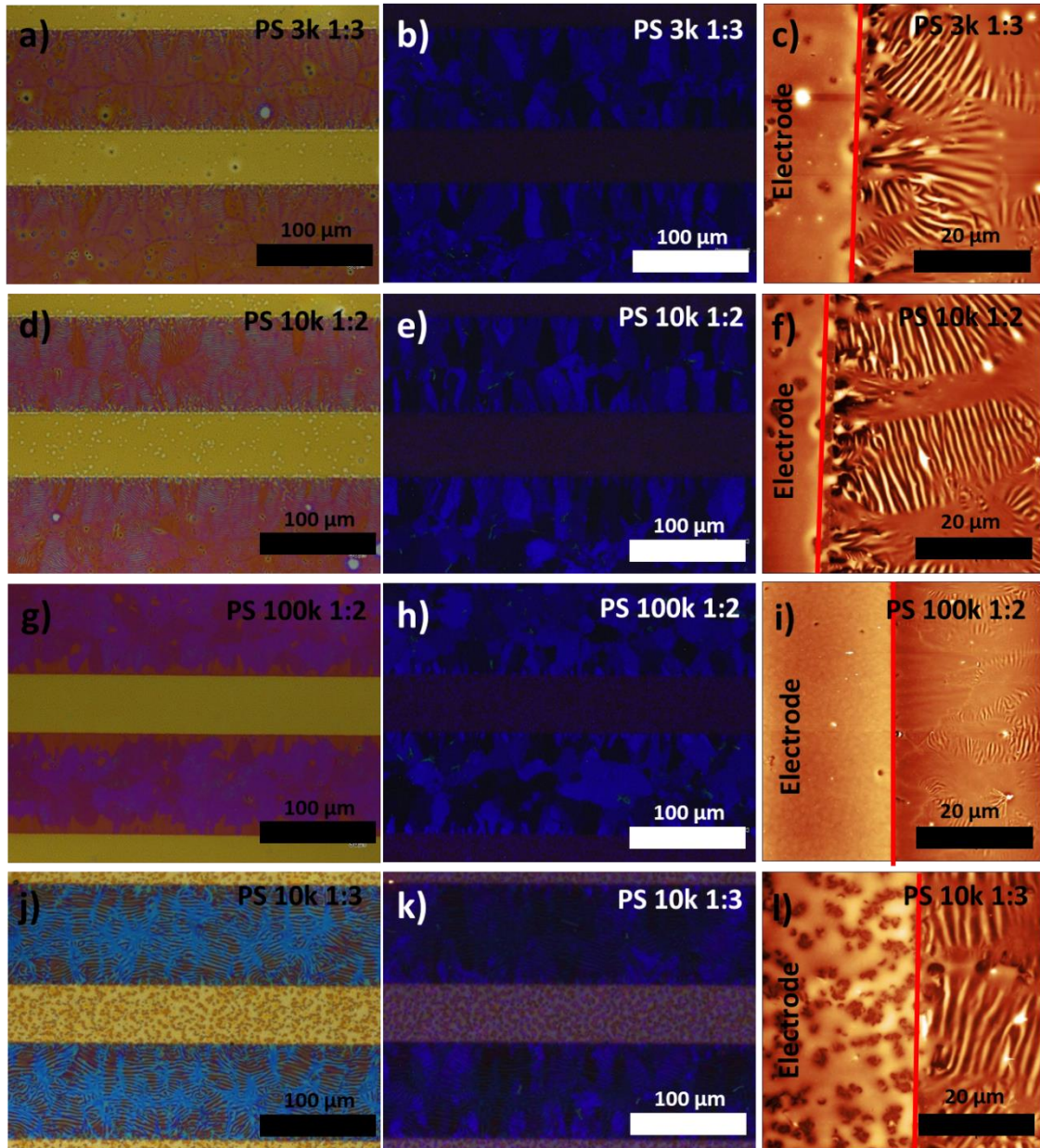


Figure 3.4. Images of the different optimised films obtained by a), d), g) and j) optical microscope, b), e), h) and k) polarized optical microscope and c), f), i) and l) AFM. Scale bars correspond to 100 and 20 μm in optical microscope and AFM images, respectively. In the AFM images the edge of the Au/PFBT electrodes is drawn to highlight the different film growth.

In **Figure 3.4**, the optical and atomic force microscopy (AFM) images of the thin films prepared with the optimized formulations are shown. Clearly, the deposited thin films exhibit a different film growth on the Au/PFBT electrodes and on the silicon oxide substrate. In the channel area crystalline domains are observed formed by wave-like microstructures which increase the roughness of the films. The roughness of the active layers, quantified with the root mean square roughness (δ_{RMS}), were found to be higher in films prepared from blends **2** ($\delta_{\text{RMS}} = 16.78$ nm) and **4** ($\delta_{\text{RMS}} = 15.48$ nm), while smoother films resulted from formulations **3** ($\delta_{\text{RMS}} = 4.96$ nm) and **1** (δ_{RMS} of 6.95 nm). However, on the Au/PBFT source/drain electrodes modified neither large crystallites nor wave-like microstructures on top are observed. Notably, the AFM

phase image shows that there is no a visible change in the surface energy between the film on the silicon oxide and on Au/PFBT (**Figure 3.5**), suggesting that both the electrodes and the active layer are covered by a PS encapsulating layer.^[14]

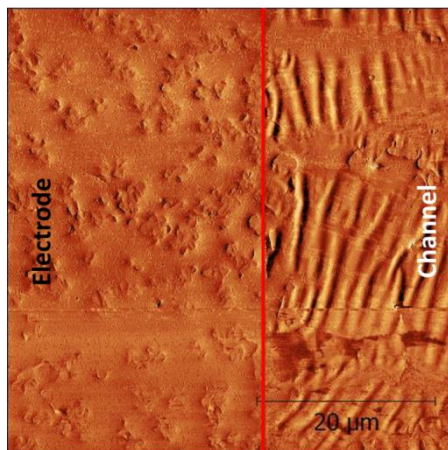


Figure 3.5. Phase AFM image of a thin-film prepared from formulation **4**. No significant phase differences can be observed between the channel and the electrodes.

X-ray powder diffraction (XRPD) analysis of the films confirmed that all the films belong to the same crystalline phase (**Figure 3.6**). Additionally, the crystalline phase observed in the films does not seem to correspond to the reported one for the single crystal.^[1] The reflections cannot be associated to any $(0\ 0\ n)$ crystallographic plane due to the lack of periodicity in the peaks spacing in the diffractogram. This indicates that the crystals are not oriented with respect to the substrate, which could be expected because of the wave-like microstructure of the film. This different polymorph of DPTTA may be associated to a surface promoted growth as it has been commonly observed in other OSCs such as in tetrathiafulvalene derivatives.^[18–21]

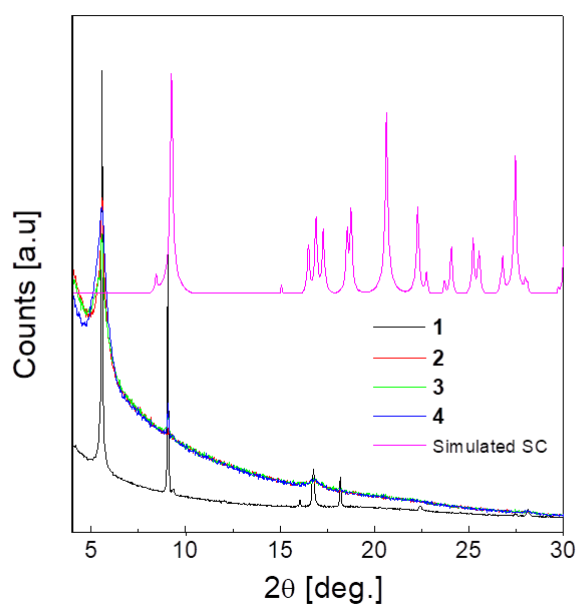


Figure 3.6. X-ray powder diffraction of the DPTTA:PS films prepared using formulations **1-4** and the simulated one for the single crystal (SC) previously reported.

3.4. OFET ELECTRICAL CHARACTERISATION

In order to evaluate the OFET electrical characteristics of all selected DPTTA:PS films, a bottom-gate bottom-contact (BG/BC) configuration employing Si/SiO₂ as gate/gate dielectric was used for the initial formulation screening (**Figure 3.7a**). All the measurements were performed under ambient conditions. As reported in **Figure 3.8**, all transfer and output characteristics show a clear *p*-type behavior in all the devices in a gate-source voltage (V_{GS}) window ranging from 10 to -20 V. The extracted field-effect mobility in saturation regime ($\mu_{FE,sat}$), threshold voltage (V_{TH}), sub-threshold slope (SS) and on/off current ratio (I_{on}/I_{off}) are summarized in **Table 3.2**. All devices exhibited a rather high average field effect mobility above 0.5 cm²/V·s. Remarkably, the OFETs fabricated with the formulation **2** showed an average mobility of ~1 cm²/V·s with a maximum value of 1.21 cm²/V·s. Even though this $\mu_{FE,sat}$ overcomes the value found for the single crystal (0.7 cm²/V·s), it should be kept in mind that the crystal phase found in these thin films is different from the reported single crystal polymorph. Hence, without the resolved crystal structure, we can only anticipate that the new polymorph discovered in this work should be more suitable for electronic transport. It should be also noticed that employing this fast deposition technique the benchmark high performing OSCs 6,13-bis(triisopropylsilylethynyl)pentacene (TIPS-PEN) and 2,8-difluoro-5,11-bis(triethylsilylethynyl)anthradithiophene (diF-TES-ADT) gave average mobilities of the same order.^[6]

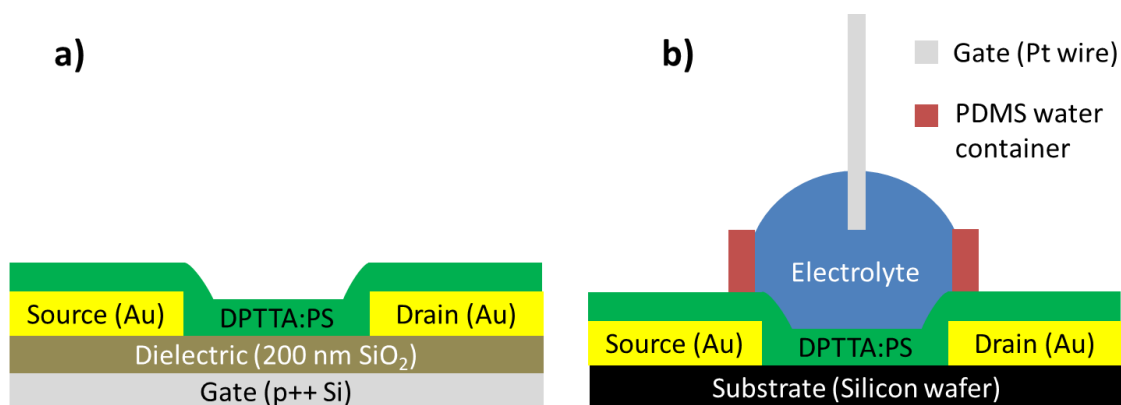


Figure 3.7. a) Bottom-gate bottom-contact OFET and (b) top-gate bottom-contact EGOFET configurations used in this chapter.

The high performance of the fabricated devices is further evidenced by the threshold voltage close to 0 V, the sharp switch on represented by a small sub-threshold swing, the low contact resistance visible with the linearity of the output curves, and the lack of hysteresis. The sharp switch on and the almost zero hysteresis suggest a low trap density (N_T) in these films.^[22–25] As previously mentioned, the density of traps can be estimated using the following expression:

$$N_T \approx \left[\frac{q SS \log(e)}{k_B T} - 1 \right] \frac{C}{q^2} \quad (3.1)$$

Where q is the electronic charge, k_B is the Boltzmann constant and T is the absolute temperature.

The values obtained here for DPTTA:PS ($N_T = 3.6 \cdot 10^{11} \text{ cm}^{-2}$) OFETs are comparable to the values obtained by Amassian *et al.* when they blend the OSC DiF-TESADT with PS exhibiting state-of-the-art performance.^[26] This low density of traps can be explained by the vertical phase separation that takes place during the crystallization. This promotes the growth of the polycrystalline layer of DPTTA on top of a PS layer that acts as a buffer layer avoiding the charge trapping in the polar hydroxyl groups present at the interface with the SiO₂ dielectric.

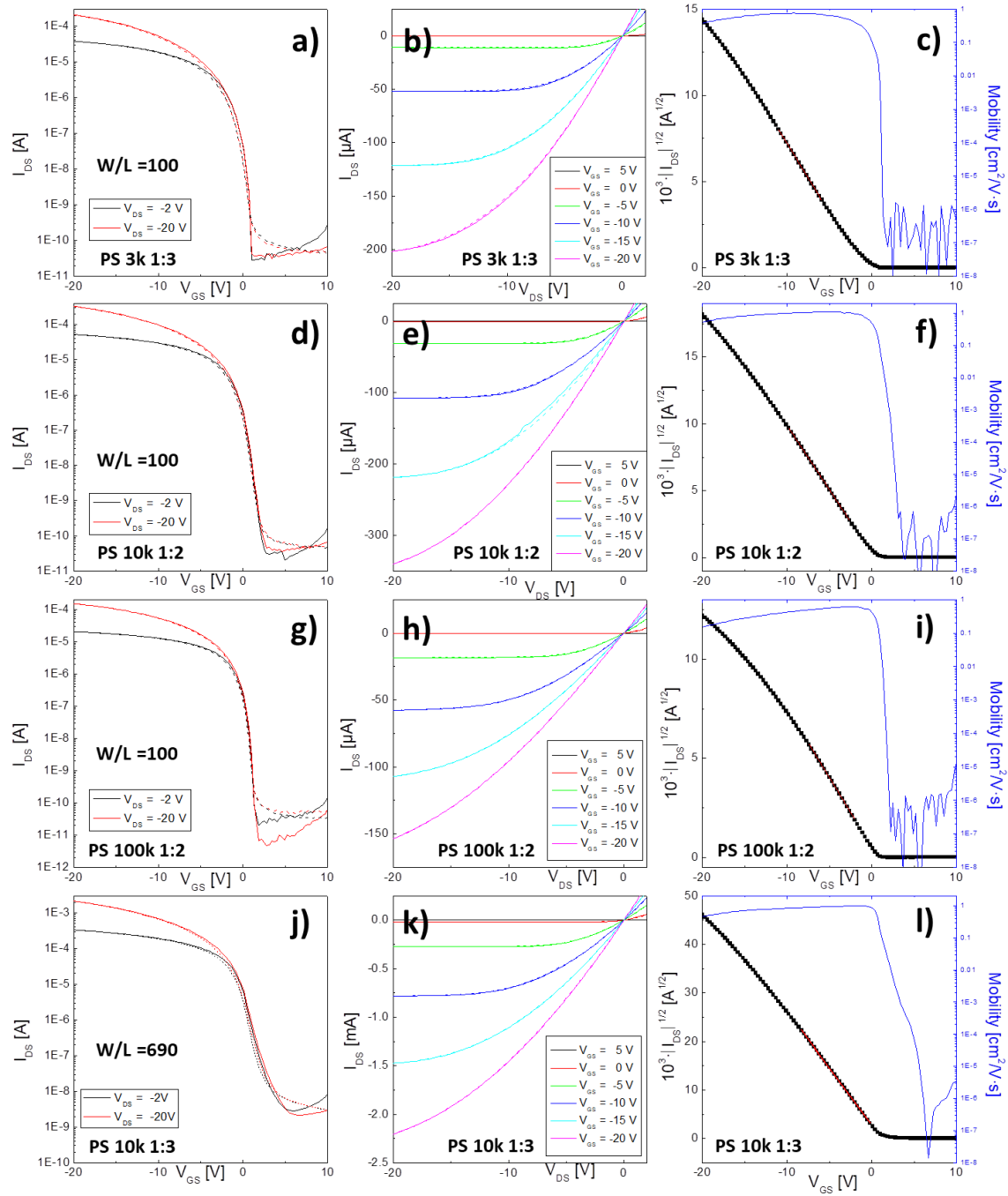


Figure 3.8. Transfer **a), d), g)** and **j)** and output **b), e), h)** and **k)** characteristics of the OFETs prepared from the formulations **1-4**. Dashed lines are used to indicate the reverse scan in both transfer and output characteristics. **c), f), i)** and **l)** are the mobility profile and the square root of the absolute value of the source-drain current vs. source-gate voltage. The linear fit used to calculate the mobility is shown with a red line.

There has been lately an open discussion in the field of organic electronics about the dependence of the mobility on the gate voltage. In an ideal case the mobility should be independent of the V_{GS} while operating in the saturation regime. However, typically mobility dependence with the electric field is observed, except in highly purified single crystals. This

effect has been mainly attributed to the contact resistance between the electrode and the OSC and traps present at the OSC/dielectric interface.^[27] In our case, although all the mobility profiles are not completely independent of the gate voltage, there is not any sharp peak and the dependence is quite weak as can be observed in **Figure 3.8 (c, f, i, l)**. Therefore, we assume that in addition to a low level of traps, the prepared devices did not present a significant contact resistance, as can also be seen from the linearity of the output characteristics. It should be noted that strongly dependent mobilities could lead to an overestimation of the device mobility, which is not occurring here.^[28]

Table 3.2. OFET parameters found in DPTTA for the different blend formulations. The reported values are the average out of 24 transistors for formulation **1** and **3**, 48 transistors for **2** and 96 for **4**. Values in parenthesis correspond to the best value found for each specific condition.

#		1	2	3	4
Blend Formulations	Polymer	PS 3k	PS 10k	PS 100k	PS 10k
	Ratio [OSC:Polymer]	1:3	1:2	1:2	1:3
	Concentration [mg/ml]	26	22.6	22.6	20
Device Parameters	$\mu_{FE,sat}$ [$\text{cm}^2/\text{V}\cdot\text{s}$]	0.57 (0.64)	1.03 (1.21)	0.55 (0.68)	0.67 (1.00)
	$\mu_{\sigma}/\mu_{average}$ [%]	9.33	12.3	18.0	25.5
	V_{TH} [V]	0.47	-0.02	0.34	0.86
	S.S. [V/dec]	0.70 (0.35)	0.70 (0.50)	0.26 (0.21)	0.41 (0.36)
	N_T [cm^{-2}]	$1.2 \cdot 10^{12}$	$1.2 \cdot 10^{12}$	$3.6 \cdot 10^{11}$	$6.3 \cdot 10^{11}$
	I_{on}/I_{off}	$5.1 (6.3) \cdot 10^6$	$4.5 (9.7) \cdot 10^6$	$1.1 (3.0) \cdot 10^7$	$6.5 (16) \cdot 10^5$

3.5. EGOFET ELECTRICAL CHARACTERISATION³

In an EGOFET configuration the aqueous media acts as the effective gate dielectric. The two Electrical Double Layers (EDLs) at the top gate/electrolyte and electrolyte/OSC interfaces bear a capacitance in the order of $\mu\text{F}/\text{cm}^2$ compared to nF/cm^2 of standard dielectrics, which ensures low voltage operation. Finding stable OSC films in this media is crucial for the progress of EGOFETs. Undoubtedly, the choice of the OSC and its processing are pivotal. For instance, a high degree of crystallinity provides a more efficient blocking against ion diffusion. Our group has already demonstrated that BAMS can produce excellent coatings based on blends of reference OSCs for achieving outperforming EGOFETs with exceptional robustness.^[12,13]

The best film found in this work for the EGOFET configuration has been obtained using the formulation DPTTA:PS 10k (1:3) (**4**). The EGOFET configuration employed is depicted in **Figure 3.7b**, where water inside a polydimethylsiloxane (PDMS) pool acts as dielectric and a gold wire immersed in the water is the gate electrode. Concerning the aqueous electrolyte media, ultrapure water was used to study the transistor operation and its stability in this media. Further, a 0.5 M NaCl electrolyte aqueous solution was also tested to demonstrate the potential application of these EGOFETs in a harsher media, more similar to certain real sensing applications. As expected, the EGOFET results exhibited clearly p-type semiconductor behavior in both media in a V_{GS} windows ranging from 0.9 to -0.3 V (**Figure 3.9a**). The corresponding output characteristics measured in ultrapure water and the 0.5 M NaCl solution are also displayed in **Figure 3.9b** and **3.9c**, respectively. For both media, a little anti-clockwise hysteresis is observed. The presence of hysteresis suggests the presence of some traps on top of the semiconductor surface probably caused by the surface roughness. Noticeably, no negative shifting of the threshold voltage was observed in the 0.5 M NaCl solution when compared with that in ultrapure water, which is typically observed when the electrolyte polarity is changed.^[29]

In order to calculate the EGOFET mobility (μ_{EGOFET}), we performed electrochemical impedance spectroscopy measurements to extract the dielectric capacitance (C). These measurements were carried out using source and drain electrodes short-circuited as counter-electrode meanwhile a Pt wire immersed in the media was acting as working electrode.^[30] Capacitance response was recorded at different DC voltages spanning from 0.6 to -0.3 V in order to resemble the gate voltage window employed during transfer characteristic. The C - V_{GS} plots extracted at a frequency of 10 Hz are displayed in **Figure 3.8d** and **3.8e**. The C trend shows the transition from OFF to ON state for the DPTTA:PS coated device, whereas this behaviour was not observed in coating-free substrates. A capacitance of $1.2 \mu\text{F}/\text{cm}^2$ and $3.4 \mu\text{F}/\text{cm}^2$ was found when ultrapure water and a 0.5 M NaCl aqueous solution were used, respectively. These values are comparable to other reported for thin films of different semiconductors such as dibenzo-tetrathiafulvalene, poly(3-hexylthiophene) or pentacene.^[9,29,30] The corresponding mobility (μ_{EGOFET}) and threshold voltage (V_{TH}) values extracted for the EGOFET are summarized

³ This work was carried out in collaboration with Qiaoming Zhang and Dr. Francesca Leonardi (ICMAB-CSIC).

in **Table 3.3**. As expected, the extracted μ_{EGOFET} is smaller than the μ found for the OFET due to the high dielectric constant of the media. This effect has been commonly observed in organic electronics and is caused by the increased energetic disorder found in high dielectric constant insulators and also to a narrower localisation of the charge-carriers in the OSC/dielectric interface increasing the activation energy for hopping transport.^[33] However, the drop of μ is not even one order of magnitude lower compared to the back-gated OFET, in contrast to what is commonly encountered in other OSC thin films.^[34] In fact, the EGOFET mobility found for this DPTTA OSC film is among the best values found for this type of devices.

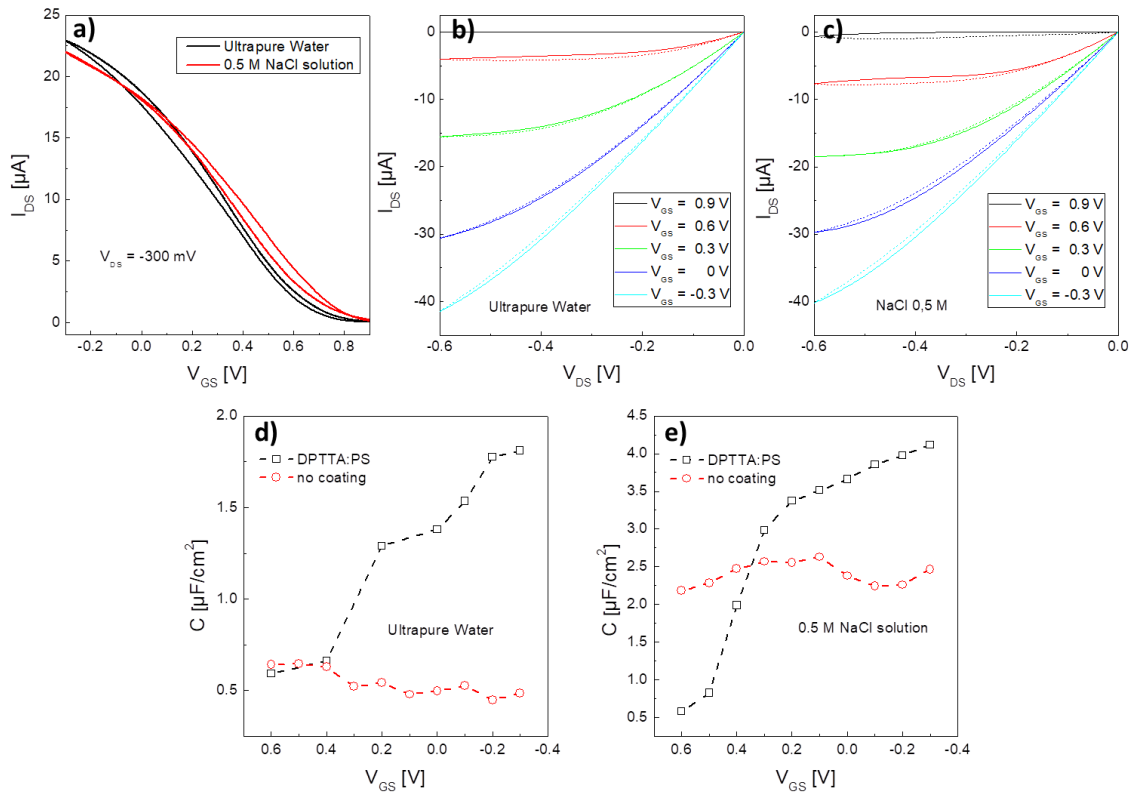


Figure 3.9. a) EGOFET transfer characteristics of a DPTTA:PS 10k (1:3) thin film, in water and in NaCl 0.5 M and (b) output characteristics. c) and (d) are the impedance spectroscopy measurements carried out to obtain the capacitance used to calculate the mobility.

Table 3.3 EGOFET parameters found for DPTTA:PS formulation **4**. μ_{EGOFET} and V_{TH} values are averaged from 16 devices and 6 devices for water and NaCl, respectively.

Media	μ_{EGOFET} [cm ² /V·s]	V_{TH} [V]	τ_{ON} [ms]	τ_{OFF} [ms]	Max. P.S. [μV]
Ultrapure Water	0.12 ± 0.03	1.0 ± 0.1	9.4	4.7	200
NaCl 0.5M	0.03 ± 0.01	1.0 ± 0.3	1.3	1.4	500

EGOFETs are promising candidates for sensing platforms due to their ability to easily transduce a chemical or biological signal into a measurable electric current.^[34–37] Therefore, it is crucial to know the lowest voltage shift that it can detect. This signal is directly proportional to the detection limit of the desired analyte. Hence, to obtain the potentiometric sensitivity (*P.S.*) of the EGOFET, square pulses of V_{GS} were applied to the device and the corresponding output current was recorded (**Figure 3.10a** and **3.10b**). Detectable responses to voltage steps as low as 200 μV have been successfully recorded for water-gated samples. However, for samples gated using 0.5 M NaCl the lowest detectable value was 500 μV because of the higher electrical noise found for this media.

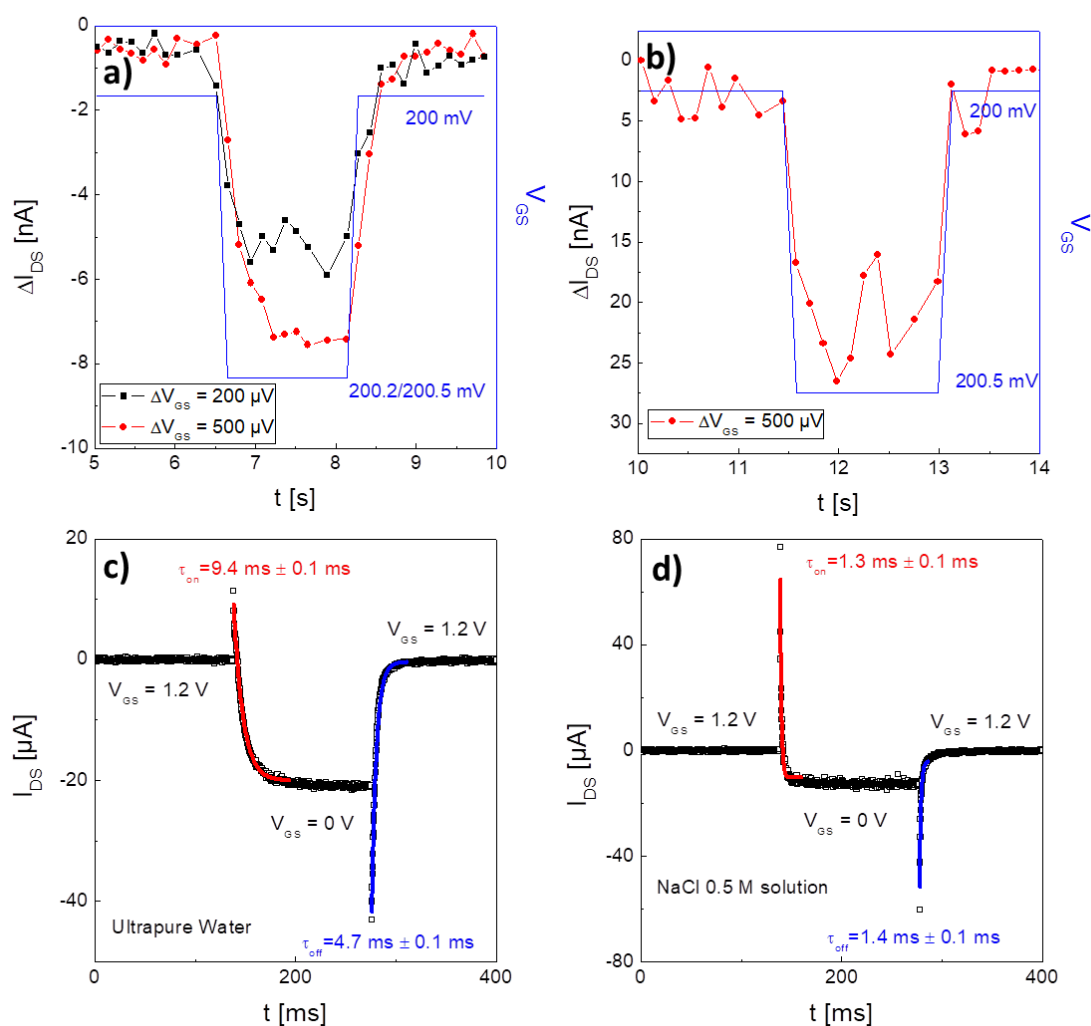


Figure 3.10. Potentiometric sensitivity of the EGOFETs measured when (a) ultrapure water and (b) 0.5 M NaCl aqueous solution was used as electrolyte dielectric. Switching speed measurements with the exponential fit used to obtain the turn on and off time using (c) ultrapure water and (d) 0.5 M NaCl. In all these measurements the V_{DS} was 300 mV.

As important as the potentiometric sensitivity is the speed of the response that would permit to detect punctual fluctuations of a chemical/biological signal. To obtain the EGOFET switching

speed (τ), a square voltage (V_{GS}) pulse from 1.2 to 0 V to switch on and *vice versa* to switch off was applied while the current was monitored with an integration time of 250 μ s (**Figure 3.10c and 3.10d**). The channel formation and disruption have been fitted through an exponential formula ($I_{DS} \propto e^{\pm(t/\tau)}$) to extract their characteristic time response, *i.e.* τ_{ON} and τ_{OFF} .^[38] The switching speed values indicate a fairly symmetric and quick turn on and off of the EGOFET in both media. These values are displayed in **Table 3.3**.

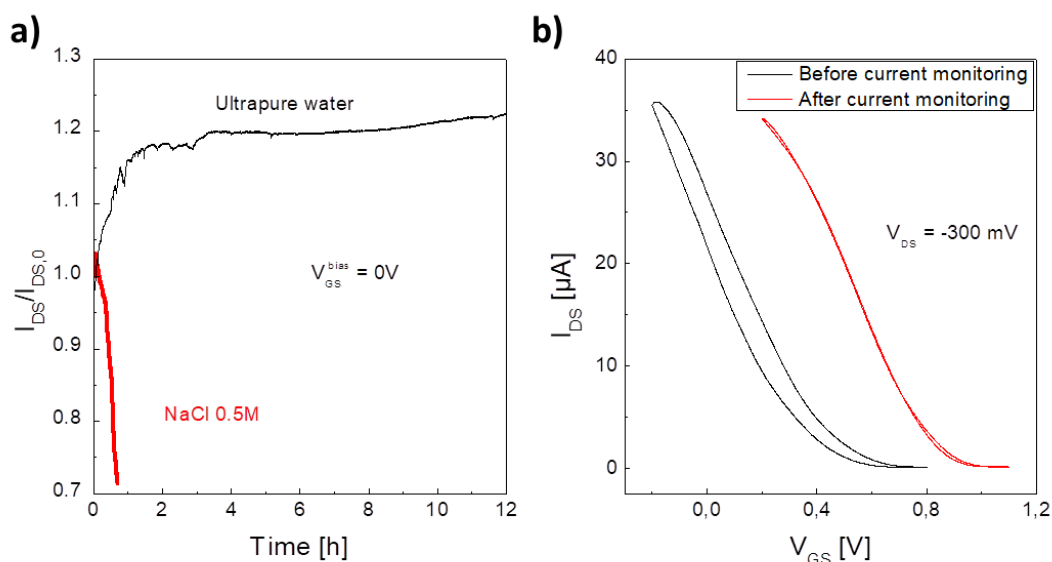


Figure 3.11. a) Real-time current monitoring of DPTTA:PS EGOFET. **b)** Transfer characteristics measured before and after the current monitoring in ultrapure water to show the stability of the device after 12 hours of continuous electrical stress.

Stability measurements represent the last figure of merit for depicting the quality of an EGOFET device. **Figure 3.11** displays real-time current monitoring which consists on applying two constant potentials, namely $V_{DS} = 300$ mV and $V_{GS} = 0$ V, while measuring the corresponding source-drain current. This kind of electrical tests are usually desirable if the platform is envisioned for monitoring the presence of a certain analyte in a continuous flow, *i.e.*, a water pollutant, a specific biomolecule, etc.^[39] OFETs fabricated with formulation **4** have demonstrated to be stable in ultrapure water. As displayed in **Figure 3.11**, the I_{DS} current increases quickly the first 2 hours and then it reaches a stable plateau with a current 20% higher compared with its initial current. Furthermore, transfer characteristics were recorded before and after the stability experiment (**Figure 3.11b**) and only a reduction of hysteresis and a positive shift of the threshold voltage were the main effects observed, which would explain the increase of the current due to an increase of the effective electric field ($V_{GS,eff} = |V_{GS} - V_{TH}|$). Unfortunately, with the NaCl 0.5 M solution the devices were deteriorating more quickly in a time scale of few minutes which is probably caused by the penetration of ions into the bulk OSC. Nonetheless, all these EGOFET results unequivocally attest the efficiency of combining OSC:PS blends with BAMS for achieving superior EGOFET performance.

3.6. SUMMARY

In summary, after synthesising DPTTA it was demonstrated for the first time that thin films of this hardly explored OSC can be prepared from solution employing a high throughput technique that resulted in excellent performing devices. A series of DPTTA:PS blend thin films with different OSC:PS ratios and different PS molecular weights have been deposited successfully by utilizing the BAMS technique using a hydrophobic PTFE bar. As confirmed by XRPD data, all the films exhibit the same crystal structure which does not correspond to the previously reported one. The OFET devices fabricated with these films exhibited state-of-the-art performance with an average mobility around $1 \text{ cm}^2/\text{V}\cdot\text{s}$ and a low level of traps. Furthermore, the films were additionally tested as active layers in EGOFETs also fulfilling the best characteristics of these reported devices, such as $\mu_{\text{EGOFET}} > 0.1 \text{ cm}^2/\text{V}\cdot\text{s}$, potentiometric sensitivity $\sim 200 \text{ }\mu\text{V}$, time response $\sim 9 \text{ ms}$ and long term stability in ultrapure water. This work does not only further support the strategy of combining OSC:PS blends with BAMS as a powerful route for achieving high performing devices, but also indicates that DPTTA can become a promising OSC for the next device generation.

3.7. REFERENCES

- [1] K. Singh, A. Sharma, J. Zhang, W. Xu, D. Zhu, *Chem. Commun.* **2011**, 47, 905.
- [2] Y. Qin, J. Zhang, X. Zheng, H. Geng, G. Zhao, W. Xu, W. Hu, Z. Shuai, D. Zhu, *Adv. Mater.* **2014**, 26, 4093.
- [3] Y. Qin, C. Cheng, H. Geng, C. Wang, W. Hu, W. Xu, Z. Shuai, D. Zhu, *Phys. Chem. Chem. Phys.* **2016**, 18, 14094.
- [4] J. Zhang, H. Geng, T. S. Virk, Y. Zhao, J. Tan, C. A. Di, W. Xu, K. Singh, W. Hu, Z. Shuai, Y. Liu, D. Zhu, *Adv. Mater.* **2012**, 24, 2603.
- [5] Y. Diao, L. Shaw, Z. Bao, S. C. B. Mannsfeld, *Energy Environ. Sci.* **2014**, 7, 2145.
- [6] I. Temiño, F. G. Del Pozo, M. R. Ajayakumar, S. Galindo, J. Puigdollers, M. Mas-Torrent, *Adv. Mater. Technol.* **2016**, 1, 1600090.
- [7] J. Panidi, A. F. Paterson, D. Khim, Z. Fei, Y. Han, L. Tsetseris, G. Vourlias, P. A. Patsalas, M. Heeney, T. D. Anthopoulos, *Adv. Sci.* **2017**, 5, 1700290.
- [8] K. Zhao, O. Wodo, D. Ren, H. U. Khan, M. R. Niazi, H. Hu, M. Abdelsamie, R. Li, E. Q. Li, L. Yu, B. Yan, M. M. Payne, J. Smith, J. E. Anthony, T. D. Anthopoulos, S. T. Thoroddsen, B. Ganapathysubramanian, A. Amassian, *Adv. Funct. Mater.* **2016**, 26, 1737.
- [9] G. Giri, S. Park, M. Vosgueritchian, M. M. Shulaker, Z. Bao, *Adv. Mater.* **2014**, 26, 487.
- [10] F. G. Del Pozo, S. Fabiano, R. Pfattner, S. Georgakopoulos, S. Galindo, X. Liu, S. Braun, M. Fahlman, J. Veciana, C. Rovira, X. Crispin, M. Berggren, M. Mas-Torrent, *Adv. Funct. Mater.* **2016**, 26, 2379.
- [11] R. Hamilton, J. Smith, S. Ogier, M. Heeney, J. E. Anthony, I. McCulloch, J. Veres, D. D. C. Bradley, T. D. Anthopoulos, *Adv. Mater.* **2009**, 21, 1166.
- [12] F. Leonardi, S. Casalini, Q. Zhang, S. Galindo, D. Gutiérrez, M. Mas-Torrent, *Adv. Mater.* **2016**, 28, 10311.
- [13] Q. Zhang, F. Leonardi, S. Casalini, I. Temiño, M. Mas-Torrent, *Sci. Rep.* **2016**, 6, 39623.
- [14] A. Pérez-Rodríguez, I. Temiño, C. Ocal, M. Mas-Torrent, E. Barrena, *ACS Appl. Mater. Interfaces* **2018**, 10, 7296.
- [15] C. Liu, Y. Xu, Y. Y. Noh, *Mater. Today* **2015**, 18, 79.
- [16] M. R. Niazi, R. Li, M. Abdelsamie, K. Zhao, D. H. Anjum, M. M. Payne, J. Anthony, D. M. Smilgies, A. Amassian, *Adv. Funct. Mater.* **2016**, 26, 2371.
- [17] S. G. J. Mathijssen, M. Kemerink, A. Sharma, M. Cölle, P. A. Bobbert, R. A. J. Janssen, D. M. De Leeuw, *Adv. Mater.* **2008**, 20, 975.

- [18] A. Brillante, I. Bilotti, R. G. Della Valle, E. Venuti, S. Milita, C. Dionigi, F. Borgatti, A. N. Lazar, F. Biscarini, M. Mas-Torrent, N. S. Oxtoby, N. Crivillers, J. Veciana, C. Rovira, M. Leufgen, G. Schmidt, L. W. Molenkamp, *CrystEngComm* **2008**, *10*, 1899.
- [19] R. Pfattner, M. Mas-Torrent, I. Bilotti, A. Brillante, S. Milita, F. Liscio, F. Biscarini, T. Marszalek, J. Ulanski, A. Nosal, M. Gazicki-Lipman, M. Leufgen, G. Schmidt, W. M. Laurens, V. Laukhin, J. Veciana, C. Rovira, L. W. Molenkamp, V. Laukhin, J. Veciana, C. Rovira, *Adv. Mater.* **2010**, *22*, 4198.
- [20] R. Pfattner, S. T. Bromley, C. Rovira, M. Mas-Torrent, *Adv. Funct. Mater.* **2016**, *26*, 2256.
- [21] M. Mas-Torrent, C. Rovira, *Chem. Rev.* **2011**, *111*, 4833.
- [22] S. Scheinert, G. Paasch, M. Schrödner, H. K. Roth, S. Sensfuß, T. Doll, *J. Appl. Phys.* **2002**, *92*, 330.
- [23] A. Wang, I. Kymissis, V. Bulović, A. I. Akinwande, *IEEE Trans. Electron Devices* **2006**, *53*, 9.
- [24] N. I. Craciun, Y. Zhang, A. Palmaerts, H. T. Nicolai, M. Kuik, R. J. P. Kist, G. A. H. Wetzelaer, J. Wildeman, J. Vandenbergh, L. Lutsen, D. Vanderzande, P. W. M. Blom, *J. Appl. Phys.* **2010**, *107*, 124504.
- [25] M. H. Yoon, C. Kim, A. Facchetti, T. J. Marks, *J. Am. Chem. Soc.* **2006**, *128*, 12851.
- [26] M. R. Niazi, R. Li, E. Qiang Li, A. R. Kirmani, M. Abdelsamie, Q. Wang, W. Pan, M. M. Payne, J. E. Anthony, D.-M. Smilgies, S. T. Thoroddsen, E. P. Giannelis, A. Amassian, *Nat. Commun.* **2015**, *6*, 8598.
- [27] H. Phan, M. J. Ford, A. T. Lill, M. Wang, G. C. Bazan, T. Q. Nguyen, *Adv. Funct. Mater.* **2018**, *1707221*, 1.
- [28] E. G. Bittle, J. I. Basham, T. N. Jackson, O. D. Jurchescu, D. J. Gundlach, *Nat. Commun.* **2015**, *7*, 10908.
- [29] J. Kofler, K. Schmoltner, A. Klug, E. J. W. List-Kratochvil, *Appl. Phys. Lett.* **2014**, *104*, 193305.
- [30] S. H. Kim, K. Hong, W. Xie, K. H. Lee, S. Zhang, T. P. Lodge, C. D. Frisbie, *Adv. Mater.* **2013**, *25*, 1822.
- [31] F. Leonardi, S. Casalini, Q. Zhang, S. Galindo, D. Gutiérrez, M. Mas-Torrent, *Adv. Mater.* **2016**, *28*, 10311.
- [32] T. Cramer, A. Kyndiah, M. Murgia, F. Leonardi, S. Casalini, F. Biscarini, *Appl. Phys. Lett.* **2012**, *100*, 143302.
- [33] J. Veres, S. D. Ogier, S. W. Leeming, D. C. Cupertino, S. M. Khaffaf, *Adv. Funct. Mater.* **2003**, *13*, 199.
- [34] O. Knopfmacher, M. L. Hammock, A. L. Appleton, G. Schwartz, J. Mei, T. Lei, J. Pei, Z.

- Bao, *Nat. Commun.* **2014**, *5*, 2954.
- [35] Q. Zhang, F. Leonardi, S. Casalini, M. Mas-Torrent, *Adv. Funct. Mater.* **2017**, *27*, 1703899.
- [36] S. Casalini, F. Leonardi, T. Cramer, F. Biscarini, *Org. Electron.* **2013**, *14*, 156.
- [37] T. Cramer, B. Chelli, M. Murgia, M. Barbalinardo, E. Bystrenova, D. M. de Leeuw, F. Biscarini, *Phys. Chem. Chem. Phys.* **2013**, *15*, 3897.
- [38] D. Khodagholy, M. Gurfinkel, E. Stavrinidou, P. Leleux, T. Herve, S. Sanaur, G. G. Malliaras, *Appl. Phys. Lett.* **2011**, *99*, 163304.
- [39] A. Campana, T. Cramer, D. T. Simon, M. Berggren, F. Biscarini, *Adv. Mater.* **2014**, *26*, 3874.

CHAPTER 4 IMPACT OF POLYMORPHISM AND MORPHOLOGY IN A THIN FILM OF A BENZOTHIENO BENZOTHIOPHENE DERIVATIVE ON THE OFET PERFORMANCE¹

4.1 INTRODUCTION AND OBJECTIVES

Organic semiconductors (OSCs) that present polymorphism open a path to study the properties of the charge transport in these materials without the need of chemically modifying their structure.^[1-4] However, a proper control and understanding of the factors that affect the polymorphism is crucial in order to optimise the device performance and achieve high device reproducibility.^[5]

The OSC family of benzo[thieno[3,2-*b*][1]benzothiophene (BTBT) (**Figure 4.1**) when applied as active layer in OFETs has demonstrated to give rise to high performance and high stability devices. BTBT derivatives have been processed both by solution-based techniques and by evaporation displaying promising device properties. However, the same characteristic that gives the molecule its high stability, its low-lying HOMO energy of -5.5 eV, also causes the misalignment between the HOMO energy and the work function of gold (5.1 eV). This misalignment creates an energy barrier that prevents the proper injection of charge carriers into the semiconductor, affecting the performance of the material as active layer for OFETs. To improve the charge injection, different strategies have been followed with good results like the use of interlayers of metal oxides as MoO_x between the BTBT and the gold electrodes,^[6] the doping of the OSC/electrode interface or the utilisation of other substitute materials for the electrodes, as for example the organic metal TTF-TCNQ.^[7,8]

Another approach has been the chemical modification of the molecular structure of the material. However, it is important to take into account that small modifications in the molecular structure could have a large impact on the crystal structure and, therefore, on the charge transport. One of the many possible modifications is the addition of side alkyl chains.

¹ This work has carried out in collaboration with Dr. Tommaso Salzillo (ICMAB) and with the group of Prof. Yves H. Geerts from the Université Libre de Bruxelles (ULB).

These alkyl chains have demonstrated to improve both the solubility of the OSC and, in some cases, the interaction between molecules.^[9,10] Following this strategy, the well-known benchmark OSC 2,7-dioctyl[1]benzothieno[3,2-*b*][1]benzothiophene (C8BTBT) was discovered (**Figure 4.1**).^[11] C8BTBT presents a very well packed herringbone type crystalline structure showing a very efficient charge transport and also, due to the presence of the alkyl chains, an improved solubility in organic solvents.^[12] However, this molecule has the same HOMO energy and the same issues with the charge injection from Au electrodes.

In order to raise the HOMO energy effectively, a common strategy has been the attachment of electron rich moieties to the OSC core.^[13] Therefore, Geerts *et al.* synthesised a new OSC with an electron rich atom (*i.e.* oxygen) between the BTBT core and the alkyl chain. In this way the OSC 2,7-bis(octyloxy)[1]benzothieno[3,2-*b*]- benzothiophene (C8OBTBT) was obtained (**Figure 4.1**). The attachment of the oxygen atom resulted in a raise of the HOMO energy of around 0.3 eV in solution. However, photoelectron spectroscopy measurements in air revealed that, in fact, in solid state C8OBTBT displayed an ionisation potential 0.6 eV larger than the unmodified C8BTBT due to its crystal structure.^[14] In any case, it was observed that OFETs made of C8OBTBT displayed lower contact resistance than C8BTBT-based transistors processed with the same methodology.

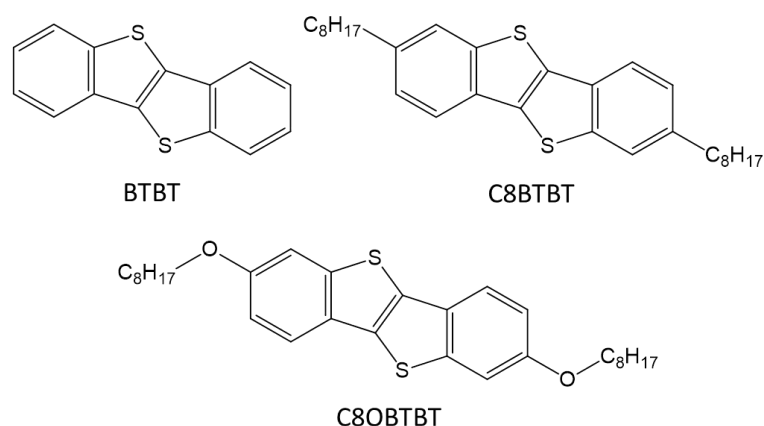


Figure 4.1. Molecular structure of BTBT and its derivatives.

The C8OBTBT molecule also presents two different crystalline phases. The first one, which was firstly obtained on surface, from now on will be named after surface-induced phase (SIP). The other phase was formed from the SIP phase after 6 months aging or after solvent vapour annealing with chloroform. This later phase is named after bulk phase.^[15]

The bulk phase shows a displaced cofacial stacking with a close contact between stacks (**Figure 4.2a**). For this structure, theoretical calculations were performed and it was concluded that the reorganisation energy for the C8OBTBT was higher than for C8BTBT.^[14] Regarding its transfer integral, it was as high as the one found for C8BTBT but only in the direction within the stack.

The inter-stack transfer integral was almost negligible remarking the 1D dimensionality of the bulk phase. On the other hand, the SIP phase presents a herringbone packing instead (**Figure 4.2b**).^[16] This structure is known to display a more 2D behaviour being beneficial for the charge transport.

To study the possible application of this OSC in devices, OFETs in top-contact bottom-gate configuration based on C8OBTBT deposited by spin coating from a 1 % wt. chloroform solution have been reported.^[17] After 10 minutes of thermal treatment at 150 °C, these devices exhibited $\mu_{FE,sat}$ values of 0.5 cm²/V·s, however, they also displayed a non-linear injection in the output characteristics indicating high contact resistance. The fabrication and characterisation of these transistors was performed entirely in an inert environment.

The two C8OBTBT polymorphs crystallise on Si/SiO₂ displaying an almost identical out-of-plane axis length making hardly possible the determination of the phase by normal X-ray powder diffraction (XRPD). However, it has been demonstrated that infrared spectroscopy and Raman spectroscopy can be used for the structure identification in bulk and in thin-films (**Figure 4.3**).^[16,18]

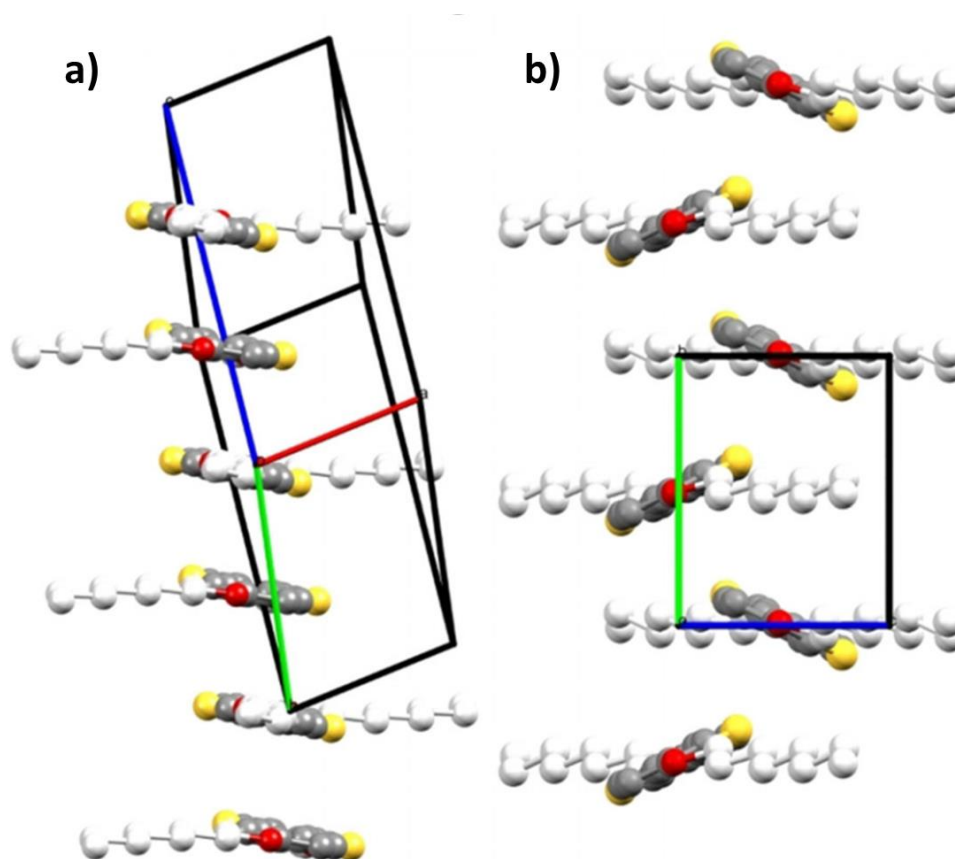


Figure 4.2. Packing of (a) the bulk phase and (b) the surface-induced phase of C8OBTBT.^[16]

Interestingly, different C8OBTBT phases could be obtained using the same solvent (hexane) and only controlling its evaporation speed.^[18] However, the deposition process was performed by drop casting, a technique that is not suitable for large area and reproducible applications.

Previously in blends of dibenzotetrathiafulvalene (DB-TTF) and polystyrene (PS) deposited by bar-assisted meniscus shearing (BAMS), it was reported that depending on the formulation and deposition parameters the polymorphism of this OSC could be controlled.^[5] Indeed, controlling the amount of polystyrene and the speed and temperature of the coating it was possible to move from the kinetic surface-induced structure (γ) to the thermodynamically most stable phase (α). The phase change from the SIP phase to the thermodynamic one had a dramatic impact on the performance of the resulting OFETs.

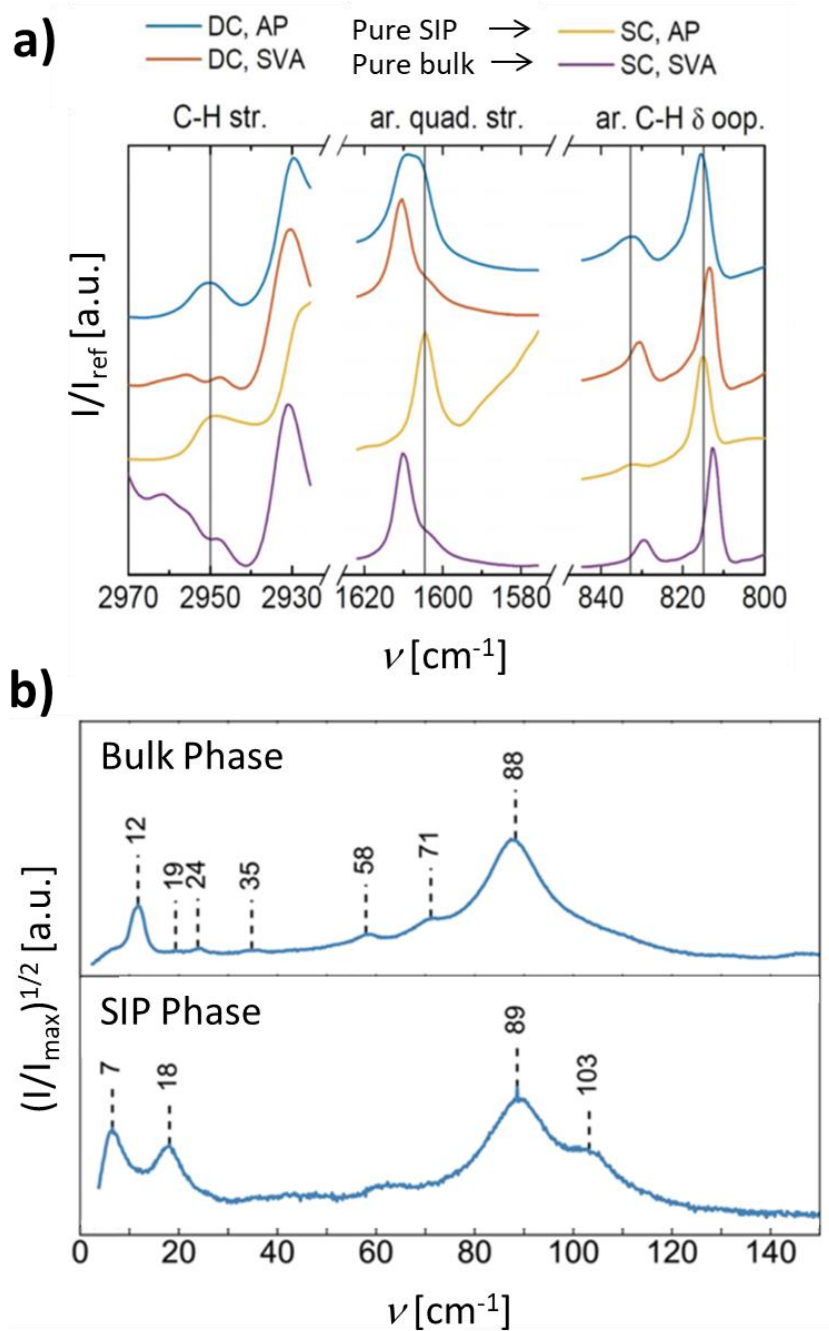


Figure 4.3. Experimental (a) infrared and (b) Raman spectra of the surface-induced phase and of the bulk phase.^[18]
 DC, SC, AP and SVA acronyms stand for drop casting, spin coating, as-prepared and solvent vapour annealing, respectively.

The main objectives of the work developed in this chapter are: i) to fabricate OFETs based on thin-films of the OSC C8OBTBT and blends of this OSC with PS using the solution shearing technique BAMS, ii) to control the resulting polymorph by tuning the deposition parameters, and iii) to study the stability of the SIP phase in the prepared films.

4.2. EFFECT OF THE POLYMER MOLECULAR WEIGHT

THIN-FILM PREPARATION AND MORPHOLOGY STUDY

Thin-films of pristine C8OBTBT and of C8OBTBT with polystyrene (PS) were processed by BAMS. Different molecular weights of PS (3 kg/mol, 10 kg/mol, 100 kg/mol and 280 kg/mol, namely PS3k, PS10k, PS100k and PS280k, respectively) were investigated to tune the thin-film morphology and to optimise the performance of the final device. The OSC:polymer ratio used was 4:1 using chlorobenzene (CB) as solvent. This ratio and solvent were previously found to be the most optimised conditions for C8BTBT films using the same deposition technique.^[8,19,20] Also reproducing the conditions found for C8BTBT, the final concentration of all the formulations (mg of C8OBTBT + mg of PS) was chosen to be 22.6 mg/mL (2% wt.). Additionally, the deposition was performed at a hotplate temperature of 105 °C and with a coating speed of 10 mm/s.^[5,20,21]

Since C8OBTBT displays a low-lying HOMO energy, to enhance the charge-carrier injection from the electrodes, the gold electrodes were covered with a self-assembled monolayer (SAM) of pentafluorobenzenethiol (PFBT). The use of this SAM has demonstrated to be an efficient way of increasing the work function of Au to 5.6 eV improving the alignment between the work function of the electrode and the HOMO energy of this *p*-type OSC.^[22,23] In addition, the presence of these molecules on the electrodes has also been reported to promote the crystallisation and packing orientation of some OSCs improving the performance of the final device.^[24] Of course, the formation of the SAM was only feasible for the bottom-contact bottom-gate (BCBG) configuration OFETs that is the architecture chosen for performing the optimisation of the film morphology.

Optical Microscope (OM) and Crossed-Polarised Optical Microscope (CPOM) images of the thin-films are shown in **Figure 4.4**. In these pictures, it can be observed that the crystalline domains in the pristine sample are bigger than in the thin-films processed with PS. However, unlike other OSC films,^[25,26] the crystalline domains are not as well defined and hence, the grain boundaries are not easily observable. The morphology and the thickness of the deposited thin-films were also investigated by Atomic Force Microscopy (AFM) (**Figure 4.5**). All the films displayed a smooth morphology and a thickness around 25-50 nm. Values of thickness and roughness (δ_{RMS}) of the different films are shown in **Table 4.1**. Interestingly, the films of C8OBTBT:PS280k displayed a kind of waves on the surface of the thin-film that we attribute to the self-organisation of the high molecular weight PS.

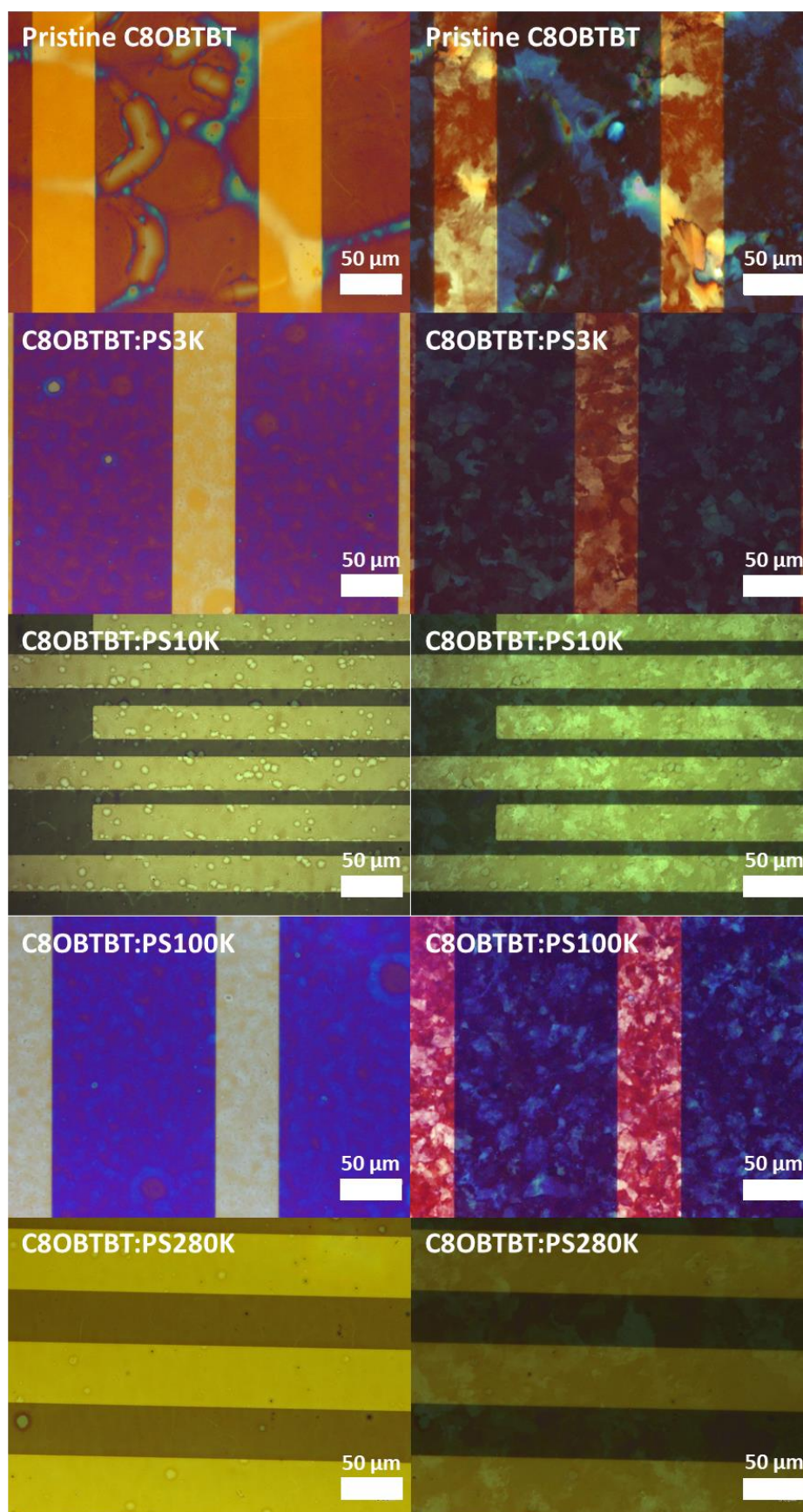


Figure 4.4. OM (left) and CPOM (right) images of the thin-films based on C8OBTBT fabricated by BAMS using different polymer weights.

Table 4.1. Thickness and roughness values of the thin-films of C8OBTBT deposited by BAMS with and without PS obtained by atomic force microscopy.

Formulation	δ_{RMS} [nm]	Thickness [nm]
Pristine C8OBTBT	2.25	32 ± 10
C8OBTBT:PS3K	3.65	50 ± 7
C8OBTBT:PS10K	2.77	36 ± 7
C8OBTBT:PS100K	2.52	60 ± 10
C8OBTBT:PS280K	2.16	40 ± 10

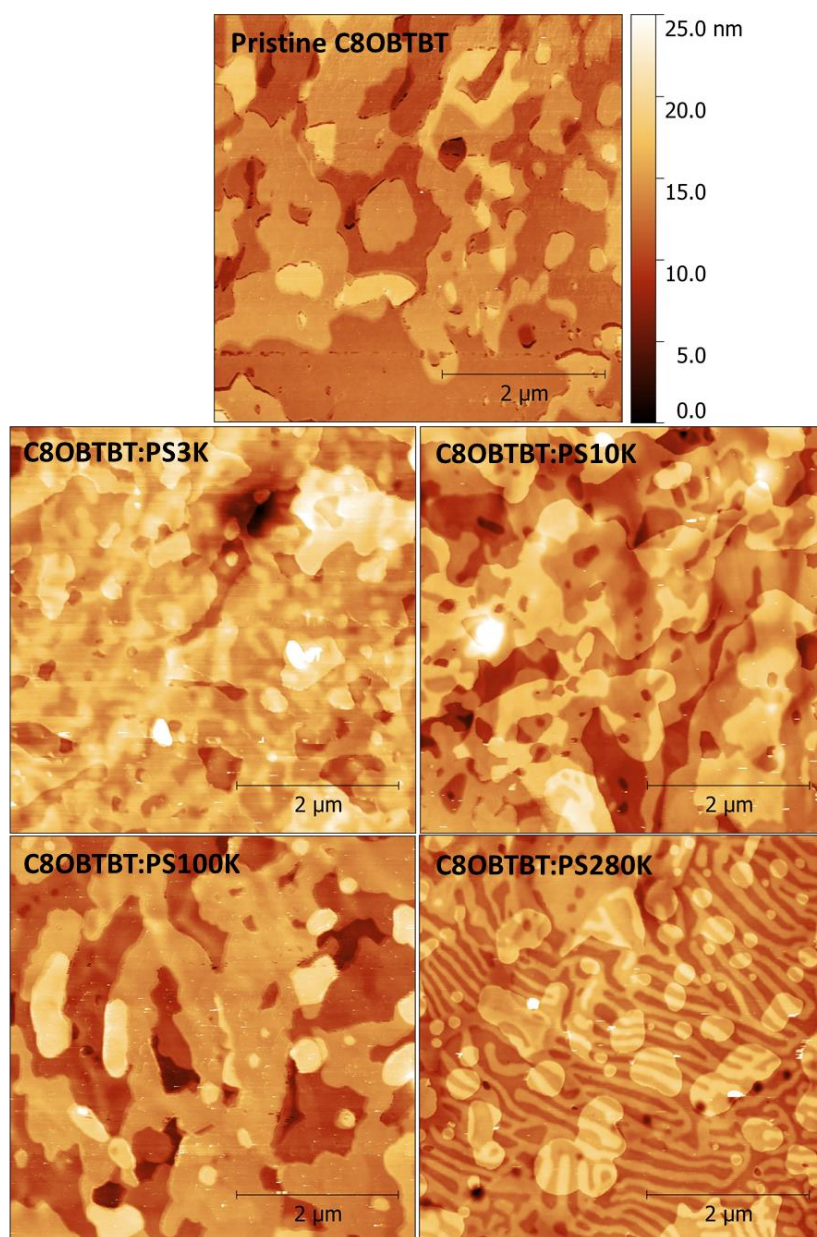


Figure 4.5. Topographic atomic force microscopy images of the thin-films based on only C8OBTBT and C8OBTBT with PS of different molecular weights. All the films were processed using the BAMS technique at 105 °C and 10 mm/s.

THIN-FILM STRUCTURAL CHARACTERISATION

The phase of all the thin-films was characterised by Polarisation-Modulated Infrared Reflection Absorption Spectroscopy (PM-IRRAS). The absorption peak used to evaluate the phase was one corresponding to the aromatic quadrant stretching located differently for the SIP phase, 1605 cm^{-1} , and for the bulk phase, 1611 cm^{-1} (**Figure 4.6**). The direct comparison of the PM-IRRAS spectra obtained for the thin-films prepared by BAMS with the reported for the SIP and bulk phase confirmed that in all the cases the SIP phase was formed.

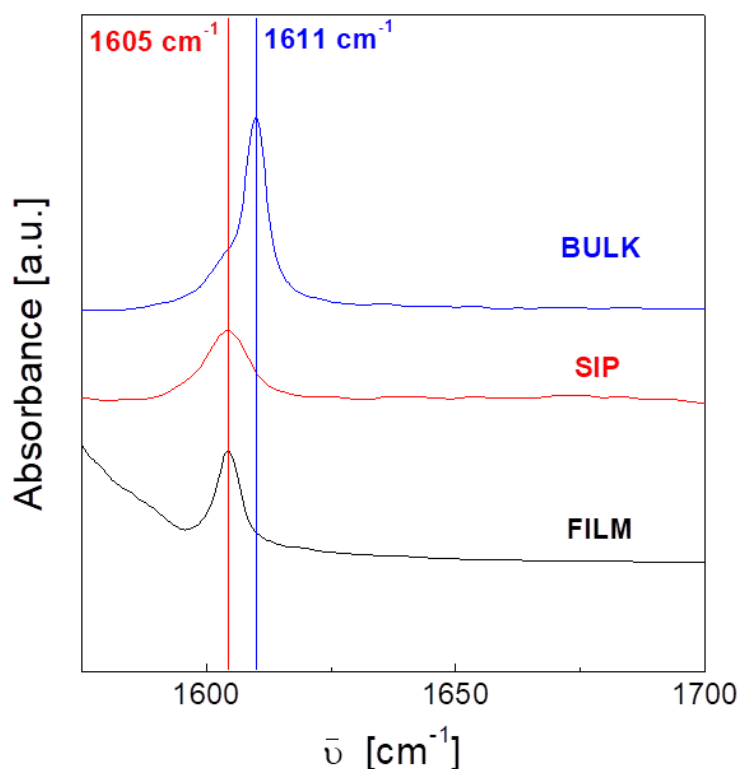


Figure 4.6. Comparison of the PM-IRRAS spectrum of a representative thin-film prepared by BAMS with the reported spectra of the Bulk and SIP phase of C8OBTBT.^[18]

EFFECT OF THE POLYMER MOLECULAR WEIGHT ON THE OFET CHARACTERISTICS

The performance of the thin-films based on C8OBTBT in OFETs in BCBG configuration was investigated. All the measurements were performed in air and darkness.

All the OFETs tested presented *p*-type behaviour. The values of the field-effect mobility in saturation regime ($\mu_{FE,sat}$), threshold voltage (V_{TH}), subthreshold slope (*SS*) and on/off current ratio ($I_{ON/OFF}$) of all the films are displayed in **Table 4.2**. From the different parameters analysed, it can be observed that films based on formulations with PS exhibited better performance than the transistors based on the film of pristine C8OBTBT, achieving improved mobility values of one order of magnitude and lower V_{TH} .

It should be noted that the films based on PS10K and PS280K presented an S-shape in the plot of the square root of the absolute value of the I_{DS} causing an overestimation of the mobility presented in **Table 4.2**.^[27,28] It was corroborated by the non-linear injection in the output characteristics that this S-shape was probably coming from the high contact resistance found in these transistors. On the other hand, devices based on C8OBTBT:PS100K displayed a linear injection in the output characteristics. In addition, these devices exhibited high field-effect mobility close to 1 cm²/V·s, a threshold voltage around 0 V, a high on/off current ratio of 10⁷ - 10⁸, and a sharp switch on in the transfer characteristics. It has been demonstrated that a sharp switch on (small subthreshold slope), as the one displayed by these OFETs, can be related to a low density of traps at the OSC/dielectric interface.^[29,30] Representative transfer and output characteristics of the BCBG OFETs fabricated with C8OBTBT:PS100K are displayed in **Figure 4.7**.

It is important to highlight that, to the best of our knowledge, this is the first time that films of the C8OBTBT SIP phase have been measured in an OFET configuration giving a mobility two times larger than the previously reported mobility for this molecule.^[17]

Therefore, after performing the measurements and comparing the parameters, it was concluded that the films based on C8OBTBT:PS100K displayed the best performance in BCBG configuration. Hence, the subsequent study of temperature and speed screening was performed with this formulation and also with the formulation that only contained C8OBTBT to study the effect of the polymer when different deposition conditions are employed.

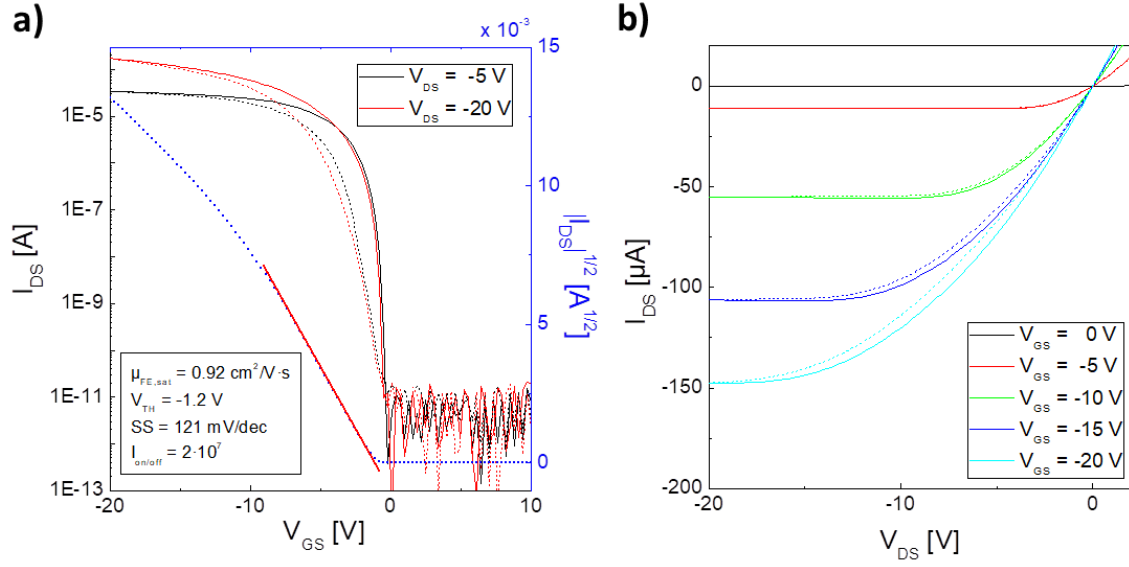


Figure 4.7. (a) Transfer and (b) output characteristics of an OFET based on the formulation C8OBTBT:PS100K; 4:1; CB; 2% wt. deposited at 105 °C and 10 mm/s using PFBT/Au electrodes in BCBG architecture.

Table 4.2. OFET parameters of the devices based on the different formulations tested deposited at 105 °C and 10 mm/s. These values were obtained from freshly prepared devices. $\mu_{FE,sat}$ of formulations with PS10K and PS280K are not reliable due to the S-shape in the $(I_{DS})^{1/2}$ vs. V_{GS} plot.

Polymer	OSC:PS	Architecture	$\mu_{FE,sat}$ [$\text{cm}^2/\text{V}\cdot\text{s}$]	V_{TH} [V]	$I_{ON/OFF}$	S.S. [V/dec]
-	-	BCBG	0.09 ± 0.03	6.9 ± 1.4	$(2 \pm 1) \cdot 10^5$	0.441 ± 0.150
PS3K	4:1	BCBG	0.43 ± 0.03	-0.6 ± 0.1	$(6 \pm 2) \cdot 10^6$	0.188 ± 0.020
PS10K	4:1	BCBG	1.40 ± 0.56	-1.2 ± 0.7	$(5 \pm 2) \cdot 10^7$	0.136 ± 0.034
PS100K	4:1	BCBG	0.92 ± 0.02	-0.9 ± 0.3	$(9 \pm 7) \cdot 10^7$	0.114 ± 0.028
PS280K	4:1	BCBG	0.89 ± 0.37	-0.9 ± 0.4	$(13 \pm 7) \cdot 10^6$	0.145 ± 0.033

4.3. EFFECT OF THE DEPOSITION SPEED AND TEMPERATURE

THIN-FILM PREPARATION AND MORPHOLOGY STUDY

As it was previously mentioned, we were interested in the control of the thin-film polymorphic phase and morphology through the deposition parameters. Therefore, films were deposited at a range of temperatures, going from 25 °C to 125 °C, and at different speeds, going from 0.1 mm/s to 10 mm/s. We also aimed at investigating the effect of the presence of PS in the formulation, so, the same deposition conditions of temperature and speed were performed using formulations with and without PS. As previously mentioned, the PS chosen to carry out this screening study was PS100K, because the thin-films formed using this molecular weight displayed the best properties as active layer for bottom-contact OFETs.

The CPOM images of the thin-films are shown in **Figure 4.8-4.13**. Each figure corresponds to the films prepared at a fixed temperature and varying the coating speed (0.1 mm/s, 1 mm/s, 5 mm/s and 10 mm/s) using the two chosen formulations (with and without PS). It can be observed that the domain size, homogeneity and directionality of the crystallites are strongly dependent on the employed deposition parameters.

It can be seen that the most homogeneous films were found at low/intermediate speed when the temperature was low and at high speed when the temperature was high (C8OBTBT:PS100k 25 °C / 1 mms; 45 °C / 5 mm/s; 105 °C / 10 mm/s; 125 °C / 10 mm/s). Therefore, it can be concluded that the homogeneity of the film depends on the evaporation rate of the solvent and the coating speed. In fact, the best films were obtained when the deposition speed and temperature led to an instantaneous drying of the solvent. Therefore, at low temperatures it is necessary to deposit the films at low speed to avoid the formation of a wet film, whereas at higher temperatures faster coatings are preferable.

In addition, the isotropy of the crystalline domains is also affected by the speed of the deposition. Only some of the thin-films prepared at the lowest speed (*i.e.* 0.1 mm/s) show some preferential alignment of the crystallites. For instance, in **Figure 4.9** it can be observed that in the film with PS deposited at 0.1 mm/s the crystallites are clearly aligned with the coating direction. On the other hand, using the same formulation at the same temperature and at 5 or 10 mm/s the crystalline domains seem to be randomly oriented.

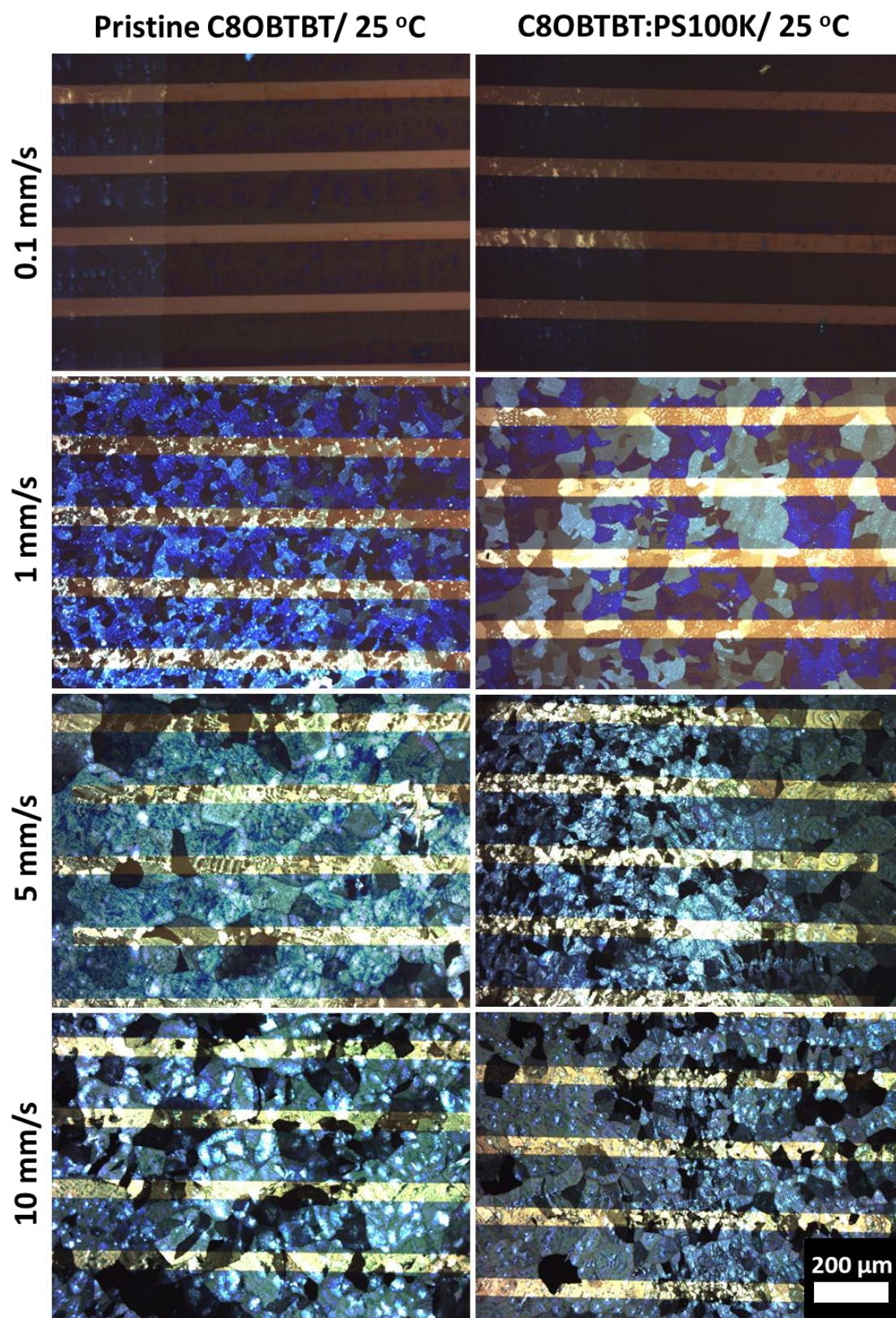


Figure 4.8. CPOM images of the thin-films based on C8OBTBT fabricated with and without PS and processed by BAMS at 25 °C and at different coating speeds.

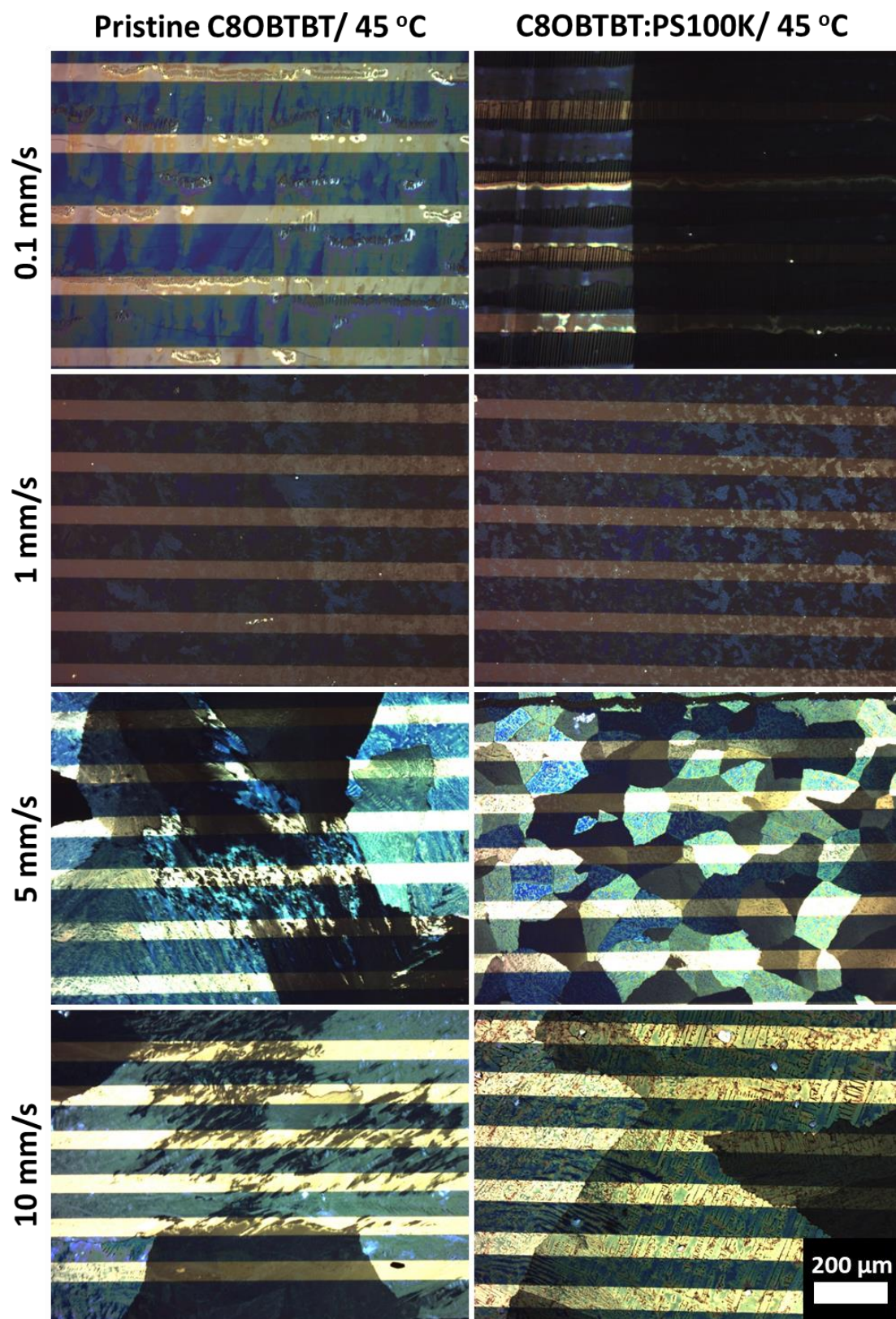


Figure 4.9. CPOM images of the thin-films based on C8OBTBT fabricated with and without PS and processed by BAMS at 45 °C and at different coating speeds.

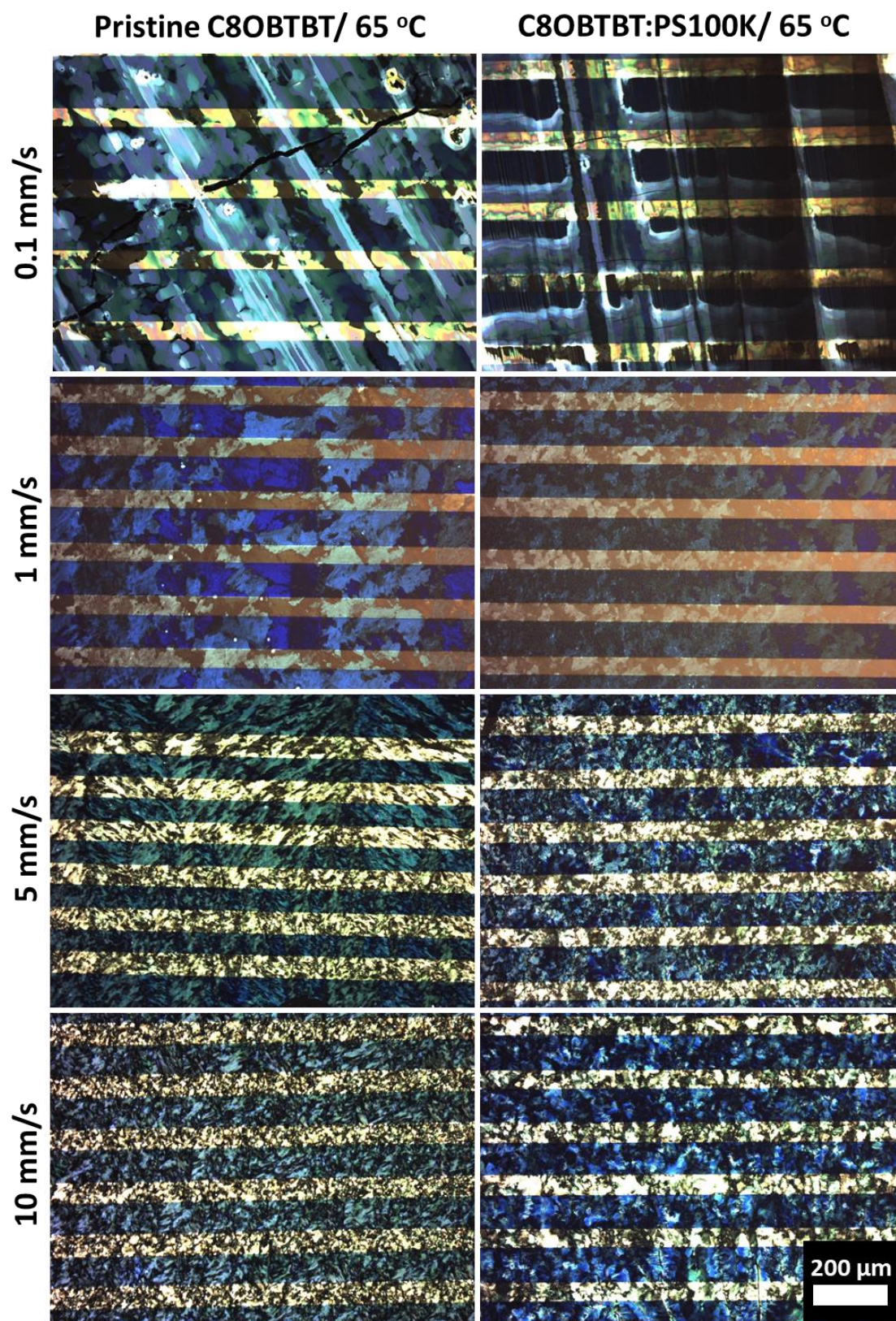


Figure 4.10. CPOM images of the thin-films based on C8OBTBT fabricated with and without PS and processed by BAMS at 65 °C and at different coating speeds.

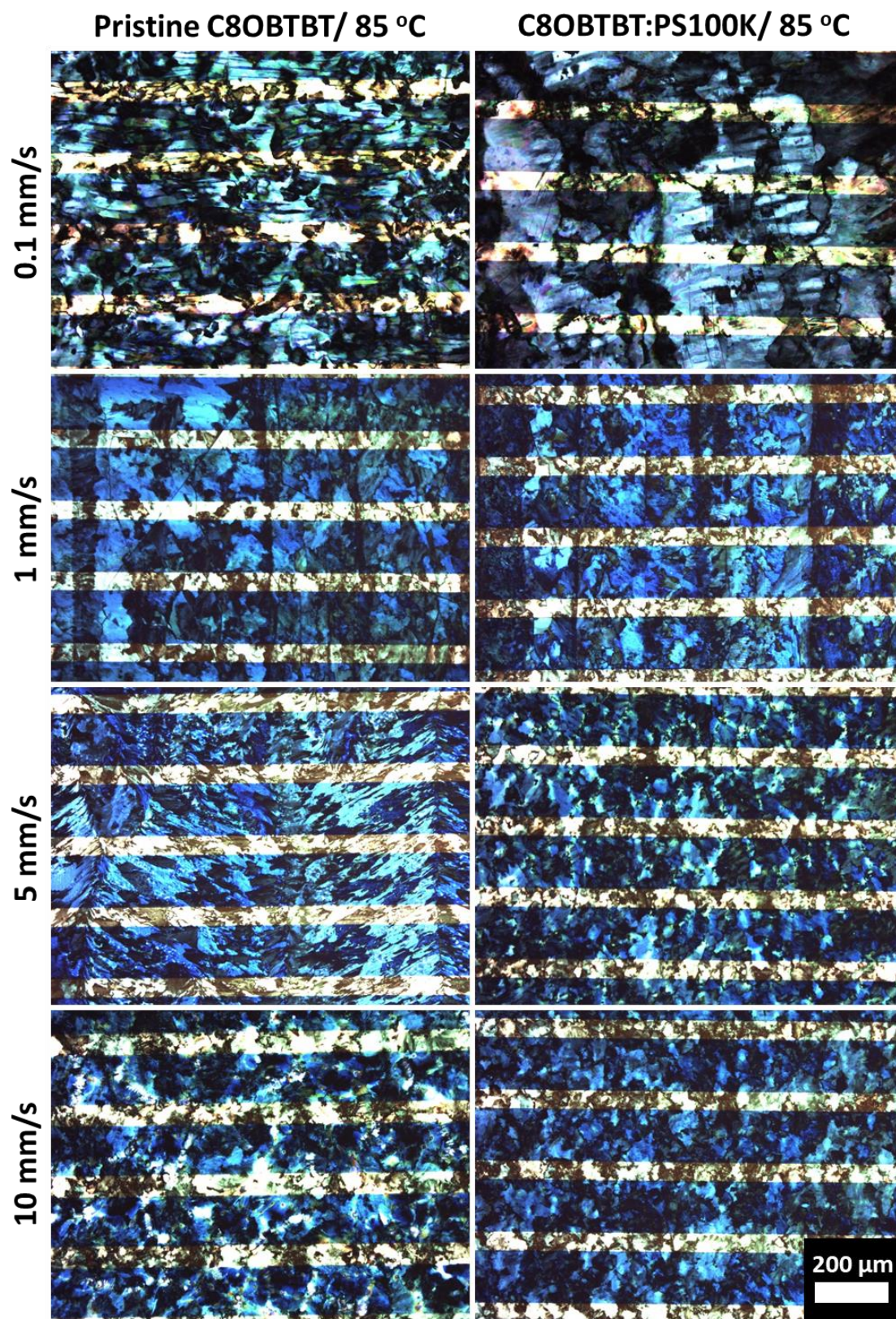


Figure 4.11. CPOM images of the thin-films based on C8OBTBT fabricated with and without PS and processed by BAMS at 85 °C and at different coating speeds.

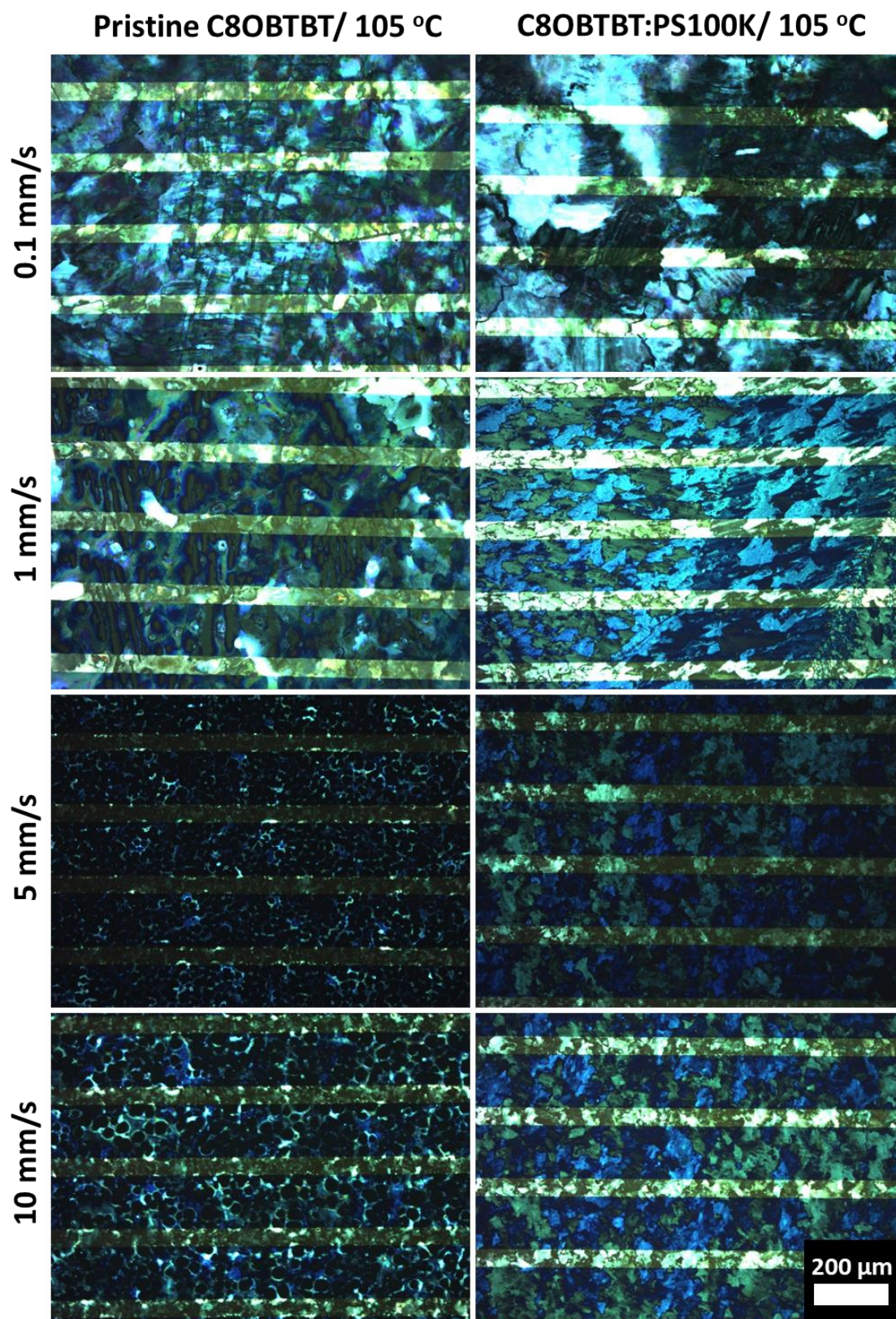


Figure 4.12. CPOM images of the thin-films based on C8OBTBT fabricated with and without PS and processed by BAMS at 105 °C and at different coating speeds.

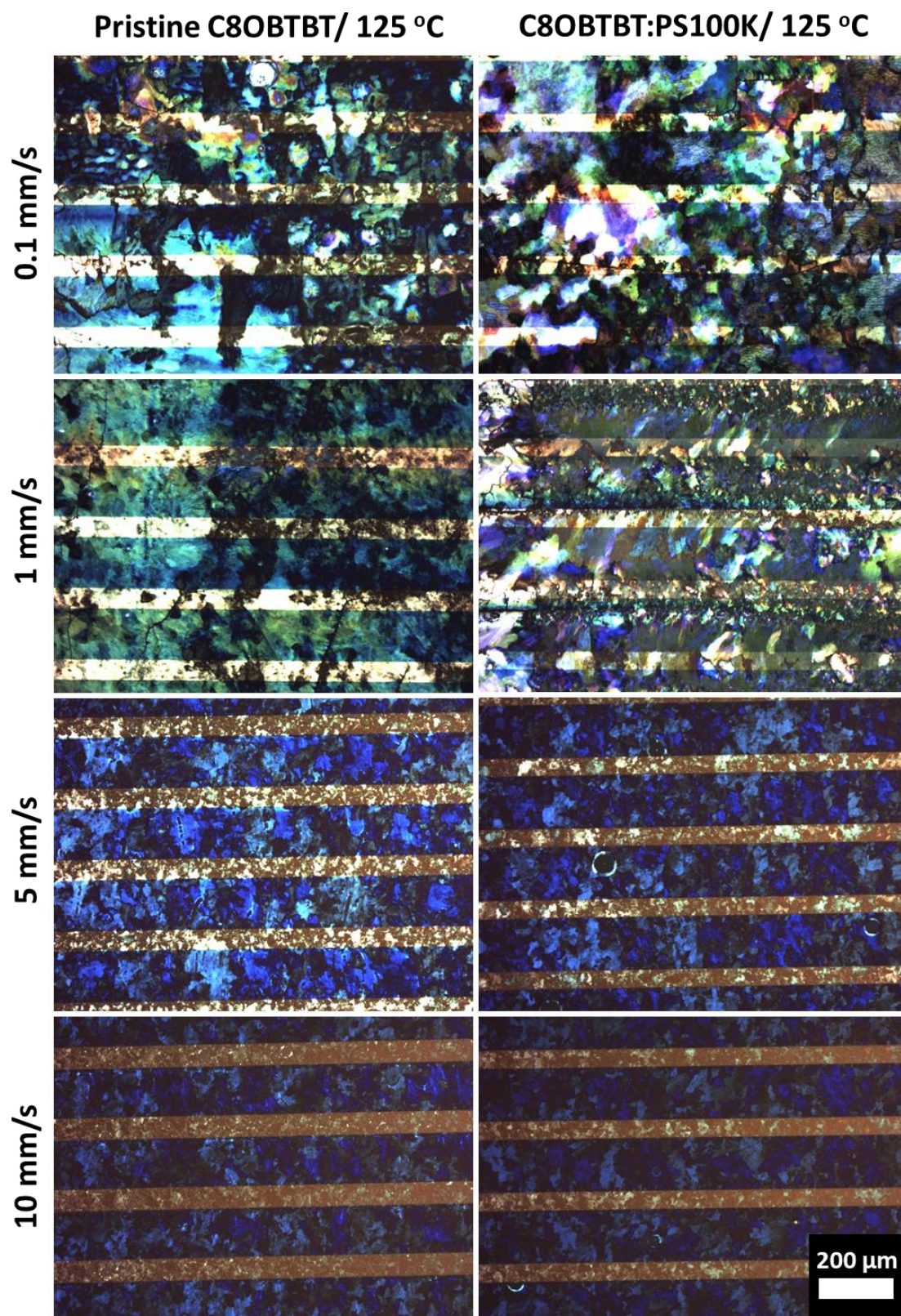


Figure 4.13. CPOM images of the thin-films based on C8OBTBT fabricated with and without PS and processed by BAMS at 125 °C and at different coating speeds.

THIN-FILM STRUCTURAL CHARACTERISATION

PM-IRRAS measurements were performed in all the thin-films based on C8OBTBT. All films displayed the same absorption peak as the sample presented in **Figure 4.6**, which corresponds to the SIP phase. Hence, surprisingly and oppositely to what was previously found for the OSC DB-TTF,^[5] even at low deposition speed and at low temperature, the bulk thermodynamic phase was not formed.

XRPD measurements (**Figure 4.14**) indicated the high crystallinity of the samples since they displayed only the reflections corresponding to the (0 0 *n*) family. This confirmed that the most favourable directions for electronic transport, the *ab* plane, laid in parallel to the substrate. Furthermore, it was observed that in the XRPD diffractograms more intense peaks were observed with the films prepared at lower coating speeds. We attributed this result to the higher thickness of the films obtained at low speed. The simulated powder diffractograms of the SIP and the bulk phase have also been included in **Figure 4.14** as reference. As previously mentioned, considering only the reflections in the plane lying in parallel to the substrate, it is not possible to distinguish them.

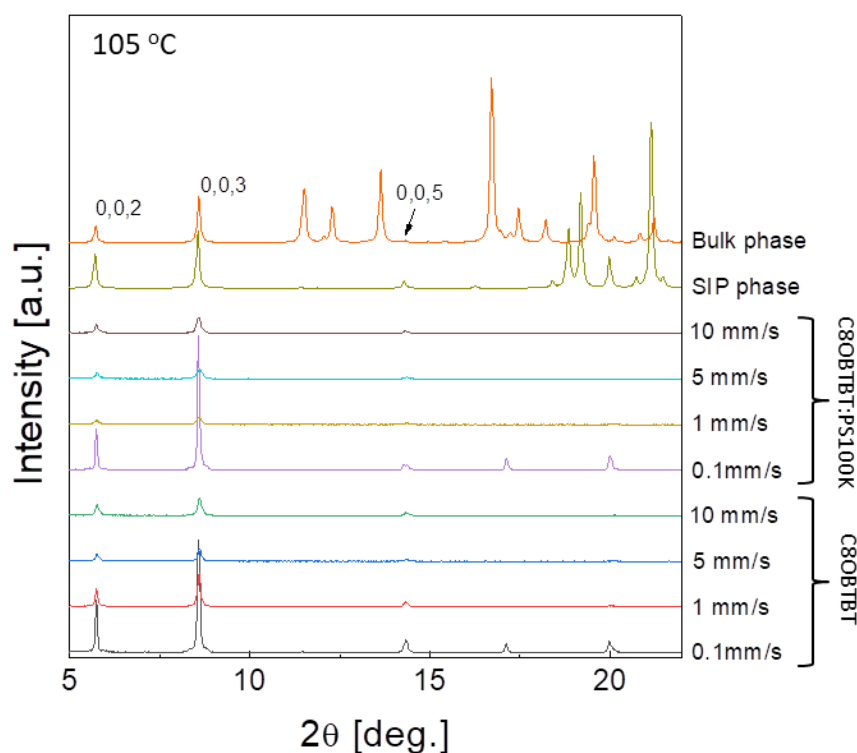


Figure 4.14. X-ray powder diffractograms of the thin-films based on C8OBTBT fabricated by BAMS with and without PS100K at 105 °C and at different coating speeds. The simulated diffractograms from the bulk and SIP phase are also included for comparison.

Thickness measurements were performed in all the thin-films based on C8OBTBT by profilometry. All the thickness values are displayed in **Figure 4.15**. Interestingly, the general trend is that the thin-films with a thickness below 50 nm are obtained at an intermediate speed when the temperature is low and at the highest speed when the temperature is high. The films prepared at the lowest coating speed are typically very thick, with the exception of the film prepared at low temperature without PS.

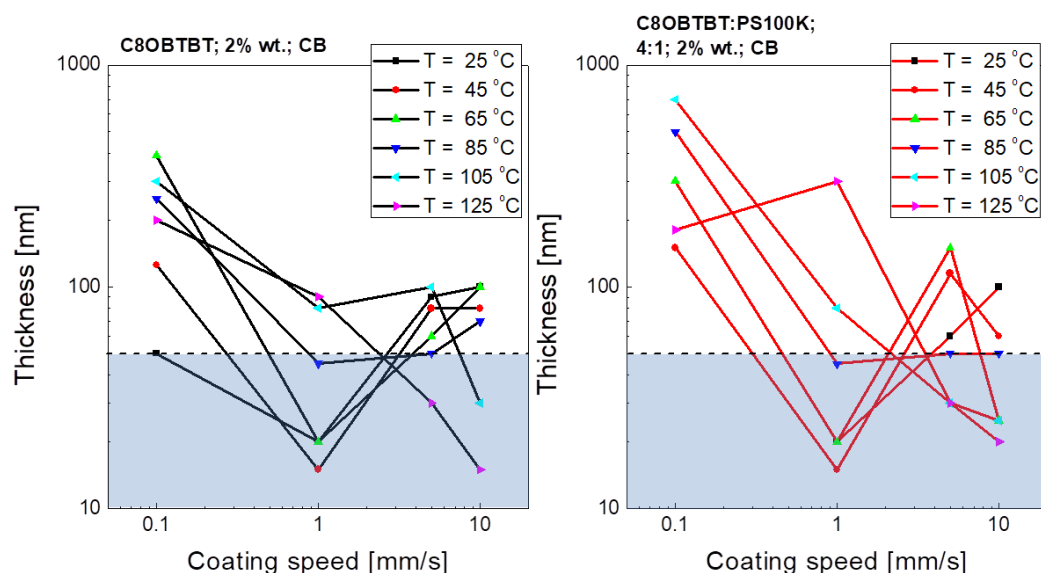


Figure 4.15. Thickness vs. coating speed of all the thin-films based on C8OBTBT (left) and on C8OBTBT:PS100K (right) deposited at different temperatures. The region of low thickness (below 50 nm) is highlighted with a blue box.

EFFECT OF THE DEPOSITION CONDITIONS ON THE OFET CHARACTERISTICS

In **Figure 4.16**, the $\mu_{FE,sat}$ of all the thin-films fabricated at different temperatures and speeds are displayed. Generally speaking, the devices based on blends tend to give rise to better OFET performances. Among the most promising results, we can highlight that the films of pristine OSC and with PS deposited at 1 mm/s and at 45 °C showed average $\mu_{FE,sat}$ values of 0.86 and 1.35 cm²/V·s, respectively, which are the highest values found for this semiconductor. Remarkably, these correspond to the thinnest films obtained (see Figure 4.15). Furthermore, thin-films based on the formulation C8OBTBT:PS100K deposited at 105 °C and at 5 and 10 mm/s also displayed high mobility values of 0.84 and 0.92 cm²/V·s, respectively.

Some tendencies in the performance of the devices were observed in this screening investigation. For example, at the lowest speed (0.1 mm/s) the performance of the devices was the lowest, except for the samples with PS deposited at 25 °C. In addition, thin-films with PS processed at 125 °C displayed a decrease in the performance. This was particularly pronounced with the devices based on blends of PS. We attribute this effect to the fact that at that temperature the PS is beyond its glass transition point and, therefore, thin-film formation and phase separation might be affected. In the case of thin-films without PS, the best conditions were found at relatively low speed and temperature (*i.e.* 1 mm/s and 45-65 °C). This is probably caused by the fact that when the formulation does not include PS it is less viscous and faster depositions lead to less homogeneous films, which display worse characteristics. Interestingly, the morphologies of the thin-films that lead to the best performing OFETs are clearly similar (CPOM images in **Figures 4.7** and **4.10**).

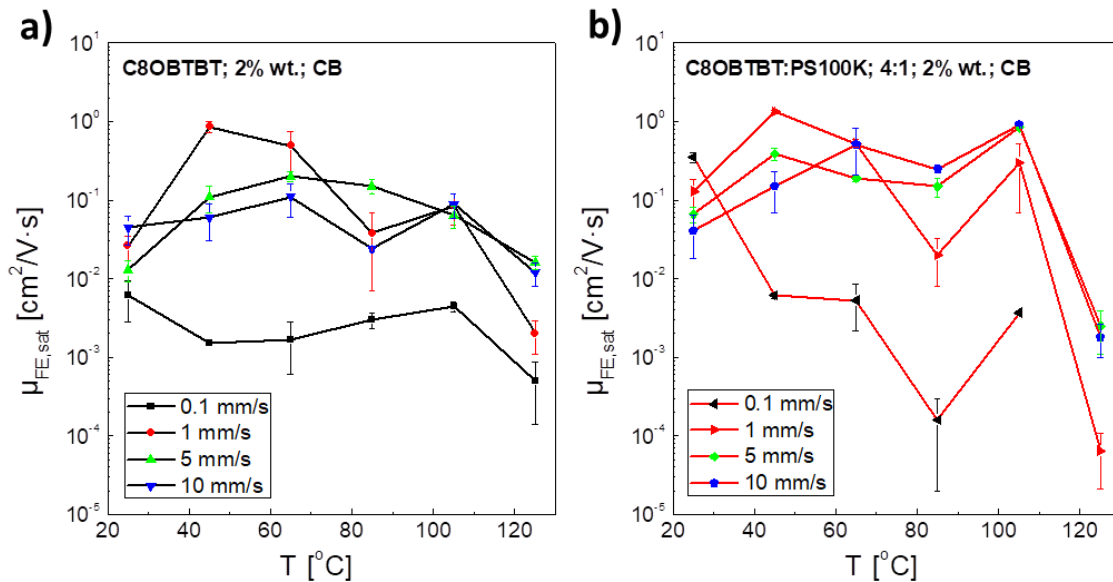


Figure 4.16. Field-effect mobility ($\mu_{FE,sat}$) values extracted from the OFETs of thin films based on the formulations (a) C8OBTBT; 2% wt.; CB and (b) C8OBTBT:PS100K; 4:1; 2% wt.; CB deposited at different speeds (values are indicated in the legend) and at different temperatures.

Even though films deposited at 45 °C displayed higher mobility, we chose 10 mm/s and 105 °C as the best conditions for the deposition of C8OBTBT:PS100K due to four main factors: i) the on/off current ratio is almost one order of magnitude higher than the one found in devices prepared at 45 °C and 1 mm/s. ii) The subthreshold slope value is smaller, which indicates a lower density of traps in the OSC/dielectric interface. iii) The threshold voltage is slightly negative instead of slightly positive (-0.9 V vs. 0.7 V), *i.e.* when no V_{GS} is applied the devices prepared with the first conditions are off and the second ones are on. iv) The higher deposition speed of the film is more suitable for roll-to-roll processes.

4.4. POLYMORPH STABILITY

It has been previously reported that films of the SIP phase of C8OBTBT after 6 months aging spontaneously convert to the bulk phase.^[15] Here we aimed at investigating the SIP polymorph stability when blends are used. In this case, we focus on thin-films of blends of C8OBTBT with PS3K and PS100K prepared at 10 mm/s and 105 °C

CPOM images of the thin-films in BCBG architecture taken shortly after the deposition and also after 3 months in air are shown in **Figure 4.17**. It can be observed that the morphology of the film based on C8OBTBT:PS100k has not changed. Interestingly, for the thin-film based on the lower molecular weight PS, while the as-prepared film displayed a homogeneous morphology, the CPOM image taken 3 months after the deposition revealed the presence of two differentiated morphologies (indicated in **Figure 4.17c** with a red and a blue dot). This change in the morphology was investigated by a Raman spectrophotometer coupled with an optical microscope. A different signal in the low Raman shift region was obtained for these two areas. In fact, the Raman spectrum of areas assigned with the blue dot coincide with the signal reported for the SIP phase, whereas the spectrum of the red dot area match with the signal reported for the bulk phase. On the other hand, films of C8OBTBT with PS100K did not display this behaviour suggesting that the presence of a higher molecular weight polymer has a beneficial effect on the stabilisation of the meta-stable SIP phase. This is an important result since it demonstrates that processing an organic semiconductor together with a binding polymer results not only in the improvement of the performance but also in the enhancement of the phase stability. This strategy could be applied to other OSCs to prevent the phase change and extend the life of devices.

In parallel, the electrical stability of these OFETs was also investigated (**Figure 4.18**). For both formulation it was observed that the measurements carried out one day after the fabrication displayed a small enhancement in the $\mu_{FE,sat}$, however, after that it remained stable for a period of three months. Regarding the V_{TH} , it was observed a small positive shift of 0.7 V during the same period. These results point to the high stability of the OFETs based on C8OBTBT.

The change from the SIP to the bulk phase observed in the thin-film based on C8OBTBT:PS3K did not affect critically, up to the moment, the performance of the OFETs. We attribute this to the fact that the modification of phase occurred only in some spots of the film while most of the film remained still unchanged. Currently we are continuing investigating the evolution over time of the OFET performance and morphology to explore the impact of the polymorph change on the device performance.

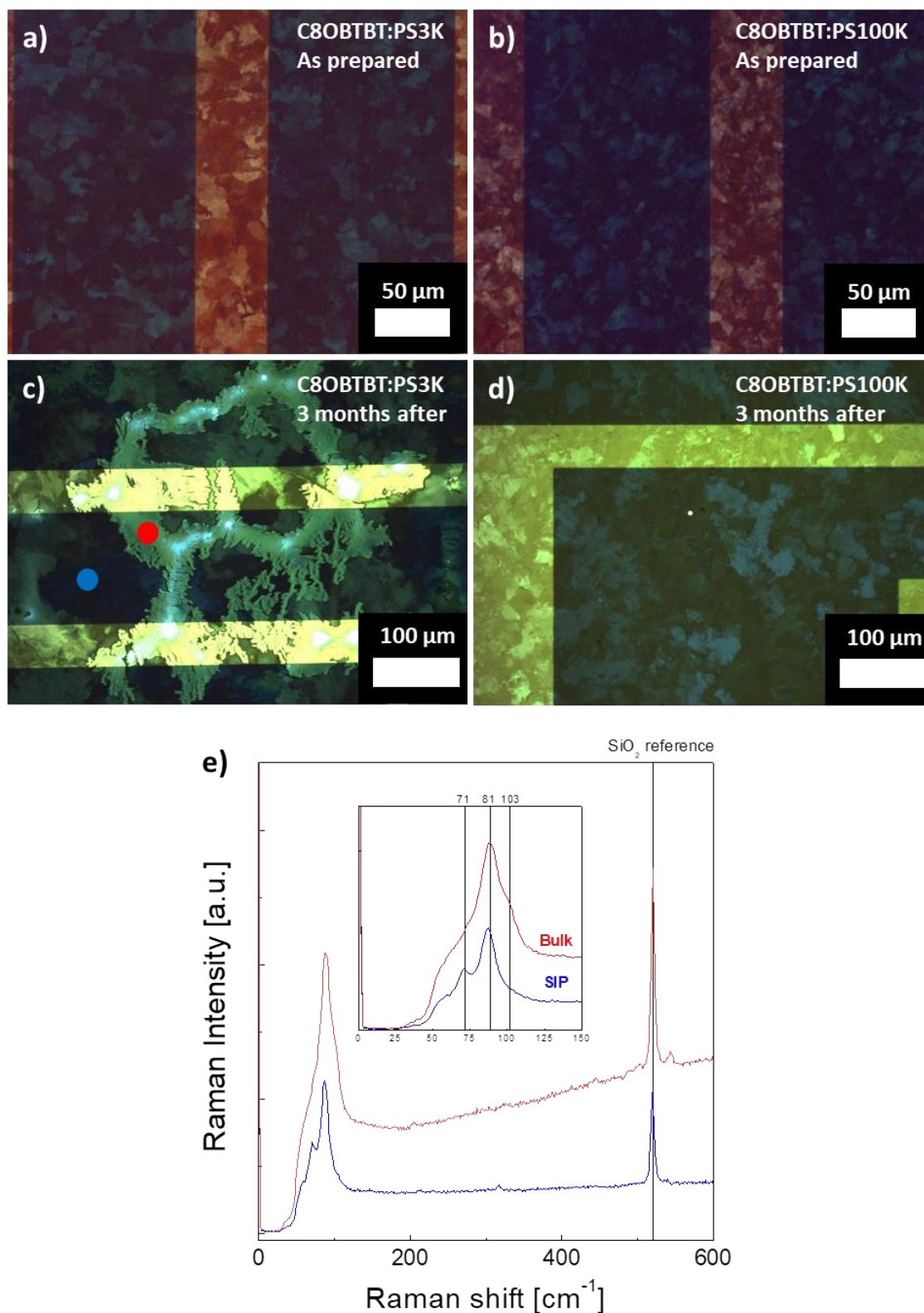


Figure 4.17. CPOM images of freshly deposited thin-films based on **(a)** C8OBTBT:PS3K and **(b)** C8OBTBT:PS100K. **(c)** and **(d)** CPOM images of the same thin-films taken 3 months after the fabrication. In **(c)** a blue and a red dot are used to indicate the two different morphologies found in the film. **(e)** Raman spectra measured in the blue and red dot areas. In the inset, there is a zoom of the spectra in the region where the phases can be identified.

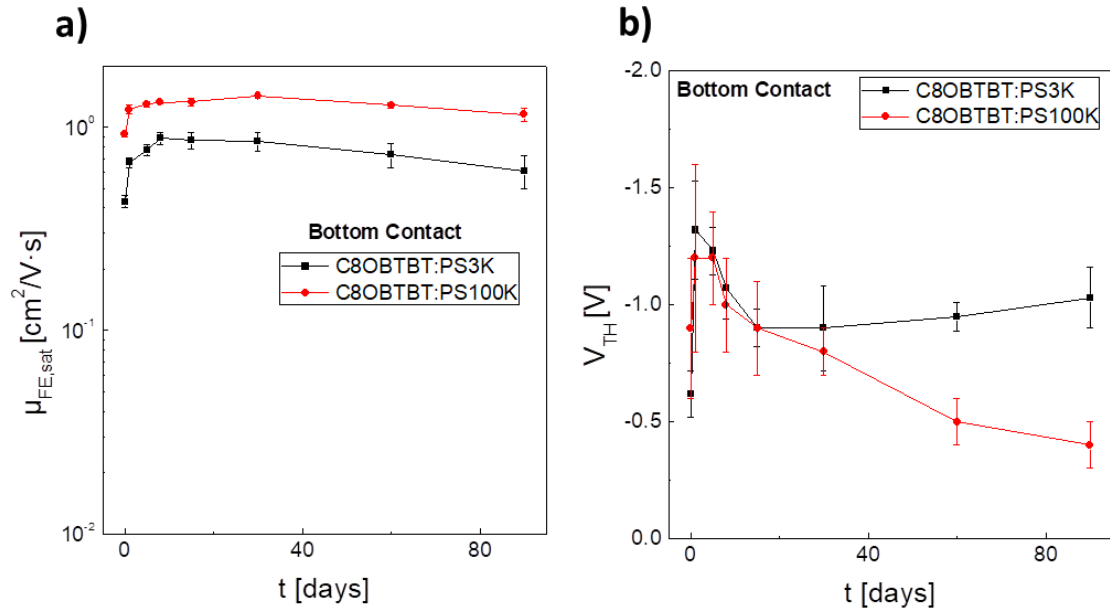


Figure 4.18. a) Evolution over time of the $\mu_{FE,sat}$ of thin-film OFETs based on C8OBTBT:PS3K and C8OBTBT:PS100K in BCBG. (b) Evolution of the V_{TH} over time of the same thin-film OFETs.

4.5. DEVICE ARCHITECTURE

Among the two bottom-gate OFET architectures, BCBG is usually the one that displays more contact resistance because of the limited area between the OSC active region (*i.e.* the first 5–10 nm OSC in contact with the dielectric) and the source-drain electrodes.^[31] On the other hand, for top-contact bottom-gate (TCBG) OFET architecture, in addition to the larger OSC/electrode contact area, the contact resistance is usually further reduced by the penetration of Au atoms into the OSC during the evaporation of the metal. However, low-lying HOMO OSCs typically require the addition of interlayers between the OSC and the electrode to enhance the charge injection. Two common options are: i) the addition of a few nanometres layer of MoO_x that has been demonstrated to raise the Au work function to 5.6 eV^[6,32,33] and ii) the addition of a thin layer of the *p*-dopant 2,3,5,6-tetrafluorotetracyanoquinodimethane (F4-TCNQ) that has also displayed good results in terms of reduction of the contact resistance,^[19,23] since the charge-transfer that takes place between the *p*-type OSC and F4-TCNQ results in a more conductive doped layer. This layer acts as an intermediate level between the OSC and the electrodes lowering the energetic barrier for the injection of charges into the semiconductor, thus, reducing the contact resistance.

Herein, the selected optimum deposition conditions for thin-films in BCBG configuration (*i.e.* deposition speed of 10 mm/s and a temperature of 105 °C) were used to deposit thin-films based on the formulations of C8OBTBT with PS10K, PS100K and PS280K and without PS. These thin-films were used as active layers of TCBG OFETs with bare Au source/drain electrodes and also F4-TCNQ/Au electrodes. These latter electrodes were fabricated depositing a thin layer of 20 nm of F4-TCNQ by evaporation between the active layer and the Au electrode. The objective of the study in TCBG configuration was optimising the performance of the devices and also to study the effect of the F4-TCNQ in the electrical characteristics.

The transfer and output characteristics of the best working formulation in TCBG configuration with bare gold electrodes (based on the formulation C8OBTBT:PS280k) and also the one fabricated with pristine C8OBTBT are displayed in **Figure 4.19**. In addition, parameters extracted from OFETs in TCBG architecture with bare gold electrodes are displayed in **Table 4.3**. In the transfer characteristics of these TCBG OFETs it can be observed that they also behave as *p*-type transistors but they do not display the same sharp switch on found in BCBG configuration. Furthermore, the threshold voltage was found to be much lower (around -20 V), which is indicative of a higher density of traps. In the output characteristics it can be observed that the injection is not linear, *i.e.* high contact resistance. We attribute this behaviour to the presence of traps in the OSC/electrodes interface that could be introduced during the deposition of the gold electrodes. All in all, we attribute the worse performance displayed by the TCBG OFET to the higher presence of traps and also to the higher contact resistance.

The OFETs fabricated with F4-TCNQ/Au in TCBG configuration displayed better performance than with the bare gold. In terms of field-effect mobility, the values found for these OFETs are around five times higher than the ones found for bare gold TCBG devices. In **Figure 4.20** the transfer and output characteristics of a representative OFET fabricated with the best

performing formulation (C8OBTBT:PS280K) and with pristine OSC are displayed. OFET parameters of transistor in TCBG with F4-TCNQ are also displayed in **Table 4.3**. In this case, the output characteristics display a linear injection meaning that the contact resistance is reduced by the addition of the F4-TCNQ interlayer.

Regarding the differences between the formulations, it can be again observed that formulations with PS displayed higher performance than the samples without PS. In addition, a clear improvement of the mobility with the use of higher molecular weight PS was also observed. We attribute this improvement to the more pronounced vertical phase separation when a higher molecular weight PS is used.

Table 4.3. OFET parameters of the devices based on the different formulations tested deposited at 105 °C and 10 mm/s. These values were obtained from freshly prepared devices.

Polymer	OSC:PS	Architecture	$\mu_{FE,sat}$ [$\text{cm}^2/\text{V}\cdot\text{s}$]	V_{TH} [V]	$I_{ON/OFF}$	S.S. [V/dec]
-	-	TCBG	0.042 ± 0.014	-6.7 ± 0.7	$(1 \pm 1) \cdot 10^5$	1.12 ± 0.32
PS10K	4:1	TCBG	0.065 ± 0.037	-15.8 ± 4.9	$(8 \pm 6) \cdot 10^6$	0.578 ± 0.455
PS100K	4:1	TCBG	0.11 ± 0.04	-17.0 ± 11.3	$(2 \pm 1) \cdot 10^6$	0.468 ± 0.307
PS280K	4:1	TCBG	0.11 ± 0.03	-19.0 ± 9.9	$(6 \pm 5) \cdot 10^6$	0.882 ± 0.293
-	-	TCBG/F4-TCNQ	0.22 ± 0.03	-3.5 ± 5.7	$(3 \pm 1) \cdot 10^6$	1.89 ± 0.97
PS10K	4:1	TCBG/F4-TCNQ	0.19 ± 0.05	-17.5 ± 0.7	$(2 \pm 1) \cdot 10^5$	3.28 ± 0.61
PS100K	4:1	TCBG/F4-TCNQ	0.40 ± 0.06	-20.5 ± 0.7	$(1 \pm 1) \cdot 10^5$	3.90 ± 0.29
PS280K	4:1	TCBG/F4-TCNQ	0.65 ± 0.21	-20.5 ± 0.7	$(7 \pm 5) \cdot 10^5$	1.47 ± 1.41

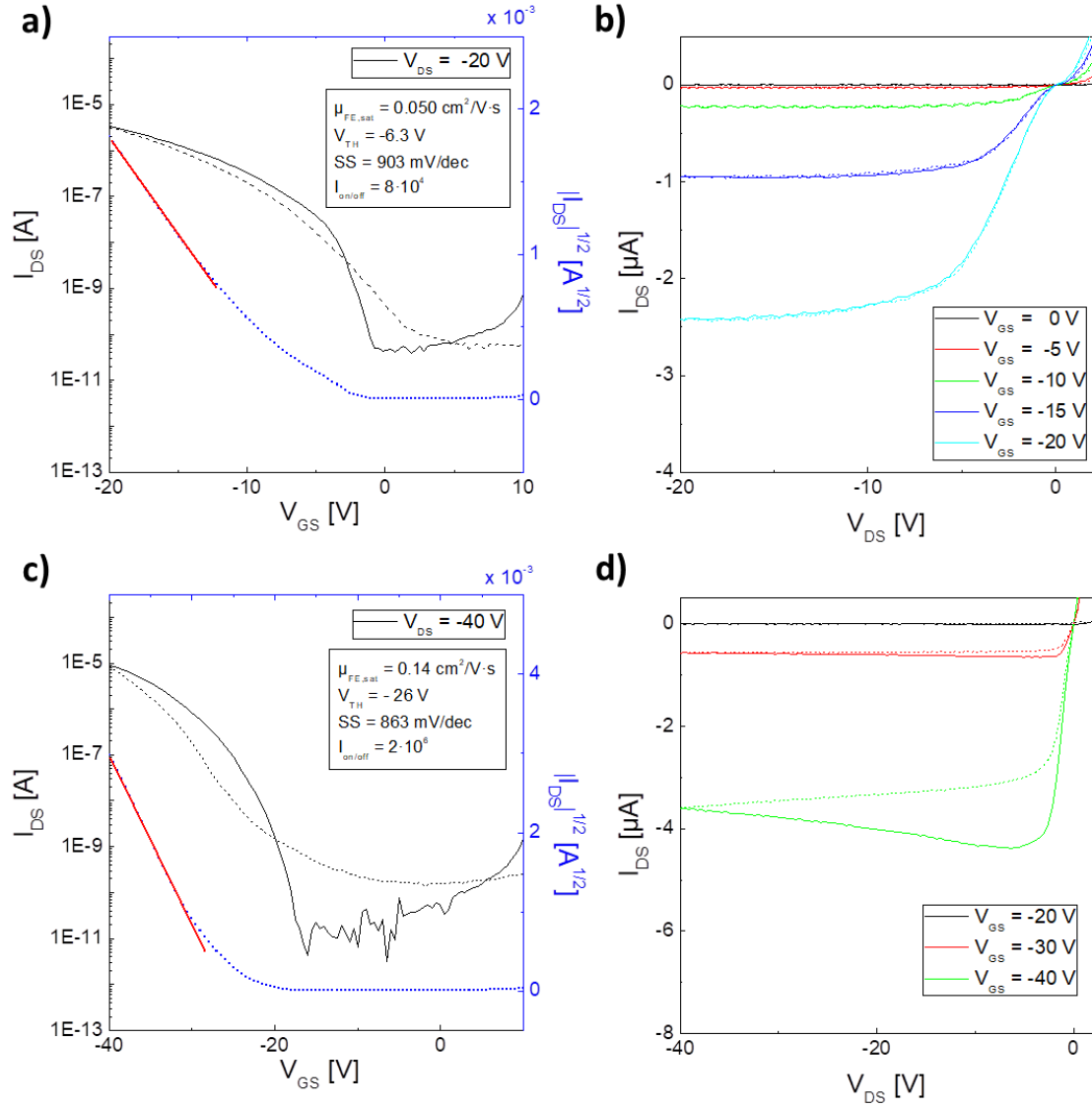


Figure 4.19. **(a)** Transfer and **(b)** output characteristics of an OFET based on the formulation C8OBTBT; CB; 2% wt. deposited at 105 °C and 10 mm/s using Au electrodes in TCBG architecture. **(c)** Transfer and **(d)** output characteristics of an OFET based on the formulation C8OBTBT:PS280K; 4:1; CB; 2% wt. deposited at the same conditions and with the same electrodes and architecture.

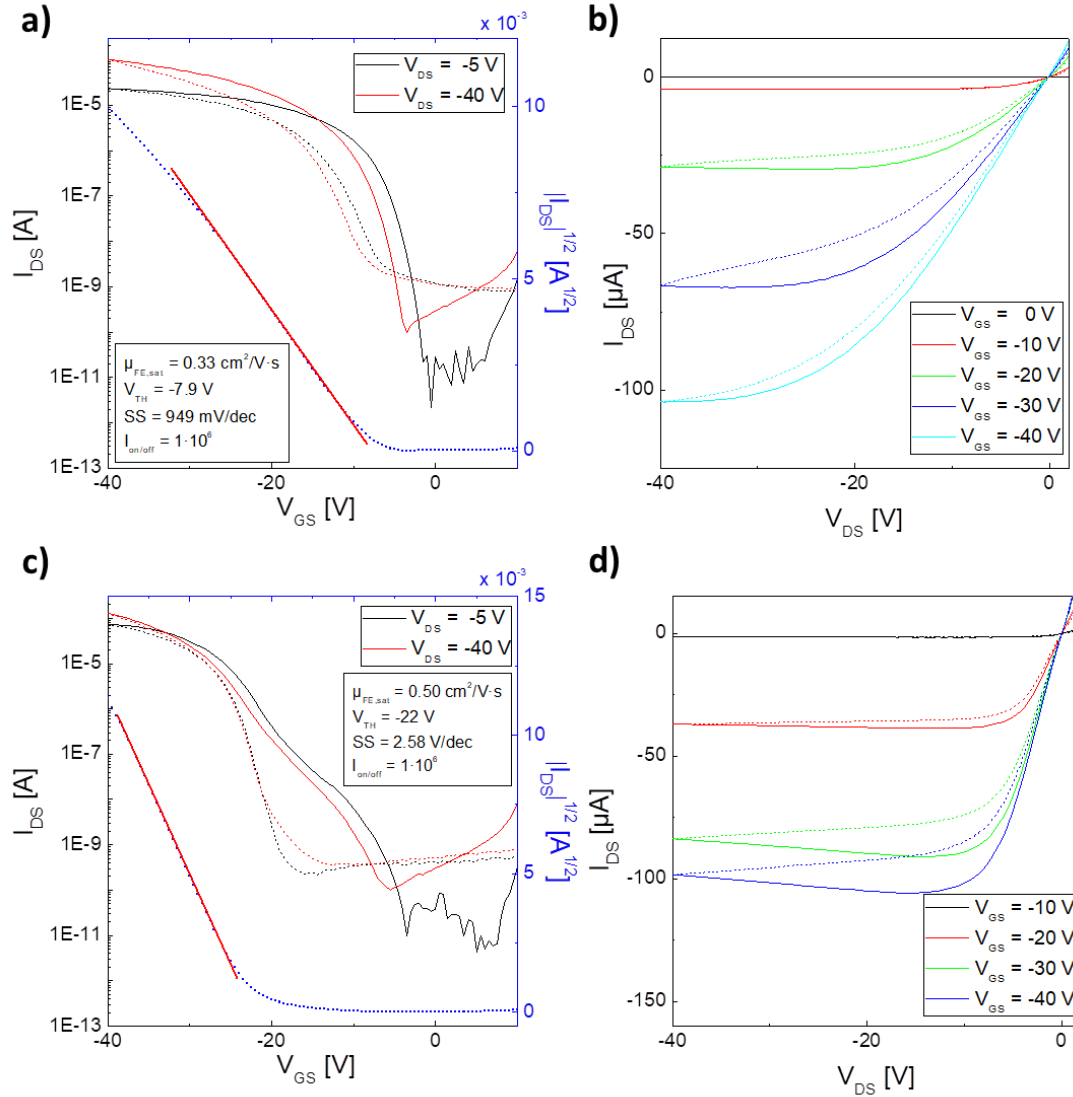


Figure 4.20. **(a)** Transfer and **(b)** output characteristics of an OFET based on the formulation C8OBTBT; CB; 2% wt. deposited at 105 °C and 10 mm/s using Au electrodes with an interlayer of F4-TCNQ in TCBG architecture. **(c)** Transfer and **(d)** output characteristics of an OFET based on the formulation C8OBTBT:PS280K; 4:1; CB; 2% wt. deposited at the same conditions and with the same electrodes and architecture.

The shelf stability of the OFETs in TCBG architectures was also investigated. It was observed that in all the cases the devices measured some days after the fabrication displayed better performance than when measured shortly after the fabrication (**Figure 4.21**). The transistors experienced an increase of one order of magnitude in the mobility reaching values up to 1.5 $cm^2/V \cdot s$, thus, overpassing the performance found in OFETs in BCBG architecture. However, after a week the mobility reached a plateau and remained fairly stable for 3 months (**Figure 4.22**). This enhancement of the performance was more pronounced in TCBG OFETs without F4-TCNQ, which were the ones that suffered more contact resistance right after the preparation. Furthermore, the V_{TH} of the OFETs experienced an initial shift of -10 V and then slowly increased to reach the initial value after 90 days. In the case of TCBG OFETs with contacts doped with F4-TCNQ, the V_{TH} slowly shifted towards more positive values.

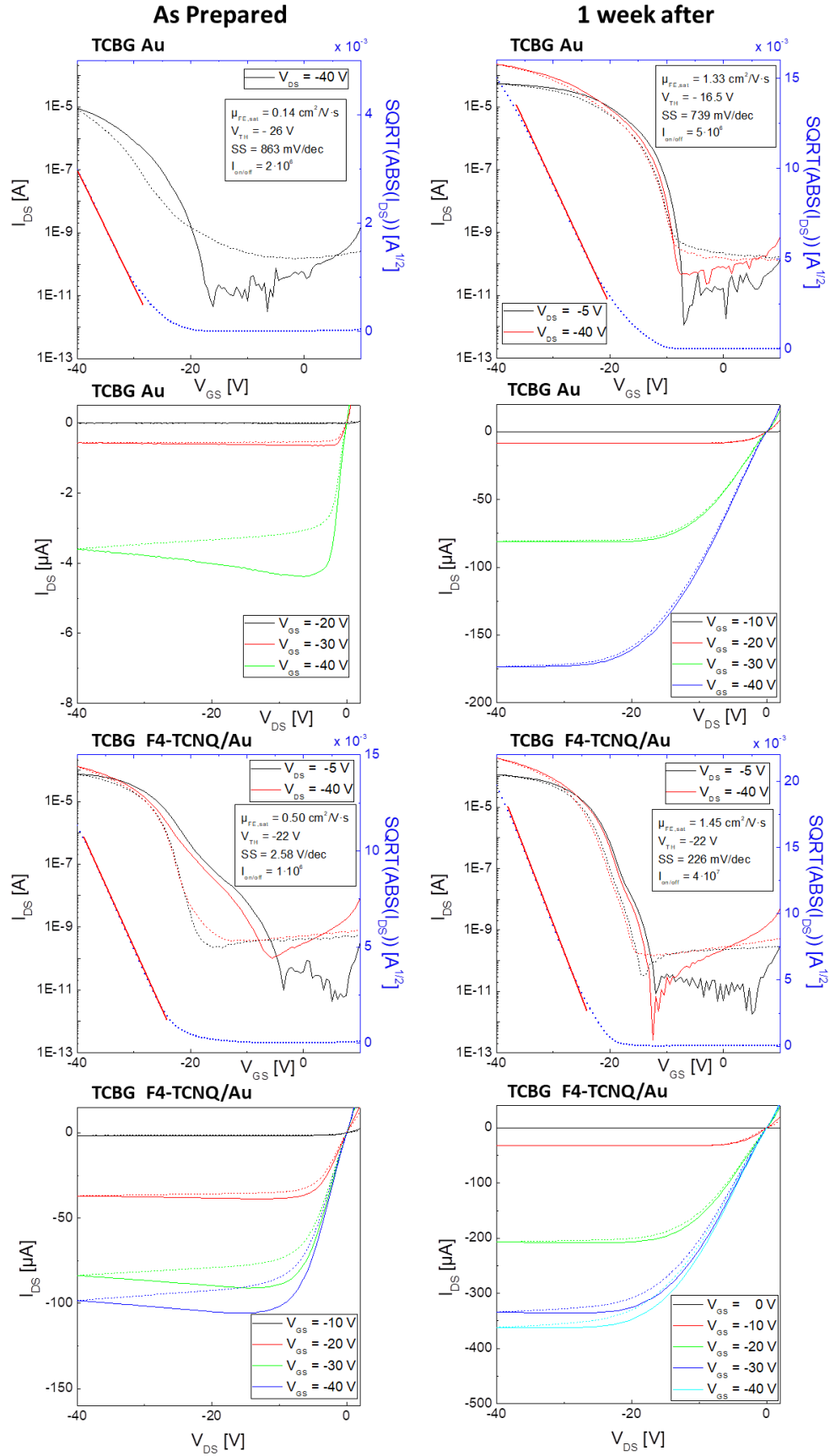


Figure 4.21. Comparison of the transistor characteristics of thin-films based on C8OBTBT:PS280K in TCBG configuration with bare gold electrode (top) and with Au/F4-TCNQ electrodes (bottom) shortly after the fabrication (left) and a week after (right)

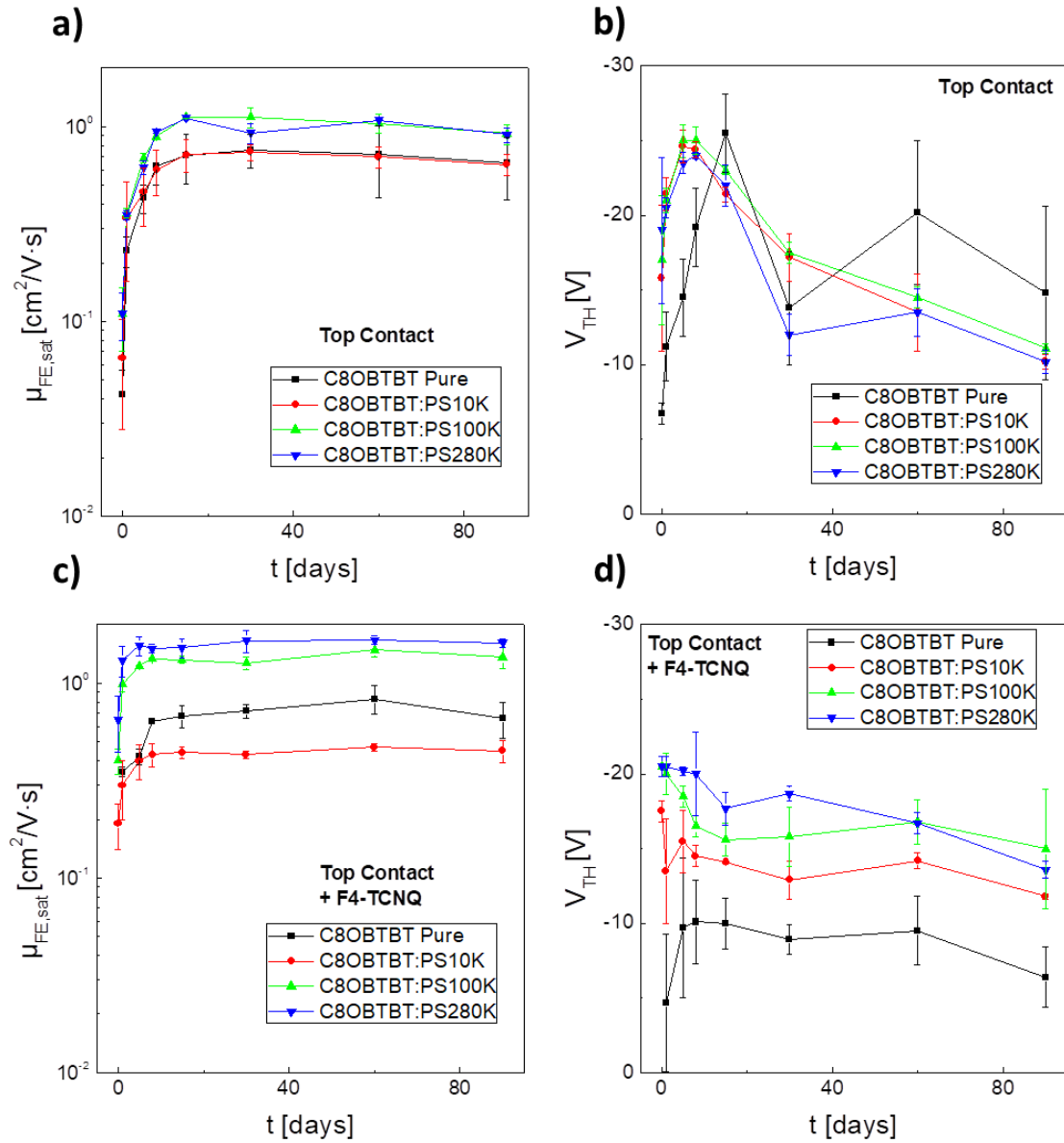


Figure 4.22. (a), (c) and (e) Evolution over time of the $\mu_{FE,sat}$ of thin-film OFETs based on C8OBTBT in BCBG, TCBG and TCBG + F4-TCNQ and BCBG architectures, respectively. (b), (d) and (f) Stability of the V_{TH} over time of the same thin-film OFETs.

In order to understand the increase of the performance with time in the first week, contact resistance measurements were carried out using the Y-function method.^[23,34] In **Figure 4.23** it is shown that all the TCBG OFETs experienced a substantial decrease of the contact resistance specially in the first week after fabrication, which would explain the increase in the device mobility. Furthermore, the reduction of the contact resistance only occurs in the top contact architecture. For comparison the evolution of the contact resistance for a BCBG device is also plotted in **Figure 4.23**. The reduction of the contact resistance was more pronounced in the transistors with bare gold electrodes, probably because their initial contact resistance was also higher. We attribute this behaviour of the contact resistance to the introduction of

unintentional doping from the environment as it has been observed in polymer-based OFETs or the diffusion of the top-contact metal into the OSC towards the conduction channel.^[35]

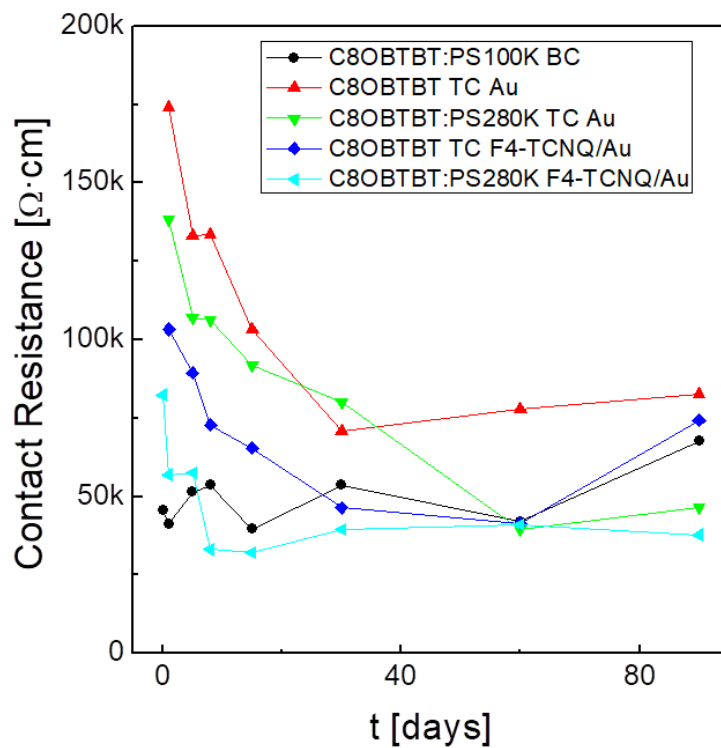


Figure 4.23. Evolution over time of the contact resistance, calculated with the Y-function method, of the OFETs based on C8OBTBT.

4.5. SUMMARY

In summary, thin-films based on the organic semiconductor C8OBTBT and on blends of it with different molecular weight PS have been successfully deposited from solution with the deposition technique BAMS. It was also investigated the effect of the temperature and deposition speed in the thin-film morphology, by CPOM, and in the thin-film phase, by PM-IRRAS and XRPD. Comparing the data obtained from the PM-IRRAS with the reported spectra, it was determined that the obtained phase for all the deposition conditions and formulations was the SIP phase. Interestingly, even when reducing the coating speed and the temperature the most thermodynamically stable phase, the bulk phase, was not obtained.

After the electrical characterisation of these films as active layers in OFETs, it was concluded that the best performing film was the one deposited from a solution of C8OBTBT:PS100K; 4:1; 2% wt.; CB at 105 °C and 10 mm/s. This film displayed a mobility in BCBG OFETs close to 1 cm²/V·s, a small threshold voltage of -0.9 V and a sharp switch on. This is the first time that the electrical characteristics of the SIP phase have been reported and the values obtained overpass the performance obtained in thin-films deposited by spin coating.

Other OFET architectures such as TCBG with Au and F4-TCNQ/Au electrodes were also studied to optimise the performance of the film as active layer. It was observed that in these architectures the presence of F4-TCNQ enhanced the performance of the devices by reducing the contact resistance. Furthermore, these devices displayed an enhancement of the performance over the first week after the fabrication that, after measuring the contact resistance using the Y-function method, was attributed to the reduction of the contact resistance.

Regarding the polymorph stability, a change in the film morphology was observed for the thin-film based on C8OBTBT with PS3K three months after the deposition. This new morphology was investigated by Raman spectroscopy and it was found that it corresponded to the bulk phase. Interestingly, the same effect was not observed in films based on C8OBTBT with PS100K, indicating the key role of the higher molecular weight PS to stabilise the SIP phase. This result opens new paths towards the control and stabilisation of OSCs polymorphism that could lead to the fabrication of more stable devices.

4.6. REFERENCES

- [1] A. Brillante, I. Bilotti, R. G. Della Valle, E. Venuti, S. Milita, C. Dionigi, F. Borgatti, A. N. Lazar, F. Biscarini, M. Mas-Torrent, N. S. Oxtoby, N. Crivillers, J. Veciana, C. Rovira, M. Leufgen, G. Schmidt, L. W. Molenkamp, *CrystEngComm* **2008**, *10*, 1899.
- [2] K. P. Goetz, J. Tsutsumi, S. Pookpanratana, J. Chen, N. S. Corbin, R. K. Behera, V. Coropceanu, C. A. Richter, C. A. Hacker, T. Hasegawa, O. D. Jurchescu, *Adv. Electron. Mater.* **2016**, *2*, 1600203.
- [3] R. Pfattner, M. Mas-Torrent, I. Bilotti, A. Brillante, S. Milita, F. Liscio, F. Biscarini, T. Marszalek, J. Ulanski, A. Nosal, M. Gazicki-Lipman, M. Leufgen, G. Schmidt, W. M. Laurens, V. Laukhin, J. Veciana, C. Rovira, L. W. Molenkamp, V. Laukhin, J. Veciana, C. Rovira, *Adv. Mater.* **2010**, *22*, 4198.
- [4] Y. Diao, K. M. Lenn, W. Y. Lee, M. A. Blood-Forsythe, J. Xu, Y. Mao, Y. Kim, J. A. Reinspach, S. Park, A. Aspuru-Guzik, G. Xue, P. Clancy, Z. Bao, S. C. B. Mannsfeld, *J. Am. Chem. Soc.* **2014**, *136*, 17046.
- [5] S. Galindo, A. Tamayo, F. Leonardi, M. Mas-Torrent, *Adv. Funct. Mater.* **2017**, *27*, 1700526.
- [6] T. Minari, M. Kano, T. Miyadera, S. D. Wang, Y. Aoyagi, K. Tsukagoshi, *Appl. Phys. Lett.* **2009**, *94*, 093307.
- [7] T. Minari, P. Darmawan, C. Liu, Y. Li, Y. Xu, K. Tsukagoshi, *Appl. Phys. Lett.* **2012**, *100*, 093303.
- [8] S. Georgakopoulos, A. Pérez-Rodríguez, A. Campos, I. Temiño, S. Galindo, E. Barrena, C. Ocal, M. Mas-Torrent, *Org. Electron.* **2017**, *48*, 365.
- [9] H. Jiang, X. Yang, Z. Cui, Y. Liu, H. Li, W. Hu, C. Kloc, *CrystEngComm* **2014**, *16*, 5968.
- [10] C. Zhang, Y. Zang, F. Zhang, Y. Diao, C. R. McNeill, C. an Di, X. Zhu, D. Zhu, *Adv. Mater.* **2016**, DOI 10.1002/adma.201602598.
- [11] H. Ebata, T. Izawa, E. Miyazaki, K. Takimiya, M. Ikeda, H. Kuwabara, T. Yui, *J. Am. Chem. Soc.* **2007**, *129*, 15732.
- [12] T. Izawa, E. Miyazaki, K. Takimiya, *Adv. Mater.* **2008**, *20*, 3388.
- [13] Y. Geng, R. Pfattner, A. Campos, W. Wang, O. Jeannin, J. Hauser, J. Puigdollers, S. T. Bromley, S. Decurtins, J. Veciana, C. Rovira, M. Mas-Torrent, S. X. Liu, *Chem. - A Eur. J.* **2014**, *20*, 16672.
- [14] C. Ruzié, J. Karpinska, A. Laurent, L. Sanguinet, S. Hunter, T. D. Anthopoulos, V. Lemaury, J. Cornil, A. R. Kennedy, O. Fenwick, P. Samorì, G. Schweicher, B. Chattopadhyay, Y. H. Geerts, C. Ruzié, J. Karpinska, A. Laurent, L. Sanguinet, S. Hunter, T. D. Anthopoulos, V.

- Lemaur, J. Cornil, A. R. Kennedy, O. Fenwick, P. Samorì, G. Schweicher, B. Chattopadhyay, Y. H. Geerts, *J. Mater. Chem. C* **2016**, *4*, 4863.
- [15] A. O. F. Jones, Y. H. Geerts, J. Karpinska, A. R. Kennedy, R. Resel, C. Röthel, C. Ruzié, O. Werzer, M. Sferrazza, *ACS Appl. Mater. Interfaces* **2015**, *7*, 1868.
- [16] N. Bedoya-Martínez, B. Schrode, A. O. F. Jones, T. Salzillo, C. Ruzié, N. Demitri, Y. H. Geerts, E. Venuti, R. G. Della Valle, E. Zojer, R. Resel, *J. Phys. Chem. Lett.* **2017**, *8*, 3690.
- [17] C. Ruzie, J. Karpinska, A. Laurent, L. Sanguinet, S. Hunter, T. D. Anthopoulos, V. Lemaur, J. Cornil, A. R. Kennedy, O. Fenwick, P. Samorì, G. Schweicher, B. Chattopadhyay, Y. H. Geerts, *J. Mater. Chem. C* **2016**, *4*, 4863.
- [18] B. Schrode, A. O. F. Jones, R. Resel, N. Bedoya, R. Schennach, Y. H. Geerts, C. Ruzié, M. Sferrazza, A. Brillante, T. Salzillo, E. Venuti, *ChemPhysChem* **2018**, *19*, 993.
- [19] A. Pérez-Rodríguez, I. Temiño, C. Ocal, M. Mas-Torrent, E. Barrena, *ACS Appl. Mater. Interfaces* **2018**, *10*, 7296.
- [20] I. Temiño, F. G. Del Pozo, M. R. Ajayakumar, S. Galindo, J. Puigdollers, M. Mas-Torrent, *Adv. Mater. Technol.* **2016**, *1*, 1600090.
- [21] F. G. Del Pozo, S. Fabiano, R. Pfattner, S. Georgakopoulos, S. Galindo, X. Liu, S. Braun, M. Fahlman, J. Veciana, C. Rovira, X. Crispin, M. Berggren, M. Mas-Torrent, *Adv. Funct. Mater.* **2016**, *26*, 2379.
- [22] O. Fenwick, C. Van Dyck, K. Murugavel, D. Cornil, F. Reinders, S. Haar, M. Mayor, J. Cornil, P. Samorì, *J. Mater. Chem. C* **2015**, *3*, 3007.
- [23] C. Liu, Y. Xu, Y. Y. Noh, *Mater. Today* **2015**, *18*, 79.
- [24] M. R. Niazi, R. Li, M. Abdelsamie, K. Zhao, D. H. Anjum, M. M. Payne, J. Anthony, D. M. Smilgies, A. Amassian, *Adv. Funct. Mater.* **2016**, *26*, 2371.
- [25] H. B. Akkerman, H. Li, Z. Bao, *Org. Electron. physics, Mater. Appl.* **2012**, *13*, 2056.
- [26] S. Hunter, A. D. Mottram, T. D. Anthopoulos, *J. Appl. Phys.* **2016**, *120*, 025502.
- [27] A. F. Paterson, S. Singh, K. J. Fallon, T. Hodsden, Y. Han, B. C. Schroeder, H. Bronstein, M. Heeney, I. McCulloch, T. D. Anthopoulos, *Adv. Mater.* **2018**, 1801079.
- [28] E. G. Bittle, J. I. Basham, T. N. Jackson, O. D. Jurchescu, D. J. Gundlach, *Nat. Commun.* **2016**, *7*, 10908.
- [29] M. H. Yoon, C. Kim, A. Facchetti, T. J. Marks, *J. Am. Chem. Soc.* **2006**, *128*, 12851.
- [30] M. R. Niazi, R. Li, E. Qiang Li, A. R. Kirmani, M. Abdelsamie, Q. Wang, W. Pan, M. M. Payne, J. E. Anthony, D. M. Smilgies, S. T. Thoroddsen, E. P. Giannelis, A. Amassian, *Nat. Commun.* **2015**, *6*, 8598.
- [31] P. Cosseddu, A. Bonfiglio, *Thin Solid Films* **2007**, *515*, 7551.

CHAPTER 4

- [32] C. Liu, T. Minari, X. Lu, A. Kumatani, K. Takimiya, K. Tsukagoshi, *Adv. Mater.* **2011**, *23*, 523.
- [33] D. Kumaki, T. Umeda, S. Tokito, *Appl. Phys. Lett.* **2008**, *92*, 013301.
- [34] Y. Xu, T. Minari, K. Tsukagoshi, J. A. Chroboczek, G. Ghibaudo, *J. Appl. Phys.* **2010**, *107*, 114507.
- [35] G. Lu, J. Blakesley, S. Himmelberger, P. Pingel, J. Frisch, I. Lieberwirth, I. Salzmänn, M. Oehzelt, R. Di Pietro, A. Salleo, N. Koch, D. Neher, *Nat. Commun.* **2013**, *4*, 1588.

CHAPTER 5 SOLUTION-PROCESSED OFETS BASED ON BLENDED *N*-TYPE SEMICONDUCTORS: THE ROLE OF THE POLYMER BINDER

5.1. INTRODUCTION AND OBJECTIVES

There has been a raising interest in the last decades in the area of organic electronics driven by the future applicability of these materials for low-cost, disposable and flexible technologies. With this goal in mind, a huge amount of small molecule organic semiconductors, both *p*- and *n*-type, have been synthesised and integrated as active material in OFETs.

However, the progress achieved with *p*-type OSCs outperforms that realized with *n*-type materials.^[1,2] This is mainly due to the lower stability of the radical anions formed upon injection of electrons into the OSC.^[3] Oxygen or water molecules penetrating into the OSC layer can easily oxidize the radical anions. Hence, it has been postulated that to achieve air stable *n*-channel OSCs, materials designed with electronic affinities (EA) around 4.0 eV are required.^[4] High EAs further help to inject efficiently electrons from conventional metal electrodes diminishing thus contact resistances. It should also be noticed that thin-film crystallinity and morphology also play a crucial role on the device stability since the physisorption of oxygen and moisture occurs mainly at grain boundaries.^[5,6] Another cause that hampers the development of *n*-type devices is derived from the fact that the hydroxyl groups present in the commonly used SiO₂ dielectric act as electron trapping centres.^[7] To avoid this, the passivation of the dielectric with hydrophobic self-assembled monolayers (SAMs) or with buffer polymeric layers has been pursued.^[8]

In the last years, synthetic chemists have tuned the properties of *n*-type OSCs by modifying the chemical structure to improve their performance, stability and processability.^[9–11] However, further work is needed in this direction since *p*- and *n*-type OSCs with similar performance are needed for their integration in circuits based on the so-called complementary metal-oxide semiconductor (CMOS) technology, which exhibits enhanced signal/noise ratio and lower power consumption.

Another current challenge in the field, which is shared with *p*-type OSCs, is the processability of the small molecule OSCs employing solution-based techniques. The preparation of

homogenous and reproducible thin-films over large areas is highly demanding due to the low viscosity of the solutions that leads to dewetting issues. As previously mentioned, in order to facilitate the processing of these materials and achieve uniform films, a promising route is to blend the OSC with an insulating polymer matrix.^[12–17] Further, this approach also often leads to films with an enhanced crystallinity, a higher environmental stability and a reduced number of interfacial traps at the semiconductor/dielectric interface.^[12,18–21] Recently, many efforts have been devoted to the deposition of OSCs blends using different coating techniques, but mainly employing *p*-type OSCs as active material.^[22] To our knowledge, only very few works report on the deposition by spin coating of blends of *n*-type or ambipolar small molecule OSCs.^[23–25]

Furthermore, the deposition of OSCs, especially *n*-type, is commonly performed under controlled environmental conditions inside a glove box with sub-ppm levels of water and oxygen. Even though these conditions can be met with the appropriate equipment, the cost of production would be increased which is undesirable for the development of an inexpensive technology. For this reason, OSCs able to be deposited in an open environment and that are not highly affected by the surroundings would be optimal for the implementation of organic electronics for mass-producing devices.

The main objective of the work developed in this chapter is to fabricate OFETs based on thin-films of the air-stable *n*-type OSCs tetracyanoquinodimethane (TCNQ) and N,N'-bis(*n*-octyl)-dicyanoperylene-3,4:9,10-bis(dicarboximide) (PDI8CN2) using a solution shearing technique (*i.e.* BAMS) in an ambient conditions to deposit the active materials. Particular emphasis was placed to understand the role of the insulating polymer matrix in the latter case.

5.2. OFETS PREPARED BY BAMS EMPLOYING BLENDS OF TCNQ:PS

The *n*-type organic semiconductor TCNQ (**Figure 5.1**) is a well-studied organic semiconductor. However, in most works it has been used as a low reduction potential molecule ($EA \approx 4.8$ eV) for producing organic charge transfer salts such as the well-known metallic charge-transfer salt tetrathiafulvalene-tetracyanoquinodimethane (TTF-TCNQ) discovered back in 1973.^[26] Nonetheless, encouraged by the high mobility displayed in single-crystal OFETs reaching values beyond $1 \text{ cm}^2/\text{V}\cdot\text{s}$,^[27,28] TCNQ was employed here as *n*-type organic semiconductor. Particularly appealing was the fact that TCNQ is a fairly soluble molecule, so can be potentially processed from solution.

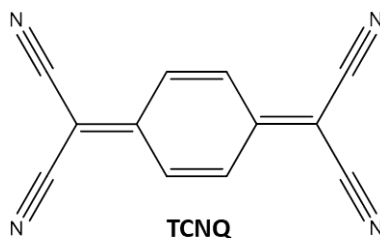


Figure 5.1. TCNQ chemical structure.

Herein, TCNQ has been used as *n*-type OSC probe to study the viability of processing this type of semiconductors, as previously mentioned, together with insulating polymers in ambient conditions using BAMS. Hence, the main focus of this part of the work was to perform a screening of the deposition parameters to achieve an optimised device performance. The films were mostly evaluated by the electrical characterisation of the transistors and by comparing the OFET parameters with the thin-film morphology. The main deposition and formulation-related parameters investigated here were the OSC:polymer ratio, coating temperature, deposition speed, solvent and polymer.

Firstly the OSC:polymer ratio was investigated, taking as starting point the formulation and coating parameters that we optimised previously for dibenzotetrathiafulvalene (DB-TTF): DB-TTF:PS3k 1:2; 2% wt.; chlorobenzene (CB); 105 °C and 10 mm/s.^[19] Fixing all the other parameters, the ratios 1:3, 1:2 and 1:1 were tested keeping the concentration of the final solution at 2% wt. Cross-Polarised Optical Microscope (CPOM) images in **Figure 5.2** show that when the relative amount of TCNQ is increased, the crystallites form bigger planar crystals (1:1), whereas when the amount of TCNQ is lower, the TCNQ crystals tend to be more needle-like shaped. All transistors fabricated with these formulations exhibited *n*-type OFET behaviour, however, 1:2 formulation presented the best OFET parameters with an average $\mu_{FE,sat} = 3 \cdot 10^{-4} \text{ cm}^2/\text{V}\cdot\text{s}$ and an average $V_{TH} = -0.3$ V. All the values of $\mu_{FE,sat}$ and V_{TH} of the three formulations are collected in **Figure 5.2d-e**.

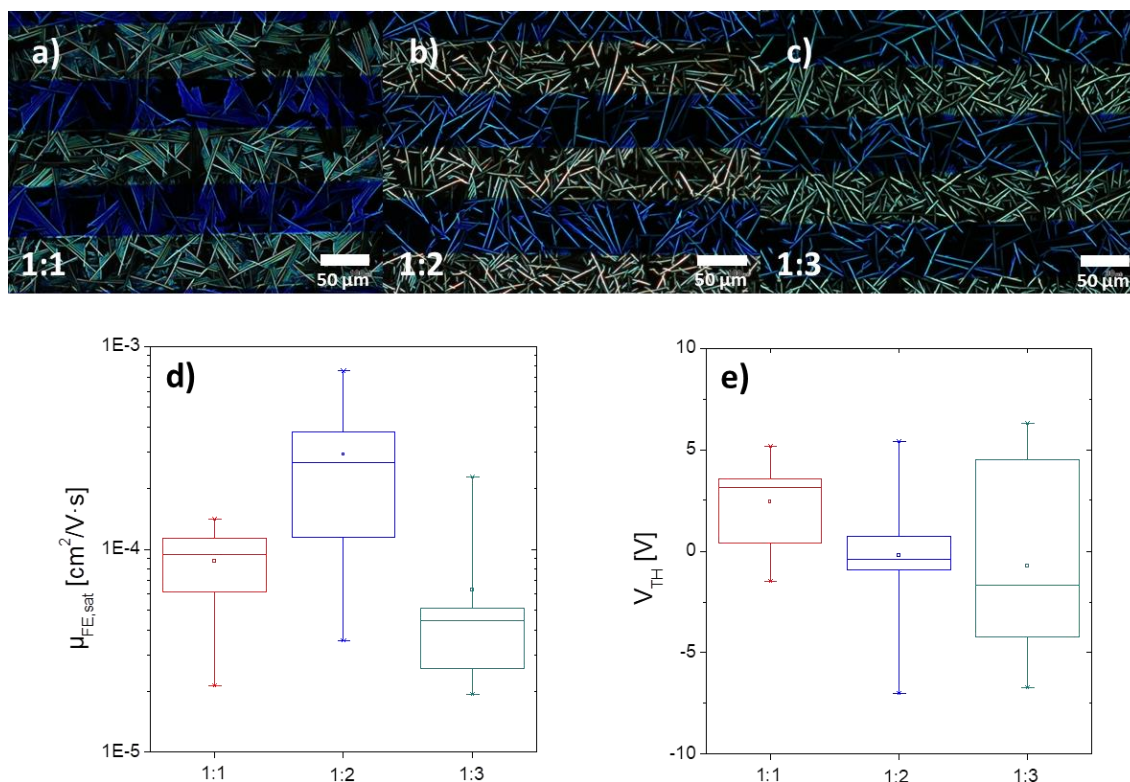


Figure 5.2. Crossed-Polarised Optical Microscope (CPOM) images of the formulation TCNQ:PS3k (a) 1:1, (b) 1:2 and (c) 1:3; CB; 2% wt.; 105 °C; 10 mm/s. (d) and (e) display the statistics of the measured mobility and threshold voltage, respectively.

Taking the most optimum TCNQ:PS3k ratio 1:2, the effect of the substrate temperature was investigated. In the deposition of organic semiconductors, temperature controls, among other interesting effects, the evaporation rate of the solvent and the solubility of the usually hardly soluble small-molecule organic semiconductor. In addition, it has been observed that in molecules exhibiting polymorphism a different deposition temperature can produce films with different crystal phases.^[29] In this case, temperatures ranging from 70 to 95 °C were chosen. CPOM images of the resulting films show that when the temperature is decreased, the formed crystals are bigger and change from needle-like crystals at 95 °C, to plate-shaped crystals at 70 °C (**Figure 5.3**). In agreement with the morphology, the OFETs fabricated at lower temperature present better mobility, up to $5 \cdot 10^{-4}$ cm²/V·s. We suggest that the formation of larger domains is caused by the slower evaporation of the solvent permitting the TCNQ molecules reorganise better. However, even though we have seen a clear effect in the morphology, the deposition temperature change did not affect significantly the device performance (**Figures 5.3g** and **5.3h**).

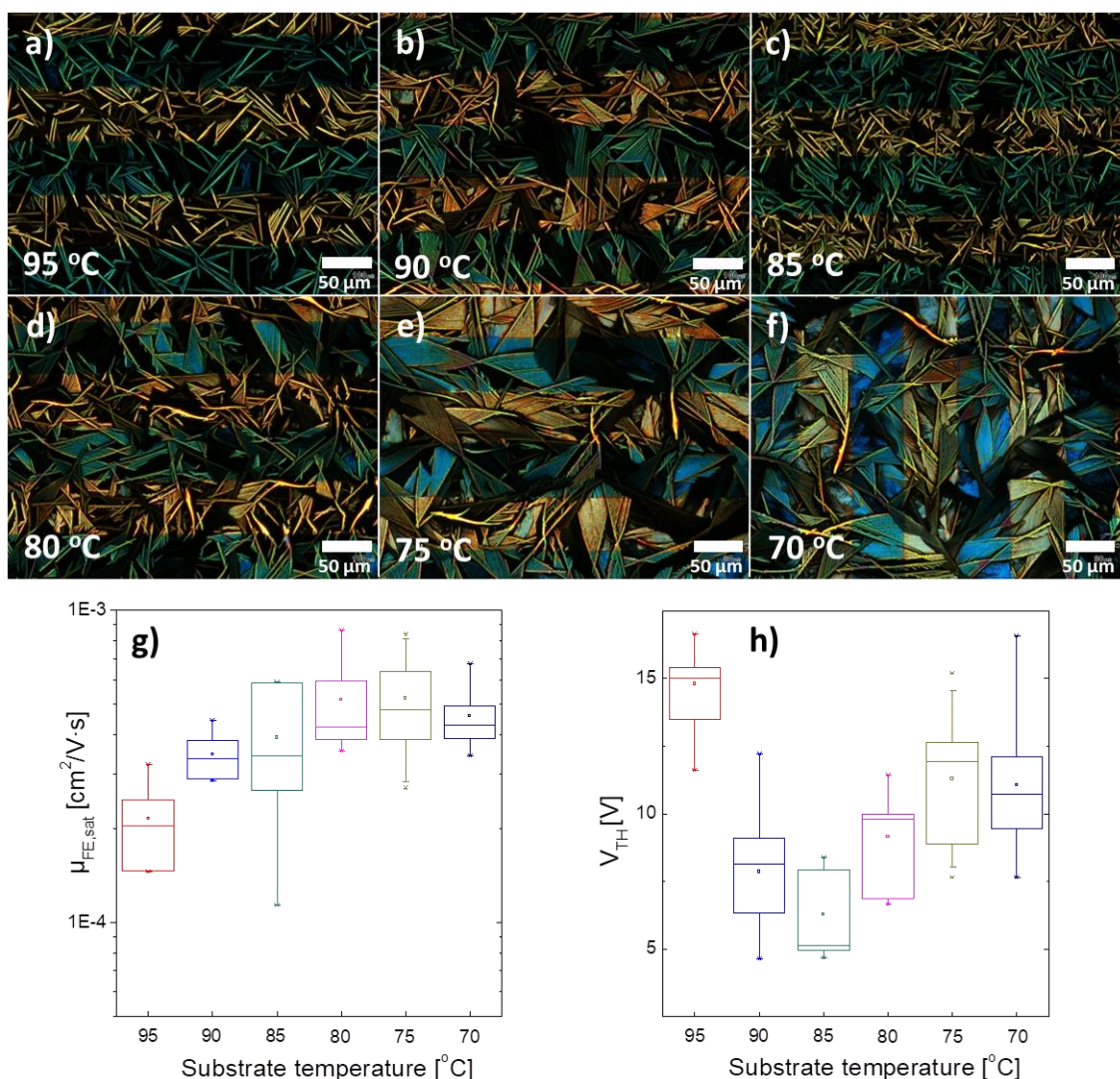


Figure 5.3. CPOM images of the formulation TCNQ:PS 3k 1:2; CB; 2% wt.; 10 mm/s; deposited at (a) 95, (b) 90, (c) 85, (d) 80, (e) 75 and (f) 70 °C. (g) and (h) display the statistics of the measured mobility and threshold voltage, respectively.

Having found the optimum temperature for the deposition of the TCNQ formulation (75 °C), the velocity of the bar, which also controls the solvent evaporation rate and hence the crystallisation, was investigated. Two speeds, 1 and 10 mm/s, were chosen. The resulting films are shown in **Figure 5.4**. With the slower speed, large crystalline domains were formed but, instead of producing randomly oriented polycrystalline films as it happened with the 10 mm/s speed, the crystallites were aligned along the casting direction. The lines that can be observed in the Optical Microscope (OM) image of the film fabricated at 1 mm/s (**Figure 5.4b**) are probably caused by a non-continuous movement of the bar. So, the different colours are probably related to different film thickness in the different zones. The electronic transport anisotropy of the crystalline domains was further investigated by fabricating TCNQ films on substrates that contained transistors with the channel aligned in parallel and in perpendicular to the bar movement. Mobility and threshold voltage values for the parallel and perpendicular OFETs are shown in **Table 5.1**. Surprisingly, even for the 10 mm/s bar velocity, the parallel

transistors displayed mobility values approximately two times higher than the perpendicular OFETs. On the other hand, as expected from the film morphology, when the bar speed was set at 1 mm/s the mobility measured in the parallel devices was found to be 10 times higher than in the perpendicular transistors, reaching an average mobility of $4 \cdot 10^{-3} \text{ cm}^2/\text{V}\cdot\text{s}$.

Table 5.1. μ and V_{TH} average values of the OFETs fabricated with the formulation TCNQ:PS3k 1:2 at 75 °C that was used for the speed screening and anisotropy test.

Speed/Orientation	$\mu_{FE,sat} [\text{cm}^2/\text{V}\cdot\text{s}]$	$V_{TH} [\text{V}]$
10 mm·s ⁻¹ / Parallel	$(3.8 \pm 2.2) \cdot 10^{-4}$	1.8 ± 0.3
10 mm·s ⁻¹ / Perpendicular	$(1.6 \pm 0.8) \cdot 10^{-4}$	1.7 ± 1.1
1 mm·s ⁻¹ / Parallel	$(3.0 \pm 1.4) \cdot 10^{-3}$	4.7 ± 2.4
1 mm·s ⁻¹ / Perpendicular	$(2.8 \pm 1.7) \cdot 10^{-4}$	5.9 ± 3.4

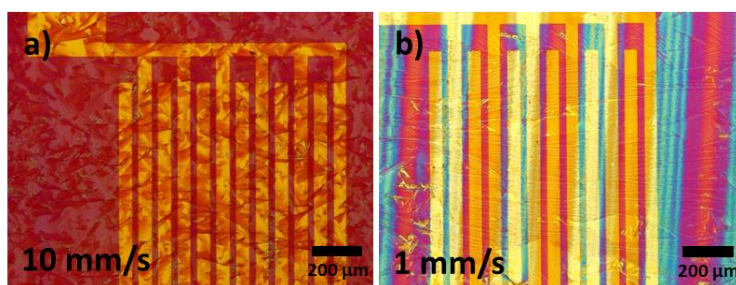


Figure 5.4. Optical microscope (OM) images of TCNQ:PS3k 1:2 films fabricated at 75 °C and at a bar speed of (a) 10 mm/s and of (b) 1 mm/s.

To further optimise the final TCNQ formulation, solvents other than CB were tested and, in order to have an isotropic film, the bar velocity was kept at 10 mm/s with the TCNQ:PS3k ratio 1:2. The solvents chosen for this screening were anisole, *o*-dichlorobenzene, tetralin, decalin and dimethylacetamide. According to the higher boiling point of these solvents, the coating temperature was increased to 105 °C so as to stay in the same deposition regime. The most homogeneous resulting films achieved are shown in **Figure 5.5**. Among the films shown, only the ones prepared from solutions of chlorobenzene and anisole worked properly. The best performance was obtained with films based on anisole displaying a mobility of $1 \cdot 10^{-3} \text{ cm}^2/\text{V}\cdot\text{s}$ (approximately 2-3 times the values obtained for CB) and a similar threshold voltage of around 8 V.

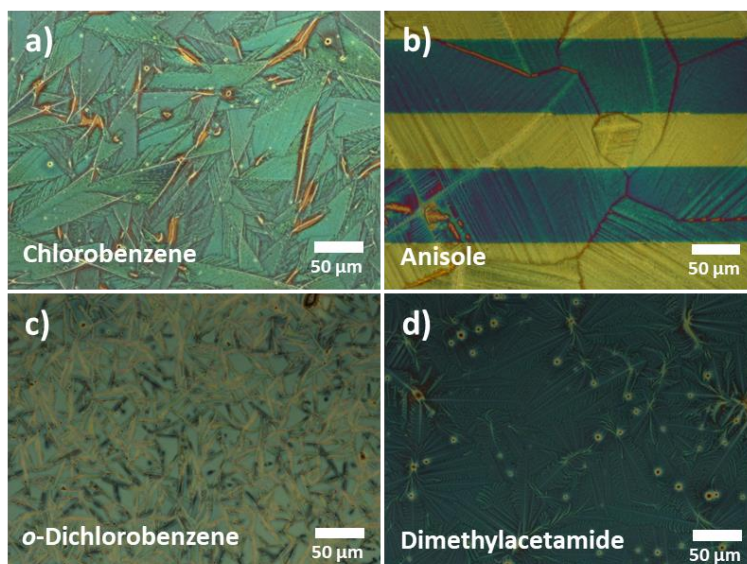


Figure 5.5. OM images of TCNQ:PS3k 1:2 films fabricated at 75 °C and at a bar speed of 10 mm/s based on (a) chlorobenzene, (b) anisole, (c) *o*-dichlorobenzene and (d) dimethylacetamide.

Finally, three different molecular weights of PS were investigated: 3k, 10k and 280k. We observed that increasing the molecular weight of the polymer had a beneficial effect in the film processability due to an increase in the viscosity. Thus, the homogeneity of the films was improved. Highly crystalline thin-films as depicted in the CPOM images of **Figure 5.6** were obtained with PS280k formulations. In addition, these films presented the highest performance obtained for TCNQ in this work, found for TCNQ:PS280k ratio 3:1, displaying an average mobility of $2 \cdot 10^{-3} \text{ cm}^2/\text{V}\cdot\text{s}$. Transfer and output characteristics of the TCNQ:PS280k ratio 3:1 film is shown in **Figure 5.7** Other formulations mobility and threshold voltage values are shown in form of box-and-whisker plot in **Figure 5.6f** and **Figure 5.6g**. Also, as it was checked before for the speed screening test, an anisotropy test for the electron mobility was performed. The test results indicated that the mobility of the transistors with the channel parallel to the coating were two-fold the mobility of the perpendicular devices as depicted in **Figure 5.6h**. Such anisotropy was similar as the one previously found for the PS3k formulations.

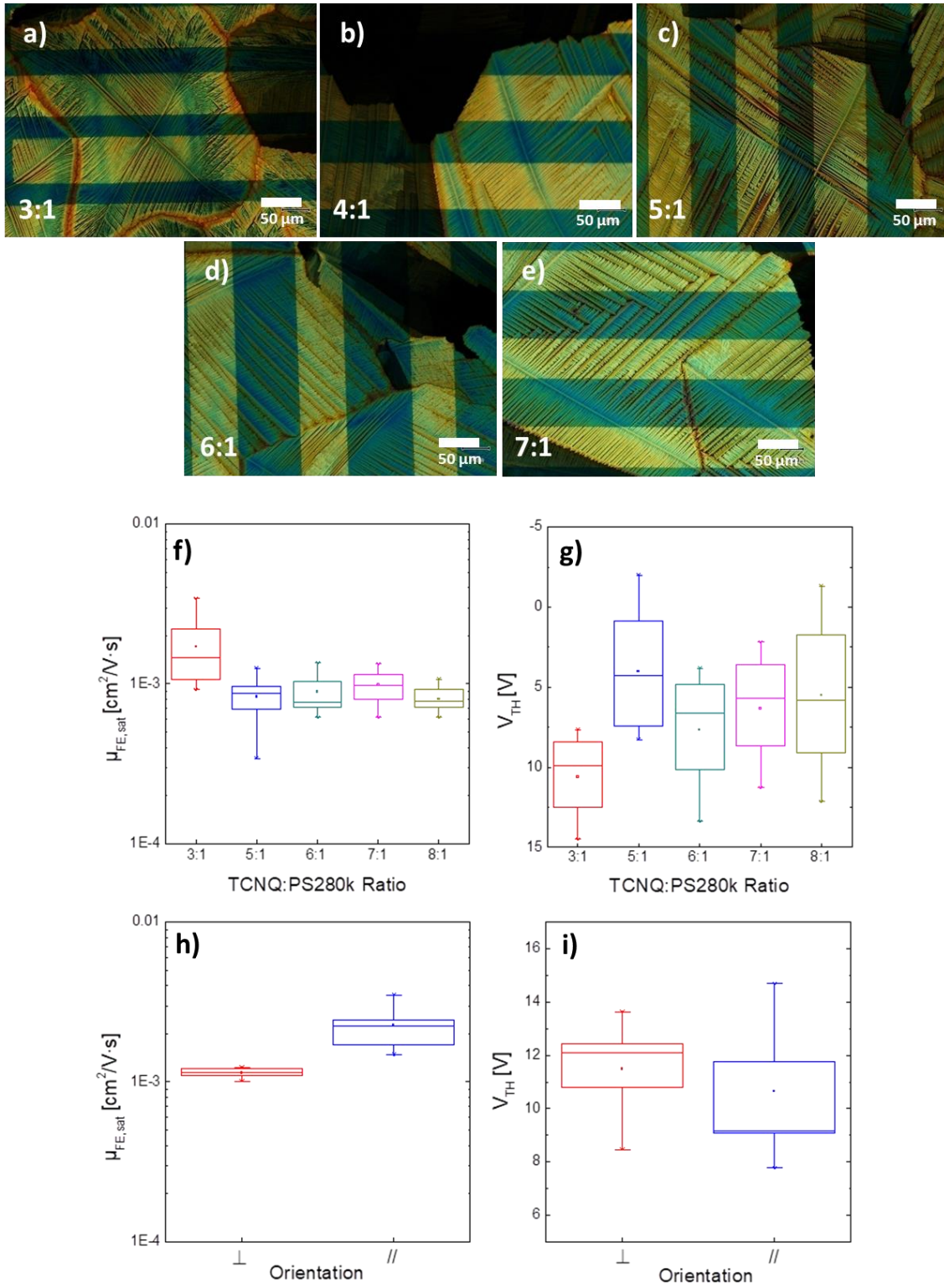


Figure 5.6. CPOM images of the thin-films deposited with the formulations TCNQ:PS280k (a) 3:1, (b) 4:1, (c) 5:1, (d) 6:1 and (e) 7:1, respectively. All formulations used anisole as solvent and the ink was deposited at 105 °C and 10 mm/s. (f) and (g) depict the mobility and threshold voltage, respectively, of the OFETs fabricated with the different OSC:polymer ratios. (h) and (i) indicate the mobility and threshold voltage, respectively, of the transistors oriented with the channel perpendicular (\perp) and parallel (\parallel) to the coating direction.

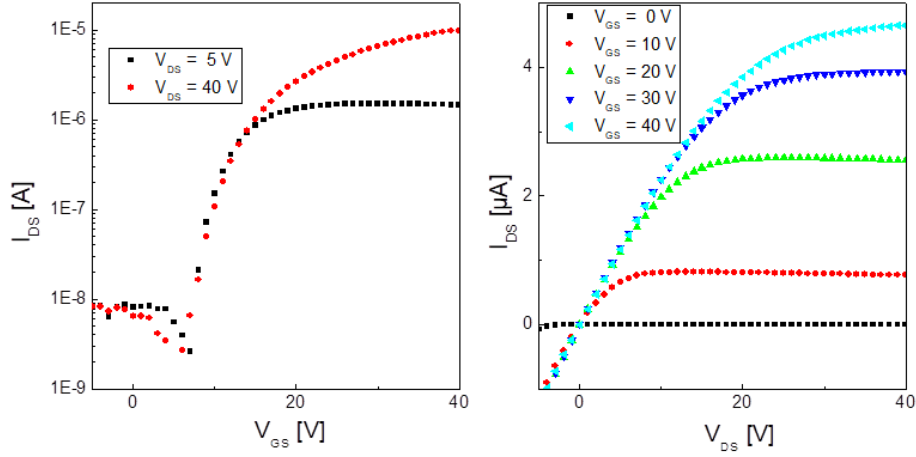


Figure 5.7. **(a)** Transfer and **(b)** output characteristics of the optimised formulation: TCNQ:PS280k; 3:1; 2% wt.; Anisole; 105 °C and 10 mm/s.

SHELF STABILITY

The shelf stability of these optimised devices was investigated by measuring them along time while the sample was kept in air and darkness. **Figure 5.8a** shows the mobility decay over a period of 34 days reaching the 30% of the initial value in the last day. Also interesting is the behaviour of the threshold voltage (depicted in **Figure 5.8b**) that only shifted a few volts in the whole period, indicating a good stability in ambient conditions. The enhanced stability can be attributed to the PS protecting the organic semiconductor.

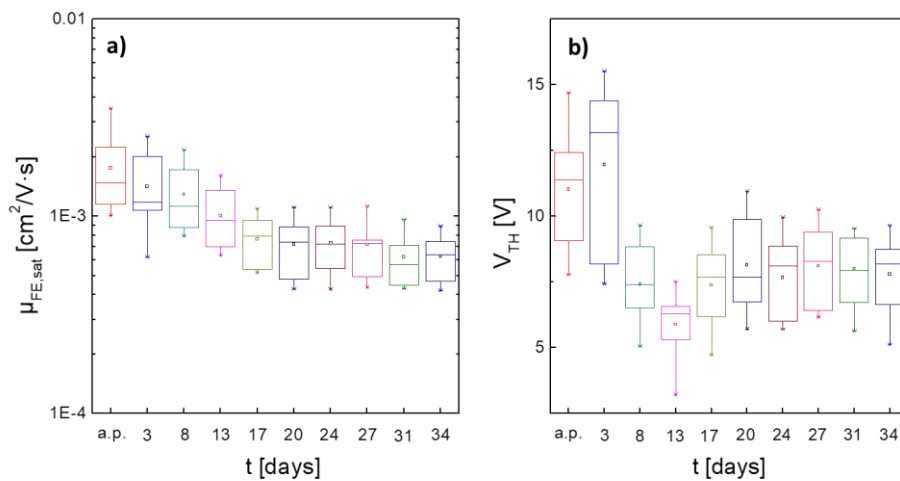


Figure 5.8. **(a)** $\mu_{FE,sat}$ and **(b)** V_{TH} measured in the as prepared (a.p.) devices and in different days after the thin-film fabrication. The devices were stored in ambient conditions and darkness. These thin-films were deposited using the optimised formulation: TCNQ:PS280k; 3:1; 2% wt.; Anisole; 105 °C and 10 mm/s.

CHAPTER 5

In this part of the thesis, we succeed in fabricating for the first time thin-films OFETs based on the *n*-type OSC TCNQ processed from solution with a solution shearing technique. Despite these encouraging results, at this point we decided to move to another benchmark *n*-type OSC in order to achieve an improved device performance.

5.3. OFETS PREPARED BY BAMS EMPLOYING BLENDS OF PDI8CN2:PS¹

Perylene bisimide (PDI) and naphthalene bisimide (NDI) derivatives have shown great potential as *n*-type OSCs.^[30–32] Particularly, in the present work, we selected the derivative PDI8CN2 (**Figure 5.9**) since it exhibits a good solubility and air stability due to its high EA and has given rise to high performance OFETs.^[11,33]

Herein, we fabricated OFETs based on thin films of PDI8CN2 deposited by BAMS and we explored the influence of adding PS as polymer matrix on the resulting device electrical properties. To better understand the influence of the binder polymer matrix on the device performance, pristine PDI8CN2 thin-films were also fabricated. The preparation of pristine PDI8CN2 films could be achieved due to the better solubility of PDI8CN2 compared with TCNQ, being possible to prepare solutions with concentrations exceeding 20 mg/mL in hot CB.

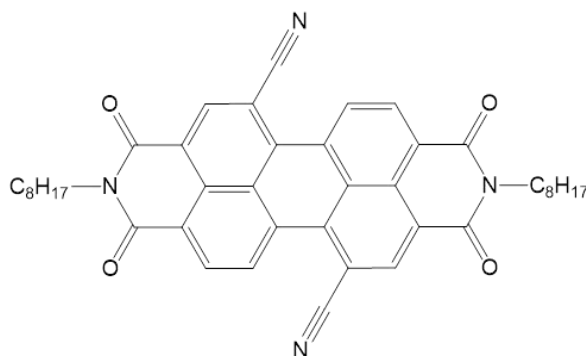


Figure 5.9. PDI8CN2 molecular structure.

OPTIMISATION OF THE PDI8CN2 FORMULATION

Solutions based on PDI8CN2 in chlorobenzene 2% wt. were prepared. In order to explore the effect of a matrix insulator two formulations were employed, one containing only the OSC and another one blended with PS. All formulations were deposited by BAMS at 10 mm/s and 105 °C, leading to continuous and homogenous crystalline films. Opposite to the results obtained for TCNQ, here varying the formulation did not have a noticeable impact on the thin-film morphology. All the films independently of the polymer and ratio employed looked similar to the one shown in **Figure 5.10**. After experimental optimisation varying the polymer, the polymer molecular weight and the OSC:PS ratio, the most optimum formulation was chosen to be PDI8CN2:PS280k in a ratio 1:2 (**Table 5.3**). From the mobility and threshold values

¹ This work has been published in Campos, A. *et al.* *ACS Appl. Mater. Interfaces* **2018**, *10*, 15952–15961.

collected in **Table 5.3**, it can be concluded that the performance of PDI8CN2-based films was hardly affected by the polymer nature.

Table 5.3. Mobility and threshold voltage values of the formulations tested to find the optimised film. PMMA, PαMS and PS are the acronyms for polymethylmethacrylate, poly(α-methyl)styrene and polystyrene, respectively.

#	Polymer - M_w [g/mol]	Ratio OSC:Polymer	$\mu_{FE,sat}$ [$cm^2/V\cdot s$]	V_{TH} [V]
1	—	—	$(5.5 \pm 0.5) \cdot 10^{-3}$	-8.4 ± 1.2
2	PMMA – 120k	4:1	$(1.3 \pm 0.1) \cdot 10^{-2}$	-7.2 ± 1.1
3	PMMA – 120k	1:1	$(1.1 \pm 0.1) \cdot 10^{-2}$	-9.3 ± 1.0
4	PαMS – 100k	4:1	$(8.4 \pm 2.1) \cdot 10^{-3}$	-15.6 ± 3.8
5	PαMS – 100k	1:1	$(4.6 \pm 0.4) \cdot 10^{-2}$	-8.8 ± 0.9
6	PS – 280k	4:1	$(1.9 \pm 0.3) \cdot 10^{-2}$	-4.3 ± 0.4
7	PS – 280k	1:1	$(2.4 \pm 0.3) \cdot 10^{-2}$	-1.5 ± 0.2
8	PS – 280k	1:2	$(2.8 \pm 0.3) \cdot 10^{-2}$	-0.9 ± 0.1
9	PS – 3k	1:2	$(1.2 \pm 0.5) \cdot 10^{-2}$	-1.1 ± 0.4

Considering all these tests, we selected formulation 8 (*i.e.* PDI8CN2:PS280k 1:2) as the most optimum blended formulation. At this point we performed an in-depth thin film characterisation of films of bare PDI8CN2 and of the optimised blended formulation (from now on simply named after PDI8CN2:PS).

THIN-FILM CHARACTERISATION

The thin film morphology of PDI8CN2 and PDI8CN2:PS films were characterized by CPOM, AFM and XRPD as shown in **Figure 5.10**, **5.11** and **5.12**, respectively. Both films are polycrystalline and their domain sizes are alike (**Figure 5.10**). However, AFM images show that grain boundaries are well defined in the PDI8CN2 film in contrast to the PDI8CN2:PS sample. This is due to the fact that in the latter case a few nm thick (around 2.5 nm; average value estimated from the analysis of more than 10 pores from 3 different AFM images) of a non-continuous layer can be differentiated on the top of the crystallites (**Figure 5.11**). Such thin skin layer can be ascribed to a PS layer which covers the PDI8CN2 polycrystalline film, as previously observed with other *p*-type OSCs.^[34] Also, X-ray diffraction confirms that the crystalline phase of the two films is the same (**Figure 5.12**), which matches the previously reported single crystal structure.^[35]

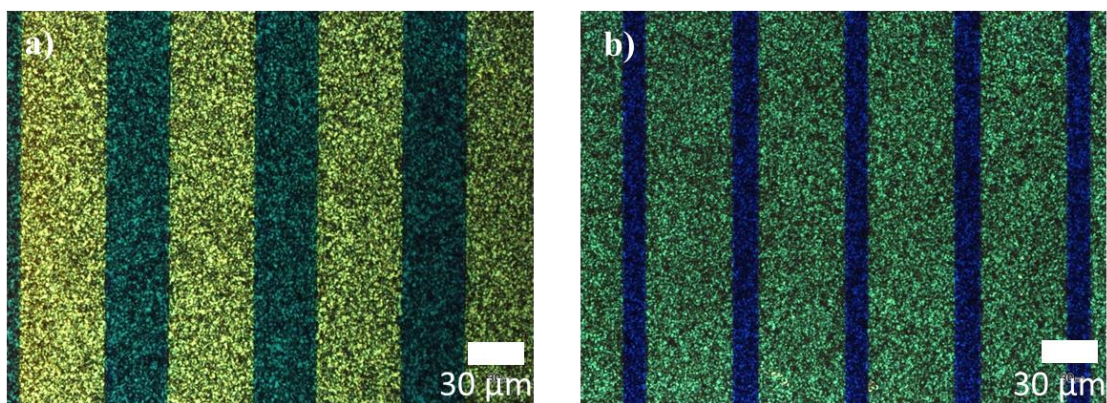


Figure 5.10. CPOM images of (a) PDI8CN2 and (b) PDI8CN2:PS films.

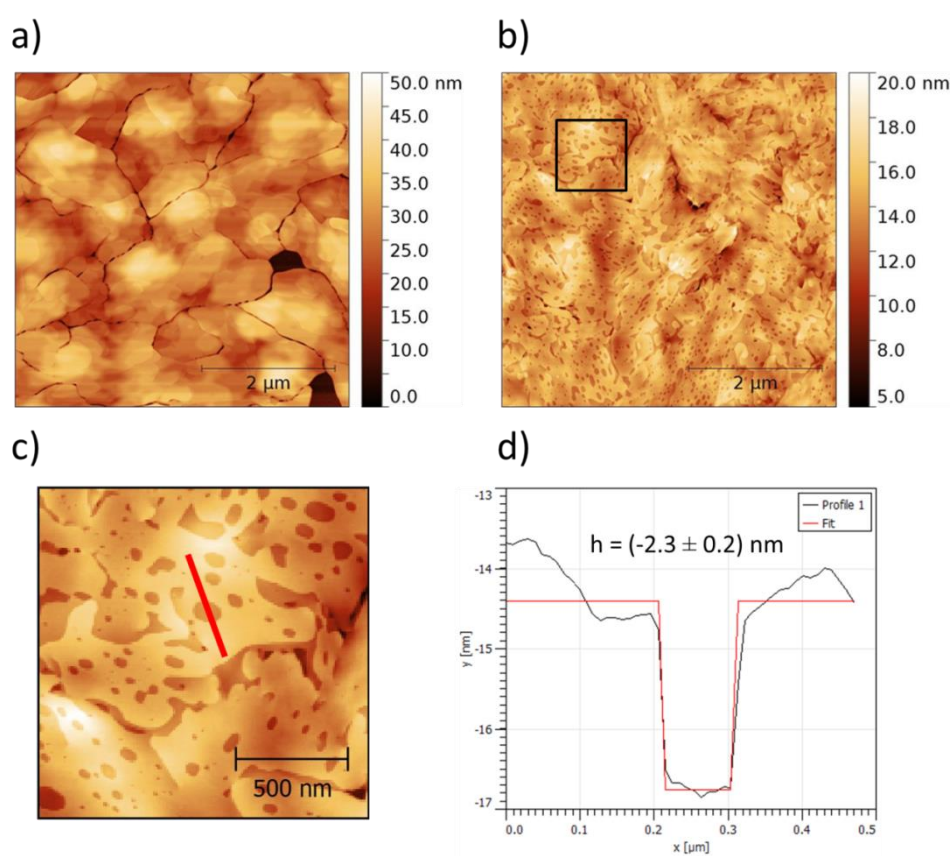


Figure 5.11. AFM topography images of (a) PDI8CN2 and (b) PDI8CN2:PS film. A zoom of the PDI8CN2:PS is shown in (c) to clarify where the height profile (d) was taken. A hole of approx. 2.3 nm can be appreciated in the height profile caused by a discontinuity in the PS skin layer covering the PDI8CN2 crystals.

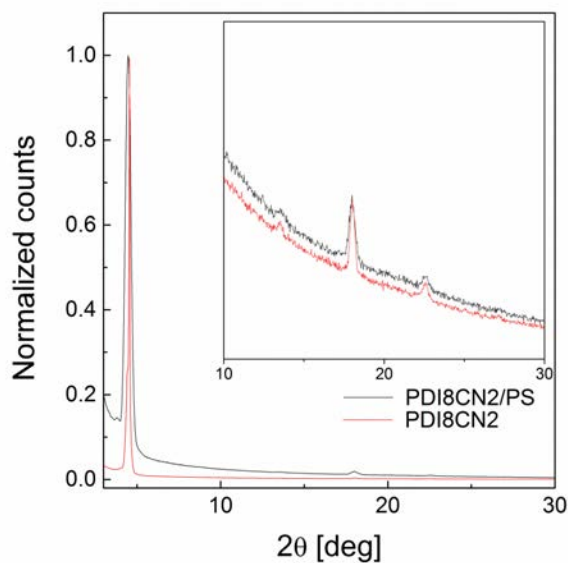


Figure 5.12. X-Ray Powder Diffraction (XRPD) measurements of PDI8CN2 and PDI8CN2:PS films.

The thickness of PDI8CN2 films, measured with AFM, were found to be (20 ± 10) nm for PDI8CN2 films with a roughness (R_{rms}) of 5.2 nm, while PDI8CN2:PS films were (35 ± 5) nm thick with a R_{rms} of 1.9 nm (**Figure 5.13**). Therefore, the addition of PS causes a thicker and smoother film.

Furthermore, ToF-SIMS measurements performed at different film depths indicate a major content of nitrogen on the top part of the film, which is in accordance with a vertical phase separation of the two materials, where the PS is in contact with the dielectric surface and the crystalline PDI8CN2 film lies on top (**Figure 5.14**). Such stratification during the OSC crystallization has been commonly observed in other blends.^[13,18] From the ToF-SIMS data the thickness of the PDI8CN2 film sitting on top of the PS layer can also be roughly estimated to be around 10 nm.

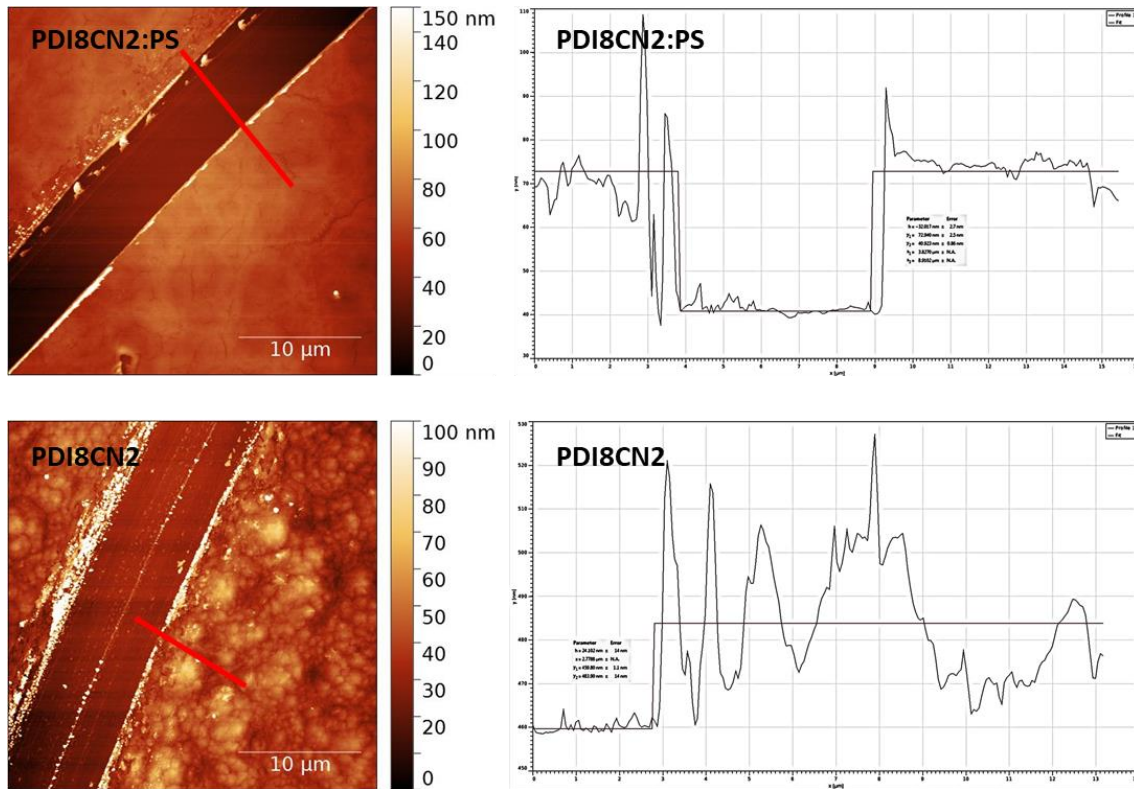


Figure 5.13. On the left, AFM images showing the scratch where the PDI8CN2-based films thickness' was measured. The red line indicates approximately where the profile was obtained. On the right, the profiles that were used to extract the films thickness'.

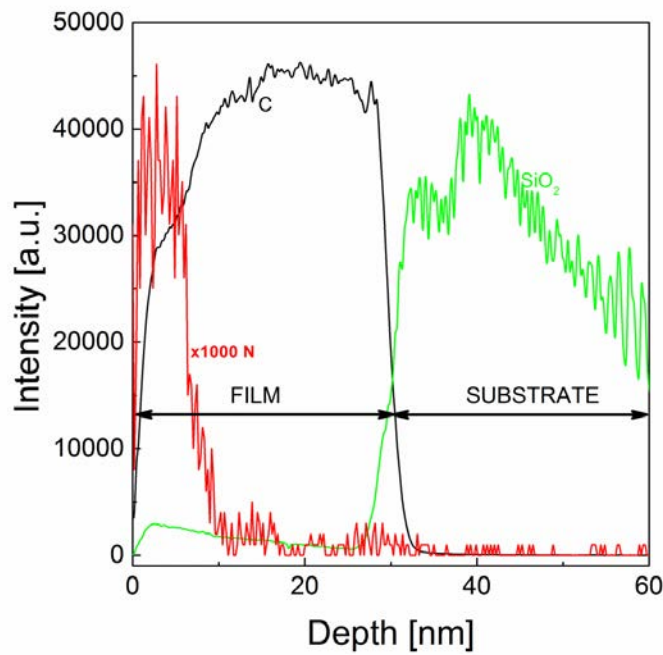


Figure 5.14. ToF-SIMS graph of the PDI8CN2:PS film. This graph confirms that there is a vertical phase separation with a PDI8CN2 top layer and a thicker PS layer underneath. The signal of the N has been increased x1000 so the phase separation can be observed.

Typical saturation transfer curves for PDI8CN2 and PDI8CN2:PS devices are shown in **Figure 5.15a** and **5.15b**, and the corresponding output curves are collected in **Figure 5.15c** and **5.15d**. The main parameters of the OFETs based on PDI8CN2 and PDI8CN2:PS are summarized in **Table 5.4**. Comparison of both transfer curves clearly shows an improvement in the performance of PDI8CN2:PS devices with an increase of the field effect mobility ($\mu_{FE,sat}$), a decrease of the threshold voltage (V_{TH} closer to 0 V), a higher on/off ratio, an improved sub-threshold swing (SS) and a reduced hysteresis. Particularly, the significant improvement in SS and V_{TH} can be attributed to a decreased interfacial charge trap density (N_T), which is directly proportional to SS and has been estimated using the equation shown in Chapter 3.^[36]

It is observed that the introduction of PS reduces about one order of magnitude the N_T (from $1.51 \cdot 10^{12} \text{ eV}^{-1} \text{ cm}^{-2}$ to $1.63 \cdot 10^{11} \text{ eV}^{-1} \text{ cm}^{-2}$). The lower interfacial charge trap density is also reflected in the reduced hysteresis in the transfer and output characteristics (**Figure 5.15**). Further, it should be noticed that the clear increase in the field-effect mobility found in the PDI8CN2:PS devices could be due to the lower interfacial traps present, although dielectric depolarization effects caused by the lower permittivity PS layer might have also an impact reducing the polaronic disorder.^[37,38]

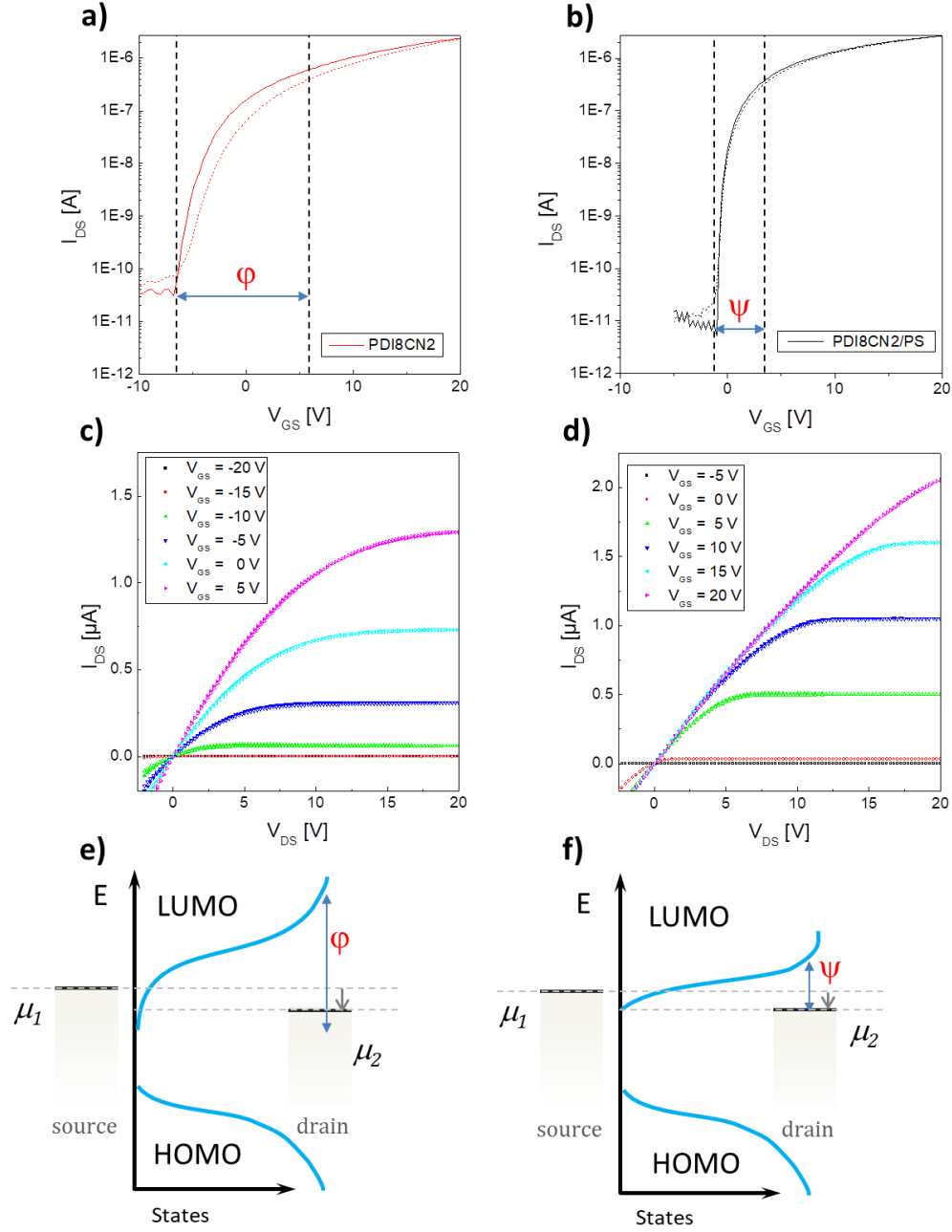


Figure 5.15. Transfer (a) and output (c) characteristics, respectively, of OFETs based on PDI8CN2. Transfer (b) and output (d) characteristics of OFETs based on PDI8CN2:PS. All transfer characteristics are depicted with a $V_{DS} = 20$ V. Continuous/dashed lines correspond to the forward/backward sweep of V_{GS} voltages. Bottom curves show a representation of the density of states (DoS) in a logarithmic scale of the active region of the OFET (e) without and (f) with PS.

Table 5.4. Main OFET parameters extracted from PDI8CN2 and PDI8CN2:PS based devices. The data shown are an average of 50 devices in both cases.

	$\mu_{FE,sat}$ [$\text{cm}^2/\text{V}\cdot\text{s}$]	V_{TH} [V]	$I_{ON/OFF}$	SS [V/decade]	N_T [$\text{eV}^{-1}\text{cm}^{-2}$]	τ (s)	θ
PDI8CN2	$(5.5 \pm 0.5) \cdot 10^{-3}$	-8.4 ± 1.2	$3 \cdot 10^5$	0.90 ± 0.30	$1.51 \cdot 10^{12}$	$3.4 \cdot 10^3$	0.80
PDI8CN2:PS	$(2.8 \pm 0.3) \cdot 10^{-2}$	-0.9 ± 0.1	$8 \cdot 10^4$	0.15 ± 0.03	$1.63 \cdot 10^{11}$	$6.6 \cdot 10^5$	0.25

At equilibrium, source and drain contacts and the semiconductor have the same electrochemical potential. In the particular case of an *n*-type OSC, the application of positive V_{DS} shifts the electrochemical potential at the contacts ($\mu_2 - \mu_1 = qV_{DS}$), so then electrons can flow from source to drain contacts in order to equilibrate the electrochemical potential of the whole system. Electron transport from source to drain contacts is realized through electronic states located on the semiconductor close to the interface with the dielectric material. The distribution of the density-of-states (DoS) on the proximity of the LUMO level determines hence the overall electronic performance of the device. The application of V_{GS} shifts the DoS to lower (for a positive V_{GS} values) or higher (negative V_{GS} values) energy values. Positive V_{GS} increases the number of available electronic states between source-drain contacts, *i.e.* higher I_{DS} current, whereas the application of a negative V_{GS} voltage decreases the number of available states, decreasing I_{DS} . Considering this, a careful analysis of the transfer characteristics of an OFET provide a qualitative picture of the distribution of electronic states in the vicinity of the mobility edge, near the LUMO energy level in an *n*-type OSC.

Figure 5.15e-f shows a schematic view of a plausible distribution of the DoS near the LUMO level according to the transfer characteristics showed in **Figure 5.15a-b**. Without the addition of PS (**Figure 5.15e**) the shape of the DoS could be described with two regions: a region with a high density of electronic states plus a region with a band-tail distribution of states extending within the band-gap of the semiconductor. The exact distribution of the region with a high density of electronic states is an open question. Whereas some authors describe this region as a Gaussian distribution of electronic states,^[39] others consider that an exponential distribution would be more accurate.^[40] For the sake of clarity, we consider here an exponential distribution. When PS is added (**Figure 5.15f**), the distribution of electronic states is modified. The slope of the exponential region is increased ($\varphi > \psi$ in **Figure 5.15**), whereas the band-tail distribution is reduced. Increase in the slope of the exponential region accounts for the improved SS value,^[41] whereas the reduction of the band-tail distribution is responsible for the lower value of the I_{DS} current in the off state of the OFET when PS is added.

The lower V_{TH} reduction found in devices where PDI8CN2 was blended with PS (*i.e.*, V_{TH} closer to 0 V (**Table 5.5**)) can be explained by the DoS shift to lower energetic levels and the reduction of band tail states. Otherwise, PDI8CN2 devices are normally ON (when $V_{GS} = 0$ V) because there are energetic sites in the semiconductor between the energies of the electrochemical potentials of the source and drain.

BIAS STRESS STABILITY

Bias stress measurements, that is, the study of the stability of OFETs under operation, provide useful information about the reliability of the devices. Typically, under bias stress a threshold voltage shift is observed, which has been attributed to the entrapment of mobile charge carriers in localized electronic states at the OSC/dielectric interface.^[42] The generation of such states in OFETs can arise from extrinsic factors such as oxidation or moisture, or intrinsic factors such as the electronic and structural disorder of the OSC films.^[43] Hence, bias stress is very sensitive to the OSC/dielectric interface quality.^[42] Most of the studies related to bias stress have been carried out on *p*-type OFETs rather than *n*-type ones.^[44–47]

The bias stress measurements of PDI8CN2 and PDI8CN2:PS OFETs were carried out in ambient conditions at constant bias voltage V_{GS} of 20 V and V_{DS} of 0 V between transfer measurements. V_{GS} was chosen in order to switch on the transistor ($V_{GS} \gg V_{TH}$). Transfer characteristics were measured for 12 hours, every 15 minutes in the first 4 hours and every hour afterwards (**Figure 5.16a-b**). The V_{TH} variation in time is shown in **Figure 5.16c**. Remarkably, PDI8CN2:PS OFET undergoes a much lower shift ($\Delta V_{TH} = 7$ V) than that observed for PDI8CN2, which saturates at 25 V after only 5 hours of measurements. The ΔV_{TH} in OFETs due to bias stress has been correlated in the literature with N_T , since the trapped charges create an electric field that has to be compensated by the gate bias before an accumulation layer can be formed.^[48] Our results are in agreement to the lower N_T found in PDI8CN2:PS films compared to the PDI8CN2 ones (**Table 5.5**). Importantly, PDI8CN2:PS devices recovered fully their initial parameters (i.e., V_{TH} and mobility) 12 hours after the bias stress measurements had been performed (**Figure 5.16d**), which could indicate that the charges are trapped in more shallow trap states.^[49] On the contrary, PDI8CN2 OFETs did not reveal an OFET behaviour anymore after the bias stress test, pointing the presence of deeper traps and a deterioration of the material.

The observed threshold voltage shift was fitted with the following equation:^[43,48,50,51]

$$\Delta V_{TH}(t) = (\Delta V_{TH}(\infty) - \Delta V_{TH}(0)) \left(1 - e^{\left(\frac{t}{\tau}\right)^\beta} \right) \quad (5.2)$$

Where t is the stress time, τ is the relaxation time for charge trapping and β is the dispersion parameter related to the characteristic width of the band tail of the semiconductor.^[52,53] In other words, β is responsible for the dispersivity or spread of barrier states.^[54] The values of these fitting parameters are shown in **Table 5.4**.

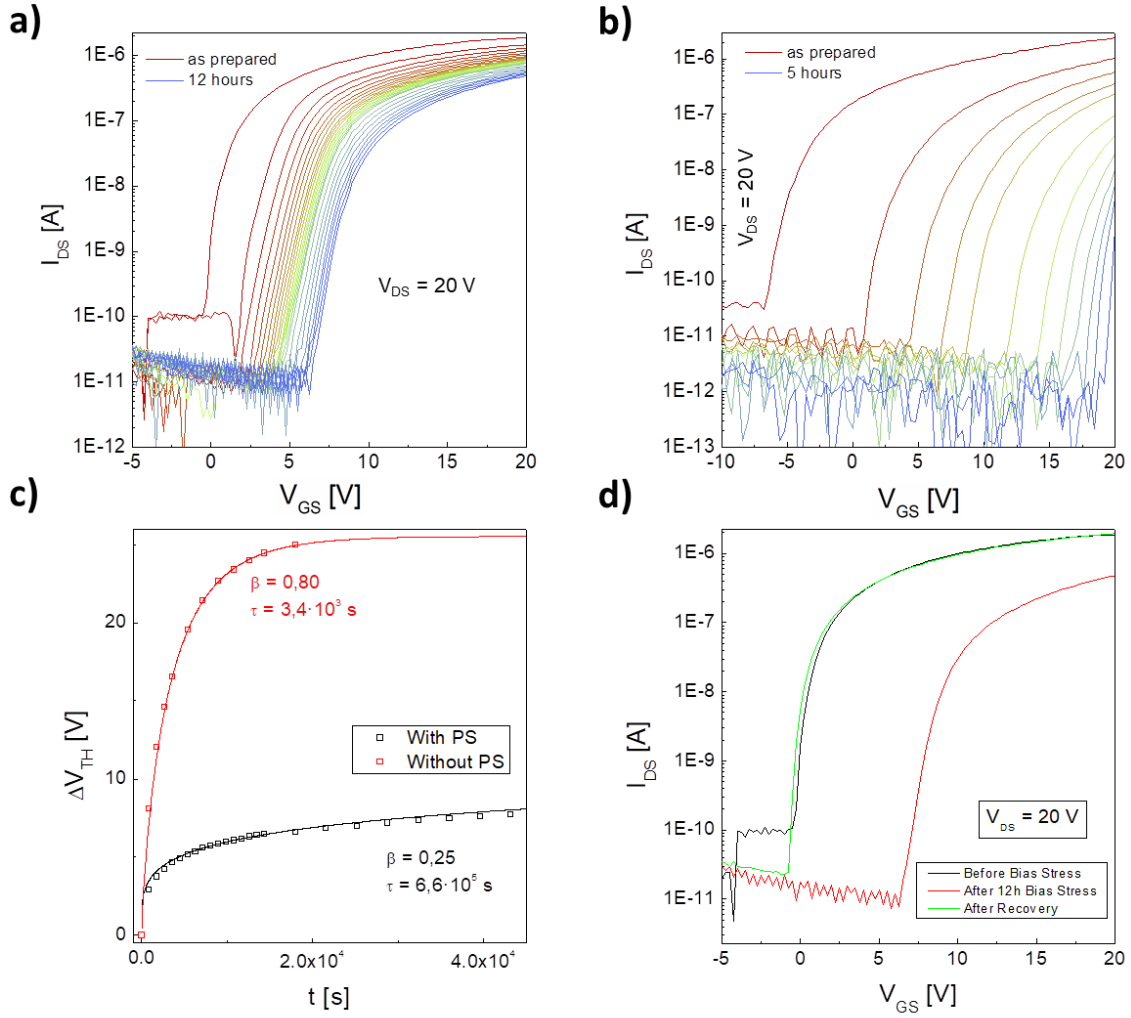


Figure 5.16. Bias stress stability measurements of **(a)** PDI8CN2:PS OFET and **(b)** PDI8CN2 ($V_{GS} = 20$ V and $V_{DS} = 0$ V). **(c)** Threshold voltage shift vs. time and fitting curves following equation 5.2. **(d)** Comparison of the transfer characteristics of the sample with PS just before the bias stress measurements, after the bias stress experiments and after the recovery. All transfer characteristics shown had a $V_{DS} = 20$ V.

For the PDI8CN2:PS devices a β value of 0.25 and a relaxation time of the order of 10^5 was found. These values are of the same order than the ones found for many previous bias stress experiments performed on p-channel devices.^[45] On the contrary, the PDI8CN2 devices showed a larger β value (0.80) and τ was two orders of magnitude lower (**Figure 5.16c**). Considering all this, we believe that the improved device stability under bias stress achieved with the blended OSC is mainly caused by a better quality of the OSC/dielectric interface. As previously mentioned, in the PDI8CN2:PS film a PS layer is covering the SiO_2 dielectric preventing charge trapping in the silanol groups of the oxide dielectric.^[55] In fact, a reduction of the β value has been previously reported when the SiO_2 dielectric was coated with a SAM^[42,45,56] or a polymer dielectric layer.^[57] However, other factors that can affect the bias stress stability are the grain sizes and the penetration of oxygen and moisture into the films. It has been reported that devices based on films with a smaller grain size exhibit a higher threshold instability since the charges are trapped at the grain boundaries.^[44] Both PDI8CN2-

based films prepared here exhibit similar crystalline domains. However, the films prepared with the blends are encapsulated by a skin PS layer which might protect them from external agents and that cover the grain boundaries.^[58] In order to disentangle the role of the bottom and top PS layer in the blended films, a cross-check experiment was performed. A bare PDI8CN2 film was encapsulated with Cytop™ shortly after its deposition and, subsequently, it was measured under bias stress. These devices exhibited a significantly lower bias stress stability compared to the PDI8CN2:PS films, although they showed a better performance with respect to the devices without the encapsulation layer (**Figure 5.17**). Accordingly, the extracted β value was 0.61 and τ was of the order of 10^4 s. This implies that, although to a lesser extent, the top PS layer has also some effect on the bias stress stability. Thus, the significant improvement in the operational electrical stability reached by blending PDI8CN2 with PS can be attributed to two-fold reasons: i) the passivation of the polar OH groups from the dielectric, and ii) the self-encapsulation of the OSC.

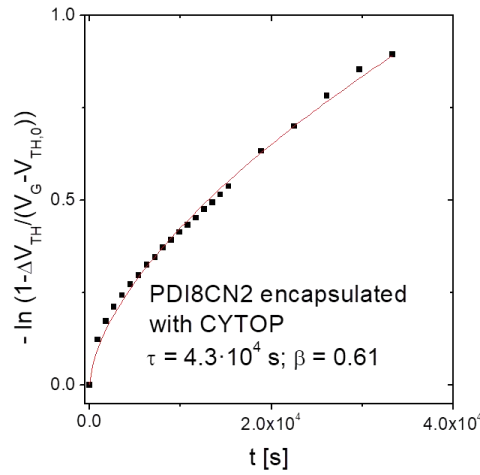


Figure 5.17. Bias stress stability of the PDI8CN2 OFET encapsulated with Cytop.

DENSITY OF STATES (DOS) ESTIMATION

The estimation of DoS calculations were performed following the method developed by Lang *et al.*,^[59] in which the transfer characteristics are measured at different temperatures (from 300 K to 390 K for PDI8CN2 and from 305 to 350 for PDI8CN2:PS, that is, below the polymer glass transition). Since the transfer characteristics were measured at a fixed V_{DS} , I_{DS} is proportional to the channel conductance for each V_{GS} . The activation energy (E_{ACT}) extracted from the Arrhenius plots of the channel conductance for each V_{GS} is shown in **Figure 5.18a-b** for PDI8CN2 and PDI8CN2:PS devices, respectively. The E_{ACT} of PDI8CN2 OFET varies exponentially from 0.7 eV to 0.1 eV, however in the case of PDI8CN2:PS OFET E_{ACT} only varies in a much smaller range, from 0.3 eV to 0.05 eV. The rate at which E_{ACT} varies with V_{GS} indicates how easily the DoS distribution shifts to lower energies. Hence, a lower range of E_{ACT} means a

lower energy required to turn the device on. The DoS in the gap of the semiconductor can be estimated from the derivative of E_{ACT} with respect to V_{GS} .^[59]

$$DoS(E) = \frac{C}{q} \left(\frac{1}{d_{acc} \frac{dE_{ACT}}{dV_{GS}}} \right) \quad (5.3)$$

where d_{acc} is the thickness of the charge accumulation layer, here estimated with a value of 7.5 nm.^[59] **Figure 5.18c-d** shows the DoS distribution of PDI8CN2 and PDI8CN2:PS active layers. PDI8CN2:PS has a sharp distribution of states with up to $\sim 10^{21} \text{ cm}^{-3} \text{ eV}^{-1}$ close the LUMO in contrast to the a more progressive distribution of PDI8CN2 ($\sim 10^{20} \text{ cm}^{-3} \text{ eV}^{-1}$). In addition, the band tail of PDI8CN2 extends deeper into the band gap compared to PDI8CN2:PS. All these results are in agreement with an improved SS observed from the transfer characteristics of **Figure 5.15** and the θ values found. Indeed, a lower θ value implies lower defects in the channel of the transistor. Hence, these results again prove that the addition of PS reduces the trap density, weakening the sub-band gap tail, called Urbach tail, and, in consequence, reducing the density of sub-gap defect states in the transistor channel, being sharper the band tail of the DoS.

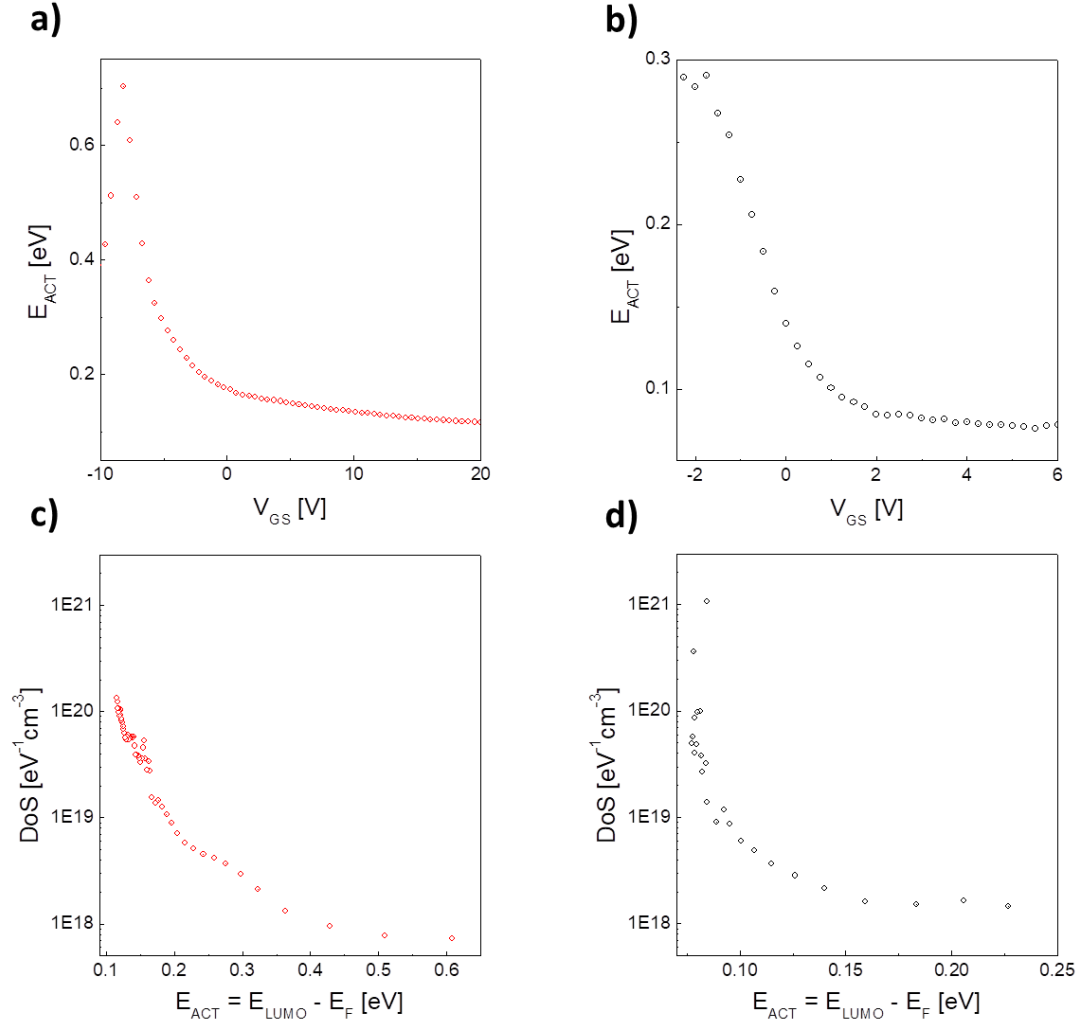


Figure 5.18. Activation energy of (a) PDI8CN2 and (b) PDI8CN2:PS devices vs. V_{GS} . Distribution of DoS of (c) PDI8CN2 and (d) PDI8CN2:PS devices.

SHELF STABILITY

The shelf stability of the transistors was also studied by measuring the devices for several days storing them under dark and ambient conditions. The variation of the V_{TH} of the devices measured for 150 days after fabrication are depicted in **Figure 5.19**. Remarkably, not significant changes in the V_{TH} of PDI8CN2:PS OFETs are observed. In sharp contrast, the V_{TH} shifts more than 10 V in PDI8CN2 based OFETs during the same period of time. The air stability enhancement found in the blends is again indicative of the self-encapsulation of the active material by the top insulating PS layer, which acts as a barrier against the penetration of water or oxygen molecules.

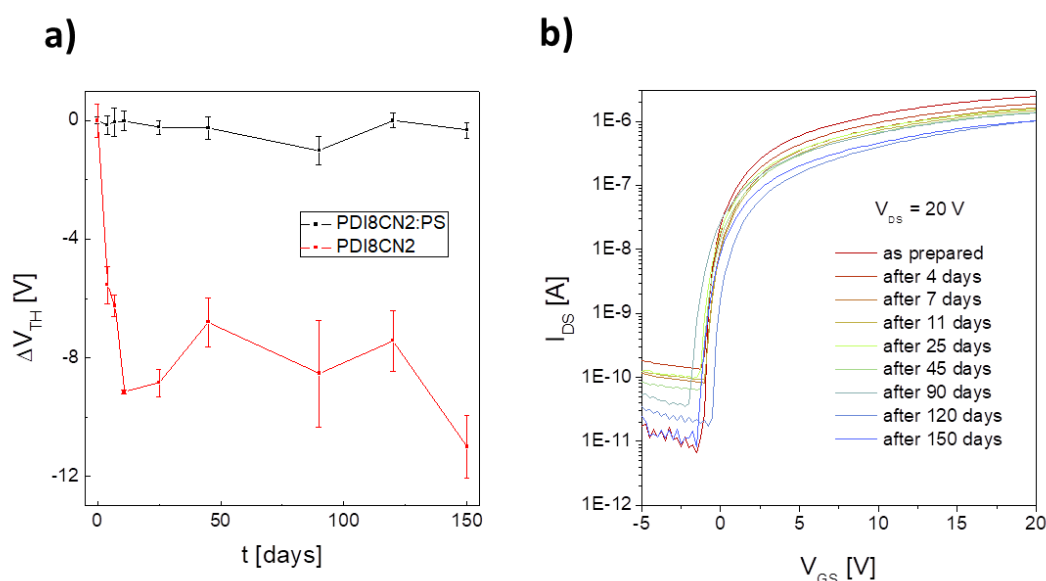


Figure 5.19. Shelf stability data of the PDI8CN2 and PDI8CN2:PS based OFETs. **(a)** Threshold voltage shift (ΔV_{TH}) and **(b)** Transfer characteristics of an OFET fabricated with PDI8CN2:PS as prepared and after different storage times.

CMOS-LIKE INVERTER

Complementary metal-oxide-semiconductor (CMOS) is a technology necessary to build integrated circuits that requires the use of *n*-type and *p*-type transistors with similar performances. CMOS technology has the advantages over unipolar technologies that the devices are more resistance to noise and that the devices consume less power. A scheme of a CMOS inverter is shown in **Figure 5.20a**. Herein, we use the term CMOS-like for noting that we are using OSCs instead of the classical inorganic semiconductors.

A CMOS-like inverter with the structure shown in **Figure 5.20a** was fabricated using PDI8CN2:PS for fabricating the *n*-type OFET and DB-TTF:PS for the *p*-type. The formulation used for the *p*-type material was the one previously reported as described in the experimental

section.^[19,29] Ink solutions were deposited simultaneously by BAMS technique separating the two solution meniscus with a teflon ring. Since DB-TTF:PS OFETs exhibit a mobility of one order of magnitude higher,^[13] we used a *n*-channel 10 times wider to balance the current of both transistors. The voltage transfer characteristics of the inverter are shown in **Figure 5.20b**. The inverter reveals a good performance with a maximum gain ($\partial V_{OUT}/\partial V_{IN}$) of 35, which is a comparable value to what it can be found in the literature for similar systems (**Figure 5.20c**).^[60]

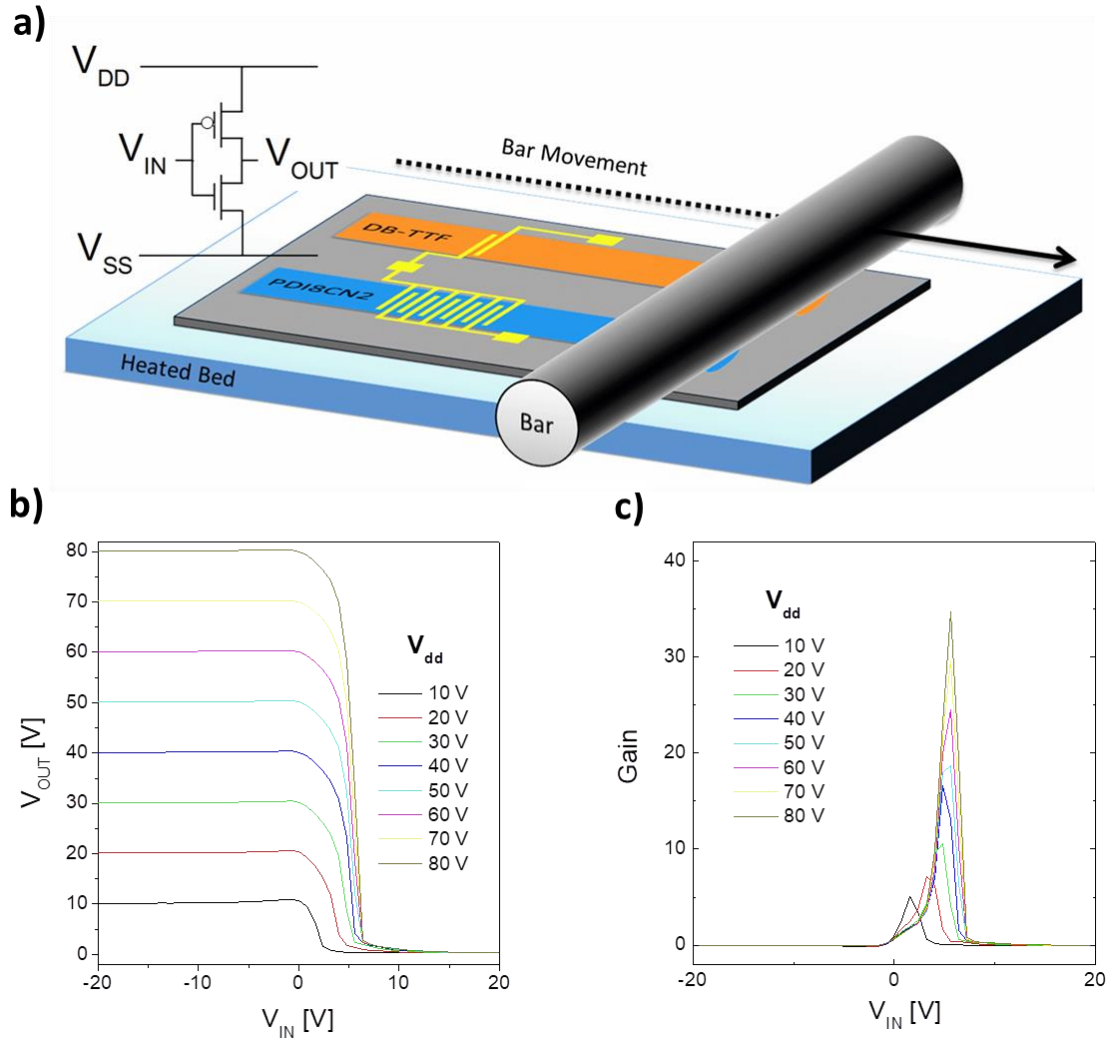


Figure 5.20. (a) Schematic representation of a CMOS inverter and scheme showing how the active layers of the inverter are fabricated using BAMS. (b) Transfer characteristics and (c) gain at different V_{DD} of the CMOS-like inverter made with PDI8CN2:PS as *n*-type OSC and DB-TTF:PS as *p*-type OSC.

5.4. SUMMARY

In conclusion, OFET devices based on the *n*-type OSCs TCNQ and PDI8CN2 have been prepared using the solution-shearing technique BAMS in ambient conditions. For TCNQ, several formulations were tested going from a partially-covered film to a fully polycrystalline layer with huge domains and improved performance as OFET. Some important parameters such as the choice of the solvent, deposition speed, coating temperature, OSC:polymer ratio and polymer molecular weight were investigated in depth. We succeeded in fabricating for the first time solution sheared TCNQ thin-film OFETs exhibiting a field-effect mobility of the order of $10^{-3} \text{ cm}^2/\text{V}\cdot\text{s}$. In addition, fairly stable transistors were obtained with the optimised formulation.

In the case of PDI8CN2, solutions of the pure OSC and also of the OSC blended with PS were employed with the aim of gaining insights into the role of the insulating matrix. Both films showed similar crystallinity and morphology. However, in the blended films a vertical phase separation occurred leading to the formation of a bottom PS layer close to the dielectric and, on the top, a crystalline layer of the OSC seated but self-encapsulated by a thin skin PS layer. The OFET electrical characteristics of PDI8CN2:PS revealed an optimised performance displaying improved device parameters ($\mu_{\text{FE,sat}}$, V_{TH} , $I_{\text{ON/OFF}}$ and SS). More importantly, the OFETs based on blends were dramatically more robust in terms of bias stress and environmental stability, which is crucial for the reliability of the devices.

The improved performance and stability was ascribed to the dual role of the PS matrix: i) passivation of the OSC/dielectric interface serving as a non-polar dielectric medium and ensuring a low level of charge traps and ii) protection of the OSC from the diffusion of oxygen and moisture which are highly detrimental for electron transport. Finally, the PDI8CN2:PS blends were combined with a blend of a *p*-type OSC to realize a CMOS-like inverter with a gain of 35.

These works advocate that by blending *n*-type OSCs with insulating polymeric matrixes *n*-channel OFETs with improved performance and reliability can be achieved even when processed with fast-deposition techniques compatible with up-scaling, which is of great importance for the development of CMOS-like technology using OSCs.

5.5. REFERENCES

- [1] M. Mas-Torrent, C. Rovira, *Chem. Soc. Rev.* **2008**, 37, 827.
- [2] K. Zhou, H. Dong, H.-L. Zhang, W. Hu, *Phys. Chem. Chem. Phys.* **2014**, 16, 22448.
- [3] J. Dhar, U. Salzner, S. Patil, *J. Mater. Chem. C* **2017**, 5, 7404.
- [4] T. D. Anthopoulos, G. C. Anyfantis, G. C. Papavassiliou, D. M. De Leeuw, *Appl. Phys. Lett.* **2007**, 90, 122105.
- [5] R. T. Weitz, K. Amsharov, U. Zschieschang, M. Burghard, M. Jansen, M. Kelsch, B. Rhamati, P. A. Van Aken, K. Kern, H. Klauk, *Chem. Mater.* **2009**, 21, 4949.
- [6] Y. Wen, Y. Liu, C. A. Di, Y. Wang, X. Sun, Y. Guo, J. Zheng, W. Wu, S. Ye, G. Yu, *Adv. Mater.* **2009**, 21, 1631.
- [7] M. H. Yoon, C. Kim, A. Facchetti, T. J. Marks, *J. Am. Chem. Soc.* **2006**, 128, 12851.
- [8] F.-C. Chen, C.-H. Liao, *Appl. Phys. Lett.* **2008**, 93, 103310.
- [9] J. H. Dou, Y. Q. Zheng, Z. F. Yao, Z. A. Yu, T. Lei, X. Shen, X. Y. Luo, J. Sun, S. D. Zhang, Y. F. Ding, G. Han, Y. Yi, J. Y. Wang, J. Pei, *J. Am. Chem. Soc.* **2015**, 137, 15947.
- [10] C. Zhang, Y. Zang, F. Zhang, Y. Diao, C. R. McNeill, C. an Di, X. Zhu, D. Zhu, *Adv. Mater.* **2016**, 28, 8456.
- [11] B. A. Jones, A. Facchetti, M. R. Wasielewski, T. J. Marks, *J. Am. Chem. Soc.* **2007**, 129, 15259.
- [12] M. R. Niazi, R. Li, E. Qiang Li, A. R. Kirmani, M. Abdelsamie, Q. Wang, W. Pan, M. M. Payne, J. E. Anthony, D. M. Smilgies, S. T. Thoroddsen, E. P. Giannelis, A. Amassian, *Nat. Commun.* **2015**, 6, 8598.
- [13] F. Leonardi, S. Casalini, Q. Zhang, S. Galindo, D. Gutiérrez, M. Mas-Torrent, *Adv. Mater.* **2016**, 28, 10311.
- [14] A. F. Paterson, N. D. Treat, W. Zhang, Z. Fei, G. Wyatt-Moon, H. Faber, G. Vourlias, P. A. Patsalas, O. Solomeshch, N. Tessler, M. Heeney, T. D. Anthopoulos, *Adv. Mater.* **2016**, 28, 7791.
- [15] Y. Yuan, G. Giri, A. L. Ayzner, A. P. Zoombelt, S. C. B. Mannsfeld, J. Chen, D. Nordlund, M. F. Toney, J. Huang, Z. Bao, *Nat. Commun.* **2014**, 5, 3005.
- [16] A. D. Scaccabarozzi, N. Stingelin, *J. Mater. Chem. A* **2014**, 2, 10818.
- [17] B. S. Hunter, J. W. Ward, M. M. Payne, J. E. Anthony, O. D. Jurchescu, T. D. Anthopoulos, *Appl. Phys. Lett.* **2015**, 106, 223304.

- [18] K. Zhao, O. Wodo, D. Ren, H. U. Khan, M. R. Niazi, H. Hu, M. Abdelsamie, R. Li, E. Q. Li, L. Yu, B. Yan, M. M. Payne, J. Smith, J. E. Anthony, T. D. Anthopoulos, S. T. Thoroddsen, B. Ganapathysubramanian, A. Amassian, *Adv. Funct. Mater.* **2016**, 26, 1737.
- [19] F. G. Del Pozo, S. Fabiano, R. Pfattner, S. Georgakopoulos, S. Galindo, X. Liu, S. Braun, M. Fahlman, J. Veciana, C. Rovira, X. Crispin, M. Berggren, M. Mas-Torrent, *Adv. Funct. Mater.* **2016**, 26, 2379.
- [20] A. Campos, Q. Zhang, M. R. Ajayakumar, F. Leonardi, M. Mas-Torrent, *Adv. Electron. Mater.* **2017**, 1700349.
- [21] Q. Zhang, F. Leonardi, S. Casalini, I. Temiño, M. Mas-Torrent, *Sci. Rep.* **2016**, 6, 39623.
- [22] I. Temiño, F. G. Del Pozo, M. R. Ajayakumar, S. Galindo, J. Puigdollers, M. Mas-Torrent, *Adv. Mater. Technol.* **2016**, 1, 1600090.
- [23] H. Zhong, J. Smith, S. Rossbauer, A. J. P. White, T. D. Anthopoulos, M. Heeney, *Adv. Mater.* **2012**, 24, 3205.
- [24] P. S. K. Amegadze, Y.-Y. Noh, *Thin Solid Films* **2014**, 556, 414.
- [25] M. Kang, H. Hwang, W. T. Park, D. Khim, J. S. Yeo, Y. Kim, Y. J. Kim, Y. Y. Noh, D. Y. Kim, *ACS Appl. Mater. Interfaces* **2017**, 9, 2686.
- [26] P. W. Anderson, P. A. Lee, M. Saitoh, *Solid State Commun.* **1973**, 13, 595.
- [27] M. Yamagishi, Y. Tominari, T. Uemura, J. Takeya, *Appl. Phys. Lett.* **2009**, 94, 053305.
- [28] E. Menard, V. Podzorov, S.-H. Hur, a. Gaur, M. E. Gershenson, J. a. Rogers, *Adv. Mater.* **2004**, 16, 2097.
- [29] S. Galindo, A. Tamayo, F. Leonardi, M. Mas-Torrent, *Adv. Funct. Mater.* **2017**, 27, 1700526.
- [30] T. He, M. Stolte, C. Burschka, N. H. Hansen, T. Musiol, D. Kälblein, J. Pflaum, X. Tao, J. Brill, F. Würthner, *Nat. Commun.* **2015**, 6, 5954.
- [31] B. A. Jones, A. Facchetti, M. R. Wasielewski, T. J. Marks, *Adv. Funct. Mater.* **2008**, 18, 1329.
- [32] J. Rivnay, L. H. Jimison, J. E. Northrup, M. F. Toney, R. Noriega, S. Lu, T. J. Marks, A. Facchetti, A. Salleo, *Nat. Mater.* **2009**, 8, 952.
- [33] D. Khim, K. J. Baeg, J. Kim, M. Kang, S. H. Lee, Z. Chen, A. Facchetti, D. Y. Kim, Y. Y. Noh, *ACS Appl. Mater. Interfaces* **2013**, 5, 10745.
- [34] A. Pérez-Rodríguez, I. Temiño, C. Ocal, M. Mas-Torrent, E. Barrena, *ACS Appl. Mater. Interfaces* **2018**, 10, 7296.
- [35] F. Liscio, S. Milita, C. Albonetti, P. D'Angelo, A. Guagliardi, N. Masciocchi, R. G. Della Valle, E. Venuti, A. Brillante, F. Biscarini, *Adv. Funct. Mater.* **2012**, 22, 943.

- [36] M. McDowell, I. G. Hill, J. E. McDermott, S. L. Bernasek, J. Schwartz, *Appl. Phys. Lett.* **2006**, *88*, 073505.
- [37] D. Khim, Y. Xu, K. J. Baeg, M. Kang, W. T. Park, S. H. Lee, I. B. Kim, J. Kim, D. Y. Kim, C. Liu, Y. Y. Noh, *Adv. Mater.* **2016**, *28*, 518.
- [38] S. Georgakopoulos, F. G. del Pozo, M. Mas-Torrent, *J. Mater. Chem. C* **2015**, *3*, 12199.
- [39] I. I. Fishchuk, A. Kadashchuk, S. T. Hoffmann, S. Athanasopoulos, J. Genoe, H. Bässler, A. Köhler, *Phys. Rev. B* **2013**, *88*, 125202.
- [40] R. Schmechel, *J. Appl. Phys.* **2003**, *93*, 4653.
- [41] S. Scheinert, G. Paasch, M. Schrödner, H. K. Roth, S. Sensfuß, T. Doll, *J. Appl. Phys.* **2002**, *92*, 330.
- [42] S. G. J. Mathijssen, M. Kemerink, A. Sharma, M. Cölle, P. A. Bobbert, R. A. J. Janssen, D. M. De Leeuw, *Adv. Mater.* **2008**, *20*, 975.
- [43] H. Sirringhaus, *Adv. Mater.* **2009**, *21*, 3859.
- [44] R. Ahmed, C. Simbrunner, G. Schwabegger, M. A. Baig, H. Sitter, *Org. Electron. physics, Mater. Appl.* **2014**, *15*, 3203.
- [45] F. Colléaux, J. M. Ball, P. H. Wöbkenberg, P. J. Hotchkiss, S. R. Marder, T. D. Anthopoulos, *Phys. Chem. Chem. Phys.* **2011**, *13*, 14387.
- [46] M. Barra, F. V. Di Girolamo, N. A. Minder, I. G. Lezama, Z. Chen, *Appl. Phys. Lett.* **2012**, *100*, 133301.
- [47] S. P. Tiwari, X.-H. Zhang, W. J. Potscavage, B. Kippelen, *J. Appl. Phys.* **2009**, *106*, 054504.
- [48] S. G. J. Mathijssen, M. Cölle, H. Gomes, E. C. P. Smits, B. De Boer, I. McCulloch, P. a. Bobbert, D. M. De Leeuw, *Adv. Mater.* **2007**, *19*, 2785.
- [49] A. Salleo, F. Endicott, R. A. Street, *Appl. Phys. Lett.* **2005**, *86*, 263505.
- [50] J. M. Lee, I. T. Cho, J. H. Lee, H. I. Kwon, *Appl. Phys. Lett.* **2008**, *93*, 093504.
- [51] K. K. Ryu, I. Nausieda, D. Da He, A. I. Akinwande, V. Bulović, C. G. Sodini, *IEEE Trans. Electron Devices* **2010**, *57*, 1003.
- [52] D. Monroe, *Phys. Rev. Lett.* **1985**, *54*, 146.
- [53] S. P. Tiwari, X.-H. Zhang, W. J. Potscavage, B. Kippelen, *J. Appl. Phys.* **2009**, *106*, 054504.
- [54] T. Jung, *J. Appl. Phys.* **2015**, *117*, 144501.
- [55] L. Chua, J. Zaumseil, J. Chang, E. C.-W. Ou, P. K.-H. Ho, H. Sirringhaus, R. H. Friend, *Nature* **2005**, *434*, 194.
- [56] J. Roh, C. M. Kang, J. Kwak, C. Lee, B. Jun Jung, *Appl. Phys. Lett.* **2014**, *104*, 173301.

CHAPTER 5

- [57] M. Alt, C. Melzer, F. Mathies, K. Deing, G. Hernandez-Sosa, U. Lemmer, *Appl. Phys. A Mater. Sci. Process.* **2016**, 122, 204.
- [58] D. Kwak, H. H. Choi, B. Kang, D. H. Kim, W. H. Lee, K. Cho, *Adv. Funct. Mater.* **2016**, 26, 3003.
- [59] D. V Lang, X. Chi, T. Siegrist, A. M. Sergent, A. P. Ramirez, *Phys. Rev. Lett.* **2004**, 93, 86802.
- [60] K. Wu, S. Zhang, Z. Xu, X. Chen, L. Li, *IEEE Trans. Electron Devices* **2015**, 62, 4220.

CHAPTER 6 SPRAY PRINTING OF ORGANIC CONTACTS AND ORGANIC SEMICONDUCTORS

6.1. INTRODUCTION AND OBJECTIVES

One of the key factors that are pushing organic electronics forward is their compatibility with processing techniques that can produce low-cost electronic devices with high throughput. Among the different available techniques, spray coating has raised considerable attention due to its compatibility with roll-to-roll methodologies and its importance in other industrial processes.

Spray printing^[1] is based on the transformation of liquid solutions into a dispersion of small droplets in a carrier gas or propellant that will eventually hit a target or substrate. Once the droplets reach the target, the carrier solvent is evaporated leaving a homogeneous layer of the desired substance. Although there are several kinds of sprays, we will focus on those where the liquid is atomised by a high-velocity gas, which is the one that we have used to develop this part of the thesis. A schematic representation of the spray technique we have used is depicted in **Figure 6.1**.

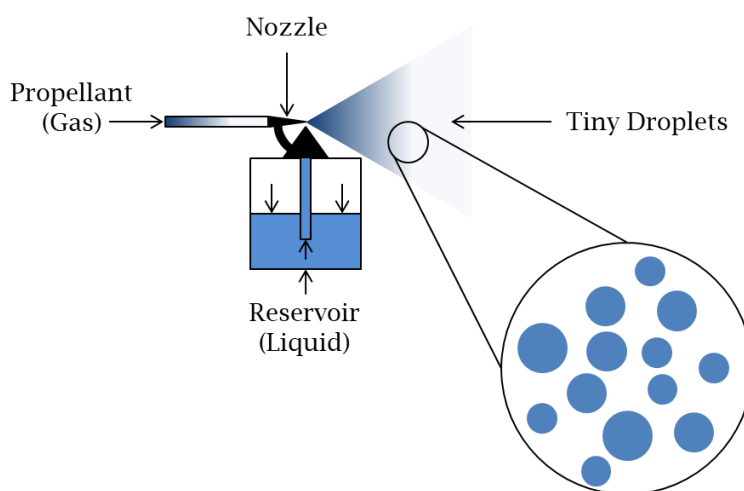


Figure 6.1. Schematic representation of the spray technique used in this chapter.

For this kind of spray, the surface tension of the liquid is overcome with the kinetic energy of the gas, thus, producing the atomisation of the solution. Among the most important parameters tuned for the optimisation of the spray deposition, we can find the propellant pressure, the solvent and the distance between the nozzle and the substrate. Regarding the propellant pressure is known that when it is increased the drop size is smaller and the drop velocity is higher. On the other hand, when a more dense solvent with higher surface tension is used the droplets are bigger and their speed is reduced. It is also important to mention that the particles are ejected from the nozzle at a random angle that on average is where the spray is pointing. This causes that if the spray is static the film is thicker in the centre and thinner at the edges of the stream. Further, to have a fine control of the amount of material that reaches the substrate the evaporation rate of the solvent can be controlled and, consequently, the crystallisation of the organic molecules.

Spray deposition has been demonstrated to be suitable and appealing for the deposition of organic semiconductors since it can form crystalline layers of organic semiconductors in a manner that is highly compatible with roll-to-roll methodologies.^[2–4] There are examples where it has been used to produce organic solar cells,^[5,6] organic light-emitting diodes,^[7,8] and organic field-effect transistors.^[9–13] Furthermore, it has also been used to deposit organic electrodes and dielectrics, indicating that there is a chance that devices could be fully fabricated with this technique.^[14,15] One of the benefits that stand out for spray among other solution-based techniques is its ability to process large volumes of solution, therefore allowing the use of low solubility compounds. It is important to remark that OSCs tend to be systems with broad π -conjugation and therefore low intrinsic solubility. It is known and it has been discussed in this thesis that the presence of alkyl side chains increase the solubility of the compounds, however, it is also known that the presence of these side chains modify the crystal structure changing the properties of the OSCs.^[16] Therefore, the use of spray printing permits to process by solution molecules that cannot be processed by solution-shearing, ink-jet printing or spin coating, hence, broadening the pool of available possibilities.

A particularly interesting case is the organic metal tetrathiafulvalene-tetracyanoquinodimethane (TTF-TCNQ) whose chemical structure is shown in **Figure 6.2**. The reason behind the electric properties of this material is that there is a partial charge-transfer between the donor and the acceptor and therefore, the energy bands are not completely full making this material inherently conductor.^[17–19] TTF-TCNQ was discovered back in 1973 starting the research on donor-acceptor charge-transfer salts, some of which have even given rise to superconducting properties.^[20] However, in the last decade this salt has been used for the fabrication of contacts in organic devices leading to an improved contact resistance with respect to the commonly used gold electrodes.^[21,22] The enhancement in charge injection has been attributed to the fact that TTF-TCNQ energy levels match better with the HOMO/LUMO of the organic semiconductor and to a more favourable organic/organic interface.^[23]

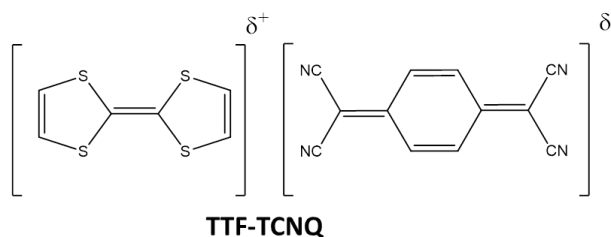


Figure 6.2. Molecular structure of the organic charge-transfer salt TTF-TCNQ.

However, due to its limited solubility, this interesting salt has been mainly processed by thermal evaporation techniques, both as coevaporation of the TTF and TCNQ compounds or as the evaporation of the already formed salt. Only two main strategies have been applied to process this salt from solution: the first consisted in the deposition of nanoparticles stabilised in an ionic liquid,^[24,25] and the second consisted in the sequential deposition by ink-jet printing of the donor and the acceptor so the solubility problem of the salt could be avoided.^[26,27] The use of spray coating to deposit TTF-TCNQ would represent an attractive possibility.

One of the issues of spray printing of OSCs for the fabrication of OFETs is the fact that when the small droplets reach the substrate they crystallise in small crystallites which is not desirable for achieving high OFET performance. That is because smaller crystallites lead to more grain boundaries which increase the number of traps hindering the performance of the final OFET.^[28] However, recently Rigas *et al.* modified the traditional spray coating technique so as to produce large single-crystals.^[29] In this methodology, the droplets of the semiconductor solution hit a thin layer of antisolvent instead of landing on the substrate permitting the crystallites to diffuse and fuse. Using this technique it was possible to form large single crystals that were used afterwards for the fabrication of single-crystal OFETs.

The main objectives of the work developed in this chapter are: i) the fabrication of the source and drain electrodes for OFETs by spray depositing a layer of the organic metal TTF-TCNQ, which has been historically processed by thermal evaporation^[19,30] and the comparison of the OFETs performance with the results obtained with conventional metallic contacts and ii) the fabrication of large single crystals of known and high-performance OSCs with the ulterior motivation of producing single cocrystals of an acceptor and a donor OSC for realising ambipolar OFETs.^[31–35]

6.2. SPRAY PRINTING OF TTF-TCNQ ELECTRODES FOR ORGANIC FIELD-EFFECT TRANSISTORS¹

The practical production of electronic devices by printing requires the utilization of conductors deposited from solution, over large areas and ideally at not excessively high temperatures. Avoiding high temperatures is essential when delicate organic semiconductor and/or plastic substrates are involved so as to prevent damaging the devices. Two of the most popular inks for the fabrication of electrodes from solution are silver nanoparticles^[36] and the conducting polymer poly(3,4-ethylenedioxythiophene)-polystyrene sulphonate (PEDOT:PSS)^[37,38] both of which require thermal treatments over 100 °C to achieve their optimum performance as conductors.

On the other hand, organic metals based on charge transfer salts such as TTF-TCNQ provide a clear alternative that has been proven to lead to high-performance OFETs because of the enhanced charge injection. The improved contact resistance that lead to a better charge injection together with the possibility of processing it at milder conditions compared to the inorganic choices has raised the interest for this material. Furthermore, it has demonstrated to inject efficiently for both *n*-type and *p*-type OSCs, which could lead to efficient injection in ambipolar transistors. This reduced contact resistance is attributed to the more favourable organic semiconductor/organic electrodes interface that is believed to contain a reduced number of traps and the dipoles present there that shift the Fermi energy of the electrodes slightly to match with the HOMO/LUMO of the organic semiconductor.^[19]

As commented before, this material has been traditionally processed by thermal evaporation with a few exceptions involving the use of nanoparticles or the sequential deposition of the donor and the acceptor. Herein, we report the processing of TTF-TCNQ using a technique more compatible with roll-to-roll processes, spray printing.

FABRICATION AND CHARACTERISATION OF THE TTF-TCNQ FILM

The spray deposition was investigated by depositing the TTF-TCNQ salt on a Si/SiO₂ substrate. This substrate had Au/Cr electrodes patterned by photolithography on it to evaluate the sheet resistance (R_s) of the resulting TTF-TCNQ film, which is a common way to report the electrical conductivity of metallic films. According to the resulting R_s values, the most optimum deposition conditions were selected.

¹ This work was carried out in collaboration with Dr. Stamatis Georgakopoulos (ICMAB-CSIC) and has been published in Georgakopoulos, S *et al. Org. Electron.* **2017**, 48, 365–370.

A schematic representation of the set-up is shown in **Figure 6.3**. Four different parameters were investigated to optimise the deposition of TTF-TCNQ: the solvent and the concentration of the solution, the pressure of the propellant (N_2), the nozzle-substrate distance and the substrate temperature.

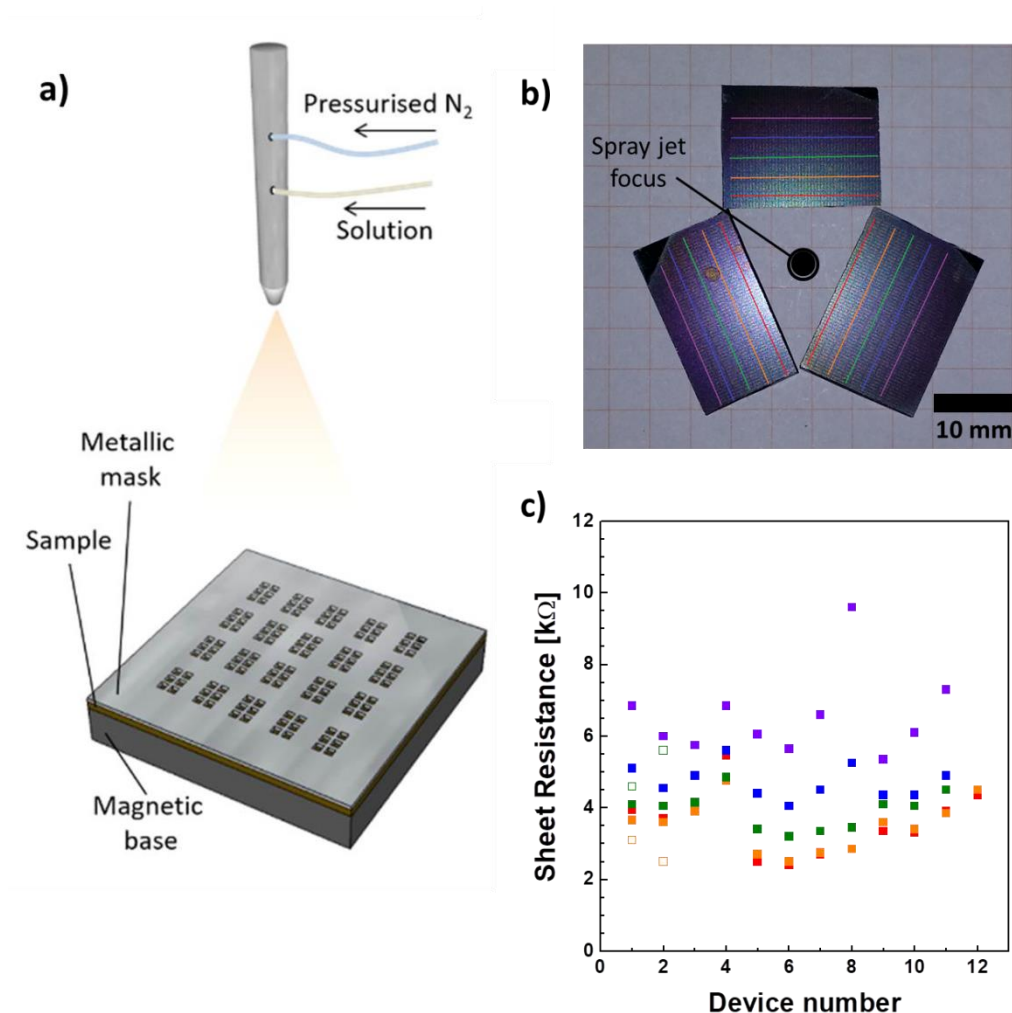


Figure 6.3. **(a)** Spray printing set up for the deposition of TTF-TCNQ source and drain electrodes. **(b)** Si/SiO₂ substrates with covered four-point probe structures. The spray jet was focused at the centre and the sheet resistance was measured along the coloured lines, as a function of distance from the centre. The values are plotted in **(c)**. Filled squares represent the initial measurements and empty squares measurements of the same samples one year later.

Regarding the solvent choice, which will also set the maximum concentration value, we wanted to have a solution concentration as high as possible so the amount of solvent required to deposit a certain amount of salt was as low as possible. Furthermore, a real solution without any particles in it was required because that could affect the spray process. Due to the small diameter of the nozzle (0.8 mm), any particle in the solution could get stuck stopping the

solution flow. Finally, we needed a volatile solvent so the droplet could evaporate quickly after reaching the substrate, consequently, making it possible to work at higher deposition rates. The apparition of a wet film on the substrate is a critical issue because it would change the regime of deposition making it similar to a drop casting, which was not the objective. So, we chose two solvents: acetone and THF. We chose these solvents because they are polar, which means that dissolve better the charge-transfer salt, and their boiling point is low (*b.p.* acetone and *b.p.* THF are 56 °C and 66 °C, respectively). It was found that the solubility limit of TTF-TCNQ in acetone was 0.3 g/L while in THF was 0.9 g/L. However, these values were only reached after strong agitation in an ultrasonic bath, afterwards the solution remained stable over time with no visible precipitation of the salt. These low solubility values remark the importance of spray coating as it would be impossible to process this material with any other solution deposition technique compatible with roll-to-roll.

Regarding the pressure of the propellant we decided to keep it at 1.5 bar that lead to a fair deposition rate of the solution of approximately 10 mL/min, and the nozzle-substrate distance was modified for a fine tuning. The deposition was performed by placing the spray 17 cm above the Si/SiO₂ substrate. Different distances were tested but when shorter distances were used the droplets coming from the spray started to form a wet film on the substrate. On the other hand, when longer distances were used the film thickness decreased dramatically becoming less conductive. Finally, the temperatures of the substrate tested were 80 °C and room temperature, but no significant changes were observed in the resulting film (*i.e.* film morphology and electrical characteristics). In summary, it was decided that the deposition parameters were the following: i) acetone or THF as solvent with a concentration of 0.3 or 0.9 g/L, respectively, ii) 1.5 bar of N₂ as propellant, iii) the deposition was performed at room temperature and iv) the nozzle to substrate distance was kept at 17 cm.

Once the deposition parameters were set, the film morphology was investigated by scanning electron microscopy (SEM) and by X-ray powder diffraction (XRPD). The SEM image of the resulting TTF-TCNQ film showed that the film consisted of needle- and plate-shaped crystals of TTF-TCNQ of approximately 1 µm long (**Figure 6.4a**). The X-ray powder diffractogram shown in **Figure 6.4b** confirmed that the crystal phase of the film matched with the reported structure.^[39] Furthermore, due to the fact that the observed reflections in the diffractogram correspond to the (0 0 *n*) family with a *d* spacing of 9.1 Å, it was extracted that the *ab* plane was lying in parallel with the substrate.

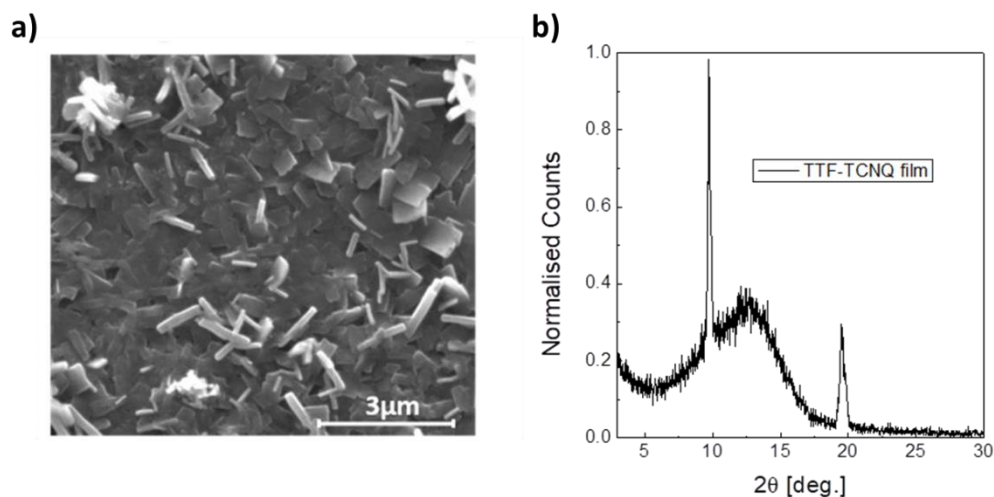


Figure 6.4. **(a)** Scanning electron microscope image and **(b)** X-ray powder diffractogram of TTF-TCNQ spray-coated film.

Regarding the electrical conductivity of the TTF-TCNQ films, the resulting sheet resistances of the films fabricated with acetone as solvent at different spray jet focus distances are plotted in **Figure 6.3c**. It was found that the sheet resistance of the film increased from 3 kΩ·cm at 0.6 cm to 6 kΩ·cm at 1.5 cm from the spray focus (for films fabricated from THF solutions these values were four times higher). The obtained values with acetone were very similar to those found in thermally evaporated 300 nm-thick films, where sheet resistances of 4 kΩ·cm were found.^[40] Thus, we concluded that for this particular experimental setup, the effective coating area was of 3 cm in diameter. Furthermore, the stability of the electrical properties of the TTF-TCNQ films was investigated over time. In this regard, it was found that the films kept the same sheet resistance values a year after the fabrication demonstrating the high stability of these organic electrodes.

SPRAYED TTF-TCNQ AS SOURCE AND DRAIN ELECTRODES FOR OFETS

In order to investigate the performance as electrodes of the sprayed TTF-TCNQ films, they were used as source and drain electrodes in OFETs. The OSC 2,7-diocetyl[1]benzothieno[3,2-*b*][1]benzothiophene (C8BTBT) (**Figure 6.5**) was chosen as organic semiconductor because of its high field-effect mobility and due to the fact that it tends to display contact resistance (R_c) issues. This injection problem is caused by the fact that the low-lying HOMO energy (-5.5 eV) of C8BTBT is misaligned with the work function (W_F) of the electrodes metal, usually Au ($W_F = 5.0$ eV). To overcome this problem, different approaches have been pursued like the use of the top-contact architecture, which is known to display a smaller R_c than the bottom-contact architecture,^[41] together with the use of an interfacial layer between the Au electrodes and

the OSC of MoO_x .^[42] The use of this oxide raises the work function of gold to 5.6 eV closing the gap between the OSC and the electrode and, hence, improving the R_c . This strategy has demonstrated to be effective enhancing dramatically the performance of the OFET devices achieving $\mu_{FE, sat}$ values above $7 \text{ cm}^2/\text{V}\cdot\text{s}$.^[43,44] Other alternatives have also demonstrated to be effective like the use of FeCl_3 to dope the OSC at the contacts.^[45] This doping results in the generation of mid band-gap states so the charges have a path instead of having to overcome the high Schottky barrier. On the other hand, TTF-TCNQ electrodes have demonstrated to also notably improve the charge-carrier injection in OFETs with contact issues.^[21,46] Because of that, as a proof-of-concept, the sprayed TTF-TCNQ films were used as source and drain electrodes in C8BTBT-based OFETs.

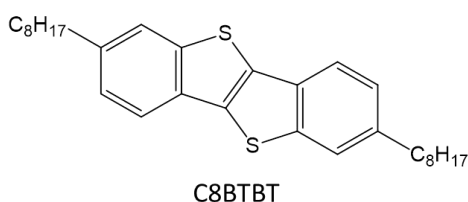


Figure 6.5. Molecular structure of C8BTBT.

OFETs were fabricated in a bottom-gate top-contact configuration (**Figure 6.6a**). A blend of C8BTBT with PS in a weight ratio 4:1 and dissolved in anhydrous chlorobenzene (2 % wt.) was deposited by bar-assisted meniscus shearing as previously reported.^[47] C8BTBT crystallised in large plate-like domains (**Figure 6.6b**). Afterwards, a solution of TTF-TCNQ was sprayed on top through a shadow mask to pattern the source and drain electrodes. The area of the targeted substrate was $(18 \times 20) \text{ mm}^2$. At this point it was observed that while acetone based solution did not seem to affect the C8BTBT:PS layer, the solution in THF dissolved totally the layer and, because of that, it could not be used for the fabrication of this OFET. However, this solution might be applicable to processes involving other materials that are not affected by THF. As a reference, devices with top MoO_x/Au contacts were also fabricated using the same active layer.

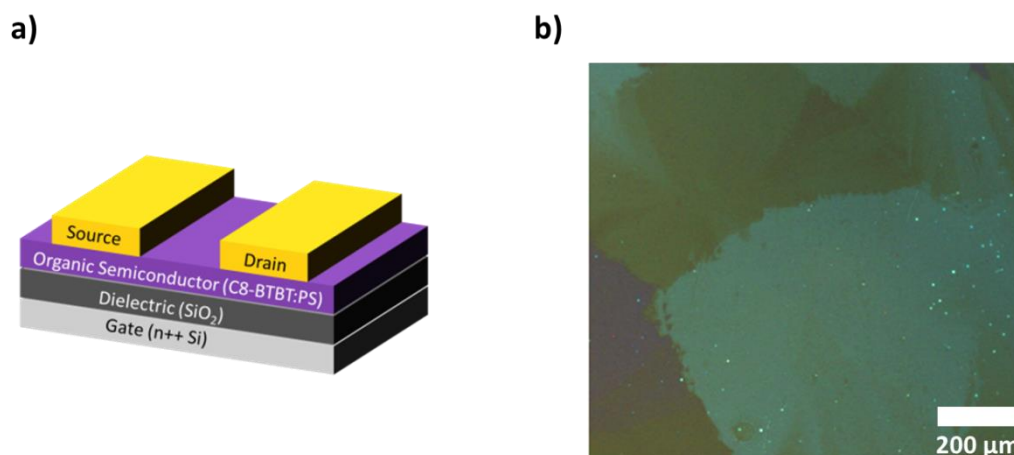


Figure 6.6. **a)** Cross-section of the device configuration of the transistor and **(b)** cross-polarised optical microscope image of the C8BTBT:PS thin-film.

In order to examine the possible impact of the spray deposition on the morphology of the semiconductor layer and the quality of the contact, the electrode edge were analysed by atomic force microscopy (AFM)². Typical topographic images are presented in **Figure 6.7**. The profile of the TTF-TCNQ electrode area revealed the high roughness of the electrode which was ascribed to the presence of crystallites as seen in the SEM images of **Figure 6.4a**. On the other hand, the channel is extremely flat even near the electrodes, which supports that the semiconductor layer has not been affected by the electrode deposition.

² This work was carried out in collaboration with Dr. Ana Pérez-Rodríguez, Dr. Esther Barrena and Prof. Carmen Ocal (ICMAB-CSIC).

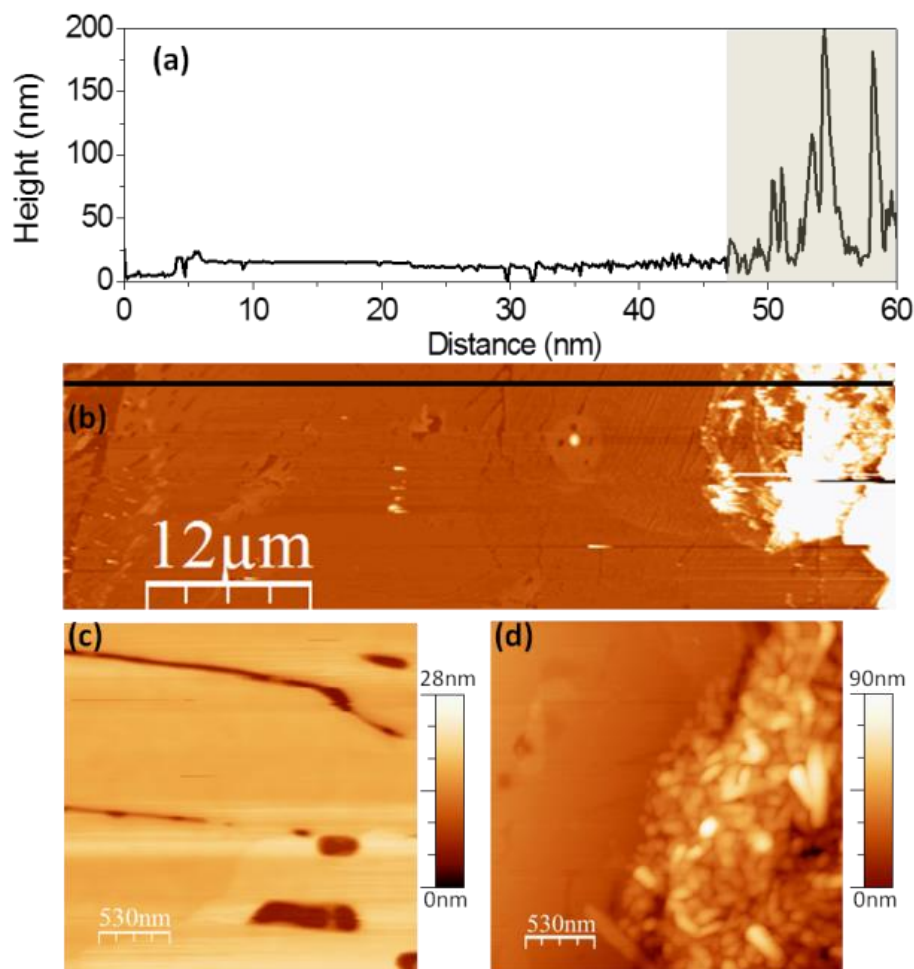


Figure 6.7. **(a)** Line profile taken along the black segment in the topography image of **(b)** which includes the electrode and most of the channel area ($L = 50 \mu\text{m}$). **(c)** Morphologic details of the central part of the channel and **(d)** of a region including the TTF-TCNQ electrode edge.

OFETs contacted with MoO_x/Au exhibited a saturation field-effect mobilities in the range of 0.1-2 cm²/V·s with a mean value of 0.7 cm²/V·s over 12 measured OFETs on 4 different substrates. The switch on voltage (V_{so}) was almost 0 V, subthreshold swing of 2 V/decade and on/off ratio of 10⁶. Also, no hysteresis was found in the transfer characteristics and the leakage current was found to be more than 5 orders of magnitude lower than the source-drain current. The OFET parameters are summarised in **Table 6.1**. Output characteristics showed low linearity at low drain voltage, which is a behaviour commonly observed in devices with significant contact resistance (**Figure 6.8b** inset). On the other hand, transistors with TTF-TCNQ top-contact electrodes exhibited peak saturation mobilities in the range of 0.2-1.4 cm²/V·s with the same mean value of 0.7 cm²/V·s over 17 measured OFETs on 6 different substrates. The other parameters were also similar to those found in MoO_x/Au devices. Nonetheless, the output characteristics exhibited noticeably better linearity at low drain voltage (*i.e.* enhanced hole injection). Independently on the source and drain electrodes, devices were stable for over a month in ambient conditions with no decay in mobility or threshold voltage.

The contact resistance was estimated by the Y-function method.^[48] This method was established for the parameter extraction (low-field μ , V_{TH} , R_C , etc.) from the transfer characteristics of transistors based on amorphous silicon. As previously mentioned, one of the advantages of this method over the commonly used transfer line method (TLM) is that only requires of one device to extract the contact resistance.^[49]

The contact resistance for the MoO_x/Au OFETs calculated by this methodology was estimated to be 53 ± 16 k Ω ·cm, which is slightly higher than the reported values (8-50 k Ω ·cm) extracted by the transmission line method for similar OFETs of C8BTBT with MoO_x/Au contacts.^[50] On the other hand, for the devices with TTF-TCNQ electrodes the extracted contact resistance in this work was 18 ± 3 k Ω ·cm, almost three times lower than with MoO_x/Au contacts.

Table 6.1. Summary of the OFET parameters found for devices fabricated with the two different kind of electrodes.

Electrodes	Range/Average $\mu_{FE,sat}$ [cm ² /V·s]	Range/Average V_{SO} [V]	Range/Average R_c [k Ω ·cm]	$I_{on/off}$
MoO _x /Au	0.1-2/0.7	-0.22-(-3.1)/-1.3	18-20/18	10^6
TTF-TCNQ	0.2-1.4/0.7	0.18-(-3.3)/-0.9	37-67/53	10^6

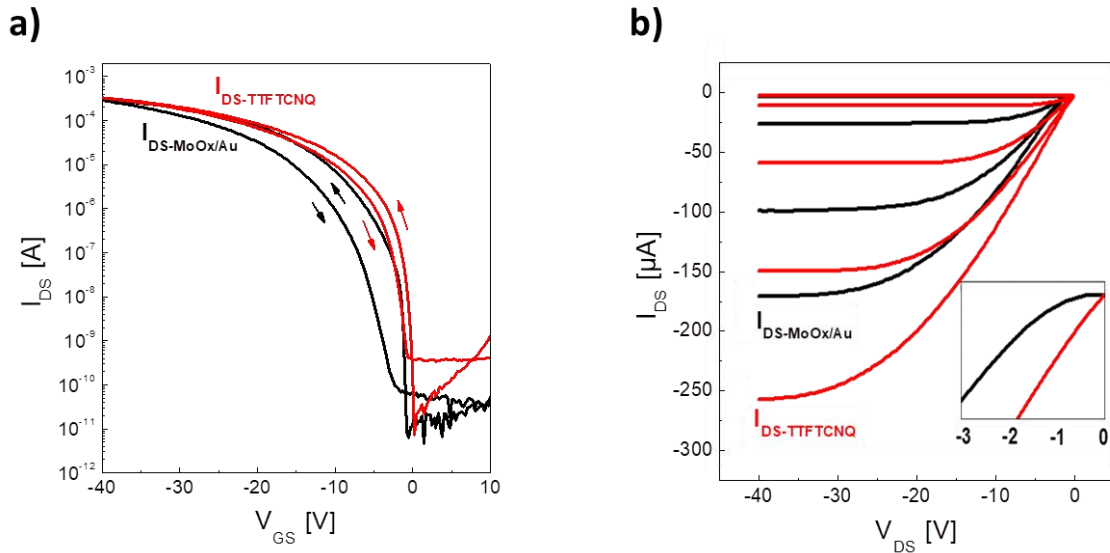


Figure 6.8. **(a)** Transfer and **(b)** output characteristics of C8BTBT OFETs with TTF-TCNQ (red) and MoO_x/Au (black) source and drain electrodes. Inset in **(b)** shows the more linear behaviour of the TTF-TCNQ sample at low V_{DS} .

Commonly, the reported work function (ϕ) values of organic CT complexes are inferred from considering the energy of the HOMO and LUMO of the isolated components and might differ from that of the compound. To have a realistic value, the work function of the TTF-TCNQ employed here was experimentally evaluated from the measured contact potential difference (CPD) between the electrodes of the particular devices and a conductive AFM tip. The CPD values are extracted from the position of the maximum in the parabolic dependence of the electrostatic force with the applied voltage measured at a minimum of 15 locations and several curves taken at each position.^[51] In order to discard tip work function uncertainty and any possible tip change, the absolute value of the ϕ was determined, under the same conditions and with the same tip, using as a reference a highly oriented pyrolytic graphite (HOPG) sample^[52] before and after measuring over the TTF-TCNQ electrode (**Figure 6.9**). Though the obtained $\phi = 4.9 \pm 0.1$ eV is somehow higher than the reported range (4.64 - 4.78 eV), this value is insufficiently high to account for the more efficient contact with the semiconductor and lower contact resistance as compared to devices with MoO_x/Au electrodes. If there was vacuum level alignment between C8BTBT and TTF-TCNQ, there would be a significant injection barrier of 0.8 eV which would noticeably affect device performance. According to our results this is not the case, as TTF-TCNQ actually seems to form a better contact than MoO_x/Au.

Therefore, it must be concluded that the specific electronic coupling of both organic compounds at the semiconductor/TTF-TCNQ interface, favours the hole injection most likely due to the formation of interface dipoles. Such dipoles have been observed for a variety of organic-organic and organic-metal interfaces and can exceed 1 eV.^[53] For organic-organic interfaces, it has been shown that charge-transfer as well as polarization effects are factors contributing to the sign and magnitude of the dipole.^[54] Interface dipoles are indeed commonly observed in donor-acceptor systems such as in multilayers of TTF/TCNQ, where the HOMO of the TTF donor and the LUMO of the TCNQ acceptor align at the interface between the two materials.^[55] It is likely that in our case at the interface between the TTF-TCNQ and C8BTBT films a dipole is induced. Another cause that could lead to a more efficient contact could be the intermixing of the organic metal with the organic semiconductor. This effect was previously observed in solution grown single crystals of a TTF derivative semiconductor on evaporated TTF-TCNQ contacts, which gave rise to devices exhibiting a lower contact resistance.^[56]

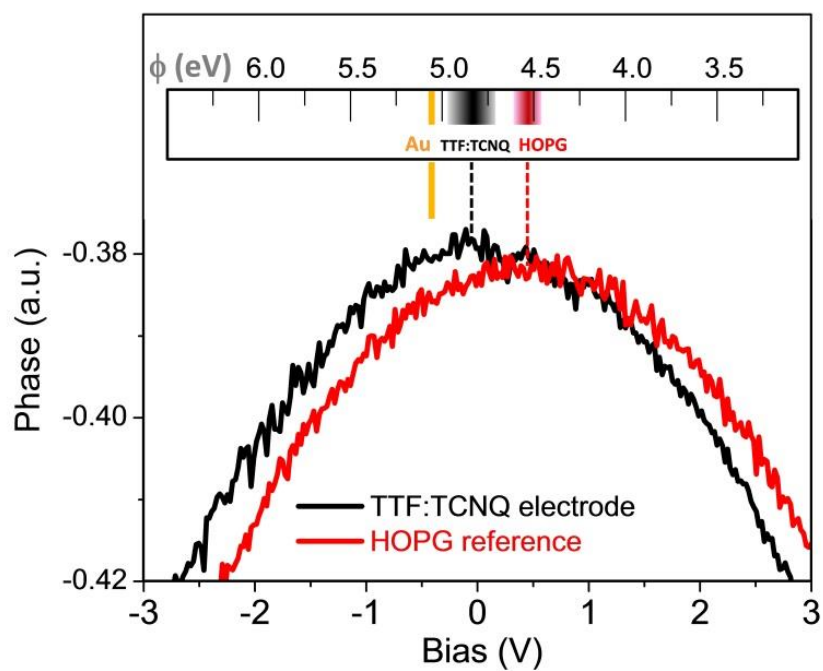


Figure 6.9. Phase $-V_{\text{Bias}}$ curves performed on top of the TTF-TCNQ electrode and on a reference HOPG sample. The corresponding work function values, obtained from the parabolic fit of the data, are given at the top panel along with that of gold ($\phi = 5.1$ eV), where the width of the colour scales indicate the statistical error of the measurements.

6.3. SPRAY PRINTING ON ANTISOLVENT FOR THE FORMATION OF ORGANIC SEMICONDUCTOR SINGLE CRYSTALS³

As previously mentioned, recently Rigas and coworkers developed a methodology to grow large single-crystals using spray coating. This technique consisted on spraying a solution of an organic semiconductor directly on a solvent in which the molecule was not soluble (*i.e.* an antisolvent). This procedure was performed for different molecules among which we can find the well-known OSCs 6,13-Bis(triisopropylsilylethynyl)pentacene (TIPS-pentacene) or C8BTBT. Furthermore, it was observed that the angle at which the spray was performed had an impact on the crystal shape and size.^[29]

In this technique, once the deposition is finished, the solvent in which the OSC is dissolved (from now on named after good solvent), which should be more volatile than the antisolvent, evaporates. Then, the OSC single-crystals are formed on the surface of the antisolvent. This procedure can lead to the formation of large single-crystals that can be very interesting for studying their properties.

Spraying on antisolvent is a delicate procedure because depends on different parameters such as the pressure of the propellant (N_2), the wettability of the surface and the angle and distance between the substrate and the nozzle among others. Spraying on antisolvent requires the contention of antisolvent on a surface that keeps it from falling when the OSC solution together with the propellant reaches the surface. It is also required that the antisolvent layer is thick enough so it does not retract when the deposition is performed. Hence the propellant pressure has to be kept low so the antisolvent is not much affected by the deposition.

First, we applied this technique to form single-crystals of the benchmark OSC TIPS-pentacene so as to get used to the methodology. The objective was to apply it subsequently for the growth of single-crystals based on Donor-Acceptor (D-A) cocrystals.^[57,58] D-A cocrystals are compounds that are formed by an electron donor (*p*-type OSC) and an electron acceptor (*n*-type OSC). In 2012, Zhu *et al.* reported the first neutral D-A cocrystal able transport both holes and electrons (*i.e.* ambipolar transport) with a remarkable μ values beyond $1\text{ cm}^2/\text{V}\cdot\text{s}$.^[31] Since then, this class of materials have attracted a lot of attention due to its potential use as active material for ambipolar OFETs.^[32,33,35,58–60] Among all the OSCs involved on the formation of D-A cocrystals, the *p*-type OSC meso-diphenyl tetrathia[22]annulene[2,1,2,1] (DPTTA) has demonstrated to form high mobility single crystals in combination with different TCNQ derivatives such as fluorinated TCNQs (F2-TCNQ and F4-TCNQ) and [1,2-*b*:4,5-*b'*]-dithiophene tetracyanoquinodimethane (DT-TCNQ). Another *p*-type OSC that has demonstrated that can form ambipolar D-A cocrystals in combination with TCNQ is dibenzotetrathiafulvalene (DB-TTF). In fact, DB-TTF:TCNQ cocrystal is a particularly interesting case as it has been reported by Jurchescu *et al.* that this system can crystallise in two different phases: α and β .^[35] Single-

³ This work was carried out during a stay at the University of Surrey in collaboration with Dr. Maxim Shkunov.

crystal OFETs of the two phases were fabricated and it was observed that in the α phase, the transport was electron dominant and that the single-crystal was displaying a higher degree of charge transfer between the donor and the acceptor. Interestingly, the β phase showed a predominant hole transport and a smaller degree of charge transfer.

Herein, to form these D-A cocrystals we selected the *n*-type OSCs TCNQ, DT-TCNQ and fullerene.^[31,32,35] Regarding the electron donors, we have chosen derivatives of TTF, such as bis(ethylenethio)tetrathiafulvalene (BET-TTF), DB-TTF and dithiophenetetrathiafulvalene (DT-TTF) as well as DPTTA. All the chemical structures of these molecules shown in **Figure 6.9**.

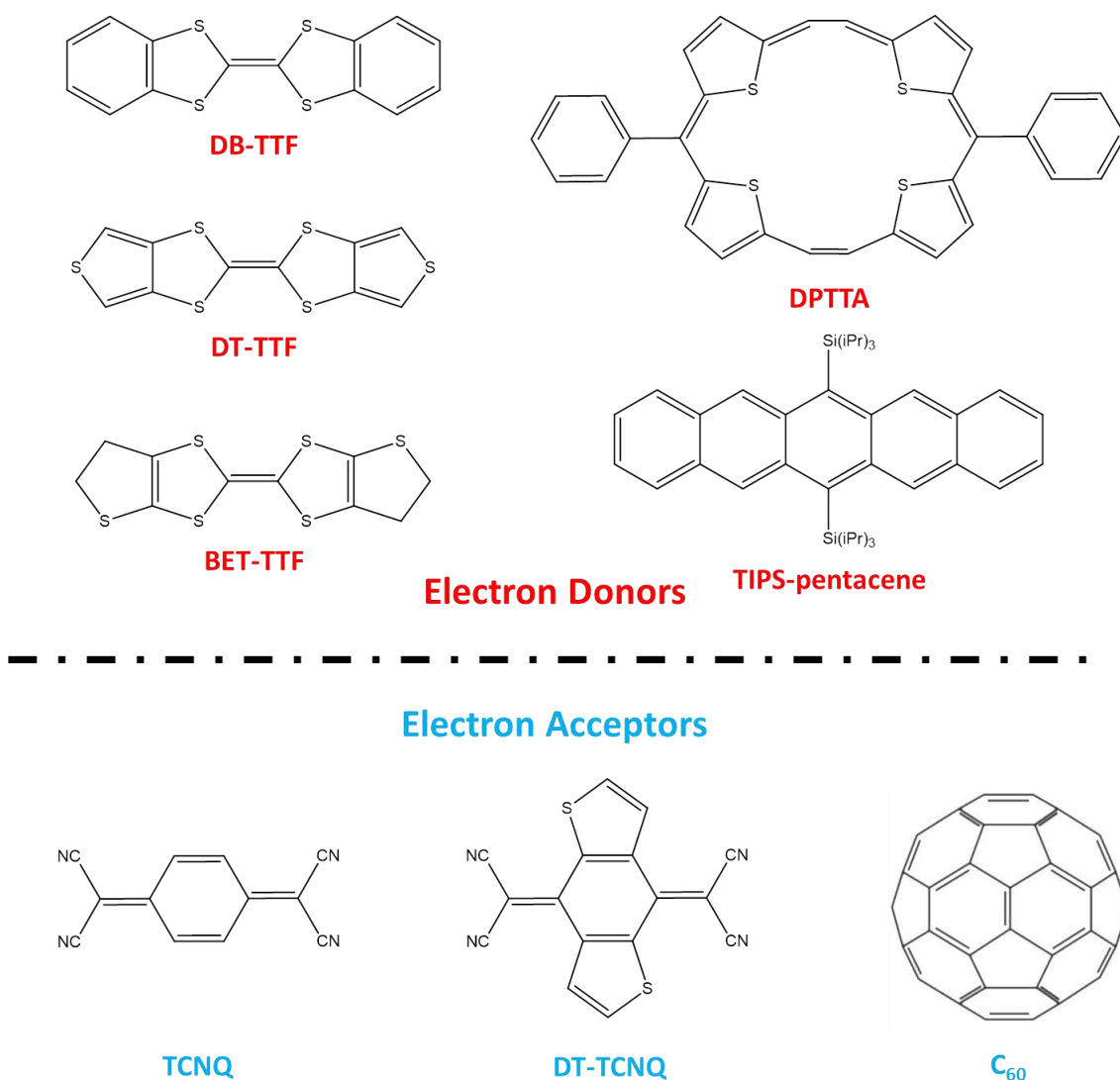


Figure 6.9. Electron donors and acceptors that have been used in this work.

The optimisation of the deposition parameters started with the fabrication of single-crystals of the OSC TIPS-pentacene. To do so, the concentration used was 6 mg/mL in toluene and the antisolvent used was dimethylformamide (DMF). These parameters were chosen because they were previously optimised by the hosting group. After several trials, it was decided to keep the nozzle to substrate distance around 25 cm, the angle between the substrate normal vector and the spray jet low (approximately 20°) and the propellant pressure below 0.7 bar with an intermittent deposition of the solution.

Furthermore, three types of Si/SiO₂ substrates were employed: untreated, treated with O₃ (more hydrophilic) and treated with an octadecyltrichlorosilane (OTS) SAM (more hydrophobic). It resulted that with the ozone treatment the amount of antisolvent to cover the whole substrate (size of the substrate = $(1.5 \times 1.5) \text{ cm}^2$) was lower. Then, the antisolvent did not cover all the substrate during the deposition and consequently, the OSC crystallised in a polycrystalline layer as it happens when no antisolvent is used. On the other hand, when an OTS SAM was used, the amount of antisolvent needed to cover the substrate was higher and even if the propellant pressure was low, it was powerful enough to make the antisolvent fly over the substrate, all in all resulting in a polycrystalline layer as the previous case. In conclusion, it was decided to keep the surface untreated with approximately 300 μL of DMF. The best obtained single-crystals during these optimisation experiments are shown in **Figure 6.10** and, as it can be seen from the optical microscope images, the formed crystals are of the order of 100 μm size, which is a suitable size to study their electrical properties.

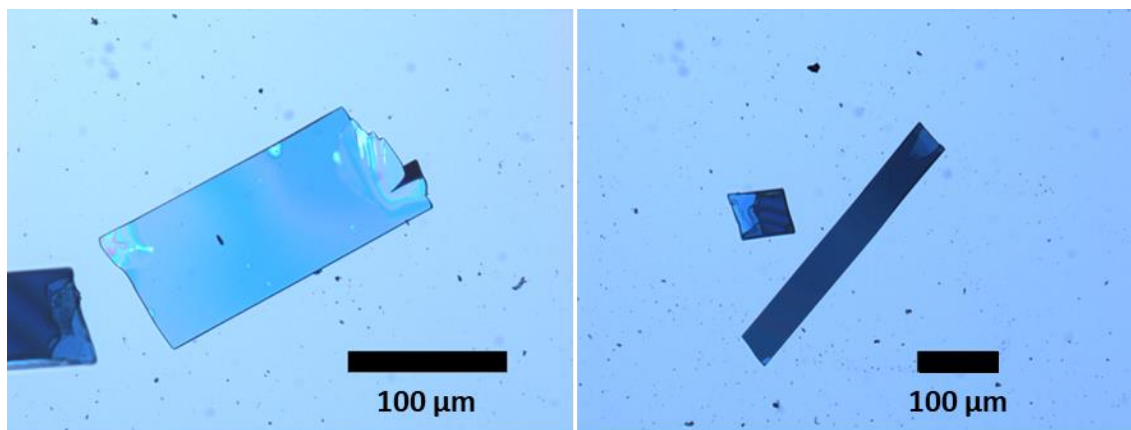


Figure 6.10. TIPS-pentacene single-crystals formed by spray printing on antisolvent.

After optimising the deposition parameters, Si/SiO₂ substrates with source and drain Au/Cr electrodes were fabricated by photolithography with the purpose of using them for measuring the electrical transport properties of the crystals formed on the top. To increase the chance that a single-crystal sat between two electrodes the pattern displayed in **Figure 6.11** was used. The pattern consisted of squares separated 50 μm from each other with more than 10^3 electrodes in a single substrate of $(1.5 \times 1.5) \text{ cm}^2$.

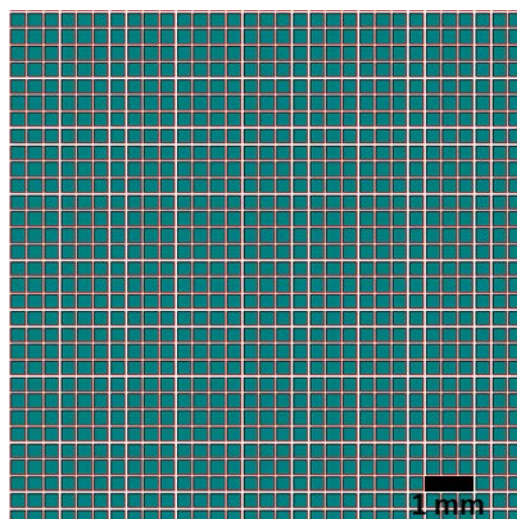


Figure 6.11. Au electrodes pattern for the fabrication of single-crystal OFETs.

Using these substrates we proceeded to the deposition of three different OSCs: DT-TTF, DB-TTF and DPTTA. In all the cases, we used a solution concentration of 6 mg/mL in toluene and DMF as antisolvent. In the case of DT-TTF, the deposition resulted in big flat and well-shaped single-crystals of DT-TTF but they did not show any field-effect (**Figure 6.12a**). This could be caused by a bad contact between the crystal and the dielectric. Hence, a top gate electrode was deposited on the single crystal. To do so, a layer of approximately 300 nm of parylene N^[61] was deposited by thermal evaporation on the single crystal for being used as dielectric and 50 nm of Al were deposited afterwards on top of the parylene N for being used as gate electrode. However, even with this OFET architecture the device did not show any response to the electrical field. It is known that OSCs are very sensitive to little amounts of defects and we believe that here the antisolvent (DMF) was somehow staying in the crystal surface preventing the crystal from working as an OSC. However, we cannot discard the option that the DT-TTF is crystallising in a different polymorph that does not display good electronic transport properties. To explore this last option X-ray powder diffraction experiments will be performed as future work.

On the other hand, DB-TTF and DPTTA crystals were formed using the same methodology and the OFET characteristics were measured successfully. The crystals presented *p*-type semiconductor behaviour with a mobility of 0.3 and 0.08 cm²/V·s, respectively (**Figure 6.12d-e**). As it happened with the reported result by Rigas et al. with C8BTBT single-crystals, the performance of these crystals was not as high as the best reported results.^[62,63] We attributed this behaviour to the presence of the antisolvent on the OSC/dielectric interface that affects the electronic transport (**Figure 6.12b-c**).

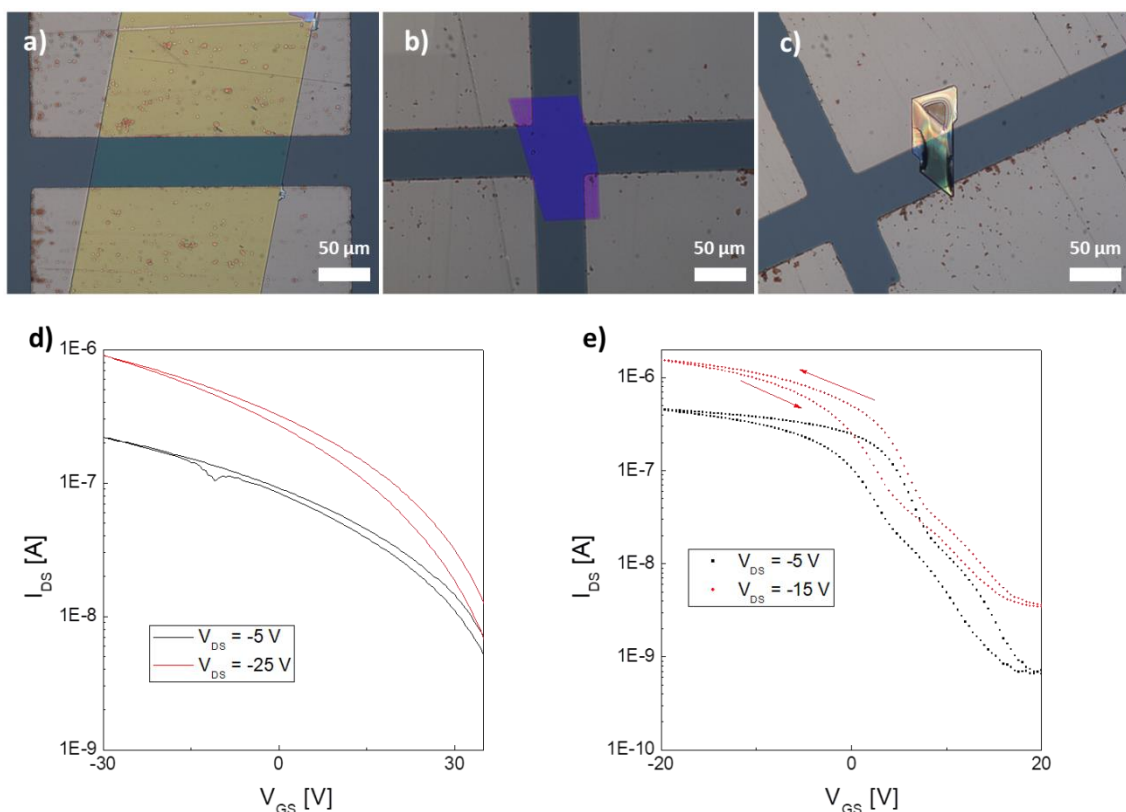


Figure 6.12. Optical microscope images of (a) DT-TTF, (b) DPTTA and (c) DB-TTF single-crystals, respectively, prepared by spray coating on antisolvent. (d) and (e) correspond to the OFET transfer characteristics of DPTTA and DB-TTF, respectively.

After processing the pure compounds, we started the optimisation of the ambipolar cocrystals following the same procedure. To do so, we focused our attention on three combinations of *p*- and *n*-type semiconductors: DPTTA/DT-TCNQ, DB-TTF/TCNQ and BET-TTF/ C_{60} . Cocrystals of the first two combinations prepared by drop casting or evaporation have already been shown to give ambipolar OFET characteristics.^[35,59] One known fact that affect the processability of this class of materials is their lower solubility when mixed because of the charge transfer that takes place between them. After trying different solvents, toluene, dichloromethane and *o*-xylene were chosen for DPTTA/DT-TCNQ, DB-TTF/TCNQ and BET-TTF/ C_{60} , respectively. The optical microscope images of the crystals prepared by spray coating a 1mg/mL solution of the materials on DMF as antisolvent are shown in **Figure 6.13**. All the crystals were smaller than the ones obtained for the single component OSCs, probably due to their lower solubility.

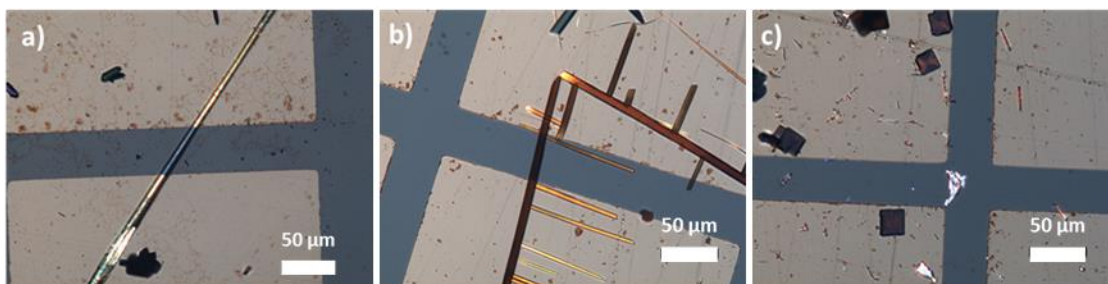


Figure 6.13. Optical microscope images of D-A cocrystals based on **(a)** DPTTA/DT-TCNQ, **(b)** DB-TTF/TCNQ and **(c)** BET-TTF/C₆₀ prepared by spray coating on antisolvent.

OFET electrical characterisation of these crystals was performed to study their properties, however, they did not respond to the external electric field. Currently we are working on the characterisation of these crystals by Raman spectroscopy and X-ray diffraction in order to characterise them and verify if they are cocrystals formed by the two OSCs or if during the crystallisation process segregation of the two materials is taking place.

6.4. SUMMARY

To sum up, in the first part of the chapter, we demonstrated the deposition of TTF-TCNQ charge-transfer complex from solution by spray printing. The resulting films exhibited the same crystal phase and sheet resistance as the films of TTF-TCNQ fabricated by thermal evaporation. The obtained resistance values were also similar to the commonly used PEDOT:PSS electrodes with the added benefit that here there was no need of applying additional thermal treatments. In addition, OFETs based on the high performance organic semiconductor C8BTBT were fabricated in top contact configuration with spray printed TTF-TCNQ, as well as with evaporated MoO_x/Au source/drain electrodes. Performance was similar between the two types of devices in terms of mobility, switch on voltage, subthreshold swing and on/off ratio. The only notable difference was better linearity in the output characteristics and lower calculated contact resistance found in TTF-TCNQ contacted devices, which could be attributed to the better OSC/electrode interface.

Regarding the second part, we managed to successfully form large single-crystal of the OSCs DT-TTF, DPTTA and DB-TTF by spray coating on an antisolvent. The devices based on single-crystals of DPTTA and DB-TTF showed OFET characteristics reaching hole mobilities of 0.08 and 0.3 cm²/V·s, respectively. We suggested that the role of the antisolvent may be detrimental for the electronic transport, hence, the deposition could be further optimised to get rid of this traces of solvent and hopefully enhance the transistor performance. Furthermore, we have fabricated single-crystals of 3 charge-transfer compounds: DB-TTF/TCNQ, DPTTA/DT-TCNQ, BET-TTF/C₆₀. These single-crystals have not shown organic semiconductor characteristics so far. Current work is being devoted to characterise the crystals formed and optimise the growth of such type of cocrystals.

6.5. REFERENCES

- [1] A. H. Lefebvre, V. G. McDonell, *Atomization and Sprays*, CRC Press, Boca Raton, Florida, **1990**.
- [2] C. Pitsalidis, A. M. Pappa, S. Hunter, M. M. Payne, J. E. Anthony, T. D. Anthopoulos, S. Logothetidis, *ACS Appl. Mater. Interfaces* **2015**, *7*, 6496.
- [3] Y. Diao, L. Shaw, Z. Bao, S. C. B. Mannsfeld, *Energy Environ. Sci.* **2014**, *7*, 2145.
- [4] A. Abdellah, B. Fabel, P. Lugli, G. Scarpa, *Org. Electron. physics, Mater. Appl.* **2010**, *11*, 1031.
- [5] K. X. Steirer, M. O. Reese, B. L. Rupert, N. Kopidakis, D. C. Olson, R. T. Collins, D. S. Ginley, *Sol. Energy Mater. Sol. Cells* **2009**, *93*, 447.
- [6] D. Vak, S.-S. Kim, J. Jo, S.-H. Oh, S.-I. Na, J. Kim, D.-Y. Kim, *Appl. Phys. Lett.* **2007**, *91*, 081102.
- [7] Y. Aoki, M. Shakutsui, K. Fujita, *Thin Solid Films* **2009**, *518*, 493.
- [8] J. Ju, Y. Yamagata, T. Higuchi, *Adv. Mater.* **2009**, *21*, 4343.
- [9] S. Han, H. Jeong, H. Jang, S. Baek, S. H. Kim, H. S. Lee, *Org. Electron. physics, Mater. Appl.* **2017**, *49*, 212.
- [10] W. Shi, S. Han, W. Huang, J. Yu, *Appl. Phys. Lett.* **2015**, *106*, 043303.
- [11] L. H. Chou, W. C. Chang, G. Y. He, Y. C. Chiu, C. L. Liu, *React. Funct. Polym.* **2016**, *108*, 130.
- [12] D. Khim, K.-J. Baeg, B.-K. Yu, S.-J. Kang, M. Kang, Z. Chen, A. Facchetti, D.-Y. Kim, Y.-Y. Noh, *J. Mater. Chem. C* **2013**, *1*, 1500.
- [13] B. S. Hunter, J. W. Ward, M. M. Payne, J. E. Anthony, O. D. Jurchescu, T. D. Anthopoulos, *Appl. Phys. Lett.* **2015**, *106*, 1.
- [14] J. Griffin, A. J. Ryan, D. G. Lidzey, *Org. Electron. physics, Mater. Appl.* **2017**, *41*, 245.
- [15] M. Shao, S. Das, K. Xiao, J. Chen, J. K. Keum, I. N. Ivanov, G. Gu, W. Durant, D. Li, D. B. Geohegan, *J. Mater. Chem. C* **2013**, *1*, 4384.
- [16] J. Y. Back, H. Yu, I. Song, I. Kang, H. Ahn, T. J. Shin, S.-K. Kwon, J. H. Oh, Y.-H. Kim, *Chem.*

Mater. **2015**, *27*, 1732.

- [17] P. W. Anderson, P. A. Lee, M. Saitoh, *Solid State Commun.* **1973**, *13*, 595.
- [18] K. P. Goetz, D. Vermeulen, M. E. Payne, C. Kloc, L. E. McNeil, O. D. Jurchescu, *J. Mater. Chem. C* **2014**, *2*, 3065.
- [19] R. Pfattner, C. Rovira, M. Mas-Torrent, *Phys. Chem. Chem. Phys.* **2014**, *17*, 26545.
- [20] T. Mori, A. Kobayashi, Y. Sasaki, H. Kobayashi, G. Saito, H. Inokuchi, *Bull. Chem. Soc. Jpn.* **1984**, *57*, 627.
- [21] Y. Takahashi, T. Hasegawa, S. Horiuchi, R. Kumai, Y. Tokura, G. Saito, *Chem. Mater.* **2007**, *19*, 6382.
- [22] M. Kraus, S. Richler, A. Opitz, W. Brütting, S. Haas, T. Hasegawa, A. Hinderhofer, F. Schreiber, *J. Appl. Phys.* **2010**, *107*, 094503.
- [23] B. Noda, H. Wada, K. Shibata, T. Yoshino, M. Katsuhara, I. Aoyagi, T. Mori, T. Taguchi, T. Kambayashi, K. Ishikawa, H. Takezoe, *Nanotechnology* **2007**, *18*, 424009.
- [24] D. De Caro, K. Jacob, H. Hahoui, C. Faulmann, L. Valade, T. Kadoya, T. Mori, J. Fraxedas, L. Viau, *New J. Chem.* **2011**, *35*, 1315.
- [25] T. Kadoya, D. De Caro, K. Jacob, C. Faulmann, L. Valade, T. Mori, *J. Mater. Chem.* **2011**, *21*, 18421.
- [26] M. Hiraoka, T. Hasegawa, Y. Abe, T. Yamada, Y. Tokura, H. Yamochi, G. Saito, T. Akutagawa, T. Nakamura, *Appl. Phys. Lett.* **2006**, *89*, 173504.
- [27] B. Mukherjee, M. Mukherjee, *Langmuir* **2011**, *27*, 11246.
- [28] T. Yamada, T. Hasegawa, M. Hiraoka, H. Matsui, Y. Tokura, G. Saito, *Appl. Phys. Lett.* **2008**, *92*, 233306.
- [29] G. P. Rigas, M. M. Payne, J. E. Anthony, P. N. Horton, F. A. Castro, M. Shkunov, *Nat. Commun.* **2016**, *7*, 13531.
- [30] T. Mori, *Chem. Lett.* **2011**, *40*, 428.
- [31] J. Zhang, H. Geng, T. S. Virk, Y. Zhao, J. Tan, C. A. Di, W. Xu, K. Singh, W. Hu, Z. Shuai, Y. Liu, D. Zhu, *Adv. Mater.* **2012**, *24*, 2603.
- [32] J. Zhang, J. Tan, Z. Ma, W. Xu, G. Zhao, H. Geng, C. Di, W. Hu, Z. Shuai, K. Singh, D. Zhu, *J. Am. Chem. Soc.* **2013**, *135*, 558.

- [33] Y. Qin, C. Cheng, H. Geng, C. Wang, W. Hu, W. Xu, Z. Shuai, D. Zhu, *Phys. Chem. Chem. Phys.* **2016**, *18*, 14094.
- [34] M. Sakai, H. Sakuma, Y. Ito, A. Saito, M. Nakamura, K. Kudo, *Phys. Rev. B - Condens. Matter Mater. Phys.* **2007**, *76*, 1.
- [35] K. P. Goetz, J. Tsutsumi, S. Pookpanratana, J. Chen, N. S. Corbin, R. K. Behera, V. Coropceanu, C. A. Richter, C. A. Hacker, T. Hasegawa, O. D. Jurchescu, *Adv. Electron. Mater.* **2016**, *2*, 1.
- [36] T. Han, L. Liu, X. Wu, L. Chen, C. Wang, M. Hanif, L. Lan, Z. Xie, Y. Ma, *J. Phys. Chem. C* **2016**, *120*, 1847.
- [37] B. A. Jones, A. Facchetti, T. J. Marks, M. R. Wasielewski, *Chem. Mater.* **2007**, *19*, 2703.
- [38] H. Rost, J. Ficker, J. S. Alonso, L. Leenders, I. McCulloch, *Synth. Met.* **2004**, *145*, 83.
- [39] T. J. Kistenmacher, T. E. Phillips, D. O. Cowan, *Acta Crystallogr. Sect. B Struct. Crystallogr. Cryst. Chem.* **1974**, *30*, 763.
- [40] K. Shibata, K. Ishikawa, H. Takezoe, H. Wada, T. Mori, K. Shibata, K. Ishikawa, H. Takezoe, *Appl. Phys. Lett.* **2008**, *92*, 023305.
- [41] P. Cosseddu, A. Bonfiglio, *Thin Solid Films* **2007**, *515*, 7551.
- [42] D. Kumaki, T. Umeda, S. Tokito, *Appl. Phys. Lett.* **2008**, *92*, 2006.
- [43] T. Minari, M. Kano, T. Miyadera, S. D. Wang, Y. Aoyagi, K. Tsukagoshi, *Appl. Phys. Lett.* **2009**, *94*, 2007.
- [44] Y. Li, H. Sun, Y. Shi, K. Tsukagoshi, *Sci. Technol. Adv. Mater.* **2014**, *15*, 024203.
- [45] T. Minari, P. Darmawan, C. Liu, Y. Li, Y. Xu, K. Tsukagoshi, *Appl. Phys. Lett.* **2012**, *100*, 093303.
- [46] S. Haas, Y. Takahashi, K. Takimiya, T. Hasegawa, *Appl. Phys. Lett.* **2009**, *95*, 2007.
- [47] I. Temiño, F. G. Del Pozo, M. R. Ajayakumar, S. Galindo, J. Puigdollers, M. Mas-Torrent, *Adv. Mater. Technol.* **2016**, *1*, 1600090.
- [48] Y. Xu, T. Minari, K. Tsukagoshi, J. A. Chroboczek, G. Ghibaudo, *J. Appl. Phys.* **2010**, *107*, 114507.
- [49] P. V Necliudov, M. S. Shur, D. J. Gundlach, T. N. Jackson, *Solid. State. Electron.* **2003**, *47*, 259.

- [50] M. Kano, T. Minari, K. Tsukagoshi, *Appl. Phys. Lett.* **2009**, *94*, 143304.
- [51] C. Ocal, R. Bachelet, L. Garzón, M. Stengel, F. Sánchez, J. Fontcuberta, *Chem. Mater.* **2012**, *24*, 4177.
- [52] W. N. Hansen, G. J. Hansen, *Surf. Sci.* **2001**, *481*, 172.
- [53] I. G. Hill, D. Milliron, J. Schwartz, A. Kahn, *Appl. Surf. Sci.* **2000**, *166*, 354.
- [54] I. Avilov, V. Geskin, J. Cornil, *Adv. Funct. Mater.* **2009**, *19*, 624.
- [55] R. J. Murdey, W. R. Salaneck, *Japanese J. Appl. Physics, Part 1 Regul. Pap. Short Notes Rev. Pap.* **2005**, *44*, 3751.
- [56] R. Pfattner, M. Mas-Torrent, C. Moreno, J. Puigdollers, R. Alcubilla, I. Bilotti, E. Venuti, A. Brillante, V. Laukhin, J. Veciana, C. Rovira, *J. Mater. Chem.* **2012**, *22*, 16011.
- [57] J. Zhang, J. Jin, H. Xu, Q. Zhang, W. Huang, *J. Mater. Chem. C* **2018**, *6*, 3485.
- [58] L. Sun, W. Zhu, F. Yang, B. Li, X. Ren, X. Zhang, W. Hu, *Phys. Chem. Chem. Phys.* **2018**, *20*, 6009.
- [59] Y. Qin, J. Zhang, X. Zheng, H. Geng, G. Zhao, W. Xu, W. Hu, Z. Shuai, D. Zhu, *Adv. Mater.* **2014**, *26*, 4093.
- [60] H.-D. Wu, F.-X. Wang, Y. Xiao, G.-B. Pan, *J. Mater. Chem. C* **2013**, *1*, 2286.
- [61] R. Ahmed, A. Kadashchuk, C. Simbrunner, G. Schwabegger, M. A. Baig, H. Sitter, *ACS Appl. Mater. Interfaces* **2014**, *6*, 15148.
- [62] K. Singh, A. Sharma, J. Zhang, W. Xu, D. Zhu, *Chem. Commun.* **2011**, *47*, 905.
- [63] R. Pfattner, M. Mas-Torrent, I. Bilotti, A. Brillante, S. Milita, F. Liscio, F. Biscarini, T. Marszalek, J. Ulanski, A. Nosal, M. Gazicki-Lipman, M. Leufgen, G. Schmidt, W. M. Laurens, V. Laukhin, J. Veciana, C. Rovira, L. W. Molenkamp, V. Laukhin, J. Veciana, C. Rovira, *Adv. Mater.* **2010**, *22*, 4198.

CHAPTER 7 EXPERIMENTAL METHODS

7.1. MATERIALS

ORGANIC SEMICONDUCTORS AND ORGANIC CHARGE-TRANSFER SALTS

2-(5,6-dimethoxy-1,3-benzodithiol-2-ylidene)-5,6-dimethoxy-1,3-benzodithiole (TTF 1); 2-(1,3-dithiol-2-ylidene)-[1,3]dithiolo[4,5-*f*]-2,1,3-benzothiadiazole (TTF 2); 6-(5,6-dimethoxy-1,3-benzodithiol-2-ylidene)-[1,3]dithiolo[4,5-*f*]-2,1,3-benzothiadiazole (TTF 3) and 6-(5,6-dimethoxy-1,3-benzodithiol-2-ylidene)-[1,3]dithiolo[4,5-*f*]-2,1,3-benzoselenadiazole (TTF 4). These four compounds were synthesised by Dr. Yang Geng in the University of Bern as described in references [1] and [2].

Bis(4,5-dihydronaphto[1,2-*d*])tetrathiafulvalene (BDHN-TTF) was purchased from Sigma-Aldrich and was used without any further purification.

Bis(naphtho[1,2-*d*])tetrathiafulvalene (BN-TTF) was synthesised from its precursor BDHN-TTF and the procedure is described in the synthesis part of this chapter.

meso-diphenyl tetrathia[22]annulene[2,1,2,1] (DPTTA) was synthesized as reported in reference [3].

2,7-bis(octyloxy)benzo[*b*]benzo[4,5]thieno[2,3-*d*]thiophene (C8OBTBT) was synthesized as described in reference [4] by the group of Prof. Yves Geerts in the Université Libre de Bruxelles (ULB).

2,3,5,6-Tetrafluoro-7,7,8,8-tetracyanoquinodimethane (F4-TCNQ) was purchased from Sigma Aldrich and was used without any further purification.

N,N'-bis(n-octyl)-dicyanoperylene-3,4:9,10-bis(dicarboximide) (PDI8CN2) was purchased from Polyera Inc and was used without any further purification.

Dibenzotetrathiafulvalene (DB-TTF) was purchased from Sigma Aldrich and was used without any further purification.

CHAPTER 7

Tetrathiafulvalene (TTF) was purchased from Sigma Aldrich and was used without any further purification.

Tetracyanoquinodimethane (TCNQ) was purchased from Sigma Aldrich and was used without any further purification.

TTF-TCNQ charge-transfer salt was purchased from Sigma Aldrich and was used without any further purification.

2,7-bis(octyl)benzo[*b*]benzo[4,5]thieno[2,3-*d*]thiophene (C8BTBT) was purchased from Sigma Aldrich and was used without any further purification.

Dithiophenetetrathiafulvalene (DT-TTF) was synthesized as described in ^[5] by Dr. Ajayakumar M. Rathamony in our group.

Bis(ethylenethio)tetrathiafulvalene (BET-TTF) was synthesized as described in ^[5] by Dr. Ajayakumar M. Rathamony in our group.

Fullerene (C₆₀) was purchased from Sigma Aldrich and was used without any further purification.

2,2'-(benzo[1,2-*b*:4,5-*b'*]dithiophene-4,8-diyl)dimalononitrile (DT-TCNQ) was synthesized as described in ^[6] by Dr. Ajayakumar M. Rathamony in our group.

POLYMERS

Polystyrene M_w 3000 g/mol (PS3k), polystyrene M_w 10000 g/mol (PS10k), polystyrene M_w 50000 g/mol (PS50k), polystyrene M_w 100000 g/mol (PS100k), polystyrene M_w 280000 g/mol (PS280k), polystyrene M_w 1000000 g/mol (PS1000k). All these polymers were purchased from Sigma Aldrich and were used without any further purification.

Poly(α-methyl)styrene M_w 100000 g/mol (PαMS100K) was purchased from Sigma Aldrich and used without any further purification.

Polymethylmethacrylate M_w 120000 g/mol (PMMA120K) was purchased from Sigma Aldrich and used without any further purification.

Cytop™ CTL-809M was purchased from Asahi Glass Co., Ltd.

MOLECULES FOR SELF-ASSEMBLED MONOLAYERS (SAMS)

***n*-Octadecyltrichlorosilane (OTS)** was purchased from Sigma Aldrich.

Phenyltrichlorosilane (PTS) was purchased from Sigma Aldrich.

2,3,4,5,6-Pentafluorothiophenol or 2,3,4,5,6-Pentafluorobenzenethiol (PFBT) was purchased from Sigma Aldrich.

Thiophenol (TP) or Benzenethiol was purchased from Sigma Aldrich.

SOLVENTS

Anhydrous chlorobenzene (CB), anisole, 1,2-dichlorobenzene (ODCB) and dimethylacetamide (DMAc) were purchased from Sigma Aldrich.

Dimethylformamide (DMF), tetrahydrofuran (THF) and acetone HPLC quality were purchased from Teknokroma Analitica S.A.

SUBSTRATES AND CHEMICALS FOR PHOTOLITHOGRAPHY

Shipley Microposit S1813 positive photoresist was purchased from Shipley.

Shipley Microposit MF-319 developer for positive photoresist Shipley Microposit S1813 was purchased from Shipley.

Highly n-doped silicon wafers were purchased from SiMat with the following characteristics:

Silicon Wafers with 200 nm SiO₂; Diameter: 100mm; Type/Dopant: N/Sb; Orientation: <1-0-0>; Resistivity: <0.05-0.02> Ω·cm; Thickness: 525±25 μm; Front Surface: Polished; Back Surface: Etched; Flats: SEMI Standard.

Gold and chromium for metal evaporation were 99.99% pure and were purchased from Kurt J. Lesker.

Test substrates for evaporation were purchased from Fraunhofer Institute, Germany. Each substrate had 16 transistors with interdigitated electrodes. The transistors were separated in groups of 4 with different channel lengths (L): 2.5 μm, 5 μm, 10 μm and 20 μm. All had a

CHAPTER 7

constant channel width (W) of 10 mm. A 230 nm thick silicon oxide layer acted as dielectric and a common n-doped Si acted as common gate electrode. Source and drain electrodes were made of a layer of 10 nm of indium tin oxide (ITO) and 30 nm of gold.

Shadow mask E2011 and stack E191 used to prepare top contact electrodes were purchased from Ossila. The mask had space for 12 substrates, each one of which had six transistors with L of 30, 40, 50, 60, 80 and 100 μm . All the channels had a constant W of 4 mm.

7.2. ORGANIC SEMICONDUCTOR SYNTHESIS

7.2.1. MESO-DIPHENYL TETRATHIA[22]ANNULENE[2,1,2,1] (DPTTA)

The synthesis of DPTTA was already described by Singh et al. in reference ^[3]. Herein, we describe step by step (**Figure 7.1**) the procedure we followed to obtain successfully the final organic semiconductor including the purification steps.

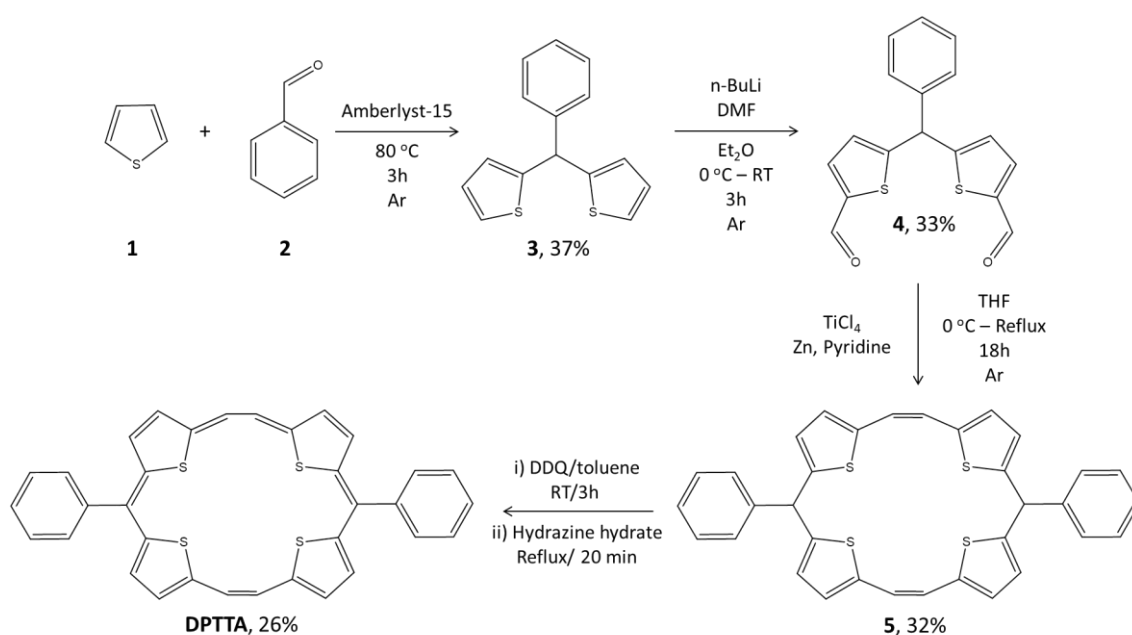


Figure 7.1. Synthetic route to DPTTA.

SYNTHESIS OF 2,2'-(PHENYLMETHYLENE)DITHIOPHENE (**3**)

10 mL of thiophene (**1**) and 4 mL of benzaldehyde (**2**) were placed in a round bottom flask together with 1.17 g of Amberlyst-15 and heated to 80 °C for 3 hours.^[7] During that time, the solution changed from colorless to dark brown. Then, the reaction mixture was cooled down to room temperature (RT) and diluted with CH₂Cl₂. After filtration of the diluted mixture, the solvent was removed by rotatory evaporation. To finish the mixture was purified by silica column (200-500 mesh) chromatography where hexane was used as eluent. The product **3** was obtained as a white powder and the reaction yield was 37%.

SYNTHESIS OF 5,5'-(PHENYLMETHYLENE)BIS(THIOPHENE-2-CARBALDEHYDE) (**4**)

500 mg of **3** were dissolved in dry diethylether and placed in an ice-salt bath. Then, *n*-BuLi (1.64 mL) was added drop wise using a syringe over a period of 30 minutes. After the addition, the solution turned to deep yellow indicating the presence of the dianion. After stirring at 0 °C for 30 min, an anhydrous solution of DMF (0.756 mL) in Et₂O (10 mL) was added also drop wise during 45 min and then the solution was gradually brought to RT. The stirring was continued for 1.5 h more. Then, the bath was removed and the solution kept for 30 min stirring at RT. The solution turned more turbid and developed a green colour on the flask wall. Afterwards, the reaction was poured into ice and the pH was adjusted to neutral by adding few drops of diluted HCl. Then, the product was extracted with ethyl acetate and washed with brine solution. After drying the organic solution with MgSO₄, the crude was purified with silica (200-500 mesh) chromatography (Hexane:EtOAc 430:70 V/V) and the purified product **4** was obtained as a brownish yellow oil. The reaction yield was 33%.

SYNTHESIS OF MESO-DIPHENYL 5,16-DIHYDRO TETRATHIA[20]ANNULENE (**5**)

First, the Zn was activated by treating the Zn dust with diluted HCl for 10-20 min and then washed with excess of ultrapure water, ethanol and diethylether. Once activated, the powder was dried under vacuum.

The previously activated Zn (3.7g) and 250 mL of dry THF were placed inside a 3-neck round bottom flask and cooled in an ice-salt bath. Then, 2.8 mL of TiCl₄ were slowly injected during 10-20 min. Once finished the addition, the mixture turned into a turbid yellowish solution and it was stirred for 30 min more. After that time, the solution was placed in a bath at 70 °C and was allowed to reflux for 2 hours. To this refluxing solution, 799 mg of **4** dissolved in 3.09 mL of dry pyridine were added drop wise over a period of 4-5 hours. After 18 hours more of reflux, the reaction mixture was brought to RT and mixed with 250 mL of K₂CO₃ (10 % aqueous) and filtered through Celite obtaining a deep yellow solution. After evaporating the THF, the mixture was extracted with CH₂Cl₂ and dried with anhydrous Na₂SO₄. Afterwards, the solvent was evaporated again and the crude product was purified by silica column (200-500 mesh) chromatography using Hexane:EtOAc 490:10 as eluent. The reaction product **5** was isolated as the first band with a 32% yield as an off-white solid.

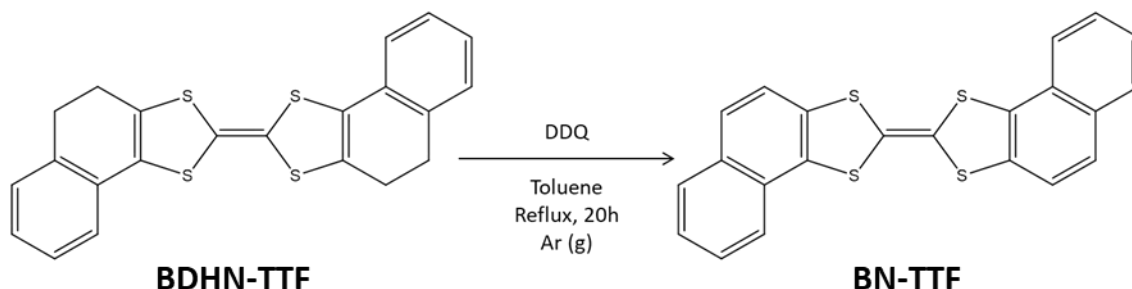
¹H NMR (400 MHz, CDCl₃; RT): δ (ppm) = 5.73 (s, 2H), 6.51-6.55 (m, 4H), 6.61-6.72 (m, 4H), 6.81-6.84 (m, 4H), 7.24-7.26 (m, 2H), 7.27-7.33 (m, 8H).

 SYNTHESIS OF MESO-DIPHENYL TETRATHIA[22]ANNULENE[2,1,2,1] (DPTTA)

234 mg of **5** were placed in 2-neck round bottom flask together with 306 mg of 2,3-dichloro-5,6-dicyano-1,4-benzoquinone (DDQ) and 12 mL of dry toluene at RT under an Ar atmosphere. The mixture was stirred for 3 hours. After that time, a black substance was isolated by filtration and then dried and transferred to another round-bottom flask with 10 mL of hydrazine hydrate. The mixture was then refluxed for 30 min. After filtration, the black precipitate was purified by silica column (200-500 mesh) chromatography using CH₂Cl₂ as eluent. DPTTA eluted as a green band in the column and after evaporating the solvent, a purple solid was obtained and washed with hexane. DPTTA was obtained with a yield of 26% and its identity was confirmed by ¹H-NMR.

¹H NMR (400 MHz, CDCl₃; RT) δ (ppm): 7.99 (d, 6H), 8.48 (s, 4H), 9.98 (d, 4H), 10.40 (d, 4H), 11.09 (s, 4H).

 7.2.2. BIS(NAPHTHO[1,2-D])TETRATHIAFULVALENE (BN-TTF)



7.3. OFET FABRICATION

7.3.1. PHOTOLITHOGRAPHY

Source and drain gold contacts for bottom-gate bottom-contact (BGBC) configuration substrates were fabricated on the aforementioned Si/SiO₂ wafers by photolithography. The fabrication process was carried out in a clean room class 10.000 by using a Micro-writer from Durham Magneto Optics Ltd. Afterwards chromium and gold metal layers were deposited by thermal evaporation at $2 \cdot 10^{-6}$ mbar using an Evaporation System Auto 306 from Boc Edwards. The whole process consisted in 7 steps described in the following:

1. A nitrogen gun was used to remove the traces of dust on the Si wafer. Then, the photoresist Shipley Microposit S1813 was spun coated at 5000 rpm for 25 s.
2. Right after the photoresist deposition, the wafer was placed on a hotplate at 95 °C for 60 s.
3. After baking the photoresist, the wafer was loaded in the Micro-writer and the previously designed pattern by the software CleWin4 was charged into the system. The quality parameter of the equipment used for this fabrication was normal with the turbo mode setting that permitted the use of multiple lasers working at the same time.
4. Once the writing process was finished, the wafer was immersed in Shipley Microposit MF-319 developer for 3 minutes to develop all the exposed photoresist. Then, the wafer was rinsed with ultrapure water and dried with a nitrogen gun to remove the remaining developer on the wafer.
5. Subsequently, the patterned wafer was placed inside the evaporator and the pumps were switched on. Once the pressure reached $2 \cdot 10^{-6}$ mbar, first chromium (5 nm) and then gold (40 nm) were evaporated.
6. Next step was to cut the full wafer, with the help of a ruler and a diamond scribe, in smaller substrates of approximately 13 mm wide and 23 mm long. Afterwards, the substrates were immersed in acetone and sonicated for 15 minutes, three times. Then, this process was repeated again in isopropanol.
7. After the lift-off, the substrates were dried with a nitrogen gun and stored in a polystyrene box until used.

Different channel widths (W) and lengths (L) have been used for the different works depending on the requirements of each material; however, an illustration of a substrate is presented in **Figure 7.3** as an example.

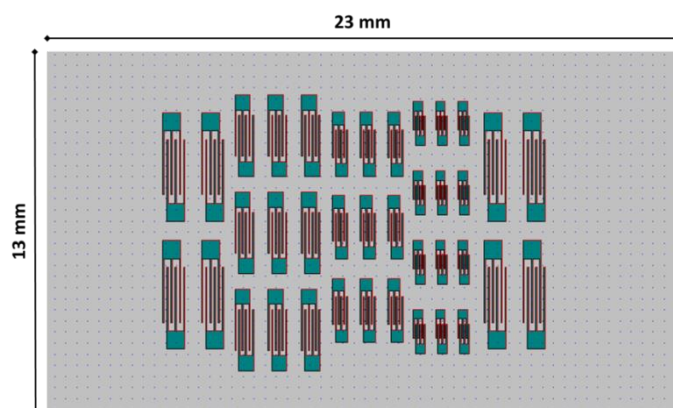


Figure 7.3. Example of a substrate with differently sized interdigitated electrodes for transistor fabrication.

7.3.2. TOP-CONTACT ELECTRODES FABRICATION

Top-contact gold electrodes were fabricated using the shadow mask E2011 and stack E191 (**Figure 7.4**) purchased from Ossila. Using this mask, channels of 4000 μm of width and 30, 40, 50, 60, 80, 100 μm were formed. Once the substrate was coated with the semiconducting film, the substrates were sandwiched between the shadow mask and the magnetic layer. To deposit the gold electrodes, the mask with the substrates was placed in the evaporation chamber and 40 nm of Au were deposited at a rate of 0.5 $\text{\AA}/\text{s}$ and a pressure of $2 \cdot 10^{-6}$ mbar.

In chapter 4, the fabrication of gold top electrodes with an interlayer of F4-TCNQ was carried out. This evaporation was performed with the same Ossila shadow mask, but this time prior to the Au deposition, a thin layer of 20 nm of F4-TCNQ was deposited at a rate of 0.1-0.2 $\text{\AA}/\text{s}$. This evaporation was performed in an evaporation chamber equipped with 2 different available sources, so, it was not necessary to depressurise the system between the two evaporations. In chapter 6, MoO_x/Au contacts (15/100 nm) were deposited following the same procedure.

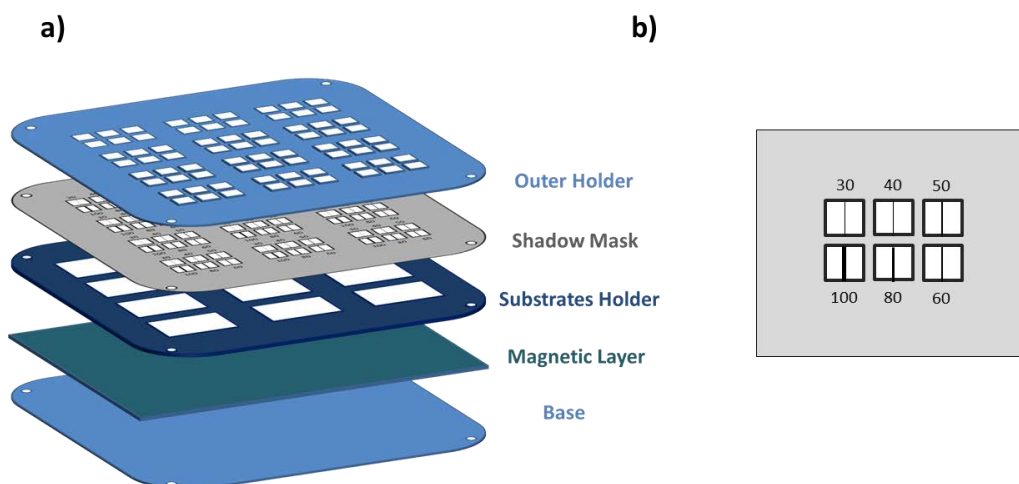


Figure 7.4. **(a)** Mask with all the layers for top contact evaporation and **(b)** a closer look to the shadow mask. The numbers correspond to the length of the channel in μm . All channels are 4 mm wide.

7.3.3. SELF-ASSEMBLED MONOLAYER FORMATION

Self-assembled monolayers (SAMs) were formed by two different methods: evaporation and immersion. The evaporation method was only used to form the OTS SAM, while for the rest of the SAMs the immersion methodology was used.

In the **evaporation method**, the samples (silicon oxide substrates) were activated using an ozone treatment during 25 minutes and immediately transferred to the vacuum chamber where a small quantity of OTS was inside a small Petri dish. Then, the vacuum pump and the temperature controller were switched on.

Once the activated samples and the OTS were in the vacuum chamber, they were covered with a bigger Petri dish and the pump was switched on. When the pressure reached 10 mbar, the pump was shut and the hotplate was set to 120 $^{\circ}\text{C}$. It stayed like that for one hour, then the heater was switched off. When the sample reached room temperature again, the chamber was opened and the samples were cleaned with toluene, acetone and isopropanol to remove the excess of molecules.

In the **immersion method**, a 15 mM concentration solution of the molecule was prepared in toluene for OTS and PTS and in isopropanol for PFBT and TP. The substrate was activated with the same ozone treatment used before (25 minutes) and placed immediately into the solution for 15 minutes. After that time, the substrates were removed from the solution and rinsed with toluene, acetone and isopropanol if the desired SAM was OTS or PTS or rinsed with isopropanol if the molecules were PFBT or TP.

7.3.4. DEPOSITION TECHNIQUES

To deposit the OSC films four techniques were used: drop casting, thermal evaporation, bar-assisted meniscus shearing and spray coating (also used to prepare organic contacts).

- **Drop casting** of TTFs **1-4** were carried out using a solution of the OSCs in anhydrous 1,2-dichlorobenzene at a concentration of 1 mg/ml at 100 °C. This solution was casted on silicon substrate which was stored in an oven at 100 °C and then covered with a Petri dish to slow down the evaporation process. After complete evaporation of the solvent, the samples were slowly cooled down to room temperature to prevent possible stress in the single crystals.

Once the single crystals were ready, source and drain electrodes were fabricated with graphite paste (Dotite XC-12) allowing the paste to dry before measuring the electrical characteristics. Later, channel length and width were measured with an Olympus BX51 optical microscope. In case of TTF-**4**, the crystals were grown directly on a Si/SiO₂ substrate with Au/Cr electrodes patterned by photolithography.

- **Thermal evaporation** of TTFs **1-4** were carried out on Si/SiO₂ test chips purchased from Fraunhofer Institute. TTFs were thermally evaporated at $T = 115\text{-}150\text{ }^{\circ}\text{C}$, $170\text{-}200\text{ }^{\circ}\text{C}$, $180\text{-}200\text{ }^{\circ}\text{C}$ and $190\text{-}230\text{ }^{\circ}\text{C}$ for TTFs **1-4**, respectively, and $P = 2 \cdot 10^{-6}$ mbar, so as to give an evaporation rate of around 0.5 \AA/s . On half of the substrates a SAM of OTS was formed on the SiO₂ prior to the thermal evaporation following the aforementioned evaporation method.

Thermal evaporation of BDHN-TTF and BN-TTF were carried out on substrates patterned by photolithography with interdigitated electrodes ($W = 25\text{ }\mu\text{m}$ and $L = 25\text{ }\mu\text{m}$) where the silicon oxide was modified with an OTS SAM. The semiconductor was deposited at a $P = 9 \cdot 10^{-7}$ mbar and at the necessary temperature, around $150\text{ }^{\circ}\text{C}$, so as to have a deposition rate of $0.2\text{-}0.3\text{ \AA/s}$.

- **Bar-assisted meniscus shearing (BAMS)** was performed on substrates with interdigitated electrodes fabricated by photolithography. Typically, $30\text{ }\mu\text{l}$ of the ink are placed in the gap of approximately $100\text{ }\mu\text{m}$ between the bar and the substrate and then the drop was sheared usually at a speed of 10 mm/s and a temperature of $105\text{ }^{\circ}\text{C}$ if not indicated otherwise. In the case of DPTTA, the stainless steel bar was changed for a polytetrafluoroethylene (PTFE) bar to obtain a crystalline film. It is important that all the OSC in the solutions are dissolved very well to avoid the formation of holes in the film caused by the precipitated particles.
- **Spray coating** of TTF-TCNQ was carried out with a solution of the charge-transfer salt in acetone/THF with a concentration of $0.3/0.9\text{ mg/mL}$ achieved after strong agitation in ultrasonic bath for four hours. TTF-TCNQ solution remained stable over time

without any significant change during one month of storage. Once the solution was prepared, it was sprayed on the substrates which were inside the shadow mask for top contact evaporation (**Figure 7.4**) with an airbrush that used pressurised nitrogen to aerosolise it. The airbrush (Sagola junior 140, 0.8 mm nozzle diameter) was fixed 18 cm above the sample (nozzle to substrate distance) and 40 ml of TTF-TCNQ solution were deposited. The deposited layer thickness was very sensitive to the distance: separation over 20 cm resulted in a significantly reduced film thickness and distances shorter than 17 cm caused the undesired formation of a wet film on the substrate surface. The process was carried out at room temperature, in ambient conditions, and took approximately 4 minutes (10 ml/min flow rate) at a nitrogen pressure of 1.5 bar. The spray coating was also performed at an elevated temperature of 80 °C without giving rise to notable differences in the TTF-TCNQ sheet resistances. Furthermore, to characterize the coating coverage, TTF-TCNQ was spray-coated onto Si/SiO₂ substrates with four point probe gold contacts patterned by photolithography.

Regarding the use of spray coating for the formation of single crystals, it was performed on Si/SiO₂ substrates of (1.5 x 1.5) cm² covered with 300 µL of dimethylformamide. The propellant (N₂) pressure was set below 10 psi and the deposition was intermittent to avoid the ejection of the DMF. The nozzle-substrate distance was set at 25 cm and the angle between the substrate normal vector and the spray jet was approximately of 20°. The OSC solution concentration was set at 6 mg/mL for the used OSCs, using toluene as solvent, and 1 mg/mL for OSC charge-transfer mixtures where toluene, dichloromethane and *o*-xylene were chosen for DPTTA/DT-TCNQ, DB-TTF/TCNQ and BET-TTF/C₆₀, respectively.

7.3.5. INK FORMULATION FOR BAMS

All the OSC inks comprising from chapter 3 to 6, were fabricated using the same methodology. First, the binding polymers were dissolved in CB heating if necessary to totally dissolve them. Then, the semiconductor was accurately weighted and the polymer solution was added using a micropipette to the solid organic semiconductor.

Even though several concentrations were tested in order to improve the resulting films characteristics, the usual concentration range used was from 1.8 to 2.3% wt. in CB. All different formulations used in this thesis are listed in the following:

- **DPTTA:** Optimized inks were prepared in a weight ratio of DPTTA:PS 1:2 for PS10k and PS100k and 1:3 for PS3k and PS10k. This last formulation was used to fabricate the active layers for EGOFETs. Solution final concentration (DPTTA+PS) was 22.6 mg/mL when PS10k and PS100k in 1:2 ratio were used, and 26 mg/mL for PS3k and 20 mg/mL for PS10k when they were mixed in a 1:3 ratio with the OSC. The solvent in all the

cases was anhydrous CB. Amber vials were used to protect the formulation against the possible harmful effects of light.

- **C8OBTBT:** Optimized inks were prepared in a weight ratio of C8OBTBT:PS 4:1 for PS3k, PS10k, PS100k and PS280k. Furthermore, a solution without PS was also prepared. Solutions final concentration (C8OBTBT+PS or C8OBTBT) was 22.6 mg/ml in anhydrous CB in all cases. With this OSC amber vials were not required.
- **PDI8CN2:** The optimized ink was PDI8CN2:PS 280k; 1:2. Furthermore, an ink without polymer was prepared. Solution final concentration (PDI8CN2+PS or PDI8CN2) in all cases was 22.6 mg/ml in anhydrous CB. Amber vials were used to protect the ink against the possible harmful effects of light.
- **DB-TTF:** Optimized inks were prepared in a weight ratio of DB-TTF:PS3K 1:2 with a final concentration of 22.6 mg/mL in anhydrous CB. Transparent vials were used with this OSC.
- **C8BTBT:** The optimized ink was C8BTBT:PS 10k; 4:1 as it was described in reference [7]. Final concentration (C8BTBT+PS) was 22.6 mg/ml in anhydrous CB. Amber vials were not required.

7.4. ORGANIC SEMICONDUCTOR CHARACTERISATION

- **Cyclic voltammetry (CV)** experiments were carried out with a VersaSTAT 3 under a dry and oxygen free atmosphere, accomplished by bubbling $\text{Ar}_{(\text{g})}$ in the solution for 30 minutes prior to the measurements. All measurements were performed using two Pt wires, one as counter electrode and the other as working electrode, with $\text{Bu}_4\text{N}(\text{PF}_6)$ ($c = 0.1 \text{ M}$) as supporting electrolyte and a scan rate of 100 mV/s (**Figure 7.5**). TTF **1**, BDHN-TTF and BN-TTF experiments were performed at room temperature in CH_2Cl_2 with an Ag/AgCl as reference electrode. On the other hand, TTF **2**, TTF **3** and TTF **4** measurements were carried out in 1,2-dichlorobenzene at 150°C using $\text{Ag}_{(\text{s})}$ as pseudo reference electrode. Afterwards, ferrocene was added as internal reference. In these conditions the redox Fc/Fc^+ process occurred at $0.44 \text{ V vs. Ag}_{(\text{s})}$.

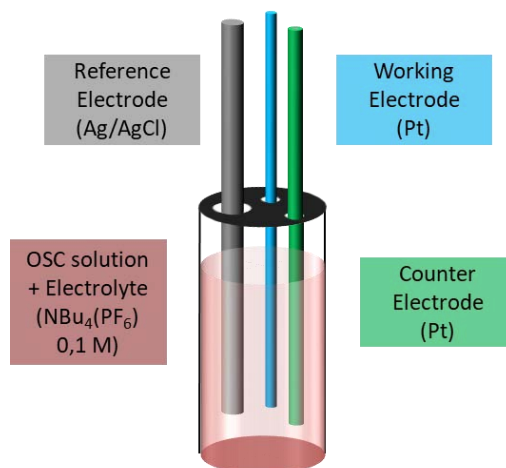


Figure 7.5. Schematic representation of the cyclic voltammetry set up.

- **UV-vis spectroscopy** spectra were recorded in CH_2Cl_2 ($c = 10^{-4} \text{ M}$) with a Cary 5000 UV-vis-NIR. Quartz cuvettes with an optical path of 1 cm were used.
- **MALDI-TOF mass spectrometry** was recorded on a Bruker Ultraflex II TOF spectrometer.
- **IR spectroscopy** was performed with a FT-IR PerkinElmer spectrometer with a diamond ATR accessory.
- **NMR** measurements were performed with a Bruker Avance 600 MHz NMR spectrometer for BN-TTF and a Bruker Ascend 400 MHz NMR spectrometer for DPTTA.

7.5. THIN FILM AND SINGLE CRYSTAL CHARACTERISATION

- **Optical microscopy and cross-polarized optical microscopy** images were obtained using an Olympus BX51 equipped with a light polariser and an analyser.
- **Atomic force microscopy (AFM)** images were acquired in tapping mode using a 5500LS SPM system from Agilent Technologies for TTFs **1-4** samples and 5100 SPM system from Agilent Technologies for the rest. All images were obtained in ambient conditions and images were analysed Gwyddion 2.47 software.
- **X-ray powder diffraction (XRPD)** measurements were performed using a Rigaku modular X-ray powder diffractometer for TTFs **1-4** samples and with a PANalytical X'PERT PRO diffractometer MRD for the rest.
- **X-ray single crystal diffraction** characterisations were carried out with a Bruker AXS SMART APEX using graphite-monochromated Mo K α radiation ($\lambda = 0.71073 \text{ \AA}$). Full-sphere data collection was carried out with ϕ and ω scans. The programs: data collection, Smart version 5.631 (Bruker AXS 1997-02); data reduction, Saint + version 6.36A (Bruker AXS 2001); absorption correction, SADABS version 2.10 (Bruker AXS 2001). Structure solution and refinement was done by using SHELXTL Version 6.14 (Bruker AXS 2000-2003). The structure was solved by direct methods and refined by full-matrix least-squares methods on F2 non-hydrogen atoms were refined anisotropically. The H-atoms were placed in geometrically optimized positions and forced to ride on the atom to which they are attached.
- **Infrared spectroscopy (IR)** spectra were obtained with an IR-spectrometer Vertex 70 from Bruker.
- **Raman spectroscopy** measurements were carried out with a Horiba XploRA PLUS spectrometer equipped with a suitable edge filter and coupled to an Olympus BX51 confocal microscope with 100x and 10x objectives which allow for a lateral resolution lower than $1 \text{ }\mu\text{m}$ with the higher magnification. This experimental configuration allowed gathering information on the polymorphic composition in crystal domains of micrometric dimensions. The excitation wavelength used was the 532 nm line from a Diode-Pumped Solid State (DPSS), a combination of Nd:YVO₄ pumped by a 808 nm diode laser and a non-linear KTP crystals as a frequency doubler, with a nominal power of 30 W. The power was reduced by neutral density filters to avoid sample damage. The Horiba LabSpec 6 software was used to operate the spectrometer.
- **Polarisation-Modulation Infrared Reflection-Absorption Spectroscopy (PM-IRRAS)** spectra were recorded by using a Bruker Vertex 70 spectrometer with PM50 module equipped with a liquid-nitrogen-cooled mercury-cadmium-telluride (MCT) photodetector and a permanently aligned Rock Solid interferometer. To reduce

absorption due to water and carbon dioxide, the spectrometer was purged by fluxing nitrogen gas. The Bruker spectroscopy software OPUS, version 4.2, was used to operate the spectrometer. Reflection measurements were performed with an aperture of 6 mm in diameter on the primary side and on aperture of the secondary side at a resolution of 2 cm^{-1} . The incidence angle was set to the Brewster angle of the SiO_2 at 57° to acquire the best signal-to-noise ratio.

- **Scanning electron microscope (SEM)** images were acquired with a QUANTA FEI 200 FEG-ESEM.
- **Time-of-flight secondary ions mass spectrometry (TOF-SIMS)** was used to determine the chemical compositional profile of the PDI8CN2/PS thin film. Surface sputter etching was accomplished with Cs beam, over a $300\text{ }\mu\text{m} \times 300\text{ }\mu\text{m}$ area using 1 keV energy settings raster. A pulsed beam of 25 keV Bi^+ ions scanned over a $50\text{ }\mu\text{m} \times 50\text{ }\mu\text{m}$ region centred within the sputtered area was used. Analysis cycle time was 100 μs and sputtering cycle was 1.6 s and 0.5 s flood gun compensation. A high current beam of low energy ($< 20\text{ eV}$) electrons was employed for charge compensation, and negative ions were analyzed.
- **Electrochemical impedance spectroscopy (EIS)** measurements were carried out with a Novocontrol Alpha-AN impedance analyser equipped with POT/GAL 30 V/2 A electrochemical interface.
- **Profilometry** measurements were carried out with a profilometer model Alphastep D500 from KLA Tencor Inc. equipped with a $2\text{ }\mu\text{m}$ diamond tip.

7.6. ELECTRICAL CHARACTERISATION

All the electrical characterisation in this work has been carried out with four different measurement systems:

- A Hewlett-Packard 4156A semiconductor parameter analyser was used to measure TTFs **1-4** thin films OFET characteristics under vacuum ($P \approx 50$ mbar) right after the thermal evaporation. It was also used to perform measurements of density of states (DoS) in ambient conditions and darkness coupled with a temperature controller.
- A Keithley 2612A Source Meter was used to perform the OFET characterisation of the TTFs **1-4** in darkness and under ambient conditions inside a Kärl SÜSS probe station. BDHN-TTF/BN-TTF films were also measured by the same source meter but inside a glovebox to prevent their rapid degradation.
- An Agilent B1500A semiconductor device analyser was used to perform all OFET and EGOFET measurements of DPTTA (except switching speed), C8OBTBT, PDI8CN2 (except DoS), DB-TTF and C8BTBT. It was also used to characterise the sheet resistance of TTF-TCNQ films. All measurements were carried out in air and darkness inside a Kärl SÜSS probe station.
- A Keithley 2604B was used with an embedded test script to perform the switching speed measurements on EGOFETs.

OFET AND EGOFET PARAMETERS EXTRACTION

Field-effect mobility ($\mu_{FE,sat}$) was extracted in saturation regime from the transfer characteristics using the slope (m) of the linear fit of $|I_{DS}|^{1/2}$ versus V_{GS} . Afterwards, the following formula was applied:

$$\mu_{FE,sat} = m \cdot \frac{2 \cdot L}{W} \cdot \frac{1}{C} \quad (7.1)$$

Where L and W stands for channel length and width, respectively, and C stands for capacitance. **Threshold voltage** (V_{TH}) was calculated with the following equation:

$$V_{TH} = -\frac{n}{m} \quad (7.2)$$

CHAPTER 7

Where n stands for the y-intercept of the linear fit.

For extracting the **subthreshold swing (SS)** the following formula was used:

$$SS = \frac{\partial V_{GS}}{\partial (\log I_{DS})} \quad (7.3)$$

The **maximum density of traps (N_T)** was estimated using the following formula extracted from reference ^[8]:

$$N_T = \frac{C_i}{q^2} \left[\frac{q SS \log e}{k_B T} - 1 \right] \quad (7.4)$$

Where k_B is Boltzmann's constant, T is the temperature and e is the base of the natural logarithm.

7.7. REFERENCES

- [1] Y. Geng, R. Pfattner, A. Campos, J. Hauser, V. Laukhin, J. Puigdollers, J. Veciana, M. Mas-Torrent, C. Rovira, S. Decurtins, S.-X. S. X. Liu, *Chem. - A Eur. J.* **2014**, *20*, 7136.
- [2] Y. Geng, R. Pfattner, A. Campos, W. Wang, O. Jeannin, J. Hauser, J. Puigdollers, S. T. Bromley, S. Decurtins, J. Veciana, C. Rovira, M. Mas-Torrent, S. X. Liu, *Chem. - A Eur. J.* **2014**, *20*, 16672.
- [3] K. Singh, A. Sharma, J. Zhang, W. Xu, D. Zhu, *Chem. Commun.* **2011**, *47*, 905.
- [4] C. Ruzie, J. Karpinska, A. Laurent, L. Sanguinet, S. Hunter, T. D. Anthopoulos, V. Lemaure, J. Cornil, A. R. Kennedy, O. Fenwick, P. Samorì, G. Schweicher, B. Chattopadhyay, Y. H. Geerts, *J. Mater. Chem. C* **2016**, *4*, 4863.
- [5] C. Rovira, J. Veciana, N. Santaló, J. Tarrés, J. Cirujeda, E. Molins, J. Llorca, E. Espinosa, *J. Org. Chem.* **1994**, *59*, 3307.
- [6] K. Kobayashi, C. L. Gajurel, K. Umemoto, Y. Mazaki, *Bull. Chem. Soc. Jpn.* **1992**, *65*, 2168.
- [7] T. S. Virk, K. Singh, Y. Qin, W. Xu, D. Zhu, *RSC Adv.* **2014**, *4*, 37503.
- [8] M. H. Yoon, C. Kim, A. Facchetti, T. J. Marks, *J. Am. Chem. Soc.* **2006**, *128*, 12851.

CONCLUSIONS

In this thesis we have studied the behaviour of organic semiconductors as active layers in organic field-effect transistors (OFETs). We have focused on the impact of the molecular and crystal structure and on the deposition conditions in the OFET electrical characteristics. Special attention has been paid to the processability of the molecules employed, enhancing it by blending the organic semiconductor with insulating polymers, and to the organic semiconductor morphology and crystalline structure. This research work has led to the following conclusions:

- i) The modification of the chemical structure of a *p*-type organic semiconductor can modify the highest occupied molecular orbital (HOMO) energies importantly impacting the stability of the electronic transport in ambient conditions. In this case, the substitution of benzothiadiazole groups for methoxy moieties in TTF derivatives resulted in an enhancement of the stability towards oxygen and moisture of the OFETs based on these semiconductors.
- ii) The modification of the chemical structure of an organic semiconductor can lead to different crystal structures having a huge impact on the electronic transport. In the case of BDHN-TTF, the extension of the π -conjugation resulted in a more planar molecule, BN-TTF, which preferred to pack following a displaced cofacial packing with a strong 1D dimensionality of the electronic transport instead of the 2D herringbone-like crystal structure displayed by the non-fully conjugated molecule BDHN-TTF. Both the strength of the electronic coupling and the electronic dimensionality are crucial parameters that determine the final charge carrier mobility.
- iii) Blending an organic semiconductor together with an insulating polymer improves the processability, performance and stability of the semiconductor when used as an active layer in an OFET. Transistors based on solution-processed thin-films of the quite unexplored *p*-type semiconductor DPTTA have been successfully fabricated when this material was blended with polystyrene. High performance OFETs were achieved showing a mobility beyond $1 \text{ cm}^2/\text{V}\cdot\text{s}$. EGOFTs based on this formulation could work in continuous in water for more than 12 hours with only a 20% increase in the initial current indicating the robustness of these devices in the media.
- iv) The stability of a kinetic phase in a polymorphic semiconductor can be stabilised by blending the organic semiconductor with an insulating polymer. In addition, the use of a larger molecular weight polymer has also a beneficial impact on the stability of the polycrystalline layer. The *p*-type organic semiconductor C8OBTBT has been studied as high performance organic semiconductor that displays polymorphism. Thin-films of this material have been used as active layer for transistors and its crystal structure, performance and morphology have been studied over time. Generally, the devices

based on films of blends of the OSC with polystyrene exhibited an enhanced performance compared with the ones based on only the OSC, especially at high coating speeds. In all the employed deposition conditions the surface-induced phase was formed exhibiting an excellent device performance with a mobility of up to $\sim 1 \text{ cm}^2/\text{V}\cdot\text{s}$. Even if the thin-films have demonstrated to be stable in terms of OFET performance over 3 months, at the end of this time a conversion to the thermodynamic phase has been observed in the edges of the domains in films of C8OBTBT:PS3K, but this conversion was absent when using a higher molecular weight polystyrene.

v) *n*-Type organic semiconductors can be stabilised by blending them with an insulating polymer. The enhancement of the electrical characteristics and stability of OFETs based on blends of the *n*-type organic semiconductor PDI8CN2 and an insulating polymer was investigated in this thesis. The OSC was deposited by BAMS together with polystyrene (PS) and without it, and the morphology, crystal structure, electrical characteristics and stability of both resulting thin-films were investigated. It was observed that the thin-film with polymer displayed better characteristics, was more stable and had a lower density of states in the gap, suggesting a more favoured dielectric/semiconductor interface. This was attributed to the vertical phase separation that takes place during the film deposition: the OSC crystallises on top of a PS layer that passivates the polar groups of the dielectric which are detrimental for the electron transport, but also the OSC is encapsulated by a thin PS layer that protects it from the environment.

vi) Spray coating is a suitable printing technique for the deposition of electrodes based on the organic metal TTF-TCNQ. In this case, source and drain electrodes were deposited successfully by spray coating on a thin-film of C8BTBT. OFETs based on C8BTBT with TTF-TCNQ electrodes displayed better charge injection than when MoO_x/Au was used as the material of the electrodes. This better injection was attributed to the dipoles present at the organic dielectric/organic semiconductor interface.

